T.R.
GEBZE TECHNICAL UNIVERSITY
GRADUATE SCHOOL

CHARACTERIZATION AND INVESTIGATION OF BIOLOGICAL EFFECTS OF THE BIOACTIVE COMPOUND LOADED MICROALGAE-BASED MICROCARRIER SYSTEMS PRODUCED BY ELECTROSPRAYING TECHNIQUE

BASAK DALBAYRAK

A THESIS OF DOCTORATE
DEPARTMENT OF BIOTECHNOLOGY

ADVISOR: PROF. DR. ELIF DAMLA ARISAN

JUNE 2025

T.R.
GEBZE TECHNICAL UNIVERSITY
GRADUATE SCHOOL

CHARACTERIZATION AND INVESTIGATION OF BIOLOGICAL EFFECTS OF THE BIOACTIVE COMPOUND LOADED MICROALGAE-BASED MICROCARRIER SYSTEMS PRODUCED BY ELECTROSPRAYING TECHNIQUE

BASAK DALBAYRAK

A THESIS OF DOCTORATE
DEPARTMENT OF BIOTECHNOLOGY

ADVISOR: PROF. DR. ELIF DAMLA ARISAN

JUNE 2025

T.C.
GEBZE TEKNİK ÜNİVERSİTESİ
LİSANSÜSTÜ EĞİTİM ENSTİTÜSÜ

ELEKTROSPREY TEKNİĞİ İLE ÜRETİLEN BİYOAKTİF BİLEŞİK YÜKLÜ MİKROALG TABANLI MİKROTAŞIYICI SİSTEMLERİN KARAKTERİZASYONU VE BİYOLOJİK ETKİLERİNİN İNCELENMESİ

BAŞAK DALBAYRAK

DOKTORA TEZİ
BİYOTEKNOLOJİ ANABİLİM DALI

DANIŞMAN: PROF. DR. ELİF DAMLA ARISAN

HAZİRAN 2025

DOCTORATE JURY APPROVAL FORM

A thesis submitted by Basak Dalbayrak, defended on 18/06/2025 before the jury formed on 11/06/2025 and 2025/31 numbered decision of the GTU Graduate Administration Board, has been accepted as a DOCTORATE thesis in the Department of Biotechnology.

JURY

MEMBER (THESIS ADVISOR)	: PROF. DR. ELİF DAMLA ARISAN
MEMBER	: PROF. DR. IŞIL KURNAZ
MEMBER	: PROF. DR. PINAR OBAKAN YERLİKAYA
MEMBER	: ASSIST. PROF. DR. BAHAR YILDIZ KUTMAN
MEMBER	: PROF. DR. OĞUZHAN GÜNDÜZ

APPROVAL

Gebze Technical University Graduate Administration Board

…..…/…..…/..…… date and ……/…….. numbered decision.

SIGNATURE/SEAL

To my family

ABSTRACT

The advancement of multifunctional biomaterials is pivotal for the next generation of regenerative medicine and tissue engineering therapies. This thesis presents the design, fabrication, and comprehensive evaluation of poly(lactic acid) (PLA)-based microparticles encapsulating microalgae-derived Spirulina extract, niacinamide, and palmitoyl tripeptide-1, with the aim of creating scalable, biocompatible microcarrier systems for skin repair. PLA, a biodegradable and FDA-approved polymer, was selected for its tunable degradation and structural versatility, while *Spirulina* was chosen for its rich repertoire of antioxidants, anti-inflammatory polysaccharides, and essential nutrients. Niacinamide and palmitoyl tripeptide-1 were incorporated to enhance antioxidant, anti-inflammatory, and extracellular matrix (ECM) remodelling effects. Microparticles were fabricated using the electrospraying technique, enabling precise control over particle size, morphology, and encapsulation efficiency. Optimization of process parameters yielded monodisperse, spherical particles with high bioactive loading and minimal agglomeration. Physicochemical characterization via SEM, FT-IR, and release profiling confirmed the preservation of bioactive integrity and demonstrated sustained, controlled release of encapsulated compounds, addressing the challenge of rapid *Spirulina* degradation and the need for prolonged niacinamide bioavailability. *In vitro* studies using human umbilical vein endothelial cells (HUVECs) and keratinocytes (HaCaTs) revealed that both blank and bioactive-loaded PLA/*Spirulina* microparticles were non-cytotoxic and promoted cell adhesion, proliferation, and migration. Notably, dual-loaded formulations exhibited superior efficacy in mitigating oxidative stress, preserving mitochondrial function, and accelerating wound closure in scratch assays, compared to single-agent or free-compound controls. These effects were attributed to the additive action of Spirulina's antioxidants and the barrier-repair and ECM-stimulating properties of niacinamide and palmitoyl tripeptide-1. Current strategies in regenerative medicine utilize synthetic polymers and natural extracts to develop advanced delivery systems for therapeutic applications. PLA-based carriers are established for their biocompatibility, but the integration of microalgae-derived antioxidants with added peptides and vitamins in a single, tunable platform remains largely unexplored. This thesis is the first to report the co-encapsulation of Spirulina extract, niacinamide, and palmitoyl tripeptide-1 within electrosprayed PLA microparticles, forming a multifunctional microcarrier system for skin repair. The approach uniquely combines natural and synthetic bioactives, harnessing their additive effects while achieving precise control over particle characteristics and sustained, controlled release. Mechanistic insights into the modulation of skin cell signaling pathways further distinguish this thesis, establishing a robust and versatile platform for regenerative applications.

Keywords: Multifunctional biomaterials, Electrospraying, Poly(lactic acid) (PLA) microparticles, Spirulina extract, Skin tissue regeneration

ÖZET

Çok fonksiyonlu biyomalzemelerin ilerlemesi, rejeneratif tıbbın ve doku mühendisliği tedavilerinin bir sonraki nesli için çok önemlidir. Bu tez, cilt onarımı için ölçeklenebilir, biyouyumlu mikrotaşıyıcı sistemler oluşturma amacıyla, mikroalg kaynaklı Spirulina özütü, niasinamid ve palmitoyl tripeptit-1'i kapsülleyen poli(laktik asit) (PLA) bazlı mikropartiküllerin tasarımını, üretimini ve kapsamlı değerlendirmesini sunmaktadır. PLA, ayarlanabilir bozunabilirliği ve yapısal çok yönlülüğü nedeniyle seçilen, biyobozunur ve FDA onaylı bir polimerdir; Spirulina ise zengin antioksidanlar, anti-inflamatuar polisakkaritler ve temel besin maddeleri repertuarı nedeniyle seçilmiştir. Antioksidan, anti-inflamatuar ve ekstrasellüler matriks (ECM) yeniden şekillendirme etkilerini artırmak için niasinamid ve palmitoyl tripeptit-1 eklenmiştir. Mikropartiküller, parçacık boyutu, morfolojisi ve kapsülleme verimliliği üzerinde hassas kontrol sağlayan elektrosprey tekniği kullanılarak üretilmiştir. Proses parametrelerinin optimizasyonu, yüksek biyoaktif yükleme ve minimum aglomerasyon ile monodisper, küresel parçacıklar elde edilmesini sağlamıştır. SEM, FT-IR ve salım profillemesi yoluyla yapılan fizikokimyasal karakterizasyon, biyoaktif bütünlüğünün korunduğunu doğrulamış ve enkapsüle edilen bileşiklerin sürekli, kontrollü salımını göstermiştir; bu da hızlı Spirulina bozunması zorluğunu ve uzamış niasinamid biyoyararlanımı ihtiyacını karşılamaktadır. *İn vitro* çalışmalar, insan göbek kordonu endotelyal hücreleri (HUVEC) ve keratinositler (HaCaT) kullanılarak hem boş hem de biyoaktif yüklü PLA/Spirulina mikropartiküllerinin sitotoksik olmadığını ve hücre adezyonu, proliferasyonu ve migrasyonunu desteklediğini ortaya koymuştur. Özellikle, çift yüklü formülasyonlar, tek ajanlı veya serbest bileşik kontrollerine kıyasla, oksidatif stresi azaltmada, mitokondriyal fonksiyonu korumada ve yara kapanmasını hızlandırmada üstün etkinlik göstermiştir. Bu etkiler, Spirulinanın antioksidanlarının ekleyici etkisine ve niasinamid ile palmitoyl tripeptit-1'in bariyer onarıcı ve ECM uyarıcı özelliklerine atfedilmiştir. Güncel rejeneratif tıp stratejileri, terapötik uygulamalar için gelişmiş taşıyıcı sistemler geliştirmek amacıyla sentetik polimerler ve doğal ekstreler kullanmaktadır. PLA bazlı taşıyıcılar biyouyumlulukları ile bilinir; ancak mikroalg kaynaklı antioksidanların, eklenen peptitler ve vitaminlerle birlikte tek, ayarlanabilir bir platformda entegrasyonu büyük ölçüde keşfedilmemiştir. Bu tez, Spirulina ekstresi, niasinamid ve palmitoyl tripeptit-1'in elektrosprey ile elde edilen PLA mikropartiküller içinde birlikte enkapsülasyonunu rapor eden ilk çalışmadır ve cilt onarımı için çok fonksiyonlu bir mikrotaşıyıcı sistem oluşturur. Bu yaklaşım, doğal ve sentetik biyoaktifleri benzersiz şekilde birleştirerek, bunların ekleyici etkilerinden faydalanırken parçacık özellikleri ve sürekli, kontrollü salım üzerinde hassas kontrol sağlar. Cilt hücresi sinyal yolaklarının modülasyonuna dair mekanistik içgörüler, bu tezi daha da ayırt ederek rejeneratif uygulamalar için sağlam ve çok yönlü bir platform oluşturur.

Anahtar Kelimeler: Çok fonksiyonlu biyomalzemeler, Elektrosprey, Poli(laktik asit) (PLA) mikropartiküller, Spirulina ekstresi, Cilt doku rejenerasyonu

ACKNOWLEDGEMENTS

I would like to express my deepest gratitude to all those who have supported and contributed to the completion of this thesis. First and foremost, I sincerely thank the Scientific and Technological Research Council of Turkey (TÜBİTAK) 2244 program – 119C116 project. This research was conducted as part of the TÜBİTAK project in collaboration with Nobel Pharma. Portions of this thesis were also supported by the Health Institutes of Turkey (TÜSEB) as part of the A3 project (project number 31227), as well as by the Erasmus+ program, all of which provided invaluable financial and institutional support throughout my research journey.

I am especially grateful to Assoc. Prof. Alexandra Stubelius and her laboratory at the Division of Chemical Biology, Department of Life Sciences, Chalmers University of Technology, for generously providing access to essential equipment and for their comprehensive assistance during my ERASMUS+ internship.

I am also grateful to the esteemed members of my thesis jury: Prof. Dr. Işıl Kurnaz, Assist. Prof. Bahar Yıldız Kutman, Prof. Dr. Pınar Obakan Yerlikaya, and Prof. Dr. Oğuzhan Gündüz, for their insightful feedback, encouragement, and constructive criticism, which have greatly enriched this work.

I would like to extend my sincere appreciation to my family for their steadfast support, patience, and encouragement throughout every stage of my academic journey. I am also grateful to all members of the Institute of Biotechnology, as well as my colleagues in the CellSol Lab, whose collaborative spirit and scientific engagement have significantly contributed to a dynamic and productive research environment. Their collective expertise and collegiality have been instrumental in advancing the quality and scope of this work.

Above all, my deepest appreciation goes to my advisor, Prof. Dr. Elif Damla Arısan. Her exceptional mentorship, patience, guidance, and constant support have been instrumental in shaping both my scientific perspective and personal growth. I am profoundly grateful for her belief in me and for everything she has done throughout this journey.

TABLE OF CONTENTS

	Page
ABSTRACT	vi
ÖZET	vii
ACKNOWLEDGEMENTS	viii
LIST OF SYMBOLS AND ABBREVIATIONS	xi
LIST OF FIGURES	xiii
LIST OF TABLES	xxv
1. INTRODUCTION	1
1.1. The Need for Advanced Biomaterials in Tissue Engineering and Regenerative Medicine	1
1.2. Targeted vs Conventional Drug Delivery Systems	3
1.3. Microparticles and Microcarrier Systems	5
1.4. Polymer-Based Biomaterials	7
1.5. Poly(lactic acid) (PLA) as a Biocompatible Carrier	10
1.6. Overview of Micro/Nanoparticle Drug Delivery	13
1.7. Spirulina and Its Bioactive Properties	14
1.8. PLA/Spirulina Hybrid Microcarriers via Electrospraying	18
1.9. Pharmaceutical Applications of Microparticles	19
1.10. Niacinamide and Palmitoyl Tripeptide-1-Loaded Microparticles	23
2. PURPOSE OF THE STUDY	28
3. EXPERIMENT	29
3.1. Materials	29
3.2. Experimental Section	31
3.2.1. Cellular Experiments Used for the Thesis	32
3.2.2. Cultivation of Spirulina	32
3.2.2.1. Mineral Analysis by ICP	33
3.2.2.2. Extraction of Spirulina	34
3.2.2.3. Cellular Experiments	35
3.2.3. Microparticle Production	36
3.2.3.1. Solution Optimization and Characterization	36
3.2.3.2. 1st set of Microparticle Production Optimization	37
3.2.3.3. 2nd set of Microparticle Production Optimization	38
3.2.3.4. Microparticle Characterization	39
3.2.3.5. Cell Fate Experiments of Produced Microparticles	39
3.2.3.6. Antimicrobial Effect	40
3.2.3.7. Antioxidant Capacity of Produced Microparticles	41
3.2.4. Biocompound-Loaded Microparticle Production	42
3.2.4.1. Nile Red-Loaded Microparticle Production and Cellular Tests	43
3.2.4.2. Bioactive Compound-Loaded Microparticle Production	43
3.2.4.3. Cellular Experiments of Loaded Microparticles	44
4. RESULTS	46
4.1. Spirulina Mineral Analysis and Extraction	46
4.1.1. Mineral Analysis	46
4.1.2. Cellular Fate of Spirulina Extractions	47
4.2. PLA/Spirulina-Based Microparticle Production and Characterization	54

4.2.1. Solution Optimization 54
4.2.2. 1st set of Microparticle Production Optimization and Characterization 55
4.2.3. 2nd set of Microparticle Production Optimization and Characterization 57
4.2.4. FT-IR and Release Profile Analysis 59
4.2.5. Cell Fate of Produced Microparticles 62
4.2.6. Antimicrobial Effects of Microparticles 78
4.2.7. Antioxidant Capacity of Produced Microparticles 80
4.3. Biocompound-Loaded Microparticle Production and Cell Fate 82
4.3.1. Nile-Loaded Microparticle Production and Cellular Uptake 83
4.3.2. Biocompound-Loaded Microparticle Production and Optimization 85
4.3.3. Cellular Experiments of Biocompound-Loaded Microparticles 90
4.3.3.1. Cellular Experiments of the Free Form of Nia and Tri 90
4.3.3.2. Cellular Experiments of Biocompound-Loaded Microparticles 92
4.3.3.3. Wound Healing Potential of Biocompound-loaded Microparticles 103
4.3.3.4. Immunoblot Assay of Biocompound-Loaded Microparticles 108
4.3.3.5. Cellular Experiments of Biocompound-Loaded Microparticles on UV-Induced Cell Lines 110
5. DISCUSSION 115
6. CONCLUSION 141
7. LIMITATIONS AND FUTURE DIRECTIONS 144

REFERENCES 145
BIOGRAPHY 168
PUBLICATIONS AND PRESENTATIONS FROM THE THESIS 169

LIST OF SYMBOLS AND ABBREVIATIONS

3D/4D	3/4-Dimensional
Abs	Absorbance
ANOVA	Analysis Of Variance
ATCC	The American Type Culture Collection
Ca	Calcium
$Ca(NO3)_2$	Calcium Nitrate
$CaCO_3$	Calcium Carbonate
CAGR	Compound Annual Growth Rate
CO_2	Carbon Dioxide
DAPI	4',6-Diamidino-2-Phenylindole
dH_2O	Water Extract
$DiOC_6$	3,3′-Dihexyloxacarbocyanine Iodide
DLS	Dynamic Light Scattering
DMEM	Dulbecco's Modified Eagle Medium
DMSO	Dimethyl Sulfoxide
DNA	Deoxyribonucleic Acid
DPPH	1,1-Diphenyl-2-Picrylhydrazyl Radical
e-Nia	0.5% Nia + 0.125% Spi + 3% PLA
e-NiaTri	0.5% Nia + 0.1% Tri + 0.125% Spi + 3% PLA
e-Spi	0.125% Spirulina + 3% PLA
e-Tri	0.1% Tri + 0.125% Spi + 3% PLA
ECM	Extracellular Matrix
FACS	Fluorescence-Activated Cell Sorting
FBS	Fetal Bovine Serum
FDA	U.S. Food And Drug Administration
FT-IR	Fourier Transform Infrared
GAE	Gallic Acid Equivalent
GHK	Gly-His-Lys
GRAS	Generally Recognized As Safe
H_2-DCFDA	2′,7′-Dichlorodihydrofluorescein Diacetate
HaCaT	Human Keratinocytes
HUVEC	Human Umbilical Vein Endothelial Cell
ICP	Inductively Coupled Plasma Atomic Emission Spectroscopy
LB	Lysogeny Broth
M1	0.125% Spirulina + 3% PLA
M2	0.25% Spirulina + 3% PLA
M3	0.5% Spirulina + 3% PLA
MMP	Matrix Metalloproteinase
MTT	(3-[4,5-Dimethylthiazol-2-Yl]-2,5 Diphenyl Tetrazolium Bromide)

Na_2CO_3	Sodium Carbonate
NAD+	Nicotinamide Adenine Dinucleotide
NADH	Nicotinamide Adenine Dinucleotide (NAD) + Hydrogen (H)
NADP	Nicotinamide Adenine Dinucleotide Phosphate
$NaNO_3$	Sodium Nitrate
NBUAM	Marmara University, Center For Nanotechnology & Biomaterials Applications And Research
Nia	Niacinamide
NK	Natural Killer
OD_{600}	Optical Density At 600 nm
Pal-Tri-1	Palmitoyl Tripeptide-1
PBS	Phosphate Buffer Saline
PCL	Polycaprolactone
PGA	Poly(Glycolic Acid)
PI	Propidium Iodide
PLA	Poly(Lactic Acid)
PLGA	Poly(Lactic-Co-Glycolic Acid)
PVDF	Polyvinylidene Fluoride
RNA	Ribonucleic Acid
ROP	Ring-Opening Polymerization
ROS	Reactive Oxygen Species
SDS-PAGE	Sodium Dodecyl-Sulfate Polyacrylamide Gel Electrophoresis
SEM	Scanning Electron Microscopy
Spi	Spirulina Platensis
SPP	Polysaccharides Extracted From Spirulina
TEAC	Trolox Equivalent Antioxidant Capacity
Tri	Palmitoyl Tripeptide-1
UV	Ultraviolet Radiation

LIST OF FIGURES

Page

Figure 1.1: Schematic overview of interdisciplinary innovations in tissue engineering and regenerative medicine (Cramer & Badylak, 2020; Rangel et al., 2023; K. Zhang et al., 2018). 3

Figure 1.2: Comparison of nanoparticles and microparticles as drug delivery systems (da Silva et al., 2023; Ghosh et al., 2022; Prabahar et al., 2021; Rafiee & Rasool, 2022). 4

Figure 1.3: Microcarrier systems and their properties (Boda et al., 2018; da Silva et al., 2023; H. Lee et al., 2018; Morais et al., 2020; Jiamian Wang et al., 2019). 7

Figure 1.4: Schematic overview of natural and synthetic polymeric biomaterials, highlighting their classification, representative examples, and key biomedical applications as microparticles (Hu et al., 2024; Oleksy et al., 2023). 8

Figure 1.5: Schematic representation of PLA's multifunctional role as a carrier system, illustrating its synthesis, biodegradation, biocompatibility, and applications in targeted and sustained delivery of bioactive molecules and cells for advanced biomedical therapies (Casalini et al., 2019; Lopes et al., 2014; Moya-Lopez et al., 2022). 12

Figure 1.6: PLA/Spirulina microcarrier system illustration. 20

Figure 1.7: NAD+ synthesis process from niacinamide (Baik et al., 2024; Marques et al., 2024). 26

Figure 3.1: Cultivation of Spirulina in a flask for stock and a 2 L glass bottle with aeration provided by a filtered cap. 33

Figure 3.2: Illustration of the Spirulina extraction method. 35

Figure 3.3: Electrospray equipment setup. a. with nozzle (0.65 mm diameter) (Marmara University, NBUAM), b. with blunt needle 0.4 x 25 mm diameter (Chalmers University of Technology, Life Science) (Created with BioRender.com). 38

Figure 4.1: a. MTT assay, b. colony formation, and c. cell survival assay of HUVEC cell lines after the application of Spirulina biomass extract for 24 h, 48 h, and 72 h for the MTT and cell survival assays, and a 24 h application for colony formation using five different concentrations (5, 10, 25, 50, 75 µg/mL). The MTT results indicated the average of three biological replicates of quartiles, with standard deviation; two biological replicates for colony formation; and two biological replicates of two technical replicates for cell survival. The analysis was performed using GraphPad 9.2.0 software with two-way ANOVA combined with Dunnett's comparison test against the initial control. ns, $p > 0.05$, *** $p < 0.001$, ** $0.001 \leq p < 0.01$, * $0.01 \leq p < 0.05$. 48

Figure 4.2: a. MTT assay, b. colony formation, and c. cell survival assay of HaCaT cell lines after the application of Spirulina 49

biomass extract for 24 h, 48 h, and 72 h for the MTT and cell survival assays, and a 24 h application for colony formation using five different concentrations (5, 10, 25, 50, 75 µg/mL). The MTT results indicated the average of three biological replicates of quartiles, with standard deviation; two biological replicates for colony formation; and two biological replicates of two technical replicates for cell survival. The analysis was performed using GraphPad 9.2.0 software with two-way ANOVA combined with Dunnett's comparison test against the initial control. ns, $p > 0.05$, *** $p < 0.001$, ** $0.001 \leq p < 0.01$, * $0.01 \leq p < 0.05$.

Figure 4.3: a. MTT assay, b. colony formation, and c. cell survival assay of HUVEC cell lines after the application of Spirulina water extract for 24 h, 48 h, and 72 h for the MTT and cell survival assays, and a 24 h application for colony formation using five different concentrations (5, 10, 25, 50, 75 µg/mL). The MTT results indicated the average of three biological replicates of quartiles, with standard deviation; two biological replicates for colony formation; and two biological replicates of two technical replicates for cell survival. The analysis was performed using GraphPad 9.2.0 software with two-way ANOVA combined with Dunnett's comparison test against the initial control. ns, $p > 0.05$, *** $p < 0.001$, ** $0.001 \leq p < 0.01$, * $0.01 \leq p < 0.05$. 50

Figure 4.4: a. MTT assay, b. colony formation, and c. cell survival assay of HaCaT cell lines after the application of Spirulina water extract for 24 h, 48 h, and 72 h for the MTT and cell survival assays, and a 24 h application for colony formation using five different concentrations (5, 10, 25, 50, 75 µg/mL). The MTT results indicated the average of three biological replicates of quartiles, with standard deviation; two biological replicates for colony formation; and two biological replicates of two technical replicates for cell survival. The analysis was performed using GraphPad Prism 9.2.0 software with a two-way ANOVA followed by Dunnett's comparison test against time 0 h. ns, $p > 0.05$, **** $p < 0.0001$, *** $0.0001 \leq p < 0.001$, ** $0.001 \leq p < 0.01$, * $0.01 \leq p < 0.05$. 51

Figure 4.5: a. MTT assay, b. colony formation, and c. cell survival assay of HUVEC cell lines after the application of Spirulina ethanol extract for 24 h, 48 h, and 72 h for the MTT and cell survival assays, and a 24 h application for colony formation using five different concentrations (5, 10, 25, 50, 75 µg/mL). The MTT results indicated the average of three biological replicates of quartiles, with standard deviation; two biological replicates for colony formation; and two biological replicates of two technical replicates for cell survival. The analysis was performed using GraphPad 9.2.0 software with two-way ANOVA combined with Dunnett's 52

comparison test against the initial control. ns, $p > 0.05$, *** $p < 0.001$, ** $0.001 \leq p < 0.01$, * $0.01 \leq p < 0.05$.

Figure 4.6: a. MTT assay, b. colony formation, and c. cell survival assay of HaCaT cell lines after the application of Spirulina ethanol extract for 24 h, 48 h, and 72 h for the MTT and cell survival assays, and a 24 h application for colony formation using five different concentrations (5, 10, 25, 50, 75 µg/mL). The MTT results indicated the average of three biological replicates of quartiles, with standard deviation; two biological replicates for colony formation; and two biological replicates of two technical replicates for cell survival. The analysis was performed using GraphPad 9.2.0 software with two-way ANOVA combined with Dunnett's comparison test against the initial control. ns, $p > 0.05$, *** $p < 0.001$, ** $0.001 \leq p < 0.01$, * $0.01 \leq p < 0.05$. 53

Figure 4.7: 3% PLA (1-M0) microparticle production using electrospraying with 20 µL/min flow rate, 18 kV electrical field, and 15 cm distance between the collector and the needle. a. The SEM image of the microparticles, and b. size distribution from 100 microparticles analysis using ImageJ and IBM SPSS Statistics software. The scale bar of the SEM is 100 µm. 55

Figure 4.8: 0.125% Spi + 3% PLA microparticle production using electrospraying with 20 µL/min flow rate, 16.8 kV electrical field, and 15 cm distance between the collector and the needle. a. The SEM image of the microparticles, and b. size distribution from 100 microparticles analysis using ImageJ and IBM SPSS Statistics software. The scale bar of the SEM is 100 µm. 56

Figure 4.9: 0.25% Spi + 3% microparticle production using electrospraying with 30 µL/min flow rate, 16.7 kV electrical field, and 15 cm distance between the collector and the needle. a. The SEM image of the microparticles, and b. size distribution from 100 microparticles analysis using ImageJ and IBM SPSS Statistics software. The scale bar of the SEM is 100 µm. 56

Figure 4.10: 0.5% Spi + 3% PLA microparticle production using electrospraying with 25 µL/min flow rate, 16.6 kV electrical field, and 15 cm distance between the collector and the needle. a. The SEM image of the microparticles, and b. size distribution from 100 microparticles analysis using ImageJ and IBM SPSS Statistics software. The scale bar of the SEM is 100 µm. 57

Figure 4.11: a. 3% PLA (2-M0), d. 0.125% Spi + 3% PLA (2-M1), g. 0.25% Spi + 3% PLA (2-M2), and j. 0.5% Spi + 3% PLA (2-M3) size distributions were measured using DLS, with calculations performed using GraphPad 9.2.0. The particle sizes represent the average of three readings. b. 2-M0, e. 2-M1, h. 2-M2, and k. 2-M3 SEM images, with scale bars set at 100 µm. c. 2-M0, f. 2-M1, i. 2-M2 and j. 2-M3 size 59

distributions were calculated from SEM images using Image J and GraphPad 9.2.0 software. At least 100 particles were measured, and the particles' diameters were recorded as averages along with their standard deviations.
Figure 4.12: FT-IR analysis of M0 (red), pure Spirulina extract (dark green), M1 (blue), M2 (green), and M3 (purple) a. particles from larger nozzle diameter and b. particles from a smaller inner needle diameter. The y-axis represents T%, which denotes the transmittance percentage of the samples. 60
Figure 4.13: Release profile of produced microparticles using PBS at pH 7.4. a. fluorescence unit at 355/535 nm, b. Standard curve for Spirulina extract, and cumulative release profile calculated using the standard curve. 61
Figure 4.14: Loading capacity of produced microparticles; the loading capacity was calculated as theoretical, gray, and measured loading, black. The loading capacity was calculated based on the released profile. 62
Figure 4.15: a. MTT assay and b. colony formation of HUVEC cell lines after the application of 1-M0, 1-M1, 1-M2, and 1-M3 microparticle application for 24 h for the MTT and colony formation using five different concentrations (0.5, 1, 5, 10, 25 μg/mL). The MTT results represented the average of three biological replicates of quartiles, with standard deviation, and two biological replicates for colony formation. The analysis was conducted using GraphPad Prism 9.2.0 software with a two-way ANOVA followed by Dunnett's comparison test against the initial control. ns $p > 0.05$, **** $p < 0.0001$, *** $0.0001 \leq p < 0.001$, ** $0.001 \leq p < 0.01$, * $0.01 \leq p < 0.05$. # $0.01 \leq p < 0.05$, ## $0.001 \leq p < 0.01$, ### $p < 0.001$ comparison between 1-M0 and Spi-included microparticles for each dosage. 63
Figure 4.16: a. 1-M0, b. 1-M1, c. 1-M2, and d. 1-M3 microparticle applied to HUVEC cell lines' cell survival results after two concentrations (5 and 10 μg/mL) applied for 24, 48, and 72 h. The results represent the average of two biological replicates, each with two technical replicates, along with the standard deviation. The analysis was conducted using GraphPad Prism 9.2.0 software with a two-way ANOVA followed by Dunnett's comparison test against the initial control. ns $p > 0.05$, **** $p < 0.0001$, *** $0.0001 \leq p < 0.001$, ** $0.001 \leq p < 0.01$, * $0.01 \leq p < 0.05$. 64
Figure 4.17: Fluorescence images of HUVEC after 5 μg/mL microparticles produced using a nozzle with a larger inner diameter (1-). Control: no treatment applied, 1-M0: 3% PLA, 1-M1: 0.125% Spi + 3% PLA; 1-M2: 0.25% Spi + 3% PLA; 1-M3: 0.5% Spi + 3% PLA. The scale bar in the images was 150 μm. 65
Figure 4.18: Fluorescence images of HUVEC after 10 μg/mL microparticles produced using a nozzle with a larger 66

inner diameter (1-). Control: no treatment applied, 1-M0: 3% PLA, 1-M1: 0.125% Spi + 3% PLA; 1-M2: 0.25% Spi + 3% PLA; 1-M3: 0.5% Spi + 3% PLA. The scale bar in the images was 150 μm.

Figure 4.19: a. MTT assay and b. Colony formation of HaCaT cell lines after the application of 1-M0, 1-M1, 1-M2, and 1-M3 microparticle application for 24 h for the MTT and colony formation using five different concentrations (0.5, 1, 5, 10, 25 μg/mL). The MTT results represented the average of three biological replicates of quartiles, with standard deviation; two biological replicates for colony formation; and two biological replicates of two technical replicates for cell survival. The analysis was conducted using GraphPad Prism 9.2.0 software with a two-way ANOVA followed by Dunnett's comparison test against the initial control. ns $p > 0.05$, **** $p < 0.0001$, *** $0.0001 \leq p < 0.001$, ** $0.001 \leq p < 0.01$, * $0.01 \leq p < 0.05$. 66

Figure 4.20: a. 1-M0, b. 1-M1, c. 1-M2, and d. 1-M3 microparticle applied to HaCaT cell lines' cell survival results after two concentrations (5 and 10 μg/mL) applied for 24, 48, and 72 h. The results represent the average of two biological replicates, each with two technical replicates, along with the standard deviation. The analysis was conducted using GraphPad Prism 9.2.0 software with a two-way ANOVA followed by Dunnett's comparison test against the initial control. ns $p > 0.05$, **** $p < 0.0001$, *** $0.0001 \leq p < 0.001$, ** $0.001 \leq p < 0.01$, * $0.01 \leq p < 0.05$. 67

Figure 4.21: Fluorescence images of HaCaT cells after 5 μg/mL microparticle, produced using a nozzle with a larger inner diameter, application. Control: no treatment applied, 1-M0: 3% PLA, 1-M1: 0.125% Spi + 3% PLA; 1-M2: 0.25% Spi + 3% PLA; 1-M3: 0.5% Spi + 3% PLA. Scale bar 150 μm. 68

Figure 4.22: Fluorescence images of HaCaT cells after 10 μg/mL microparticle, produced using a nozzle with a larger inner diameter, application. Control: no treatment applied, 1-M0: 3% PLA, 1-M1: 0.125% Spi + 3% PLA; 1-M2: 0.25% Spi + 3% PLA; 1-M3: 0.5% Spi + 3% PLA. The scale bar was 150 μm. 69

Figure 4.23: a. MTT assay and b. colony formation of HUVEC cell lines after the application of 1-M0, 1-M1, 1-M2, and 1-M3 microparticle application for 24 h for the MTT and colony formation using five different concentrations (0.5, 1, 5, 10, 25 μg/mL). The MTT results represented the average of three biological replicates of quartiles, with standard deviation; two biological replicates for colony formation; and two biological replicates of two technical replicates for cell survival. The analysis was conducted using GraphPad Prism 9.2.0 software with a two-way ANOVA followed by Dunnett's comparison test against the initial 70

control. ns $p > 0.05$, **** $p < 0.0001$, *** $0.0001 \leq p < 0.001$, ** $0.001 \leq p < 0.01$, * $0.01 \leq p < 0.05$. # $0.01 \leq p < 0.05$, ## $0.001 \leq p < 0.01$, ### $p < 0.001$ comparison between 1-M0 and Spi-included microparticles for each dosage.

Figure 4.24: a. 1-M0, b. 1-M1, c. 1-M2, and d. 1-M3 microparticle applied to HUVEC cell lines' cell survival results after two concentrations (5 and 10 µg/mL) applied for 24, 48, and 72 h. The results represent the average of two biological replicates, each with two technical replicates, along with the standard deviation. The analysis was conducted using GraphPad Prism 9.2.0 software with a two-way ANOVA followed by Dunnett's comparison test against the initial control. ns $p > 0.05$, **** $p < 0.0001$, *** $0.0001 \leq p < 0.001$, ** $0.001 \leq p < 0.01$, * $0.01 \leq p < 0.05$. 71

Figure 4.25: Fluorescence images of HUVEC cells after 5 µg/mL 2-microparticle, Control: no treatment applied, 2-M0: 3% PLA, 2-M1: 0.125% Spi + 3% PLA, 2-M2: 0.25% Spi + 3% PLA, 2-M3: 0.5% Spi + 3% PLA. 72

Figure 4.26: Fluorescence images of HUVEC cells after 10 µg/mL 2-microparticle, Control: no treatment applied, 2-M0: 3% PLA, 2-M1: 0.125% Spi + 3% PLA, 2-M2: 0.25% Spi + 3% PLA, 2-M3: 0.5% Spi + 3% PLA. 72

Figure 4.27: a. MTT assay and b. Colony formation of HaCaT cell lines after the application of 1-M0, 1-M1, 1-M2, and 1-M3 microparticle application for 24 h for the MTT and colony formation using five different concentrations (0.5, 1, 5, 10, 25 µg/mL). The MTT results represented the average of three biological replicates of quartiles, with standard deviation; two biological replicates for colony formation; and two biological replicates of two technical replicates for cell survival. The analysis was conducted using GraphPad Prism 9.2.0 software with a two-way ANOVA followed by Dunnett's comparison test against the initial control. ns $p > 0.05$, **** $p < 0.0001$, *** $0.0001 \leq p < 0.001$, ** $0.001 \leq p < 0.01$, * $0.01 \leq p < 0.05$. # $0.01 \leq p < 0.05$, ## $0.001 \leq p < 0.01$, ### $p < 0.001$ comparison between 1-M0 and Spi-included microparticles for each dosage. 74

Figure 4.28: a. 1-M0, b. 1-M1, c. 1-M2, and d. 1-M3 microparticle applied to HaCaT cell lines' cell survival results after two concentrations (5 and 10 µg/mL) applied for 24, 48, and 72 h. The results represent the average of two biological replicates, each with two technical replicates, along with the standard deviation. The analysis was conducted using GraphPad Prism 9.2.0 software with a two-way ANOVA followed by Dunnett's comparison test against the initial control. ns $p > 0.05$, **** $p < 0.0001$, *** $0.0001 \leq p < 0.001$, ** $0.001 \leq p < 0.01$, * $0.01 \leq p < 0.05$. # $0.01 \leq p$ 75

< 0.05, ## 0.001 ≤ p < 0.01, ### p < 0.001 comparison between each time point's control group.
Figure 4.29: Fluorescence images of HaCaT cells after 5 µg/mL 2-microparticle, Control: no treatment applied, 2-M0: 3% PLA, 2-M1: 0.125% Spi + 3% PLA, 2-M2: 0.25% Spi + 3% PLA, 2-M3: 0.5% Spi + 3% PLA. The scale bar was 150 µm. 76
Figure 4.30: Fluorescence images of HaCaT cells after 5 µg/mL 2-microparticle, Control: no treatment applied, 2-M0: 3% PLA, 2-M1: 0.125% Spi + 3% PLA, 2-M2: 0.25% Spi + 3% PLA, 2-M3: 0.5% Spi + 3% PLA. The scale bar was 150 µm. 77
Figure 4.31: Disc diffuson assay results for all microparticles and Spirulina ethanol extract in a. *S.epidermidis*, b. *S.aureus*, c. *E.coli*, and d. *P.aeruginosa*. Negative control was dH2O, and positive control was 2 mg/mL ciprofloxacin. 79
Figure 4.32: Standard curve of gallic acid at different concentrations (0.005-1 mg/mL) obtained by the Folin-Ciocalteu test and read at 765 nm. 81
Figure 4.33: Concentration-dependent DPPH reactive inhibition graph obtained from the DPPH antioxidant test of Spirulina. Values are the average of at least three repeated measurements. 82
Figure 4.34: Trolox curve obtained with TEAC at different concentrations (0-40 µM) and read at 715 nm. Values are the average of at least three replicates. 82
Figure 4.35: 0.1% Nile Red + 3% PLA microparticle a. SEM image and b. size distribution by selecting 100 microparticles from SEM images using ImageJ software, and the distribution graph was achieved by GraphPad 9.2.0; the scale bar of the SEM image is 20 µm. 83
Figure 4.36: Cellular uptake of Nile Red-loaded PLA microparticles in HUVEC and HaCaT cells after 24 h incubation. a. Fluorescence microscopy images show intracellular localization of Nile Red released from e-Nile microparticles at concentrations of 5 and 10 µg/ml. Scale bar: 100 µm. b. Flow cytometry results, graphs, and analyses for HUVEC cells exposed to Nile Red-loaded microparticles at concentrations of 5 µg/mL (HUVEC5) and 10 µg/mL (HUVEC10) for 24 hours are presented. The counted cells were limited to live cells. c. Flow cytometry, the result graphs, and analyses for HaCaT cells exposed to Nile Red, including microparticles at concentrations of 5 µg/mL (HaCaT5) and 10 µg/mL (HaCaT10) for 24 h. The counted cells were limited to live cells. 84
Figure 4.37: 0.1% Nia + 0.125% Spi + 3% PLA microparticle. a. SEM image and b. size distribution by selecting 100 microparticles from SEM images using ImageJ software, 86

and the distribution graph was achieved using GraphPad 9.2.0. The scale bar of the SEM image is 20 μm.
Figure 4.38: The 0.25% Nia + 0.125% Spi + 3% PLA microparticles' a. SEM image and b. Size distribution by selecting 100 microparticles from SEM images using ImageJ software, and the distribution graph was achieved using GraphPad 9.2.0. The scale bar of the SEM image is 20 μm. 86
Figure 4.39: The 0.5% Nia + 0.125% Spi + 3% PLA microparticles' a. SEM image and b. Size distribution by selecting 100 microparticles from SEM images using ImageJ software, and the distribution graph was achieved using GraphPad 9.2.0. The scale bar of the SEM image is 20 μm. 86
Figure 4.40: SEM images of a. 1% Nia-loaded, b. 5% Nia-loaded and c. 10% Nia-loaded microparticles. The scale of the SEM images was 20 μm. 87
Figure 4.41: The 0.1% Tri + 0.125% Spi + 3% PLA microparticles' a. SEM image and b. Size distribution by selecting 100 microparticles from SEM images using ImageJ software, and the distribution graph was achieved using GraphPad 9.2.0. The scale bar of the SEM image is 20 μm. 88
Figure 4.42: The 0.25% Tri + 0.125% Spi + 3% PLA microparticles' SEM image. The scale bar of the SEM image is 20 μm. 88
Figure 4.43: The 0.5% Tri + 0.125% Spi + 3% PLA microparticles' a. SEM image and b. Size distribution by selecting 100 microparticles from SEM images using ImageJ software, and the distribution graph was achieved using GraphPad 9.2.0. The scale bar of the SEM image is 20 μm. 89
Figure 4.44: The 0.5% Nia + 0.1% Tri + 0.125% Spi + 3% PLA microparticles a. SEM image and b. Size distribution by selecting 100 microparticles from SEM images using ImageJ software, and the distribution graph was achieved using GraphPad 9.2.0. The scale bar of the SEM image is 20 μm. 89
Figure 4.45: SEM images of a. 0.5% Nia + 0.25% Tri-loaded and b. 0.5% Nia + 0.5% Tri-loaded; the scale of images was 20 μm. 90
Figure 4.46: MTT results of 24 h a. Nia and b. Tri application for HUVEC (orange) and HaCaT (red) cell lines. Standard errors were from 3 biological replicates, and bars were an average of 3 biological replicates with four technical replicates. Statistical analysis were conducted two-way ANOVA combined with Dunnett's comparasion tests for each cell line, ns $p > 0.05$, **** $p < 0.0001$, *** $0.0001 \leq p < 0.001$, ** $0.001 \leq p < 0.01$, * $0.01 \leq p < 0.05$ for HUVECs, # $0.01 \leq p < 0.05$, ## $0.001 \leq p < 0.01$, ### $p < 0.001$ for HaCaT cell line compared to the control. 91
Figure 4.47: a. Nia, b. Tri in HUVEC cells, c. Nia and d. Tri in HaCaT cell lines' cell survival results after two concentrations (10 and 25 μM for Nia, 5 and 10 μM for Tri) applied for 24, 48, and 72 h. The results represent the average of two 92

biological replicates, each with two technical replicates, along with the standard deviation. The analysis was conducted using GraphPad Prism 9.2.0 software with a two-way ANOVA followed by Dunnett's comparison test against the initial control. ns $p > 0.05$, **** $p < 0.0001$, *** $0.0001 \leq p < 0.001$, ** $0.001 \leq p < 0.01$, * $0.01 \leq p < 0.05$. # $0.01 \leq p < 0.05$, ## $0.001 \leq p < 0.01$, ### $p < 0.001$ comparison between each time point's control group.

Figure 4.48: MTT results of microparticles a. e-Nia, b. e-Tri, and c. e-Niatri, and d. e-Spi. Orange represents HUVEC, and ed indicates HaCaT cell lines. Standard errors were from 3 biological replicates, and bars were an average of 3 biological replicates with four technical replicates. Statistical analysis were conducted two-way ANOVA combined with Dunnett's comparasion tests for each cell line, ns $p > 0.05$, **** $p < 0.0001$, *** $0.0001 \leq p < 0.001$, ** $0.001 \leq p < 0.01$, * $0.01 \leq p < 0.05$ for HUVECs, # $0.01 \leq p < 0.05$, ## $0.001 \leq p < 0.01$, ### $p < 0.001$ for HaCaT cell line compared to the control. 94

Figure 4.49: a. e-Nia, b. e-Tri, c. e-NiaTri, and d. e-Spi microparticle applied to HUVEC cell lines' cell survival results after two concentrations (5 and 10 µg/mL) applied for 24, 48, and 72 h. The results represent the average of two biological replicates, each with two technical replicates, along with the standard deviation. The analysis was conducted using GraphPad Prism 9.2.0 software with a two-way ANOVA followed by Dunnett's comparison test against the initial control. ns $p > 0.05$, **** $p < 0.0001$, *** $0.0001 \leq p < 0.001$, ** $0.001 \leq p < 0.01$, * $0.01 \leq p < 0.05$. # $0.01 \leq p < 0.05$, ## $0.001 \leq p < 0.01$, ### $p < 0.001$ comparison between each time point's control group. 95

Figure 4.50: Fluorescence images of HUVEC after 5 and 10 µg/mL e-Nia application for 24 h. Control: non-treatment. The scale bar of the images was 150 µm. 96

Figure 4.51: Fluorescence images of HUVEC after 5 and 10 µg/mL e-Tri application for 24 h. Control: non-treatment. The scale bar of the images was 150 µm. 97

Figure 4.52: Fluorescence images of HUVEC after 5 and 10 µg/mL e-NiaTri application for 24 h. Control: non-treatment. The scale bar of the images was 150 µm. 97

Figure 4.53: ROS intensity level of HUVEC cells, analyzed from 3 biological replicates of HUVEC cells after fluorescence imaging using ImageJ software. The statistical analysis was calculated using two-way ANOVA with Dunnett's comparison test. At least 50 cells were selected for ROS for each biological replicate. ns $p > 0.05$, **** $p < 0.0001$, *** $0.0001 \leq p < 0.001$, ** $0.001 \leq p < 0.01$, * $0.01 \leq p < 0.05$, comparison between treated groups and control group. 98

Figure 4.54: a. e-Nia, b. e-Tri, c. e-NiaTri, and d. e-Spi microparticle applied to HaCaT cell lines' cell survival results after two concentrations (5 and 10 µg/mL) applied for 24, 48, and 72 h. The results represent the average of two biological replicates, each with two technical replicates, along with the standard deviation. The analysis was conducted using GraphPad Prism 9.2.0 software with a two-way ANOVA followed by Dunnett's comparison test against the initial control. ns $p > 0.05$, **** $p < 0.0001$, *** $0.0001 \leq p < 0.001$, ** $0.001 \leq p < 0.01$, * $0.01 \leq p < 0.05$. # $0.01 \leq p < 0.05$, ## 0.001. 100

Figure 4.55: Fluorescence images of HaCaT after 5 and 10 µg/mL e-Nia application for 24 h. Control: non-treatment. The scale bar of the images was 150 µm. 101

Figure 4.56: Fluorescence images of HaCaT after 5 and 10 µg/mL e-Tri application for 24 h. Control: non-treatment. The scale bar of the images was 150 µm. 101

Figure 4.57: Fluorescence images of HaCaT after 5 and 10 µg/mL e-NiaTri application for 24 h. Control: non-treatment. The scale bar of the images was 150 µm. 102

Figure 4.58: ROS level of HaCaT cells, analyzed from 3 biological replicates of HaCaT cells after fluorescence imaging using ImageJ software. The statistical analysis was calculated using two-way ANOVA with Dunnett's comparison test. For ROS expression, at least 50 cells were selected for a biological replication. ns $p > 0.05$, **** $p < 0.0001$, *** $0.0001 \leq p < 0.001$, ** $0.001 \leq p < 0.01$, * $0.01 \leq p < 0.05$, comparison between treated groups and control group. 103

Figure 4.59: Wound healing analysis of HUVEC cells after applying 5 and 10 µg/mL of a. e-Nia, b. e-Tri, c. e-NiaTri, and d. e-Spi. The bars represent the average of two biological replicates, each containing two technical replicates, and the error bars indicate the the standard deviation of the replicates. A two-way ANOVA with Dunnett's multiple comparisons was used to analyze the differences between time zero and each time point for each treatment, ns $p > 0.05$, **** $p < 0.0001$, *** $0.0001 \leq p < 0.001$, ** $0.001 \leq p < 0.01$, * $0.01 \leq p < 0.05$. 105

Figure 4.60: Wound healing analysis of HaCaT cells after applying 5 and 10 µg/mL of a. e-Nia, b. e-Tri, c. e-NiaTri, and d. e-Spi. The bars represent the average of two biological replicates, each containing two technical replicates, and the error bars indicate the standard deviation of the replicates. A two-way ANOVA with Dunnett's multiple comparisons was used to analyze the differences between time zero and each time point for each treatment, ns $p > 0.05$, **** $p < 0.0001$, *** $0.0001 \leq p < 0.001$, ** $0.001 \leq p < 0.01$, * $0.01 \leq p < 0.05$. 106

Figure 4.61: Wound healing analysis of a. Nia for HUVEC, b. Tri for HUVEC, c. Nia for HaCaT, and d. Tri for HaCaT. The bars 107

represent the average of two biological replicates, each containing two technical replicates, and the error bars indicate the standard deviation of the replicates. A two-way ANOVA with Dunnett's multiple comparisons was used to analyze the differences between time zero and each time point for each treatment, ns $p > 0.05$, **** $p < 0.0001$, *** $0.0001 \leq p < 0.001$, ** $0.001 \leq p < 0.01$, * $0.01 \leq p < 0.05$.

Figure 4.62: Representative Western blot analysis of AKT, Smad2/3, and β-Actin protein expression in HUVEC cells after 24-hour treatment with control, e-Nia (5 µg/mL), e-Tri (5 µg/mL), e-NiaTri (5 µg/mL), e-Spi (5 µg/mL), Nia (25 µM), and Tri (5 µM). Densitometric quantification of each protein band is shown below the blots, normalized to control (set as 1) used by Image J software. β-Actin was used as a loading control to confirm equal protein loading across samples. 108

Figure 4.63: Representative Western blot analysis of AKT, Smad2/3, and β-Actin protein expression in HaCaT cells after 24-hour treatment with control, e-Nia (5 µg/mL), e-Tri (5 µg/mL), e-NiaTri (5 µg/mL), e-Spi (5 µg/mL), Nia (25 µM), and Tri (5 µM). Densitometric quantification of each protein band is shown below the blots, normalized to control (set as 1) used by Image J software. β-Actin was used as a loading control to confirm equal protein loading across samples. 109

Figure 4.64: MTT assay results for 1200 J UV applied HUVEC and HaCaT cells before a. Nia (Nia, 5-75 µM) and b. Tri (Tri, 1-50 µM) affects the viability of HUVEC and HaCaT cells after 1200 J UV exposure and 24 h treatment. Data represent mean ± SD of ≥3 biological replicates (4 technical replicates each). Statistical analysis by two-way ANOVA with Dunnett's post-hoc test: ****$p < 0.0001$ (HUVEC), #### $p < 0.0001$ (HaCaT) vs untreated control; ns ($p > 0.05$). 110

Figure 4.65: Cell survival assay results for HUVEC, a. Nia, and b. Tri and HaCaT cells c. Nia and d. Tri application for 24 h after 1200 J UV induction. Data represent mean ± SD of three independent biological replicates (two technical replicates each). Statistical analysis was performed using two-way ANOVA with Dunnett's post-hoc test: ns $p > 0.05$, **** $p < 0.0001$, *** $0.0001 \leq p < 0.001$, ** $0.001 \leq p < 0.01$, * $0.01 \leq p < 0.05$. # $0.01 \leq p < 0.05$, ## $0.001 \leq p < 0.01$, ### $p < 0.001$ comparison between each time point's control group. 111

Figure 4.66: MTT assay results showing cell viability of a. e-Nia (0.5-25 µg/mL), b. e-Tri (0.5-25 µg/mL), c. e-NiaTri (0.5-25 µg/mL), and d. e-Spi (0.5-25 µg/mL) treated HUVEC and HaCaT cells following 1200 J UV irradiation and 24 h incubation. Data represent mean ± SD of three 112

independent biological replicates (four technical replicates each). Statistical analysis was performed using two-way ANOVA with Dunnett's post-hoc test (*p < 0.05 vs untreated control; ns = not significant p > 0.05).

Figure 4.67: Cell survival assay results for a. e-Nia (5 and 10 µg/ml), b. e-Tri 5 and 10 µg/mL), c. e-NiaTri (5 and 10 µg/ml), and d. e-Spi (5 and 10 µg/ml) treated HUVECs following 1200 J UV irradiation and 24 h incubation. Data represent mean ± SD of three independent two biological replicates (two technical replicates each). Statistical analysis was performed using two-way ANOVA with Dunnett's post-hoc test (ns p > 0.05, **** p < 0.0001, *** 0.0001 ≤ p < 0.001, ** 0.001 ≤ p < 0.01, * 0.01 ≤ p < 0.05. # 0.01 ≤ p < 0.05, ## 0.001 ≤ p < 0.01, ### p < 0.001 comparison between each time point's control group). 113

Figure 4.68: Cell survival assay results for a. e-Nia (5 and 10 µg/ml), b. e-Tri 5 and 10 µg/mL), c. e-NiaTri (5 and 10 µg/ml), and d. e-Spi (5 and 10 µg/ml) treated HaCaT following 1200 J UV irradiation and 24 h incubation. Data represent mean ± SD of three independent two biological replicates (two technical replicates each). Statistical analysis was performed using two-way ANOVA with Dunnett's post-hoc test (ns p > 0.05, **** p < 0.0001, *** 0.0001 ≤ p < 0.001, ** 0.001 ≤ p < 0.01, * 0.01 ≤ p < 0.05. # 0.01 ≤ p < 0.05, ## 0.001 ≤ p < 0.01, ### p < 0.001 comparison between each time point's control group). 114

LIST OF TABLES

Page

Table 3.1: Materials and equipment used in the thesis. 29

Table 3.2: Modified Spirulina medium for 1 L of distilled water and Zarrouk medium (Albicance, 2015). 33

Table 4.1: ICP results of commercially available and cultivated Spirulina with modified medium Spirulina. 47

Table 4.2: Solution characterization of 0.125% Spi + 3% PLA, 0.25% Spi + 3% PLA, and 0.5% Spi + 3% PLA. The results indicated an average of three replicates of two reads of each solution, with standard deviations. 55

Table 4.3: Inhibition zone diameters (cm) of *S. epidermidis*, *S. aureus*, *E. coli*, and *P. aeruginosa* from **Figure 4.31**. 80

1. INTRODUCTION

1.1. The Need for Advanced Biomaterials in Tissue Engineering and Regenerative Medicine

The field of tissue engineering and regenerative medicine has experienced remarkable advancements over the past three decades, prompted by the urgent need for effective therapies to repair, replace, or regenerate damaged tissues and organs. Traditional clinical approaches, such as autografts, allografts, and organ transplantation, face limitations due to donor shortages, immunological rejection, and post-surgical complications. Consequently, there is a growing focus on developing advanced biomaterials that can function as scaffolds, delivery vehicles, or instructive microenvironments to enhance tissue regeneration and functional restoration **(Rangel et al., 2023; K. Zhang et al., 2018)**.

Biomaterials are engineered materials specifically designed to interact with biological systems for therapeutic or diagnostic purposes. In regenerative medicine, their primary role is to provide structural support, mimic the extracellular matrix (ECM), and create a conducive environment for cell attachment, proliferation, and differentiation **(Ciarlantini et al., 2024; Cramer & Badylak, 2020; Rangel et al., 2023)**. The selection of an appropriate biomaterial is guided by several critical factors, including biocompatibility, biodegradability, mechanical properties, and the ability to support integration with host tissues. Modern biomaterials encompass metals, ceramics, degradable and nondegradable polymers, and hydrogels, each offering unique advantages for specific clinical applications **(Nair & Laurencin, 2007; Revete et al., 2022; Trucillo, 2024)**.

Recent innovations have expanded the functionality of biomaterials beyond their passive scaffolding capabilities. Innovative and cell-instructive biomaterials now incorporate bioactive cues, such as peptides, growth factors, and ECM-mimetic ligands, that actively modulate cellular behavior, immune responses, and tissue remodeling **(Cramer & Badylak, 2020; Rangel et al., 2023; Trucillo, 2024)**. Advances in material science, such as 3D and 4D bioprinting, have enabled the

fabrication of complex, patient-specific constructs that closely replicate the architecture and mechanical properties of native tissues **(Rangel et al., 2023)**. These developments are complemented by the integration of stem cells, which, when combined with biomaterial scaffolds, can be directed toward specific lineages for targeted tissue regeneration.

In summary, the development of advanced biomaterials is central to the progress of tissue engineering and regenerative medicine. By leveraging interdisciplinary approaches from materials science, cell biology, and biomedical engineering, researchers can now design multifunctional biomaterials that actively guide tissue regeneration, modulate biological responses, and address unmet clinical needs. As the field continues to evolve, the focus is shifting toward creating dynamic, adaptive materials that can respond to the complex and changing environment of the human body, ultimately paving the way for transformative therapies in regenerative medicine **(Cramer & Badylak, 2020; Rangel et al., 2023; K. Zhang et al., 2018)** (Illustration in **Figure 1.1**). The medical biomimetics industry, a growing field, reached a market valuation of $33.28 billion in 2023, with analysts forecasting a compound annual growth rate (CAGR) of 7.6% through 2030, according to Grand View Research. A key growth driver has been the innovation in nanotechnology, particularly in advanced drug delivery systems that enhance biomimetic applications. Nanomaterials have emerged as particularly promising for biomimetic medicine due to their exceptional biocompatibility, making them ideally suited for various biomedical implementations.

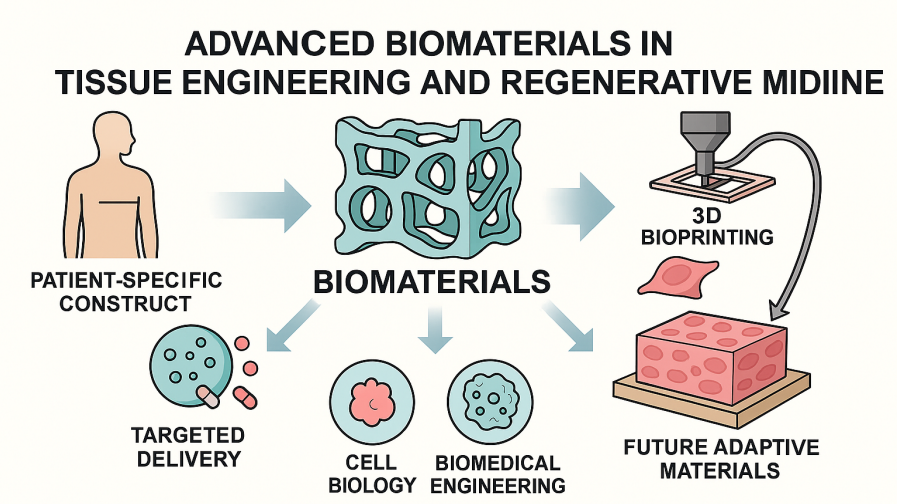


Figure 1.1: Schematic overview of interdisciplinary innovations in tissue engineering and regenerative medicine **(Cramer & Badylak, 2020; Rangel et al., 2023; K. Zhang et al., 2018)**.

1.2. Targeted vs Conventional Drug Delivery Systems

The evolution of drug delivery systems has transformed the landscape of modern therapeutics, shifting from traditional approaches, where drugs are distributed systemically throughout the body, to advanced targeted delivery strategies that localize therapeutic agents precisely at the site of disease. In conventional drug delivery, such as oral or intravenous administration, medications are absorbed across biological membranes and distributed via systemic circulation, often resulting in only a small fraction of the drug reaching the intended target. At the same time, the remainder can cause off-target effects and toxicity in healthy tissues **(Ghosh et al., 2022; Sultana et al., 2022)**. In contrast, targeted drug delivery systems are engineered to concentrate medications at specific tissues or cells, thereby enhancing therapeutic efficacy, minimizing side effects, and reducing the frequency of required dosages **(Ghosh et al., 2022; Meyers, 2023; Prabahar et al., 2021)**. These systems can be designed for active targeting, such as antibody-mediated delivery, or passive targeting, such as exploiting the enhanced permeability and retention effect in tumors.

The importance of advanced drug delivery systems lies in their ability to maximize therapeutic benefits while minimizing adverse effects, improve patient compliance through controlled or sustained release, and enable the development of personalized

and novel therapies, including those based on gene and RNA treatments **(Meyers, 2023; Prabahar et al., 2021)**. Nanoparticles, typically less than 1 µm in diameter, serve as delivery systems, offering several advantages, including a high surface area, enhanced cellular uptake, and the ability to cross biological barriers such as the blood-brain barrier **(Goldberg et al., 2006)**. They can be engineered from a variety of materials, including polymers, lipids, and inorganic substances, and are often functionalized for targeted delivery **(Goldberg et al., 2006)**. However, nanoparticles face significant challenges: their small size can result in rapid clearance by the mononuclear phagocyte system, potential accumulation in non-target organs (e.g., liver and spleen), and concerns regarding long-term toxicity, immunogenicity, and manufacturing variability **(De Jong & Borm, 2008; Desai, 2012)**. These issues can complicate regulatory approval and limit clinical translation.

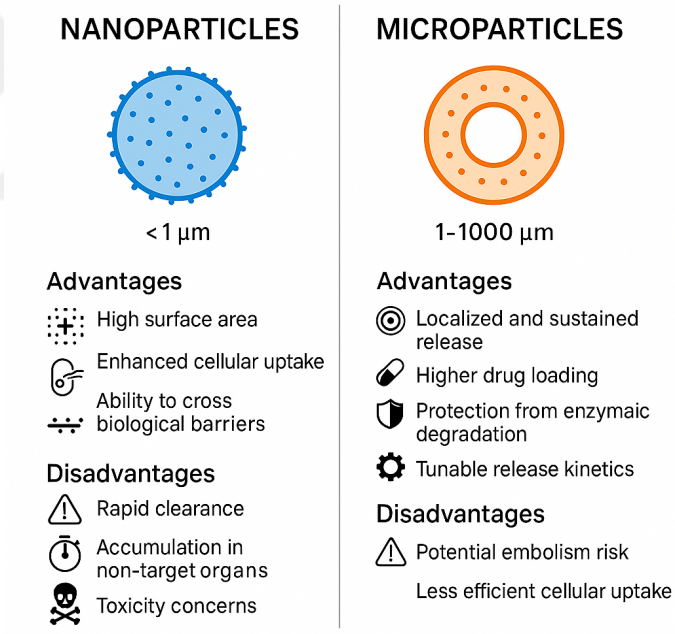


Figure 1.2: Comparison of nanoparticles and microparticles as drug delivery systems **(da Silva et al., 2023; Ghosh et al., 2022; Prabahar et al., 2021; Rafiee & Rasool, 2022)**.

Microparticles, on the other hand, generally ranging from 1 to 1000 µm, have emerged as a preferable alternative for many drug delivery applications **(da Silva et al., 2023; Rafiee & Rasool, 2022)**. Unlike nanoparticles, microparticles are less likely to cross unintended biological barriers, enabling more localized and sustained drug release

(Vinayak A. Katekar et al., 2023). Their larger size allows for higher drug loading, protection of encapsulated agents from enzymatic degradation, and the ability to modulate release kinetics over hours, weeks, or months **(Ganju et al., 2025)**. Microparticles are also less prone to rapid systemic clearance and can be engineered for various administration routes, including injection, inhalation, and implantation **(Rafiee & Rasool, 2022)**. Furthermore, they are easier to manufacture reproducibly at scale, and their size and surface properties can be tuned to minimize immune responses and optimize therapeutic outcomes **(da Silva et al., 2023; Moore et al., 2022; Vinayak A. Katekar et al., 2023)**.

Despite these advantages, microparticles do have limitations, such as the potential for embolism if not properly designed for parenteral administration, and sometimes less efficient cellular uptake compared to nanoparticles. However, their benefits in controlled release, patient compliance, and safety often outweigh these drawbacks for many clinical applications. A comparison of nanoparticles and microparticles was illustrated.

1.3. Microparticles and Microcarrier Systems

Microcarrier systems and microparticles are foundational technologies in modern biotechnology, cell therapy, and drug delivery, offering versatile platforms for both cell expansion and controlled therapeutic administration. Microparticle-based drug delivery systems are typically composed of natural or synthetic polymers, ceramics, or composites, and can encapsulate both hydrophilic and hydrophobic drugs **(A. K. Soni & Patil, 2023)**. Production methods include emulsification-solvent evaporation, electrospraying, spray drying, and microfluidic techniques, each allowing precise control over size, morphology, and drug loading **(Rafiee & Rasool, 2022; Teekamp et al., 2015)**. Emulsification–solvent evaporation is widely used for encapsulating peptides and proteins, involving the dispersion of a polymer solution in an immiscible phase followed by solvent removal to form solid particles **(Teekamp et al., 2015)**. Spray drying offers a continuous, scalable approach for producing dry microparticles, while microfluidic methods enable precise control over particle monodispersity and architecture by templating droplets in microchannels **(W. Li et al., 2018)**.

Among these, the electrospraying technique has emerged as a robust and versatile method for fabricating micro- and nanoparticulate materials with tailored size, morphology, and encapsulation properties **(Boda et al., 2018; H. Lee et al., 2018; Morais et al., 2020; Jiamian Wang et al., 2019; Leilei Zhang et al., 2012)**. Electrospraying, also known as electrohydrodynamic atomization, utilizes a high-voltage electric field to generate a fine jet of polymer solution from a capillary nozzle. As the jet breaks up into charged droplets, rapid solvent evaporation leads to the formation of solid microparticles, which are collected on a grounded substrate. By adjusting key parameters—such as applied voltage, flow rate, needle diameter, polymer concentration, and solvent properties—it is possible to finely tune the diameter (typically 1–100 μm), shape, and surface texture of the resulting particles **(Boda et al., 2018; H. Lee et al., 2018; Morais et al., 2020; Jiamian Wang et al., 2019)**.

Electrospraying offers several advantages over conventional techniques. It can be performed at ambient temperature and pressure, which is ideal for encapsulating sensitive biomolecules, such as proteins, peptides, and antioxidants **(Jiamian Wang et al., 2019)**. The process enables high encapsulation efficiency and uniform distribution of active ingredients within the particle matrix, while minimizing agglomeration and residual solvent content **(Tanhaei et al., 2021)**. These features make electrospraying particularly attractive for the development of advanced drug delivery systems, tissue engineering scaffolds, and multifunctional biomaterials, where precise control over particle characteristics is crucial for therapeutic efficacy and safety.

In summary, as illustrated in **Figure 1.3**, microparticles are versatile carriers whose biomedical utility is closely linked to the method of their fabrication. Electrospraying stands out as a highly controllable, reproducible, and scalable approach for generating polymeric microparticles with well-defined properties, supporting their expanding role in next-generation biomedical applications. However, the success of any microcarrier or microparticle system depends critically on the selection of biomaterials. Ideal materials must be biocompatible, biodegradable, mechanically robust, and capable of protecting and releasing the therapeutic agent in a controlled manner **(da Silva et al., 2023)**.

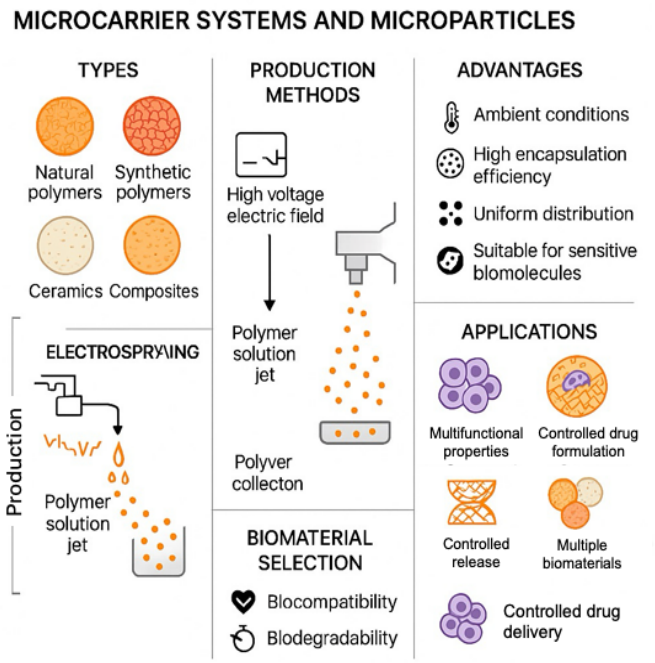


Figure 1.3: Microcarrier systems and their properties **(Boda et al., 2018; da Silva et al., 2023; H. Lee et al., 2018; Morais et al., 2020; Jiamian Wang et al., 2019)**.

1.4. Polymer-Based Biomaterials

Biomaterials are a cornerstone of modern biomedical science, engineered to interact with biological systems for therapeutic, diagnostic, or regenerative purposes. Their evolution from inert, structural supports to dynamic, bioactive platforms has enabled significant progress in tissue engineering, regenerative medicine, and drug delivery. The selection of an appropriate biomaterial relies on criteria such as biocompatibility, biodegradability, mechanical properties, and the ability to support cellular attachment, proliferation, and differentiation. Among the diverse classes of biomaterials, polymers—both natural and synthetic—have emerged as particularly versatile due to their tunable properties and broad application spectrum **(Khouri et al., 2024; Ranakoti et al., 2023)**.

Polymeric biomaterials are generally classified as natural or synthetic, each category offering distinct advantages and limitations for biomedical applications (**Figure 1.4**). Natural polymers—including collagen, gelatin, chitosan, and alginate—are derived

from biological sources and are widely recognized for their excellent biocompatibility, biodegradability, and close resemblance to the native extracellular matrix (ECM) of tissues **(Hu et al., 2024; Oleksy et al., 2023)**. Their inherent bioactivity enables them to support cell adhesion, proliferation, and differentiation, making them highly suitable for applications where biomimicry is essential, such as scaffolds for tissue engineering and regenerative medicine **(M. L. Becker & Burdick, 2021; Oleksy et al., 2023)**.

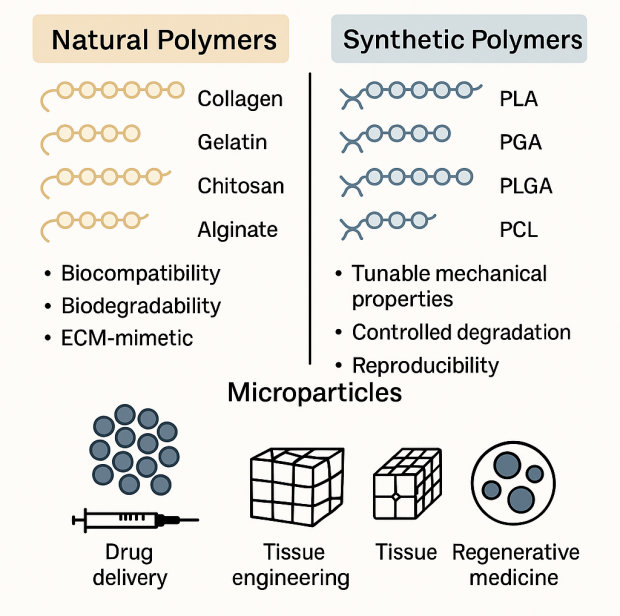


Figure 1.4: Schematic overview of natural and synthetic polymeric biomaterials, highlighting their classification, representative examples, and key biomedical applications as microparticles **(Hu et al., 2024; Oleksy et al., 2023)**.

Collagen, for example, is the most abundant protein in mammalian tissues and serves as a primary structural component of the ECM. Its use in biomaterials is well-established due to its biocompatibility and ability to promote the formation of new tissue **(Hu et al., 2024; Oleksy et al., 2023)**. Gelatin, a denatured form of collagen, retains many of these cell-interactive properties while offering improved solubility and processability. Chitosan, derived from chitin found in crustacean shells and fungal cell walls, exhibits not only biocompatibility and biodegradability but also intrinsic antibacterial and hemostatic properties, making it a valuable material for wound healing, drug delivery, and as a scaffold. As another example, alginate, extracted from brown seaweed, is non-immunogenic and forms hydrogels in the presence of divalent

cations, facilitating its use in cell encapsulation, injectable scaffolds, and controlled drug release systems **(Hu et al., 2024)**.

Despite these favorable biological characteristics, natural polymers often face significant challenges. A major drawback is batch-to-batch variability, which can arise from differences in biological source, extraction, and purification methods, leading to inconsistent material properties and clinical outcomes **(Amponsah et al., 2025; Oleksy et al., 2023)**. Furthermore, natural polymers typically exhibit limited mechanical strength and structural stability, which restricts their use in load-bearing applications, such as bone or cartilage regeneration **(Amponsah et al., 2025; Oleksy et al., 2023)**. Their rapid enzymatic degradation *in vivo* can also compromise scaffold longevity, necessitating chemical modification or blending with synthetic polymers to enhance mechanical and degradation profiles **(M. L. Becker & Burdick, 2021; Kohane & Langer, 2008)**. In summary, while natural polymeric biomaterials offer outstanding biocompatibility, degradability, and ECM-mimetic properties, their clinical translation is often hindered by variability and mechanical limitations. These limitations have driven the development of hybrid systems and chemical modifications to maximize the benefits of both natural and synthetic polymers in biomedical fields.

On the other hand, synthetic polymers, including poly(lactic acid) (PLA), poly(glycolic acid) (PGA), poly(lactic-co-glycolic acid) (PLGA), and polycaprolactone (PCL), provide greater control over mechanical, chemical, and degradation characteristics compared to their natural counterparts. These materials can be synthesized with precisely defined molecular weights, architectures, and copolymer compositions, allowing for the fine-tuning of their physicochemical properties to meet specific biomedical requirements **(Makadia & Siegel, 2011; Middleton & Tipton, 2000)**. For instance, the degradation rate of PLGA can be tailored by adjusting the ratio of lactic acid to glycolic acid, making it suitable for applications that require either rapid or prolonged resorption **(Danhier et al., 2012)**. One of the key advantages of synthetic polymers is their reproducibility and batch-to-batch consistency, which is critical for regulatory approval and clinical translation. Their processability enables the fabrication of a variety of forms, including fibers, films, microspheres, and porous scaffolds, through techniques such as electrospinning, solvent casting, and 3D printing **(Place et al., 2009)**. In tissue engineering, synthetic polymer scaffolds provide temporary mechanical support and guide tissue regeneration while gradually

degrading to be replaced by new tissue. For example, PCL's slow degradation rate and favorable mechanical properties make it suitable for long-term applications such as bone and cartilage engineering **(Woodruff & Hutmacher, 2010)**. In contrast, the faster-degrading PLA and PLGA are often used for soft tissue regeneration and drug delivery, where a more rapid resorption is desirable **(Danhier et al., 2012)**. Moreover, the chemical versatility of synthetic polymers allows for functionalization with bioactive molecules, such as peptides, growth factors, or drugs, to enhance cellular responses and therapeutic efficacy **(Place et al., 2009)**.

Among synthetic polymers, poly(lactic acid) (PLA) stands out due to its unique combination of biocompatibility, biodegradability, and mechanical strength. PLA is an aliphatic polyester derived from renewable resources such as corn starch or sugarcane, aligning with the increasing demand for sustainable materials. It has received U.S. Food and Drug Administration (FDA) approval for various medical applications, including resorbable sutures, orthopedic implants, and drug delivery systems, underscoring its safety and clinical relevance **(Khouri et al., 2024; Ranakoti et al., 2023; Zhenqi Yang et al., 2024)**. PLA-based biomaterials are extensively used in drug delivery systems and tissue engineering applications.

PLA's ability to form nanoparticles, microparticles, and hydrogels enables the encapsulation and controlled release of a wide range of therapeutic agents, including small molecules, proteins, and nucleic acids. This controlled release minimizes systemic side effects and enhances treatment efficacy **(Kaval et al., 2023; Ranakoti et al., 2023; Zhenqi Yang et al., 2024)**. Moreover, PLA scaffolds, fabricated via techniques such as electrospinning, 3D printing, and phase separation, provide structural support for cell attachment and proliferation in bone, cartilage, nerve, and skin regeneration. Their tunable porosity and degradation rates can be matched to specific tissue requirements **(Capuana et al., 2022; Khouri et al., 2024; Ranakoti et al., 2023; Zhenqi Yang et al., 2024)**.

1.5. Poly(lactic acid) (PLA) as a Biocompatible Carrier

The versatility of PLA extends to its use as a carrier system for bioactive molecules and cells (**Figure 1.5**). PLA-based carriers can be engineered to respond to environmental stimuli, enabling targeted and sustained delivery of therapeutics. This

is particularly valuable in cancer therapy, wound healing, and regenerative medicine, where localized and controlled release is critical for therapeutic success. PLA is a linear aliphatic polyester obtained from renewable resources, consisting of repeating lactic acid units. Its structure includes two stereoisomers—L-lactic acid and D-lactic acid—with the L-form dominating in biomedical applications due to its compatibility with human metabolism **(Moya-Lopez et al., 2022)**. PLA is synthesized through ring-opening polymerization (ROP) of lactide (a cyclic dimer of lactic acid) or direct polycondensation of lactic acid monomers. The ROP method is preferred for producing high-molecular-weight PLA with controlled crystallinity and degradation rates, which are critical for customized biomedical applications **(Casalini et al., 2019; Lopes et al., 2014)**.

PLA undergoes hydrolytic degradation in aqueous environments, where water molecules cleave ester bonds, yielding lactic acid oligomers and monomers. These breakdown products are further metabolized via the Krebs cycle into carbon dioxide and water, ensuring complete biocompatibility and elimination from the body **(Elsawy et al., 2017)**. This degradation profile can be modulated by adjusting the molecular weight, crystallinity, and stereochemistry of PLA, making it adaptable for both short-term drug delivery and long-term structural scaffolds.

PLA as an FDA approved polymer, safety and biocompatibility have been rigorously validated in both *in vitro* and *in vivo* models. In human umbilical vein endothelial cells (HUVECs) and keratinocytes (HaCaTs), PLA supports cell adhesion, proliferation, and viability without inducing cytotoxicity or inflammatory responses **(Bazgir et al., 2022; Černochová et al., 2020)**. Studies demonstrate that PLA scaffolds maintain mitochondrial membrane integrity and reduce oxidative stress, even under prolonged culture conditions **(Jesús Villarreal-Gómez et al., 2014; Karabay et al., 2019)**. *In vivo*, PLA implants exhibit minimal foreign body reaction, with gradual degradation and replacement by host tissue, underscoring their suitability for clinical use.

PLA is utilized in various biomedical applications, including micro- and nanoparticles, scaffolds, drug delivery systems, and tissue engineering. PLA-based microparticles and nanoparticles enable controlled release of therapeutics, protecting labile compounds (e.g., proteins, antioxidants) from degradation while minimizing systemic toxicity **(Rachmawati et al., 2016; Rancan et al., 2009; Thauvin et al., 2019)**. PLA

scaffolds mimic the extracellular matrix (ECM), providing mechanical support and topographic cues for cell migration and differentiation **(Gregor et al., 2017; Rodrigues et al., 2016)**. Their porosity and surface functionalization enhance nutrient diffusion and bioactive loading.

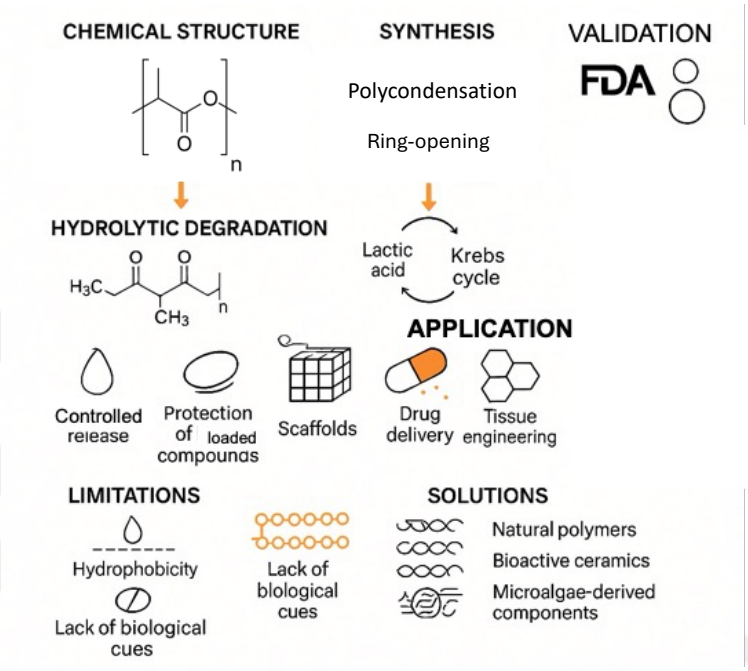


Figure 1.5: Schematic representation of PLA's multifunctional role as a carrier system, illustrating its synthesis, biodegradation, biocompatibility, and applications in targeted and sustained delivery of bioactive molecules and cells for advanced biomedical therapies **(Casalini et al., 2019; Lopes et al., 2014; Moya-Lopez et al., 2022)**.

Despite its many advantages, PLA is not without limitations. Its hydrophobic nature and lack of intrinsic biological cues result in poor cell adhesion and limited protein adsorption, which can impede tissue integration and regeneration **(Capuana et al., 2022; Khouri et al., 2024).** To address these challenges and enhance the biological functionality of PLA-based materials, researchers have developed hybrid systems that incorporate natural polymers, bioactive ceramics, and, more recently, microalgae-derived components, leveraging the complementary properties of each to create scaffolds with improved cellular interactions, bioactivity, and regenerative potential.

1.6. Overview of Micro/Nanoparticle Drug Delivery

The evolution of biomaterials in regenerative medicine has increasingly emphasized the integration of bioactive compounds from natural sources to enhance therapeutic efficacy and functional outcomes. Among these, microalgae-derived bioactives have emerged as a promising class of natural therapeutics, offering a sustainable and biocompatible alternative to synthetic agents. Microalgae, such as *Spirulina platensis and Chlorella vulgaris*, are rich in antioxidants (e.g., phycocyanin, carotenoids), anti-inflammatory agents (e.g., polysaccharides, phenolic compounds), and essential nutrients (e.g., vitamins, omega-3 fatty acids) **(Bortolini et al., 2022; El-Naggar et al., 2020; Park et al., 2018; Saberian & Shahidi Delshad, 2023)**. These compounds not only mitigate oxidative stress and inflammation but also actively promote cellular proliferation, migration, and tissue repair—critical processes in wound healing and vascular regeneration. For instance, Spirulina's phycocyanin has been shown to protect keratinocytes from UV-induced damage by scavenging reactive oxygen species (ROS) and preserving mitochondrial function **(Jang & Kim, 2021)**. At the same time, its polysaccharides enhance endothelial cell viability and angiogenesis **(De Freitas Brito et al., 2019; L. Yang et al., 2009)**. The inherent biocompatibility and multifunctionality of microalgae-derived compounds position them as ideal candidates for integration into advanced biomaterial systems.

The convergence of microalgae bioactives and biodegradable polymers has catalyzed innovations in micro- and nanoparticle drug delivery systems. These systems address critical limitations of conventional therapies, such as poor bioavailability, rapid clearance, and off-target effects. For instance, PLGA nanoparticles, functionalized with ligands for targeted delivery, have demonstrated enhanced accumulation in tumor tissues through the enhanced permeability and retention effect, reducing systemic toxicity **(Acharya & Sahoo, 2011)**. Recent advances also highlight the role of microalgae-derived extracellular vesicles and genetically engineered algal cells in crossing biological barriers, such as the blood-brain barrier, further expanding their therapeutic potential **(Adamo et al., 2021)**.

However, challenges persist in optimizing these systems for clinical translation. Issues such as burst release, encapsulation efficiency, and scalability require innovative

solutions, including polymer blending, surface functionalization, and advanced fabrication techniques **(Eze et al., 2023)**.

1.7. Spirulina and Its Bioactive Properties

Spirulina, scientifically classified within the domain Bacteria, phylum Cyanobacteriota, and class Cyanophyceae, belongs to the order Spirulinales and family Spirulinaceae (**Sinetova et al., 2024)**. Although the term "Spirulina" is commonly used in the dietary supplement industry, most commercial products are derived from species of the genus Arthrospira, particularly *Arthrospira platensis* and *Arthrospira maxima*, which were formerly grouped under Spirulina **(Thangsiri et al., 2024)**. These filamentous, spiral-shaped cyanobacteria are among the earliest life forms on Earth, with fossil records dating back over 3.5 billion years **(Thangsiri et al., 2024)**. They are characterized by their unique helical trichomes, multicellular structure, and the absence of a nucleus, reflecting their prokaryotic nature. The cells contain chlorophyll a, carotenes, and phycobilisomes (notably phycocyanin), which are responsible for their intense blue-green coloration and high photosynthetic efficiency **(Ahmad et al., 2023)**.

Spirulina's cell wall is relatively thin and composed primarily of peptidoglycan, making it easily digestible and facilitating the release of its rich nutrient content during consumption. The organism's ability to fix carbon dioxide through photosynthesis, coupled with its tolerance for high pH and saline environments, allows for robust growth in conditions that limit contamination by other microorganisms **(Masojídek et al., 2021)**. Spirulina naturally inhabits warm, alkaline lakes in regions such as Africa, Asia, and Central America, but its commercial production has been optimized through controlled cultivation systems.

Modern Spirulina cultivation utilizes two primary methods: open raceway ponds and closed photobioreactor systems **(Branyikova & Lucakova, 2021; Sow & Ranjan, 2021)**. Open pond systems, particularly raceway ponds, are the most commonly used for large-scale production due to their cost-effectiveness and simplicity. These shallow, oval-shaped ponds are fitted with paddle wheels to circulate the culture, ensuring uniform light exposure and nutrient distribution. Spirulina flourishes in warm temperatures (30–35°C), high alkalinity (pH 8.5–11), and abundant sunlight, with

shallow pond depths (15–30 cm) to maximize photosynthetic efficiency **(Branyikova & Lucakova, 2021)**. Nutrient-rich media, generally containing nitrogen, phosphorus, potassium, magnesium, and trace elements, are vital for optimal growth. The high pH environment also serves as a natural barrier against contamination from most other microalgae and pathogens.

For higher-value applications or environments that require stricter control, closed photobioreactors are utilized. These systems provide precise control of temperature, light, gas composition, and sterility, resulting in increased biomass productivity and quality. After cultivation, Spirulina biomass is harvested through filtration or centrifugation, washed to eliminate any residual medium, and then processed—commonly by spray drying—to preserve its nutritional and bioactive properties **(Novoveská et al., 2023)**.

The adaptability of Spirulina to diverse cultivation systems, coupled with its rapid growth rate, high protein content (> 60%), and rich repertoire of bioactive compounds, underpins its growing importance in biotechnology, nutrition, and biomedical research **(ElFar et al., 2022; Khan et al., 2005; Q. Liu et al., 2016; R. A. Soni et al., 2017)**. These characteristics make Spirulina an ideal candidate for integration into advanced biomaterial systems, with applications in drug delivery, tissue engineering, and regenerative medicine.

Spirulina is widely recognized as a nutritional powerhouse, earning its reputation as a "superfood" due to its exceptionally rich and balanced composition of macronutrients and micronutrients. The most abundant component of Spirulina is protein, which constitutes between 50% and 70% of its dry weight, making it one of the highest natural sources of complete protein available **(Bortolini et al., 2022; Jung et al., 2019; Spínola et al., 2024)**. Notably, Spirulina provides all essential amino acids—including leucine, lysine, methionine, phenylalanine, threonine, tryptophan, and valine—at proportions comparable to animal-derived proteins, thus serving as an excellent dietary option for vegetarians and vegans **(Bortolini et al., 2022; Spínola et al., 2024)**.

Beyond proteins, Spirulina is a rich source of vitamins vital for human health. It contains significant amounts of vitamin A (as beta-carotene), vitamin D, vitamin E, vitamin K, and a comprehensive range of B vitamins, including thiamin (B1),

riboflavin (B2), niacin (B3), pantothenic acid (B5), pyridoxine (B6), folic acid (B9), and cobalamin (B12) **(Baylan et al., 2012; Grosshagauer et al., 2020; Liestianty et al., 2019)**. Vitamin E and beta-carotene contribute to Spirulina's potent antioxidant properties, supporting cellular protection and immune function **(Sahil et al., 2024)**.

Minerals are another cornerstone of Spirulina's nutritional value. The microalga is especially rich in iron, calcium, magnesium, potassium, zinc, phosphorus, manganese, copper, and selenium **(Janda-Milczarek et al., 2023; Rosario & Josephine, 2015)**. Additionally, Spirulina's lipid fraction, though modest in overall fat content, is distinguished by its abundance of essential fatty acids, particularly gamma-linolenic acid, as well as polyunsaturated fatty acids such as linoleic and docosahexaenoic acids (DHA) **(Agustini & Wijayanto, 2020; Otleş & Pire, 2001)**.

In summary, the unique synergy of highly digestible proteins, a broad spectrum of vitamins and minerals, and a valuable profile of essential fatty acids supports Spirulina's increasing use in functional foods, dietary supplements, and biomedical applications. Its nutrient density and bioactive variety make it an ideal candidate for integration into advanced biomaterial systems designed to promote tissue repair, immune modulation, and overall health maintenance.

The remarkable ingredients of Spirulina, which provide health-promoting properties, are primarily attributed to its diverse array of bioactive compounds, most notably phycocyanin, carotenoids, and polysaccharides. These molecules not only contribute to Spirulina's characteristic blue-green color but also endow it with potent antioxidant, anti-inflammatory, and immunomodulatory activities, making it a valuable nutraceutical and functional food ingredient **(Calella et al., 2022; Finamore et al., 2017; Wu et al., 2016)**.

Phycocyanin is a unique pigment-protein complex found in high concentrations in Spirulina. It is responsible for the intense blue hue of the microalga and is recognized for its strong antioxidant capacity. Phycocyanin scavenges reactive oxygen species (ROS) and free radicals, thereby protecting cells from oxidative damage and lipid peroxidation **(Finamore et al., 2017; Wu et al., 2016)**. Beyond its antioxidant action, phycocyanin has been shown to modulate cellular signaling pathways, such as

ERK1/2, JNK, and p38, resulting in anti-inflammatory effects and the suppression of pro-inflammatory cytokines **(Jiang et al., 2018)**.

Carotenoids in Spirulina, including β-carotene, zeaxanthin, echinenone, and 3-hydroxyechinenone, further enhance its antioxidant profile **(Calella et al., 2022; Vasudevan et al., 2021)**. These fat-soluble pigments neutralize singlet oxygen and other free radicals, thereby contributing to cellular defense against oxidative stress and supporting the health of the skin and eyes.

Polysaccharides extracted from Spirulina (SPP) are increasingly recognized as vital, pharmacologically active biomacromolecules **(Ai et al., 2023; Finamore et al., 2017)**. SPPs exert multiple biological effects, including antioxidant, immunomodulatory, anti-cancer, hypolipidemic, and hypoglycemic activities. They enhance macrophage and natural killer (NK) cell activity, stimulate T-cell proliferation, and upregulate key immune organs, thereby strengthening the body's defense against pathogens and environmental toxins **(Ai et al., 2023)**.

Collectively, these bioactive compounds enable Spirulina to activate cellular antioxidant enzymes (e.g., superoxide dismutase, catalase), inhibit lipid peroxidation and DNA damage, and modulate immune responses. Clinical and preclinical studies confirm that Spirulina supplementation can prevent exercise-induced oxidative stress, reduce inflammation, and enhance immune function in both animals and humans. The synergy among phycocyanin, carotenoids, and polysaccharides positions Spirulina as a powerful agent for combating oxidative stress, inflammation, and immune dysfunction—key factors in the development of chronic diseases and tissue degeneration.

Spirulina exhibits significant therapeutic potential due to the excellent ingredients, supported by extensive research on cell proliferation, wound healing, and oxidative stress protection. It enhances stem cell growth, boosting proliferation by over 40% at low concentrations (62 ng/mL) in bone marrow and CD34+ cells while counteracting TNFα-induced suppression in neural progenitors **(Bachstetter et al., 2010)**, suggesting a role in tissue regeneration. In wound healing, Spirulina accelerates repair by promoting re-epithelialization, collagen deposition, and neovascularization in just days, with mature hair follicle formation by day 12 in rat models **(Ahmed Bahei-Eldin**

et al., 2017)—effects attributed to phycocyanin and chlorophyll. Additionally, its potent antioxidant properties reduce oxidative damage, lowering lipid peroxidation by 30–40% in brain tissues and enhancing catalase activity by 25%. This correlates with a reduction in amyloid-β plaques and an improvement in memory in aging models **(J.-H. H. Wang et al., 2011)**. These benefits stem from the additive effect of bioactive compounds, including phycocyanin (anti-inflammatory, modulation of ERK/JNK), polysaccharides (immune activation), and carotenoids (free radical scavenging).

Also, it is a promising therapeutic for diabetics, obesity, neurodegenerative diseases, cancer, and image-guided **(Karizi et al., 2023; Tamtaji et al., 2023; Zizhen Yang et al., 2022)**. However, this profitable agent delivery is a limited factor because of rapid degradation and instability. Therefore, the encapsulation of Spirulina was preferred to enhance its biological effects for an extended period; for this reason, silver nanoparticles, liposomes, or niosomes have been chosen as encapsulated materials **(Abdelghany et al., 2023; Gul et al., 2023)**. Besides the encapsulated molecule, Spirulina is a suitable biomaterial as a microcarrier because of its biological properties. Although Spirulina has successfully encapsulated chemical or biological bioactive molecules in the literature, it is possible to enhance the microcarrier capability and antioxidant properties of Spirulina by combining it with polymers, resulting in a more stable, controllable, efficient, and targeted microcarrier system, as evidence that the combination of Spirulina and polymers has become popular in the literature due to their properties for medicinal applications **(Aquino et al., 2020; Ronggang Liu et al., 2023; Mishra et al., 2021; J. Xu & Hsu, 2023; Zewail et al., 2023; Zhong et al., 2020)**.

1.8. PLA/Spirulina Hybrid Microcarriers via Electrospraying

Combining biocompatible poly(lactic acid) (PLA) with superior Spirulina for microcarrier systems represents a promising strategy to harness the mechanical robustness and biodegradability of PLA alongside the bioactivity and sustainability of microalgae-derived components. Electrospraying, as an advanced fabrication technique, enables the production of PLA/Spirulina microparticles with precise control over particle size, morphology, and encapsulation efficiency, all under mild, ambient conditions that preserve the integrity of sensitive bioactives (Illustrated in **Figure 1.6**).

This approach allows for uniform dispersion of Spirulina within the PLA matrix, enhancing both the mechanical properties and biological functionality of the resulting microcarriers. Electrosprayed PLA/Spirulina microparticles offer several advantages, such as enhanced biocompatibility and bioactivity, sustainable and green, tailored drug delivery, and process flexibility. The incorporation of Spirulina provides antioxidant, anti-inflammatory, and cell-supportive properties, which can improve cellular responses and therapeutic outcomes. Utilizing renewable PLA and microalgae aligns with green chemistry and sustainability goals, reducing the environmental footprint of biomedical materials. Electrospraying allows for the encapsulation of diverse bioactives and drugs, enabling controlled, sustained, and targeted release profiles essential for advanced delivery systems. The technique supports the fabrication of various particle architectures (e.g., core–shell, porous, hollow), further expanding their biomedical utility. As research advances, expectations for these hybrid systems include improved therapeutic efficacy, enhanced scaffold integration, and broader applicability in personalized medicine and sustainable healthcare solutions.

1.9. Pharmaceutical Applications of Microparticles

These advanced delivery strategies are becoming particularly crucial in addressing skin aging - a complex process where both the skin's barrier function and underlying structures undergo progressive deterioration. Skin aging is a multifaceted biological process influenced by both intrinsic factors—such as genetics, cellular metabolism, and hormonal changes—and extrinsic factors, including chronic sun exposure, pollution, and lifestyle habits **(Ganceviciene et al., 2012; Karimi, 2023; Shin et al., 2023)**. These mechanisms lead to cumulative structural and physiological alterations in all skin layers, resulting in visible signs such as wrinkles, sagging, dryness, uneven pigmentation, and loss of elasticity **(Ganceviciene et al., 2012; Karimi, 2023; Shin et al., 2023)**. At the molecular level, aging skin is characterized by a decline in collagen synthesis, increased matrix metalloproteinase (MMP)-mediated collagen degradation, reduced hyaluronic acid content, and the accumulation of senescent cells, which together compromise the skin’s structural integrity and barrier function **(Karimi, 2023; Shin et al., 2023)**. Photoaged skin, in particular, exhibits pronounced changes including thickening of the epidermis, solar elastosis, and mottled pigmentation **(Ganceviciene et al., 2012; Pandel et al., 2013)**.

The global demand for anti-aging and skin health solutions has surged in response to these age-related changes and the growing desire for youthful appearance and skin vitality. The anti-aging products market, encompassing cosmeceuticals, dermal fillers, and topical agents, was valued at approximately USD 52.4 billion in 2024 and is projected to grow at a CAGR of 7.7% through 2030, reaching over USD 101 billion by 2034. This growth is propelled by rising consumer awareness, increased life expectancy, and the popularity of premium, science-backed skincare solutions. Notably, the Asia-Pacific region is emerging as the fastest-growing market, while North America remains the largest, reflecting both demographic trends and evolving beauty standards. In parallel, the global microparticles and microspheres market—including cosmetic and pharmaceutical microparticles—was valued at USD 6.85 billion in 2023 and is expected to reach USD 13.41 billion by 2030, with the cosmetics sector representing a significant and expanding application area.

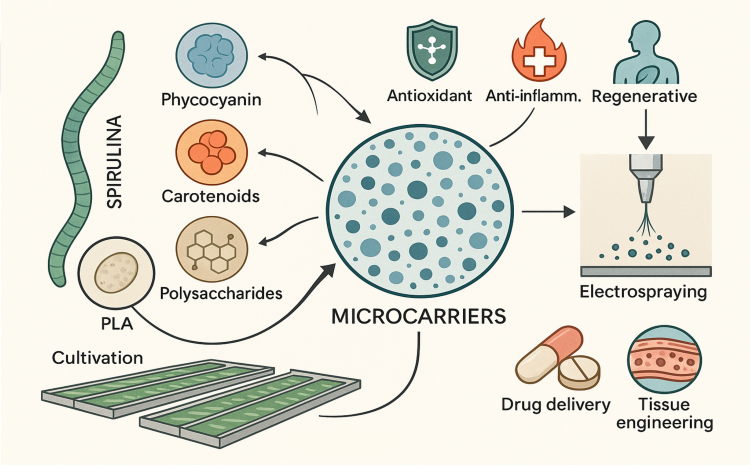


Figure 1.6: PLA/Spirulina microcarrier system illustration.

Microparticle-based technologies have become increasingly important in the pharmaceutical sector, offering innovative solutions for controlled, sustained, and targeted drug delivery. Their adoption is particularly significant for transdermal and topical formulations, where overcoming the skin's formidable barrier properties is essential for therapeutic efficacy. The skin, as the largest organ of the body, is composed of three major layers: the epidermis (including the stratum corneum), dermis, and hypodermis. The stratum corneum, a thin but highly effective barrier

formed by tightly packed corneocytes embedded in a lipid matrix, is the principal obstacle to drug permeation and is responsible for the skin's low permeability to most hydrophilic and large molecular weight drugs **(Brito et al., 2024; Gorzelanny et al., 2020; Yu et al., 2021)**. Drug delivery systems must therefore be carefully engineered to either facilitate passage through or around this barrier, using strategies such as chemical enhancers, physical methods, or advanced carrier systems like microparticles and microneedles **(Nguyen et al., 2025; Samiksha B. Rotake et al., 2024; Tapfumaneyi et al., 2022)**.

For transdermal and dermal delivery, the design of microparticle carriers is closely tied to the unique structure and physiology of the skin. Drugs can penetrate the skin via the transepidermal (transcellular and intercellular) and transappendageal (hair follicles and sweat glands) routes, with each pathway favoring different physicochemical properties of the drug and carrier **(Brito et al., 2024)**. Microparticles can be engineered to exploit these routes, particularly the transappendageal pathway, which is advantageous for delivering macromolecules and hydrophilic drugs that would otherwise be hindered by the dense lipid matrix of the stratum corneum **(Brito et al., 2024)**. Furthermore, combining microparticles with physical enhancement techniques such as microneedles has been shown to significantly increase skin permeability and drug deposition, as demonstrated in recent studies with PLGA microparticles and microneedle-assisted delivery **(Nguyen et al., 2025)**.

A critical factor in the advancement of pharmaceutical microparticles is the use of materials with enhanced biological properties. Incorporating bioactive or naturally derived components—such as proteins, peptides, or microalgae extracts—can significantly improve biocompatibility, cellular interactions, and therapeutic outcomes. For example, natural polymers like gelatin, chitosan, and hyaluronic acid are favored for their biomimicry and biodegradability, while synthetic polymers such as poly(lactic acid) (PLA) offer tunable mechanical and degradation characteristics, as well as regulatory acceptance for clinical use **(Tapfumaneyi et al., 2022; Yu et al., 2021)**. The combination of natural and synthetic materials maximizes both biological activity and structural performance, supporting the development of next-generation, sustainable drug delivery systems. These systems improve the performance of anti-aging creams, serums, and exfoliants by enabling sustained delivery of peptides,

vitamins, antioxidants, and moisturizing agents directly to specific skin layers **(Kozlowska et al., 2019; Mukherjee et al., 2011)**. Biopolymer-based microparticles, such as those made from sodium alginate or PLA, are increasingly preferred over traditional synthetic microbeads due to their biodegradability and skin compatibility, as well as regulatory restrictions on microplastics in cosmetics **(Kozlowska et al., 2019)**. Studies have shown that biopolymer microparticles can match or exceed the efficacy of synthetic particles in improving skin hydration, texture, and barrier function, without causing irritation or environmental harm **(Giménez Martínez et al., 2025; Kozlowska et al., 2019)**.

The integration of bioactive compounds—especially those derived from natural resources like microalgae—has further advanced the field of anti-aging cosmetics and dermal therapeutics **(Giménez Martínez et al., 2025; Mukherjee et al., 2011)**. Microalgae extracts are rich in polysaccharides, fatty acids, amino acids, and pigments, many of which possess antioxidant, anti-inflammatory, photoprotective, and collagen-promoting properties **(Mukherjee et al., 2011)**. These compounds can help counteract photoaging, stimulate skin regeneration, and maintain hydration, making them attractive ingredients for next-generation cosmeceutical formulations. Among the most clinically validated anti-aging actives, niacinamide (vitamin B3) and palmitoyl tripeptide-1 have emerged as particularly promising candidates for microalgae-enhanced delivery systems due to their complementary mechanisms of action. Sustainable extraction and production of microalgal bioactives also align with the growing consumer demand for eco-friendly and ethically sourced skincare products **(Ikeda et al., 2022; Sharafeldein et al., 2023)**.

In summary, the intersection of skin aging biology, consumer demand, and technological innovation is fueling rapid growth in the global cosmetic and anti-aging market. Microparticle-based delivery systems—especially those incorporating bioactive peptides, antioxidants, and sustainable natural ingredients—are at the forefront of this evolution, offering new possibilities for effective, targeted, and environmentally responsible skin rejuvenation.

1.10. Niacinamide and Palmitoyl Tripeptide-1-Loaded Microparticles

As bioactive molecules, extracellular matrix (ECM) proteins are vital, like collagen and elastin, which decrease with aging, causing wrinkles, fine lines, structural deformations, and skin thinning. Collagen, which is 80% of dermis content, is one of the most critical proteins in the ECM in terms of the aging processes and the protection of skin structures **(Lijuan Zhang & Falla, 2009)**. Especially collagen types I, III, and IV are the most preferred proteins in cosmeceuticals for anti-aging creams and serums, which aim to prevent wrinkles, fine lines, and sagging skin, while also promoting skin regeneration and wound healing. Due to the high molecular weight nature of the ECM proteins, peptides to stimulate the production of these proteins are preferred over whole proteins in cosmeceutical applications **(Shete & Birade, 2024)**. Additionally, transdermal delivery is enhanced with smaller bioactive molecules (<500 Da), which increases the efficacy of activating the peptides **(Veiga et al., 2023)**. Several types of peptides are used in cosmetic products for various purposes, such as signal, carrier, neurotransmitter-inhibitory, and enzyme-inhibitory peptides **(Shete & Birade, 2024)**. Depending on the desired aim, peptide selection and, if necessary, combinations of peptides are crucial to enhance efficiency, as peptides play a key role in protein regulation and synthesis, cellular proliferation, and skin-related processes. Signal peptides, like palmitoyl peptides with polar C-terminal and hydrophobic core, stimulate collagen and elastin synthesis, fibroblast proliferation, and migration, and mimic the ECM protein production signals for the regeneration of skin **(Shete & Birade, 2024; F. Yang et al., 2024)**. Additionally, palmitic acid permeates the skin barrier positively, minimizing skin irritation. As a signal peptide, palmitoyl tripeptide-1 includes a palmitoyl group, glycine, histidine, and lysine (Pal-Gly-His-Lys) and promotes ECM protein synthesis; moreover, Pal-tripeptide-1 enhances fibroblast proliferation, which provides cell regeneration and reverses aging processes **(F. Li et al., 2023; Veiga et al., 2023)**. Pal-tripeptide-1 is a part of collagen type I, which has a hydrophobic tail with hydrophilic bioactive peptide to make it easier to penetrate the skin barrier **(Chou et al., 2024)**, and it is accepted as a collagen boost peptide, which makes it preferable in cosmetic products; however, safety assessment of the Pal-tripeptide-1 is critical due to toxicity effect. According to the Personal Care Products

Council, in 2014, the accepted concentration for this peptide was $1x10^{-7}$% **(Johnson et al., 2018)**.

Besides ECM proteins, with aging, reactive oxygen species (ROS**)** levels increase; therefore, using antioxidants becomes more essential to balance ROS levels in the skin **(Jianqiang Wang et al., 2022)**. Biomolecules like niacinamide (nicotinamide), a reduced form of NADH and NADP, can play a critical role in DNA repair and antioxidation mechanisms **(Baik et al., 2024)**. Additionally, niacinamide is recognized for its properties that help minimize UV-induced skin aging by triggering DNA repair mechanisms, decreasing keratinocyte apoptosis, and preventing ROS accumulation and cellular senescence **(Baik et al., 2024; Marques et al., 2024)**. Niacinamide is also vital to synthesizing NAD+ (nicotinamide adenine dinucleotide**),** used in NADH/NADPH coenzymes synthesis, used in energy production mechanisms**,** and redox reactions (Marques et al., 2024). It is widely accepted that one of the primary reasons for skin aging is a reduction in NAD+. Therefore, using NAD+ activators (the mechanism shown in **Figure 1.7**) may help reverse the aging process while increasing NAD+ levels.

Niacinamide is not only effective in DNA repair mechanisms but is also used in treating skin disorders like acne vulgaris, rosacea, and melasma. In addition, niacinamide is gaining popularity in cosmetic products for its anti-aging properties, which involve, and reverse mechanisms related to DNA damage, cellular senescence, and inflammation. In another way, niacinamide is accepted as a GRAS (generally recognized as safe) additive and food; moreover, it is safe and approved for use in cosmetics in the European Union and Japan **(Marques et al., 2024)**. In leave-on cosmetics and creams, niacinamide is used in the ratio of 0.001% to 0.5%, while this number increases to 1-5% if the product is used for cleaning purposes like shampoo, mask, and makeup removal. Although a low percentage of applications exist, niacinamide is recognized as safe and non-toxic in higher concentrations, such as 20%, in dermal applications. However, niacinamide is a hydrophilic component, which poses challenges for transdermal delivery; thus, improving delivery strategies becomes a step forward in enhancing the efficacy of niacinamide in boosting collagen production, preventing keratinocyte senescence, and increasing fibroblast proliferation, which allows for its use as an anti-aging agent **(Marques et al., 2024; Ong & Goh, 2024)**.

Collectively, collagen peptides and antioxidants have become cornerstone ingredients in the global cosmetics industry, driven by their scientifically supported benefits for skin health and appearance. Collagen peptides, which are short chains of amino acids derived from the hydrolysis of collagen, play a crucial role in stimulating the skin's natural collagen production, thereby improving skin elasticity, firmness, and hydration. Numerous studies have shown that topical and ingestible collagen peptides can enhance the general condition of the skin, delay the aging process, and reduce the appearance of fine lines and wrinkles **(Jadach et al., 2024)**. In cosmetic practice, collagen-based products are used in creams, serums, and minimally invasive aesthetic procedures such as fillers, where they help smooth wrinkles, fill atrophic scars, and contour facial features. The global collagen peptides market reflects this growing demand, reaching USD 699 million in 2023 and projected to grow to USD 922 million by 2028, with significant applications in cosmetics and personal care. Antioxidants are another essential class of cosmetic actives, protecting the skin from oxidative stress caused by environmental factors like UV radiation and pollution. These compounds, which include vitamins (such as vitamin C and E), polyphenols, carotenoids, and plant-derived extracts, neutralize free radicals and help prevent premature skin aging, hyperpigmentation, and loss of elasticity. The global cosmetic antioxidants market was valued at USD 162.29 million in 2025 and is forecasted to reach USD 266.45 million by 2034, with rapid growth in the Asia-Pacific region due to increasing consumer awareness and demand for high-quality, natural skincare products. Together, collagen peptides and antioxidants form the backbone of many modern anti-aging and skin health formulations, offering additive effects that address multiple aspects of skin aging and protection. Their expanding use in both topical and ingestible products underscores a global trend toward holistic, science-driven beauty solutions that cater to the demands of a diverse and increasingly informed consumer base.

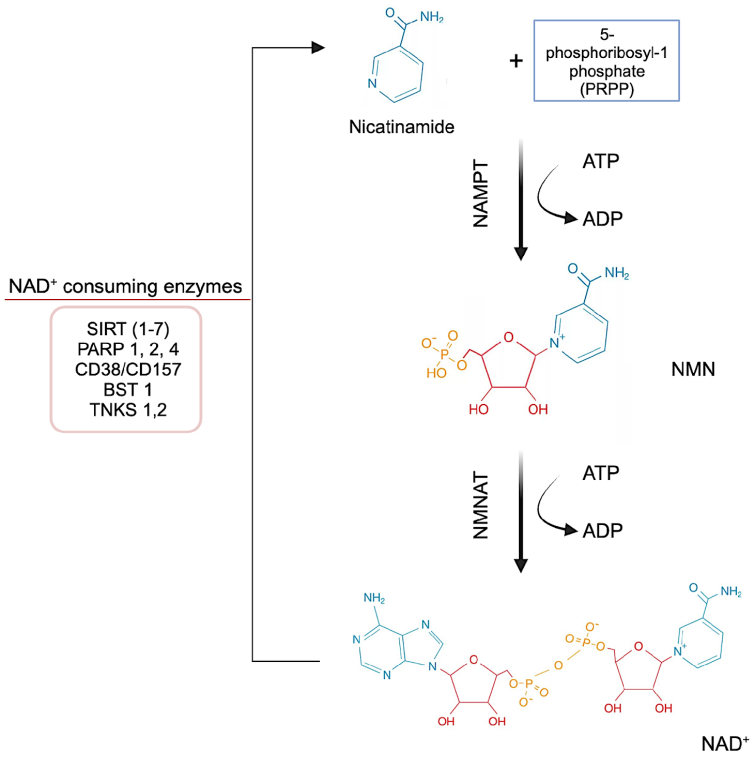


Figure 1.7: NAD+ synthesis process from niacinamide **(Baik et al., 2024; Marques et al., 2024)**.

Given the multifactorial nature of skin aging—characterized by the decline of essential extracellular matrix (ECM) proteins like collagen and elastin, and the accumulation of oxidative damage—there is a clear need for advanced delivery systems that can efficiently transport bioactive agents such as peptides and antioxidants to targeted skin layers. PLA/Spirulina microparticles represent a promising solution to these challenges, particularly for the delivery of niacinamide and palmitoyl tripeptide-1 (Pal-Tri-1). Poly(lactic acid) (PLA) offers biocompatibility, biodegradability, and controlled release properties, enabling sustained and localized delivery of encapsulated actives. When combined with Spirulina, a microalga rich in proteins, amino acids, vitamins, antioxidants, and anti-inflammatory compounds, the resulting hybrid microparticles not only enhance the stability and bioavailability of loaded actives but also provide additive skin benefits—including antioxidant protection, stimulation of collagen synthesis, and support for skin regeneration. Electrospraying, a gentle and precise fabrication method, enables the production of PLA/Spirulina microparticles with well-controlled size, morphology, and encapsulation efficiency, preserving the biological activity of sensitive actives like Pal-Tri-1 and niacinamide. This approach addresses the limitations of

hydrophilic molecules such as niacinamide, which typically struggle to penetrate the skin barrier, and peptides, which are prone to enzymatic degradation and rapid clearance. The inclusion of Spirulina further boosts the antioxidant and regenerative potential of the formulation, as its components—such as phycocyanin, vitamins E and C, and polysaccharides—have been shown to combat oxidative stress, promote wound healing, and enhance skin elasticity and hydration.

Importantly, the dual delivery of Pal-Tri-1 and niacinamide via PLA/Spirulina microparticles is designed to address both the structural and biochemical hallmarks of skin aging. Pal-Tri-1 acts as a signal peptide, stimulating collagen and elastin synthesis and supporting fibroblast proliferation, while niacinamide enhances DNA repair, reduces inflammation, and replenishes NAD+ levels, counteracting both intrinsic and extrinsic aging processes. Spirulina's additional nutrients and antioxidants further amplify these effects, making the hybrid system uniquely suited for comprehensive skin rejuvenation.

In summary, PLA/Spirulina microparticles fabricated by electrospraying offer a biocompatible, sustainable, and multifunctional platform for the efficient delivery of niacinamide and Pal-Tri-1. This advanced system not only overcomes the inherent limitations of traditional topical formulations but also leverages the additive actions of bioactive peptides, antioxidants, and microalgal compounds to promote skin health, resilience, and youthful appearance—meeting the growing demand for effective, science-driven, and environmentally responsible cosmeceutical solutions.

2. PURPOSE OF THE STUDY

The primary aim of this thesis is to develop, characterize, and evaluate novel and multifunctional poly(lactic acid) (PLA)/Spirulina-based microparticles loaded with niacinamide and palmitoyl tripeptide-1 for applications in tissue engineering, wound healing, and skin regeneration. This research is intended to; (1) Optimize the fabrication of PLA-based microparticles using the electrospraying technique to achieve controlled morphology, high encapsulation efficiency, and sustained release profiles. (2) Investigate the edditive effects of combining PLA/Spirulina and bioactive compounds on the biological performance of the microparticles, with emphasis on antioxidant, anti-inflammatory, and regenerative properties. (3) Assess the biocompatibility, cellular uptake, and therapeutic efficacy of the developed microparticles in relevant *in vitro* models, including human umbilical vein endothelial cells (HUVECs) and keratinocytes (HaCaTs). (4) Address formulation and translational challenges such as burst release, encapsulation efficiency, and scalability, and propose strategies to enhance the clinical potential of microalgae-polymer-based delivery systems.

Ultimately, this thesis aims to advance the design of next-generation, bioactive-loaded microcarrier systems that bridge natural bioactivity with engineered delivery platforms, thereby contributing to the development of safe, effective, and sustainable solutions for regenerative medicine and biomedical applications.

3. EXPERIMENT

The following sections detail the materials and methods that were used for this thesis, including the selection and sourcing of all reagents and biomaterials, the fabrication and optimization of PLA-based microparticles, comprehensive physicochemical characterization techniques, and the *in vitro* assays performed to evaluate the biological performance of the developed systems.

3.1. Materials

The following sections detail the materials, reagents, and experimental procedures employed for the fabrication, characterization, and biological evaluation of the PLA-based microparticles encapsulating Spirulina extract, niacinamide, and palmitoyl tripeptide-1 (**Table 3.1**).

Table 3.1: Materials and equipment used in the thesis.

Category	Item	Brand/Supplier
Cell Culture	HUVEC cell line	ATCC (PCS-100-013)
	HaCaT cell line	Cytion (CLS=300493)
	DMEM (Dulbecco's Modified Eagle Medium)	Gibco
	Fetal Bovine Serum (FBS)	Gibco
	Penicillin-Streptomycin	Pan Biotech
	T25 Flasks	TPP or BIOFIL
	CO_2 Incubator	NUVE and/or Binder
	DMSO (Dimethyl Sulfoxide)	BioFroxx
	PBS (Phosphate Buffer Saline, pH 7.4)	Gibco
	Trypsin/EDTA (0.25%)	Gibco
	Hemocytometer	ISOLAB
	Cell Counter (QuantaCell)	Optofil

Continued Table 3.1: Materials and equipment used in the thesis.

Spirulina Cultivation	Spirulina Culture	Algae Research (California)
	Geotextile Membrane (for filtration)	-
	Glass Petri Dishes	Borox
ICP Analysis	Microwave Digestion System (Mars Express)	CEM Corp.
	Filter Paper (Ø125 mm, blue band)	Macherey-Nagel
	ICP-OES Standards	National Institute of Standards and Technology (NIST)
Extraction & Lyophilization	Freeze-Dryer (Lyophilizer)	Teknosem
	Rotary Evaporator	Wiggens Strike 280
Electrospraying	Syringe Pump (IPS-12)	Innovenso
	Electrospinning Device Controller	BasicSystem (Innovenso)
	PLA (Poly(lactic acid))	NatureWork 2003D
	Chloroform, Ethanol	Merck
	Brookfield Viscometer (DV-E)	Brookfield
	Density Bottle	ISOLAB
	Tensiometer	Attension
Characterization	FT-IR Spectrophotometer	PerkinElmer Spectrum
	SEM (Scanning Electron Microscopy)	Philips XL30 SFEG
	DLS (Zetasizer Advance)	Malvern Panalytical
Cellular Assays	MTT Reagent (5 mg/mL)	BioFroxx
	Microplate Reader (BioTek 800 TS)	BioTek
	Crystal Violet	KimyaLab
	Fluorescence Microscopy	SOPTOP ICX41
	EVOS M5000 Imaging System	Thermo Fischer Scientific
	Fluoresence Dyes	BioLegend, MedChem
	Niacinamide	Hangzhou Rebtech Novel Material Co.
	Palmitoyl Tripeptide-1	Elabscience
	Flow Cytometer	BD Biosciences

Continued Table 3.1: Materials and equipment used in the thesis.

Antimicrobial Testing	LB Broth & LB Agar	BioShop
	Ciprofloxacin	Biofarma
Protein Analysis	Bradford Reagent	BioShop
	SDS-PAGE Gels (Acrylamide, TEMED, APS)	NeoFroxx, BioShop
	PVDF Membrane (0.45 µm)	GVS
	Luminol, p-Coumaric Acid)	Merck, Sigma-Aldrich
	iBright CL750 Imaging System	Invitrogen
Antibodies	SMAD2/3 (D7G7, Rabbit mAb)	Cell Signaling Technology
	Anti-AKT1/2/3 (EPR16798)	Abcam
	HRP-linked Anti-Rabbit IgG (#7074)	Cell Signaling Technology
	Direct-Blot™ HRP Anti-β-Actin	BioLegend

3.2. Experimental Section

Spirulina culture, harvest, ICP analysis, extractions, and the cellular experiments on HUVEC and HaCaT cell lines were conducted as the first part of the thesis. The second part of the thesis focused on the microparticle production, optimization, characterization, and cellular experiments using poly(lactic acid) (PLA) and Spirulina ethanol extracts in various concentrations via the electrospraying technique. Moreover, for microparticle production, two different experimental setups were used at Marmara University, Center for Nanotechnology & Biomaterials Applications and Research (NBUAM) (Prof. Dr. Oguzhan Gunduz's Lab), and the Division of Chemical Biology, Department of Life Sciences, Chalmers University of Technology (Assoc. Prof. Alexandra Stubelius' Lab). The final part of the thesis focused on the production, optimization, characterization, and cellular fate of biocompound-loaded microparticles.

During the thesis, cellular experiments were examined using primary umbilical vein endothelial cells (HUVEC) (ATCC, PCS-100-013), and human keratinocytes (HaCaT) were grown with DMEM (Dulbecco's Modified Eagle Medium) (Gibco) containing 10% fetal bovine serum (FBS, Gibco) and 1% penicillin-streptomycin (Pan Biotech)

in T25 flasks (TPP or BIOFIL) with a 25 cm^2 surface area, at 37°C and 5% CO_2 (NUVE and/or Binder, growth conditions).

3.2.1. Cellular Experiments Used for the Thesis

For all cellular experiments, cells were thawed that were stored at -80 °C in freezing medium containing 90% FBS and 10% DMSO (dimethyl sulfoxide, BioFroxx) using 4 mL DMEM and 1 mL cell-containing freezing medium and centrifuged at 1500 rpm for 5 min (DLAB minicentrifuge). The supernatant was discarded, and the pellet was seeded onto the T25 flask and incubated under the growth conditions. When cells were reached up to 80% confluency, the cell passaging procedure was applied which included discarding the existing medium, washing the cells with 1x PBS (phosphate buffer saline pH 7.4, Gibco), trypsinization (0.25% trypsin/EDTA, Gibco), collecting cells with DMEM in the ratio of 1:5 to the trypsin, centrifugating at 1500 rpm and 5 min, then seeded cells T25 or plates depending on the purpose. For cell freezing, after centrifugation, the cell pellet was dissolved with freezing medium and stored at -80 °C for further experiments. The cells were counted using a hemocytometer (ISOLAB) and a QuantaCell (Optofil) cell counter for the experiment set. The cells were centrifuged, and the pellet was resuspended with the appropriate amount of DMEM.

3.2.2. Cultivation of Spirulina

Spirulina medium was prepared with a modified Zarrouk medium, shown in **Table 3.2**. The medium was prepared in a 2 L glass bottle with a filter on the cap, and aeration was provided via a pump (**Figure 3.1**). 15 mL Spirulina culture that grew in the lab as the stock was added into the medium and cultivated for one month. For the Zorrouk medium modification (Albicance, 2015), Ca sources were increased using $CaCO_3$ and $Ca(NO_3)_2$ instead of $NaNO_3$ to provide Ca-rich Spirulina biomass after harvesting and to enhance the growth yield.

After one month of Spirulina growth (Algae Research, California), the medium was filtered using a geotextile membrane to collect biomass on the membrane and transfer it to glass Petri dishes. Glass Petri dishes containing Spirulina were incubated at 70˚C overnight to obtain the dry biomass. The harvested Spirulina, a gift from Assoc. Prof. Muge Isleten Hosoglu was used for mineral analysis to compare with commercially

available Spirulina by inductively coupled plasma (ICP) at Gebze Technical University, KutmanLab.

Table 3.2: Modified and Zarrouk medium recipe **(Albicance, 2015)**.

Modified Zarrouk medium		Zarrouk medium	
Macronutrient	**Amount (g/L)**	**Macronutrient**	**Amount (g/L)**
$NaHCO_3$	13.61	$NaHCO_3$	16.8
K_2HPO_4	0.5	$NaNO_3$	2.5
$NaNO_3$	2.5	K_2SO_4	1.0
K_2SO_4	1.0	NaCl	1.0
NaCl	1.0	$MgSO_4$	0.2
$MgSO_4.7H_2O$	0.2	$CaCl_2$	0.04
$CaCl_2.2H_2O$	0.04	$FeSO_4$	0.01
$FeSO_4.7H_2O$	0.01	Na-EDTA	0.08
Na-EDTA	0.08	H_3BO_3	2.860
Boric Acid	1		
Micronutrient media	**5 mL**	$MnCl_2.4H_2O$	1.810
		$ZnSO_4.7H_2O$	0.222
		$Na_2MoO_4.H_2O$	0.007
		$CuSO_4.5H_2O$	0.079



Figure 3.1: Cultivation of Spirulina in a flask for stock and a 2 L glass bottle with aeration provided by a filtered cap.

3.2.2.1. Mineral Analysis by ICP

Following the harvesting of Spirulina, the mineral analysis of harvested and commercially available Spirulina biomass was conducted using ICP-OES. Ground samples weighing 0.19-0.21 grams were precisely measured into microwave digestion tubes. Each sample was treated with 2 mL of hydrogen peroxide and 5 mL of nitric

acid before undergoing closed-vessel microwave digestion in a Mars Express system (CEM Corp., Matthews, NC, USA). After sufficient cooling, the total mixture was diluted to 20 mL with ultra-distilled water. The resulting solution was filtered through filter paper (Macherey-Nagel, Ø125 mm, blue band) to obtain a clear filtrate for analysis. The filtered samples were subsequently subjected to macro- and micro-mineral analysis using ICP-OES. To ensure analytical accuracy, certified standard reference materials from the National Institute of Standards and Technology (Gaithersburg, MD, USA) were used for quality control and instrument calibration throughout the analytical process.

3.2.2.2. Extraction of Spirulina

Commercially available Spirulina was extracted using either ethanol or pure water as solvents. In the literature, various extraction methods have been employed in different cell lines and applications. Therefore, instead of focusing solely on biomass extraction, three different Spirulina extraction methods were studied to identify the most promising method that alters the cellular fate of HUVEC and HaCaT cell lines. Phycocyanin is obtained through water extraction, as demonstrated in the literature, with anti-cancer effects **(Jiang et al., 2018)**. Antioxidant effects of Spirulina ethanol extraction are higher due to alcohol-soluble molecules such as flavonoids, carotenoids, etc. **(Rutar et al., 2021)**.

In the biomass and water extraction methods, 5 g of Spirulina powder was dissolved in 40 mL of distilled water at 300 rpm and room temperature overnight **(J. J. Lee et al., 2017; Pez Jaeschke et al., 2021; Yağmur et al., 2021)**. Dissolved Spirulina was precipitated at 9000 rpm for 15 mins, the supernatant was used as water extract (dH_2O), and the pellet was used as biomass extract. The extracts were freeze-dried to obtain a powder form. After lyophilization, the extracts were stored at room temperature for further experiments. The same method was used for ethanol extraction; however, 70% ethanol was preferred instead of distilled water. Also, before lyophilization, the ethanol was evaporated using an evaporator (175 mPa, 37°C, with 100 rpm). The powder form of the extracts was stored at room temperature for further experiments. The extraction method was illustrated in **Figure 3.2**.

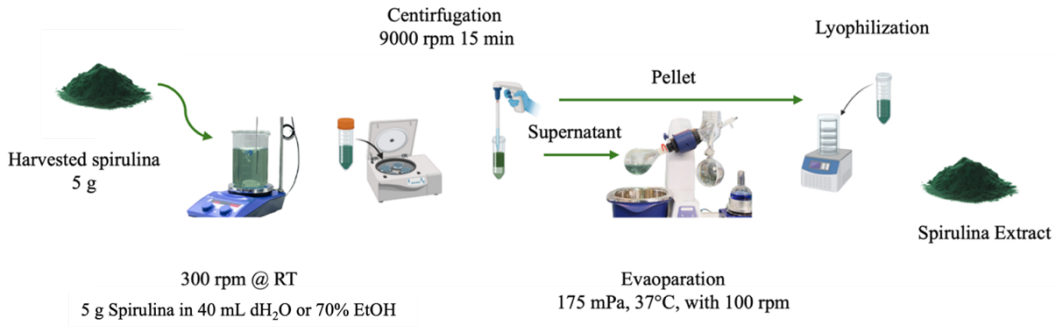


Figure 3.2: Illustration of the Spirulina extraction method.

3.2.2.3. Cellular Experiments

Primary umbilical vein endothelial cells (HUVEC) (ATCC, PCS-100-013) and human keratinocytes (HaCaT) were grown with DMEM (Dulbecco's Modified Eagle Medium) (Gibco) containing 10% fetal bovine serum (FBS) (Gibco) and 1% penicillin-streptomycin (Pan Biotech) in T25 flasks (TPP) with a 25 cm^2 surface area, at 37°C and 5% CO_2.

The MTT (3-(4,5-Dimethylthiazol-2-yl)-2,5-Diphenyltetrazolium Bromide) assay, colony formation assay, and cell survival assay were conducted with HUVEC and HaCaT cell lines for three different Spirulina extractions. The cytotoxicity of these extractions was confirmed with the MTT assay and colony formation; moreover, the proliferative effects of extracts were analyzed via the cell survival assay (Berrak et al., 2016; Coker-Gurkan et al., 2019).

The extracts were prepared at a 10 mg/mL concentration with ultra-pure water under sterile conditions (laminar flow cabinet, Class II) and filtered with a 0.22 µm syringe filter. For the MTT assay, the cells were seeded on a 96-well plate at a density of 3 × 10^3 cells/well, and after cell attachment was provided, 0, 5, 10, 25, 50, and 75 µg/mL of each extract (diluted with cell medium) was applied for 24h, 48h, and 72h. When the treatment was over, the MTT reagent (5 mg/mL, BioFroxx) was used, and a 4h incubation was conducted under the same conditions as growth. The formazan crystals were produced due to the MTT reagent, and these crystals were dissolved in dimethyl sulfoxide (DMSO). The colorimetric results were read at 570 nm via a microplate reader (BioTek, 800 TS). Based on each day's control, the results were calculated with

equation (3.1) and analyzed using two-way ANOVA with Dunnett's comparison tests via GraphPad 9.2.0.

$$\%\ Cell\ viability = \frac{average\ absorbance\ values\ of\ sample\ applied\ group}{average\ absorbance\ values\ of\ control\ group} \quad (3.1)$$

For colony formation experiments, $2.5x10^3$ cells were seeded onto a 6-well plate, after attachment was provided, Spirulina extracts with the same concentrations as the MTT assay were applied, and the treatment period was 24h. Then, the medium was rechanged with a fresh medium, and the plate was left in growth conditions (37°C and 5% CO_2) for 10-14 days. Before imaging, the colonies were fixed with a fixation solution (acetic acid 1: 3 methanol) and dyed with 0.5% crystal violet.

The survival assay was conducted by seeding 1×10^4 cells per well onto the 24-well plate. The optimized two dosages were applied to the cells after they had attached to the surface. Cells were detached using trypsin at each treatment time and counted with Thoma via a cell counter, QuantaCell. The statistical analysis was achieved by comparing each period's control using two-way ANOVA with Dunnett's comparison test in GraphPad 9.2.0 software.

3.2.3. Microparticle Production

Depending on the cellular experiments from Spirulina extracts combined with the solvents previously optimized by lab members of Marmara University, Center for Nanotechnology & Biomaterials Applications and Research (NBUAM), 70% ethanol extract was selected for microparticle production (3% PLA was used as a reference microparticle).

3.2.3.1. Solution Optimization and Characterization

Previously optimized PLA microparticle production using the electrospraying technique was produced based on 3% PLA microparticles using 19:1 chloroform: ethanol **(Tasci et al., 2021)**. A pure PLA solution was prepared for 10 mL; after 9.5 mL of chloroform and 0.3 g of PLA were added, the solution was stirred at 500 rpm at 40˚C for 1 hour; meanwhile, 0.5 mL of ethanol was added to the solution dropwise. For Spirulina-included solutions, the selected amount of Spirulina extract (0.0125 g

for 0.125% Spirulina (Spi), 0.025 g for 0.25% Spi, and 0.05 g for 0.5% Spi-included solutions) was mixed in the ethanol phase and added dropwise onto the PLA-included solution. After the mixture was apparent, the solution characterizations were carried out as viscosity (Brookfield, DV-E Viscometer), density (ISOLAB, density bottle), and surface tension (Attension, Tensiometer) to identify the solution injectability for the electrospraying technique.

3.2.3.2. 1st set of Microparticle Production Optimization

The electrical field and the flow rate of the electrospraying technique were optimized for each solution except 3% PLA (1-M0) because it has already been optimized by the lab members at NBUAM as 20 µL/min with 18 kVa at a distance between the collector and needle as 15 cm **(Tasci et al., 2021)**. Syringe pump (IPS-12 innovenso), and electrospinning device controller (BasicSystem, innovenso) were used as a part of electrospraying device with a needle which have inner diameter of 0.65 mm.

The optimization conditions of the microparticles were controlled by using light microscopy and scanning electron microscopy (SEM) until obtaining ideal monodispersity with acceptable particle size compared to 3% PLA microparticles, which is 3 µm **(Tasci et al., 2021)**. 3% PLA microparticles were produced based on the optimized conditions (20 µL/min flow rate, 18 kV electrical field, and 15 cm distance between the collector and the needle).

0.25% Spirulina extract + 3% PLA (1-M1), the flow rate was changed from 10 to 80 µL/min with an electrical field between 9.8 and 18 kV. The distance from the collector to the needle was fitted at 15 cm. Microparticle production was not achieved for the above or below these values for M1. The M1 solution was sprayed more than 50 times within the specified ranges, until the optimized microparticles, characterized by their size distribution and monodispersity, were collected.

0.25% Spirulina extract + 3% PLA (1-M2); the flow rate was 15 to 100 µL/min, with an electric field between 13 and 25 kV. The distance from the collector to the needle was 15 cm. M2 solution was loaded into the 5 mL syringe and sprayed more than 120 times until optimized microparticles were found.

0.25% Spirulina extract + 3% PLA (1-M3). The flow rate was tried from 20 to 60 µL/min with an electrical field between 10 and 24 kVa. The distance from the collector to the needle was 15 cm. The M3 solution was loaded into the 5 mL syringe and sprayed more than 80 times until optimized microparticles were found.

3.2.3.3. 2nd set of Microparticle Production Optimization

The effect of small changes in the electrospraying setup, such as adjusting the nozzle diameter, on microparticle production and characterization (**Figure 3.3**) was studied to reduce particle diameter **(Morais et al., 2020)**. The blunt needle diameter was 27 G-0.4 x 25 mm, whereas the nozzle had a 0.65 mm inner diameter. The second set of equipment was studied at Chalmers University, the Life Science department at Gebze Technical University, and the Chemistry Department and the Material Science department.

The electrospraying method was used with minor changes. The equipment setup and the nozzle diameter were changed (**Figure 3.3**) to reduce the particle diameter (Morais et al., 2020). The blunt needle diameter was 27 G-0.4 x 25 mm, whereas the nozzle had a 0.65 mm inner diameter. The optimized microparticle solution and production conditions was identical to 1st experiment set up, which were 20 µL/min were 18 kV & 20 µL/min, 16.8 kV & 20 µL/min, 16.8 kV & 30 µL/min, and 16.7 kV & 30 µL/min for 3% PLA, 0.125% Spi + 3% PLA, 0.25% Spi + 3% PLA, and 0.5% Spi + 3% PLA, respectively.

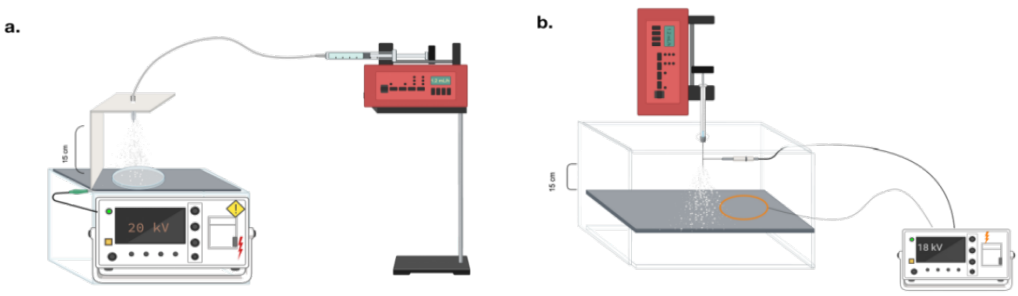


Figure 3.3: Electrospray equipment setup. a. with nozzle (0.65 mm diameter) (Marmara University, NBUAM), b. with blunt needle 0.4 x 25 mm diameter (Chalmers University of Technology, Life Science) (Created with BioRender.com).

3.2.3.4. Microparticle Characterization

DLS (Dynamic Light Scattering) was used to analyze the particle size to identify the microparticle size distribution. When particles were removed from the collector, they were weighed for loading capacity calculations and further usage. Approximately 1 mg of microparticles was dissolved in 1 mL DMSO, sonicated with a bath sonicator for 30 minutes, and particle size was measured via Zetasizer Advance with a low-volume disposable sizing cell kit (Malvern Panalytical).

The particle morphology was corrected via scanning electron microscopy (SEM) (Gebze Technical University, Material Science Department), and the particle chemical bonding characteristics were analyzed with FT-IR from 600 - 4000 cm-1 (Gebze Technical University, Chemistry Department).

The produced particles were also analyzed for Spirulina ingredient capacity, depending on the fluorescence property of Spirulina. The standard curve for extracted Spirulina (70% ethanol extraction) was calculated at 355/535 nm for 0-400 µg/mL Spirulina. The release profile of microparticles was determined in PBS at 7.4 pH and 37°C at 0, 15 min, 30 min, 45 min, 1h, 2h, 3h, 4h, 20h, 24h, 44h, and 48h, respectively. Depending on the release profile, the loading capacity of the microparticles was calculated.

3.2.3.5. Cell Fate Experiments of Produced Microparticles

The MTT assay, colony formation, fluorescence imaging, and cell survival assay were conducted with HUVEC and HaCaT cell lines for eight microparticles produced from electrospraying using PLA and Spirulina. The cytotoxicity of these microparticles was confirmed with MTT assay and colony formation; reactive oxygen species (ROS) and mitochondrial activity were examined with fluorescence staining, and the proliferative effects were analyzed via cell survival assay.

For the MTT assay, the cells were seeded on a 96-well plate at a density of 3×10^3 cells/well, and after cell attachment was provided, 0.5, 1, 5, 10, and 25 µg/mL of each microparticle, with the non-treated control group, were applied for 24 hours. When the treatment was completed, the MTT reagent was added, and a 4h incubation was conducted under the same conditions as growth. The formazan crystals were produced

because of the MTT reagent, and these crystals were dissolved with DMSO. The colorimetric results were read at 570 nm. The results were calculated based on control and analyzed using two-way ANOVA with Dunnett's comparison tests via GraphPad 9.2.0.

$2.5x10^3$ cells were seeded onto a 6-well plate for the colony formation test. After attachment, microparticles with the same concentrations of MTT assay were applied, and the treatment period was 24h. After the treatment was completed, the medium was replaced with fresh medium, and the plate was incubated under growth conditions for 10-14 days. Before imaging, the colonies were fixed with a fixation solution (acetic acid 1:3 methanol) and dyed with 0.5% crystal violet.

Fluorescence staining was applied to understand the ROS activity using H_2-DCFDA (5µM final concentration), mitochondrial activity via MitoSPY (5 µM final concentration) and $DiOC_6$ (4 nM final concentration), nucleus identification with DAPI (10 µM final concentration) and PI (5 µg/mL final concentration). $3x10^4$ cells/well were seeded on a 24-well plate, and cellular attachment was provided at growth conditions, and the optimized dosages from MTT and colony formation assays were applied for each microparticle (5 and 10 µg/mL) for 24 hours. After the incubation, the cells were stained and imaged using SOIF fluorescence microscopy and an EVOS M5000 imaging system under relevant wavelengths.

The cell survival assay utilized a 24-well plate with 1×10^4 cells per well. The selected dosages were administered for 24 hours, 48 hours, and 72 hours, respectively, in each period. Cells were detached using trypsin at each incubation time and counted via a hemacytometer and QuantaCell. The statistical analysis was achieved using two-way ANOVA with Dunnett's comparison test in GraphPad 9.2.0 software.

3.2.3.6. Antimicrobial Effect

For bacterial growth, 7 µL of -80˚C bacterial stocks (from Prof. Dr. Elif Damla Arisan's lab) were incubated in 5 mL LB Broth (BioShop) overnight at 37˚C to provide bacterial growth. Then, 7 µL of bacterial inoculum from medium containing bacteria was spread onto the LB Agar (BioShop) to obtain single colonies, and the agar plate was incubated under the same conditions as a liquid medium. The single colony was

inoculated in 5 µL LB Broth overnight at 37˚C, and 1 mL of bacterial culture was seeded in 180 mL of LB Broth to obtain a "1" value OD_{600} nm for identification of colony-forming units (CFU) via UV-Vis spectrophotometer (Shimadzu, UV-1280). After the culture's optical density reached 1 at 600 nm, it was stored at 4˚C. Furthermore, the bacterial stock was prepared using 625 µL of 80% glycerol, 375 µL of bacterial culture for -20 ˚C stock, and 375 µL of 80% glycerol with 625 µL culture for -80˚C stock for further experiments.

Spirulina extract was dissolved with distilled water at 10 mg/mL, and the mixture was filtered via a 0.22 µm syringe filter. The paper disk diffusion assay was applied to four different Spirulina ethanol extracts at four concentrations (1 mg/mL, 2.5 mg/mL, 5 mg/mL, and 10 mg/mL) **(Abdel-Moneim et al., 2022)**. Distilled water was used for the negative control, while the positive control was penicillin-streptomycin (10000 U/mL, Pan Biotech). For antimicrobial effects, the disk diffusion assay **(Abdel-Moneim et al., 2022)** was applied for Staphylococcus epidermidis, a beneficial bacterium found on the skin **(Zheng et al., 2022)**. The microparticles were examined with *S. epidermidis*, *S. aureus*, *E. coli*, and *P. aeruginosa*, which were used for the disc diffusion test. The microparticles in powder form were used in combination with distilled water as a negative control and Ciprofloxacin (2 mg/mL) as a positive control. The bacterial selection, except for S. epidermidis, was performed according to the European Standard EN ISO 17516:2014, ISO 11930, and the Personal Care Products Council M-3 & M-4 regulations for the antimicrobial preservative efficacy of cosmetics. *S. epidermidis* was used as a beneficial bacterium to provide homeostasis in the skin **(Leonel et al., 2019; Zheng et al., 2022)**.

100 µL of each bacterial strain (8×10^8 CFU/mL) was spread onto the LB AGAR plate, and microparticles, negative, and positive controls were seeded with or without disc diffusion. Afterward, the plates were incubated at 37˚C overnight and imaged under light for zone inhibition analysis.

3.2.3.7. Antioxidant Capacity of Produced Microparticles

Colorimetric methods were determined using a spectrophotometer to investigate the effect of antioxidant activity on 3% PLA microparticles, pure Spirulina extract, and PLA/Spirulina microparticles. The total phenolic content of Spirulina (ethanol

extract), 3% PLA, and PLA/Spirulina microparticles was tested using the Folin–Ciocalteu method, with at least two replicates **(Machu et al., 2015)**. To release the microparticle content, 1x PBS was added to the test samples and mixed at 300 rpm overnight to ensure homogeneity. The samples in PBS were centrifuged at 7,000 x g for 10 minutes to collect supernatant, which was used as the analysis sample. For the reaction, 0.5 N Folin reagent and 7.5% Na_2CO_3 solution were added to the samples and completed with distilled water. Gallic acid solutions (0.2–1.2 mg/mL) were prepared as standards and treated like the samples. The prepared samples were incubated at room temperature and in the dark for 60 minutes, and their absorbance values at 765 nm were measured using a spectrophotometer. A standard curve of gallic acid concentrations was used, and the phenolic content per dry weight (mg) was determined (mg GAE/1 g extract) **(Machu et al., 2015)**.

The radical scavenging activity of the obtained samples was determined using the DPPH method developed by Brand-Williams, Cuvelier, and Berset **(Brand-Williams et al., 1995)**. A 0.6 M DPPH (1,1-diphenyl-2-picrylhydrazyl radical) solution was prepared in methanol, and the samples were added to 1 mL of DPPH solution. After incubation at room temperature and in the dark for 45 minutes, the absorbance values of the samples were read at 515 nm using a spectrophotometer. The percentage inhibition of DPPH absorbance was calculated using the following equation (3.2):

$$\text{Inhibition } \% \; = \; [(\text{Abs}_t = 0 - \text{Abs}_t = 45 \text{ min}) \; / \; \text{Abs}_t = 0] \; \times \; 100 \qquad (3.2)$$

Where Abs_t=0 is the absorbance of the DPPH reagent at 0 minutes, and Abs_t=45 min is the absorbance of the DPPH reagent after 45 minutes **(Cepoi et al., 2009)**. Additionally, the Trolox equivalent antioxidant capacity (TEAC) was calculated by preparing a Trolox curve with the DPPH reagent and determining the ratio of the slopes of the two graphs.

3.2.4. Biocompound-Loaded Microparticle Production

0.125% Spirulina + 3% PLA (1-M1, e-Spi), selected as the best promising particle, were loaded, optimized, and produced with Nile Red (e-Nile), niacinamide (e-Nia), Pal-tripeptide-1 (e-Tri), and niacinamide and Pal-tripeptide-1 (e-NiaTri) by the electrospraying technique. Also, the cellular fate effects of the microparticles were

examined using MTT assay, cell survival tests, wound healing, and fluorescence imaging assays. For cellular uptake tests, a flow cytometer and fluorescence imaging were used.

3.2.4.1. Nile Red-Loaded Microparticle Production and Cellular Tests

0.1% Nile Red was dissolved in ethanol and added dropwise into the 3% PLA-included chloroform with the final ratio of 19:1; the solution was mixed at 300 rpm for 1 hour and at room temperature. Nile Red has already been used in the literature for cellular uptake tests due to its detectable fluorescence properties. Microparticles containing 0.1% Nile Red and 3% PLA were produced under the same conditions as microparticles containing 3% PLA: 18 kV, 20 µL/min, 15 cm distance between collector and nozzle. To test whether these particles were taken up by cells, fluorescence-activated cell sorting (FACS) analysis was performed after a 24-hour treatment with 5 and 10 µg/mL concentrations, which were optimized based on cell viability test results.

For cellular uptake experiments, e-Nile microparticles were dissolved in DMSO at 5 mg/mL and diluted to 1 mg/mL with DMEM. The HUVEC and HaCaT cells were seeded onto 6-well plates, and after confluency reached 100%, 5 and 10 µg/mL e-Nile were applied for 24 hours. The cells were collected with trypsin after the treatment, and the cell pellets were dissolved with sterile, cold 70% ethanol. The cells were stored at -20°C until the flow cytometer read. Before the collection of cells, fluorescence microscopy was used to identify the existence of Nile Red in the cells.

For FACS analysis, ethanol was removed from the samples by centrifugation and PBS washing. The final pellet was resuspended in 300 µL PBS with 1 µL RNAse, and measurements were conducted using the BD Accuri C6 flow cytometer, limited to 20,000 events.

3.2.4.2. Bioactive Compound-Loaded Microparticle Production

A previously optimized method was applied in the studies carried out for microparticle production: electrospraying techniques with a 15 cm distance between the collector and nozzle. First, the hydrophilic bioactive compound niacinamide was loaded into the e-Spi at different concentrations: 0.1%, 0.5%, 1%, 5%, and 10%. This was achieved by

dissolving the niacinamide in the ethanol part of the solution containing Spirulina extract. The flow rate and electrical field were fixed at the same values as the e-Spi, which were 20 µL/min and 16.8 kV. Depending on the scanning electron microscopy (SEM) images, the optimized particle was selected for further experiments.

Next, amphiphilic peptide palmitoyl-tripeptide-1 was encapsulated from e-Spi in the ratio of 0.1%, 0.25%, and 0.5%, dissolved in ethanol with Spirulina extract. Other parameters were fixed with e-Spi and e-Nia production. The optimized concentration of the peptide was determined via SEM imaging.

After both niacinamide- and palmitoyl-tripeptide-1-loaded microparticles were optimized separately, 0.5% niacinamide + 0.5% palmitoyl-tripeptide-1, 0.5% Nia + 0.25% Tri, and 0.5% Nia + 0.1% Tri were loaded into the e-Spi while mixing these compounds on the ethanol phase of the solution. SEM images were used as a selection composition of optimized microparticles.

3.2.4.3. Cellular Experiments of Loaded Microparticles

Cellular experiments were conducted to determine if the produced microparticles were toxic to HUVEC and HaCaT cell lines. Cytotoxicity tests were performed using an MTT assay. For the MTT assay, five different concentrations of microparticles (1, 5, 10, 25, and 50 µg/mL) were applied to HUVEC and HaCaT cell lines. The stock solutions were prepared in DMSO at concentrations of 4.6 mg/mL for e-Nia, 7.5 mg/mL for e-Tri, and 6.1 mg/mL for e-NiaTri. To obtain an optimal dissolution, particles were sonicated for 30 min via an ISOLAB bath sonicator. After dissolution, all particles were diluted with DMEM to 1 mg/mL and applied to cells using a 1 mg/mL stock solution. For the MTT assay, 3×10^3 cells/well in a 96-well plate were seeded, and after attachment was provided, the treatments were applied for 24h.

Depending on MTT test results, two optimal microparticle concentrations were selected and applied for cell survival and wound healing tests. For cell survival, 1×10^4 cells/well were seeded on a 24-well plate, and after treatment, cells were counted in 24, 48, and 72h application time via QuantaCell, Optofil. For wound healing capacity determination, cells were seeded onto the 24-well plate; after cell confluency reached 100%, a 10 µL sterile pipette tip was used to obtain the wound in a “+” shape.

Cells were washed with 1x PBS after scratching, and microparticles were applied. Wounds were imaged at 0, 2, 4, 6, 12, 24, and 48 hours with inverted light microscopy, and the ImageJ software with WoundHealing Tool was used to analyze the wound closure area **(Suarez-Arnedo et al., 2020)**.

The same experiments (MTT, cell survival, and wound healing assays) were conducted with free forms of loaded biomolecules (Nia and Tri) at 5, 10, 25, 50, and 75 µM concentrations for Nia, and 1, 5, 10, 25, and 50 µM for Tri. The stock solutions were prepared with ultrapure water under sterile conditions (filtered with a 0.22 µm syringe filter) at the concentrations of 10 mM for Nia and 5 mM for Tri. The dilution of the application dosages was examined using cell medium before treatment.

4. RESULTS

4.1. Spirulina Mineral Analysis and Extraction

4.1.1. Mineral Analysis

Spirulina was cultivated in an optimized Zarrouk medium formulation (**Table 3.1**), which significantly improved both biomass production and elemental content compared to standard cultivation methods. Inductively Coupled Plasma (ICP) analysis demonstrated substantial compositional differences between commercial Spirulina powder and modified-culture biomass. The optimized, modified growth medium induced marked elevations in essential minerals, including calcium (38 times higher), sodium (3 times), magnesium (1.7 times), boron (60 times), and potassium (34 times) relative to conventional preparations. Simultaneously, it was observed that substantially reduced levels of sulfur (2× lower), aluminum (4.9×), zinc (414×), and copper (4.67×) (**Table 4.1**). Notably, biomass productivity nearly doubled compared to traditional Zarrouk medium cultivation, demonstrating the method's commercial viability, as well as its nutritional benefits.

Table 4.1: ICP results of commercially available and cultivated Spirulina with modified medium Spirulina.

Element (mg/kg)	Commercial	Modified
	Macroelements	
Ca	5669 ± 168	221000 ± 3920
K	12414 ± 51	425000 ± 170
P	8463 ± 81	8560 ± 0
Mg	3729 ± 29	6490 ± 20
S	6532 ± 25	3280 ± 130
Na	4193 ± 197	14634 ± 510
	Microelements	
Fe	309 ± 32	415 ± 26.5
Al	40 ± 1	8.11 ± 3.51
Zn	5588 ± 102	13.5 ± 1.04
Mn	94 ± 3	5.83 ± 0.24
Cu	24 ± 3	5.13 ± 2.07
	Trace Elements	
Ni	0.9 ± 0.3	1.13 ± 0.27
Co	n.d.	n.d.
Cd	n.d.	0.03 ± 3.51
Pb	2.1 ± 0.3	0.41 ± 0.05
B	8.8 ± 0.1	528 ± 3.51
Mo	0.77 ± 0.14	n.d.

4.1.2. Cellular Fate of Spirulina Extractions

The MTT, colony formation, and cell survival assays were conducted with HUVEC and HaCaT cell lines for three different Spirulina extractions (dH_2O, 70% ethanol, and biomass) (Prabakaran et al., 2020). The cytotoxicity of these extractions was confirmed via the MTT assay and colony formation; moreover, the proliferative effects of extracts with selected two dosages (10 and 25 μg/mL) were analyzed with the cell survival assay.

The first extract examined was biomass; HUVEC (**Figure 4.1**) and HaCaT (**Figure 4.2**) cells were treated with biomass extract for three days in MTT tests to identify the cytotoxic properties of the extract on selected cell lines. Cell viability results from the MTT assay of the HUVEC cell line indicated that no statistically significant differences were observed after 24, 48, or 72 hours of biomass extract application (**Figure 4.1a**). Similar colonization was noted in the HUVEC cell lines after 24 hours of this extract application (**Figure 4.1b**). On the other hand, cell proliferation was significantly increased with the application of 10 μg/mL after 72 hours, while no statistical changes were observed in the control and 25 μg/mL applied cells compared to time 0 hours (**Figure 4.1c**).

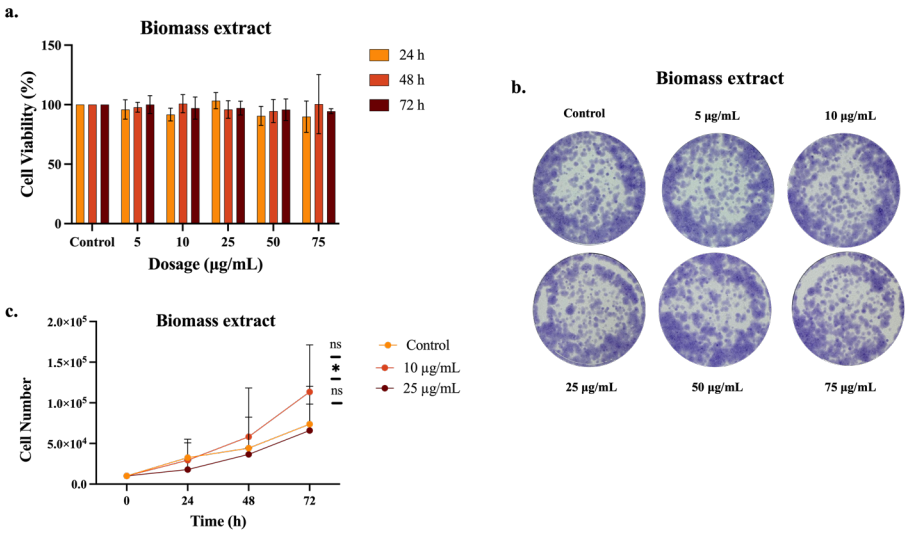


Figure 4.1: a. MTT assay, b. colony formation, and c. cell survival assay of HUVEC cell lines after the application of Spirulina biomass extract for 24 h, 48 h, and 72 h for the MTT and cell survival assays, and a 24 h application for colony formation using five different concentrations (5, 10, 25, 50, 75 µg/mL). The MTT results indicated the average of three biological replicates of quartiles, with standard deviation; two biological replicates for colony formation; and two biological replicates of two technical replicates for cell survival. The analysis was performed using GraphPad 9.2.0 software with two-way ANOVA combined with Dunnett's comparison test against the initial control. ns, $p > 0.05$, *** $p < 0.001$, ** $0.001 \leq p < 0.01$, * $0.01 \leq p < 0.05$.

The MTT results for the biomass extract of Spirulina applied to HaCaT cell lines showed no statistical differences. That means this extract had no cytotoxic effect on the HaCaT cell line (**Figure 4.2a**). The colonization capability was not negatively affected after the biomass extract was applied for 24 h at the applied dosages (**Figure 4.2b**). The cell survival assay significantly increased cellular proliferation after 48 h with or without the biomass extract application. The statistical analysis indicated that the 10 µg/mL of this extract caused a similar trend of proliferation increase compared to the control group. The 25 µg/mL concentration caused a statistically significant enhancement compared to the control at time 0 (**Figure 4.2c**). As expected, the biomass extract of Spirulina did not adversely affect cell viability and proliferation for both cell lines at the applied dosages.

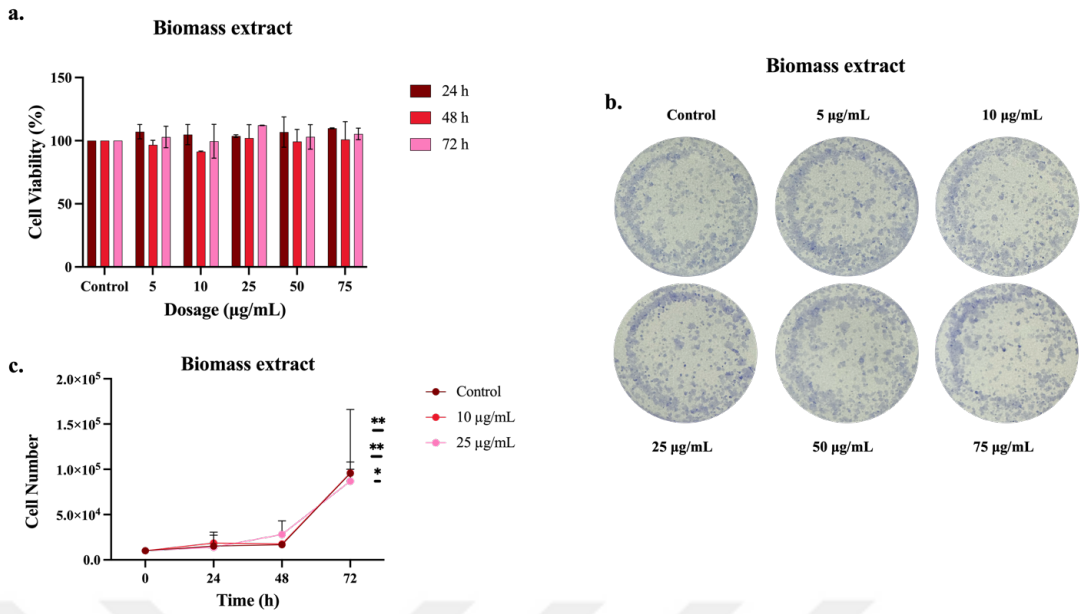


Figure 4.2: a. MTT assay, b. colony formation, and c. cell survival assay of HaCaT cell lines after the application of Spirulina biomass extract for 24 h, 48 h, and 72 h for the MTT and cell survival assays, and a 24 h application for colony formation using five different concentrations (5, 10, 25, 50, 75 µg/mL). The MTT results indicated the average of three biological replicates of quartiles, with standard deviation; two biological replicates for colony formation; and two biological replicates of two technical replicates for cell survival. The analysis was performed using GraphPad 9.2.0 software with two-way ANOVA combined with Dunnett's comparison test against the initial control. ns, $p > 0.05$, *** $p < 0.001$, ** $0.001 \leq p < 0.01$, * $0.01 \leq p < 0.05$.

The water extract of Spirulina showed similar results to the biomass extract for HUVECs, with no adverse effects observed after 24, 48, and 72 hours of application in MTT and colony formation assays. However, when the statistical analysis was conducted for each dose with the 24-hour application, the 50 µg/mL application significantly increased cell viability ($p < 0.05$) for the 48-hour application (**Figure 4.3a**). The ability was not qualitatively changed for colonization with 24 h water extract application for the HUVEC cell line (**Figure 4.3b**). From cell survival assay results, after 72 h of application, the cell numbers were decreased by 25 µg/mL concentration application. In comparison, 10 µg/mL application caused the enhancement of cell viability statistically for 72 h compared to the control of 0 h (**Figure 4.3c**).

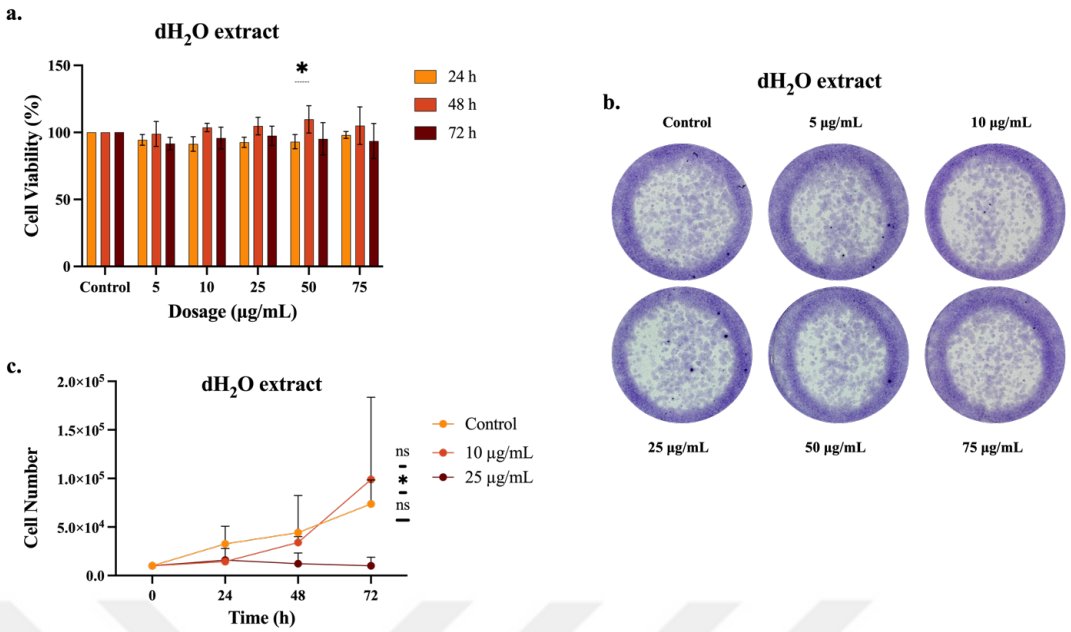


Figure 4.3: a. MTT assay, b. colony formation, and c. cell survival assay of HUVEC cell lines after the application of Spirulina water extract for 24 h, 48 h, and 72 h for the MTT and cell survival assays, and a 24 h application for colony formation using five different concentrations (5, 10, 25, 50, 75 µg/mL). The MTT results indicated the average of three biological replicates of quartiles, with standard deviation; two biological replicates for colony formation; and two biological replicates of two technical replicates for cell survival. The analysis was performed using GraphPad 9.2.0 software with two-way ANOVA combined with Dunnett's comparison test against the initial control. ns, $p > 0.05$, *** $p < 0.001$, ** $0.001 \leq p < 0.01$, * $0.01 \leq p < 0.05$.

From the MTT assay results of the dH_2O extract application in HaCaT cell line, cell viability decreased at 72 h, although this reduction was not statistically significant for nearly all applied dosages (**Figure 4.4a**). However, the colony formation results indicated increased colony numbers at applied dosages of 5 and 10 µg/mL (**Figure 4.4b**). From the cell survival results, the control group and the 10 and 25 µg/mL groups showed a significant enhancement in proliferation at 72 h ($p < 0.001$) (**Figure 4.4c**). As expected, the cellular fate results of Spirulina water extract for HUVEC and HaCaT cell lines indicated no adverse effects.

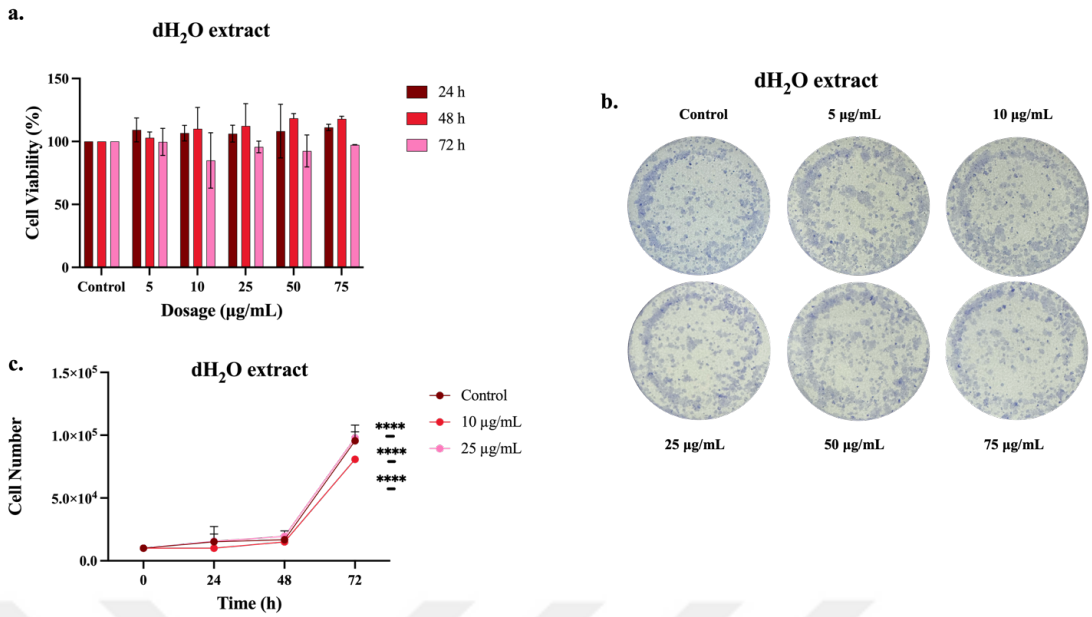


Figure 4.4: a. MTT assay, b. colony formation, and c. cell survival assay of HaCaT cell lines after the application of Spirulina water extract for 24 h, 48 h, and 72 h for the MTT and cell survival assays, and a 24 h application for colony formation using five different concentrations (5, 10, 25, 50, 75 µg/mL). The MTT results indicated the average of three biological replicates of quartiles, with standard deviation; two biological replicates for colony formation; and two biological replicates of two technical replicates for cell survival. The analysis was performed using GraphPad Prism 9.2.0 software with a two-way ANOVA followed by Dunnett's comparison test against time 0 h. ns, $p > 0.05$, **** $p < 0.0001$, *** $0.0001 \leq p < 0.001$, ** $0.001 \leq p < 0.01$, * $0.01 \leq p < 0.05$.

For 70% ethanol extraction of Spirulina for HUVECs, the MTT assay indicated a statistical increase between 24 h and 48 h when five µg/mL was applied. Viability also improved for 50 and 75 µg/mL dosages between 24 h and 72 h ($p < 0.01$ for 50 µg/mL and $p < 0.05$ for 75 µg/mL) (**Figure 4.5a**). However, in the colony formation assay, the application of 75 µg/mL caused a reduction in colonization, while no adverse effects were observed at lower concentrations (**Figure 4.5b**). From the cell survival assay, proliferation was significantly enhanced after 72 h with 25 µg/mL of 70% ethanol extraction applied, compared to the control at 0 h ($p < 0.01$). While the 10 µg/mL dose did not result in a significant increase in proliferation ($p > 0.05$), non-treated cells showed significant proliferation ($p < 0.05$) (**Figure 4.5c**).

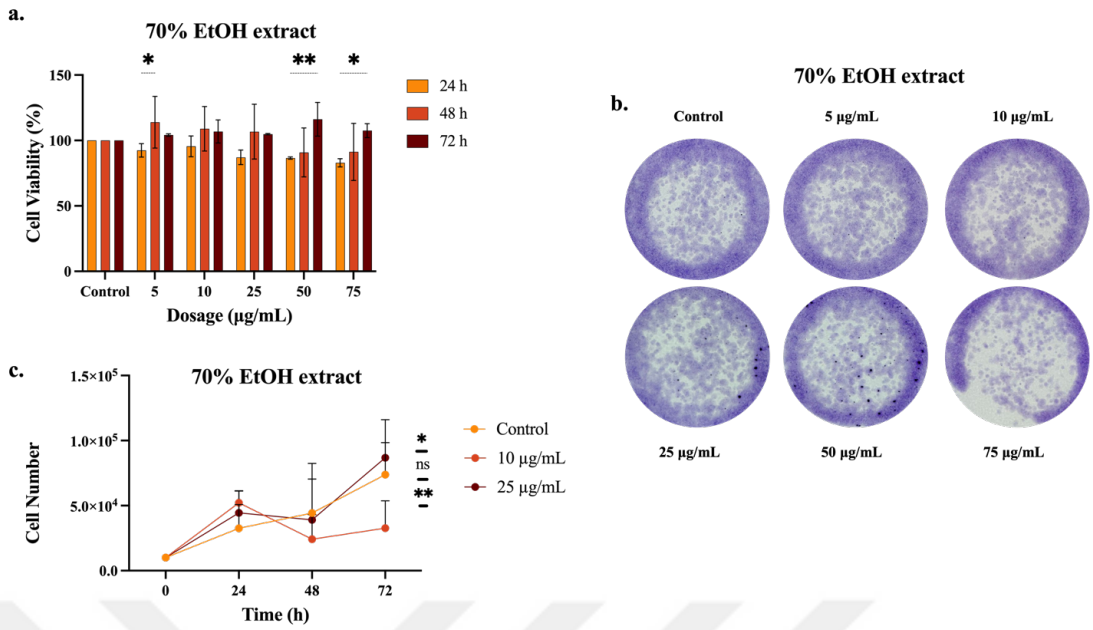


Figure 4.5: a. MTT assay, b. colony formation, and c. cell survival assay of HUVEC cell lines after the application of Spirulina ethanol extract for 24 h, 48 h, and 72 h for the MTT and cell survival assays, and a 24 h application for colony formation using five different concentrations (5, 10, 25, 50, 75 µg/mL). The MTT results indicated the average of three biological replicates of quartiles, with standard deviation; two biological replicates for colony formation; and two biological replicates of two technical replicates for cell survival. The analysis was performed using GraphPad 9.2.0 software with two-way ANOVA combined with Dunnett's comparison test against the initial control. ns, $p > 0.05$, *** $p < 0.001$, ** $0.001 \leq p < 0.01$, * $0.01 \leq p < 0.05$.

The MTT assay results after 72 h of treatment with a 70% ethanol extract of Spirulina on HaCaT cell lines indicated no cytotoxicity across all applied dosages (**Figure 4.6a**). In the colony formation assay, the colonization capability of HaCaT cell lines improved following 24 h of 70% ethanol extraction, particularly at a concentration of 25 µg/mL, where both the colony areas and numbers increased qualitatively (**Figure 4.6b**). Cell proliferation exhibited a similar trend to the non-treated control groups after applying the 25 µg/mL ethanol extract at 72 h ($0.01 < p \leq 0.001$ compared to the control at 0 h). In comparison, the 10 µg/mL concentration resulted in a slight reduction in cell proliferation ($p < 0.01$) (**Figure 4.6c**).

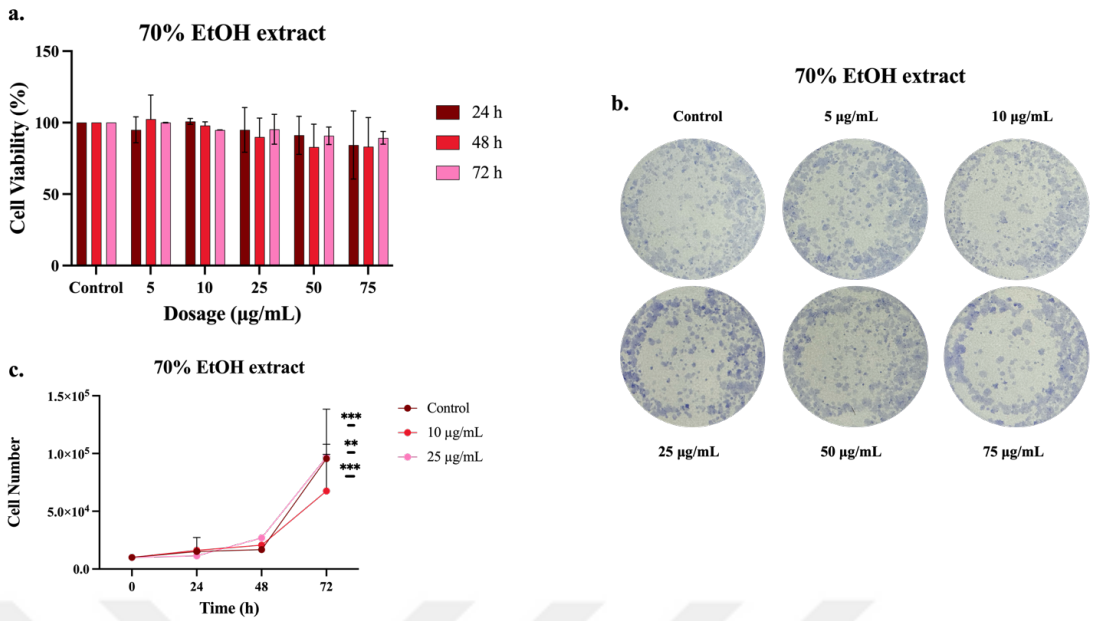


Figure 4.6: a. MTT assay, b. colony formation, and c. cell survival assay of HaCaT cell lines after the application of Spirulina ethanol extract for 24 h, 48 h, and 72 h for the MTT and cell survival assays, and a 24 h application for colony formation using five different concentrations (5, 10, 25, 50, 75 µg/mL). The MTT results indicated the average of three biological replicates of quartiles, with standard deviation; two biological replicates for colony formation; and two biological replicates of two technical replicates for cell survival. The analysis was performed using GraphPad 9.2.0 software with two-way ANOVA combined with Dunnett's comparison test against the initial control. ns, $p > 0.05$, *** $p < 0.001$, ** $0.001 \leq p < 0.01$, * $0.01 \leq p < 0.05$.

The study evaluated the effects of three Spirulina extracts (biomass, dH_2O, and 70% ethanol) on HUVEC and HaCaT cell lines using MTT, colony formation, and cell survival assays. The biomass extract exhibited no cytotoxicity in either cell line, with increased proliferation observed in HUVECs at 10 µg/mL after 72 hours and enhanced proliferation in HaCaT cells at 25 µg/mL. The dH_2O extract similarly exhibited no adverse effects, though higher concentrations (25 µg/mL) reduced HUVEC survival at 72 hours, while lower doses (10 µg/mL) improved viability. The 70% ethanol extract increased HUVEC viability at higher doses (50–75 µg/mL) but reduced colony formation at 75 µg/mL. In HaCaT cells, the ethanol extracts enhanced colony formation at 25 µg/mL and maintained proliferation comparable to controls. Overall, Spirulina extracts demonstrated non-cytotoxic and often proliferative effects, with dose- and time-dependent variations in efficacy. Subsequently, the 70% ethanol

extract of Spirulina was selected for microparticle production based on its solvent compatibility and extraction efficiency.

4.2. PLA/Spirulina-Based Microparticle Production and Characterization

A 70% ethanol extraction of Spirulina was used for the further experiments, based on the cell fate experiments and solvent selection. The 3% poly(lactic acid) was dissolved in a chloroform: ethanol (19:1) mixture for microparticle production, a solution previously optimized at the NBUAM **(Tasci et al., 2021)**.

4.2.1. Solution Optimization

The PLA/Spirulina solutions were prepared in an ethanol phase with concentrations of 0.125% Spi, 0.25% Spi, and 0.5% Spi, along with 3% PLA in chloroform. The injectability of the formulations for electrospraying was assessed by characterizing key solution properties, including viscosity, density, and surface tension. Density measurements demonstrated consistency across all formulations, with values of 1.42 ± 0.03 g/L for 0.125% Spirulina + 3% PLA (M1), 1.41 ± 0.02 g/L for 0.25% Spirulina + 3% PLA (M2), and 1.43 ± 0.01 g/L for 0.5% Spirulina + 3% PLA (M3). In contrast, viscosity exhibited an increasing trend with higher Spirulina concentrations, registering 13.86 ± 1.28 mPa·s (M1), 15.79 ± 1.82 mPa·s (M2), and 15.6 ± 0.59 mPa·s (M3). Surface tension also showed a progressive rise with elevated Spirulina content, with values of 26.00 ± 1.24 mN/m (M1), 26.53 ± 2.03 mN/m (M2), and 27.42 ± 0.29 mN/m (M3) (**Table 4.2**). These findings confirm that all three Spirulina-PLA formulations possess suitable rheological and interfacial properties for successful microparticle encapsulation via electrospraying.

Table 4.2: Solution characterization of 0.125% Spi + 3% PLA, 0.25% Spi + 3% PLA, and 0.5% Spi + 3% PLA. The results indicated an average of three replicates of two reads of each solution, with standard deviations.

Solution	Density (g/L)	Viscosity (mPas)	Surface Tension (mN/m)
0.125% Spi + 3% PLA	1.42 ± 0.03	13.86 ± 1.28	26.00 ± 1.24
0.25% Spi + 3% PLA	1.41 ± 0.02	15.79 ± 1.82	26.53 ± 2.03
0.5% Spi + 3% PLA	1.43 ± 0.01	15.6 ± 0.59	3.42 ± 0.29

4.2.2. 1st set of Microparticle Production Optimization and Characterization

3% PLA (1-M0) microparticle was produced using the optimized parameters, which were 20 µL/min, 18 kV, and 15 cm distance between the collector and nozzle (Tasci et al., 2021). The collected microparticles were imaged using SEM, and their size distribution was determined using ImageJ software and IBM SPSS Statistics software. The homogeneous microparticles' diameter was calculated to be 3.69 ± 0.636 µm after selecting and analyzing 100 particles (**Figure 4.7**).

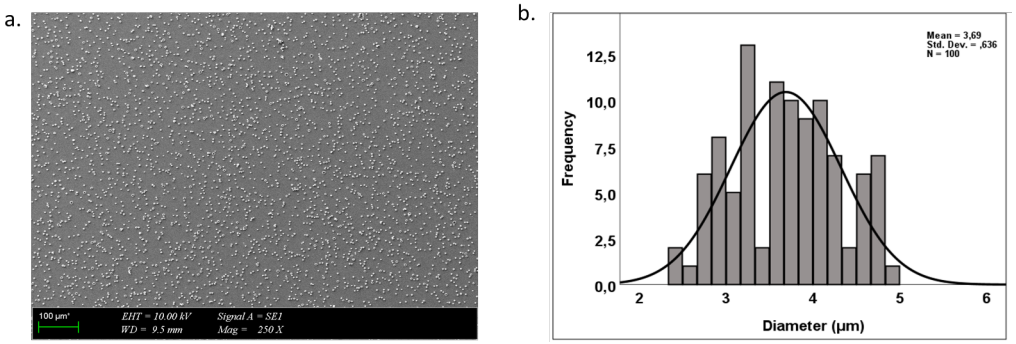


Figure 4.7: 3% PLA (1-M0) microparticle production using electrospraying with 20 µL/min flow rate, 18 kV electrical field, and 15 cm distance between the collector and the needle. a. The SEM image of the microparticles, and b. size distribution from 100 microparticles analysis using ImageJ and IBM SPSS Statistics software. The scale bar of the SEM is 100 µm.

For 0.125% Spirulina + 3% PLA (1-M1), monodisperse microparticles (5.6 ± 0.772 µm, n = 100) were obtained at 20 µL/min and 16.8 kV (**Figure 4.8**). The calculations and analysis were conducted in the same way as M0.

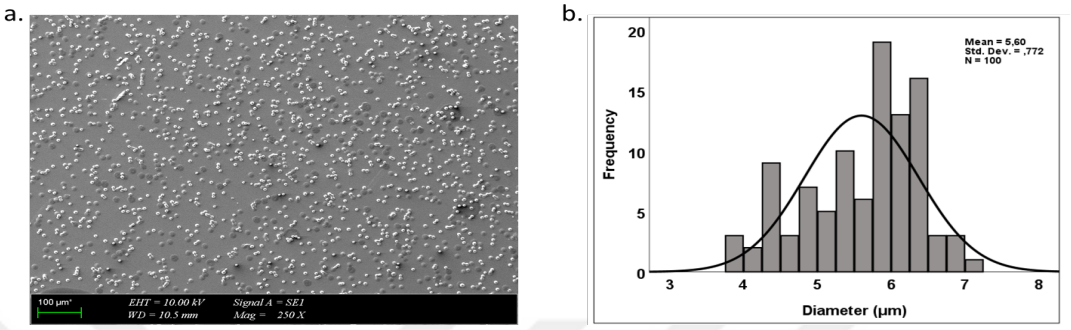


Figure 4.8: 0.125% Spi + 3% PLA microparticle production using electrospraying with 20 µL/min flow rate, 16.8 kV electrical field, and 15 cm distance between the collector and the needle. a. The SEM image of the microparticles, and b. size distribution from 100 microparticles analysis using ImageJ and IBM SPSS Statistics software. The scale bar of the SEM is 100 µm.

Similarly, 0.25% Spirulina + 3% PLA (1-M2) required a higher flow rate (30 µL/min) and 16.7 kV, resulting in particles with an average diameter of 5.08 ± 0.551 µm (**Figure 4.9**).

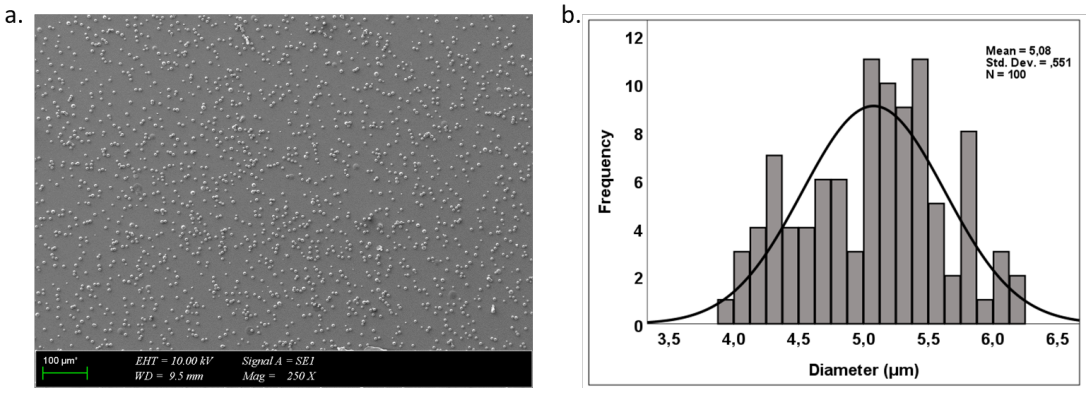


Figure 4.9: 0.25% Spi + 3% microparticle production using electrospraying with 30 µL/min flow rate, 16.7 kV electrical field, and 15 cm distance between the collector and the needle. a. The SEM image of the microparticles, and b. size distribution from 100 microparticles analysis using ImageJ and IBM SPSS Statistics software. The scale bar of the SEM is 100 µm.

0.5% Spirulina + 3% PLA (1-M3) exhibited optimal monodisperse microparticle formation at 25 µL/min and 16.6 kV, with a mean size of 5.9 ± 0.653 µm (**Figure 4.10**).

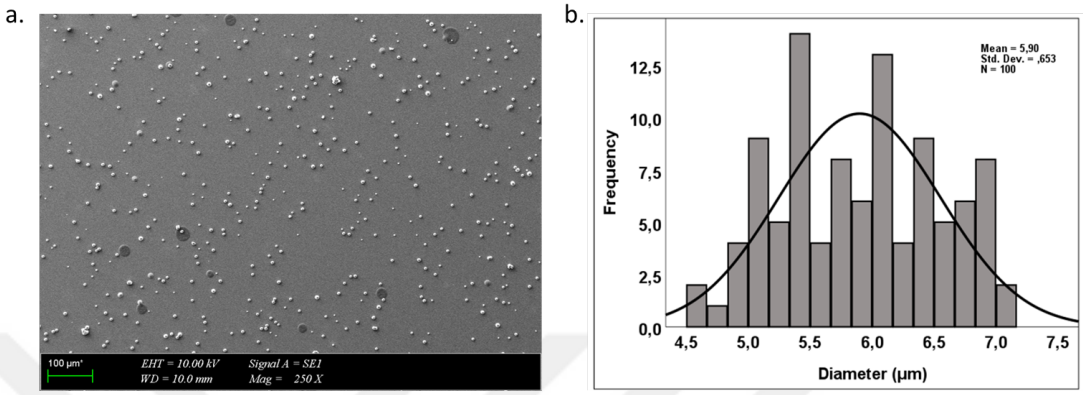


Figure 4.10: 0.5% Spi + 3% PLA microparticle production using electrospraying with 25 µL/min flow rate, 16.6 kV electrical field, and 15 cm distance between the collector and the needle. a. The SEM image of the microparticles, and b. size distribution from 100 microparticles analysis using ImageJ and IBM SPSS Statistics software. The scale bar of the SEM is 100 µm.

Consistent with expectations, the incorporation of Spirulina resulted in increased particle sizes for formulations M1, M2, and M3 relative to the Spirulina-free control (M0).

4.2.3. 2nd set of Microparticle Production Optimization and Characterization

To further reduce particle size, a narrower nozzle diameter (27 G, 0.4 × 25 mm) was used, while maintaining consistent electrospraying parameters (flow rate, voltage, and nozzle-to-collector distance). This modification reduced the particle size by 25% compared to a standard nozzle with an inner diameter of 0.65 mm. Particle sizing was conducted using SEM and dynamic light scattering (DLS) in DMSO; however, DLS proved unreliable due to PLA's poor solubility, resulting in discrepancies (e.g., 3% PLA (2-M0): 1.85 µm by DLS vs. 4.15 ± 0.89 µm by SEM). Consequently, SEM-derived size distributions were analyzed using ImageJ and GraphPad Prism 9.2.0, revealing the following: 2-M1 (4.25 ± 0.74 µm), 2-M2 (4.62 ± 0.62 µm), and 2-M3 (4.44 ± 0.44 µm) (**Figure 4.11**).

The particle sizes of the produced microparticles were measured using dynamic light scattering (DLS) in dimethyl sulfoxide (DMSO), and SEM images were used for comparison of size distribution. The particles were measured for one batch three times, and the particle sizes are represented in **Figures 4.11a, d, g, and j**. The particle sizes were also analyzed using SEM (**Figures 4.11b, e, h, and k**), and the size distribution graph was plotted in GraphPad 9.2.0 software after the particle sizes were calculated in ImageJ (**Figure 4.11c, f, i, and j**).

Although the DLS results indicated microparticle sizes of around 1 μm, the SEM analysis revealed microparticle sizes of 4-5 μm, which could be contributing to the solubility problem. Due to the low solubility of PLA in DMSO and its tendency to aggregate, the particles could not be suspended homogeneously; therefore, particle size differences were observed between DLS and SEM. Comparative evaluation of particle size variation relative to nozzle diameter reduction revealed differential effects across formulations. Specifically, the control formulation (M0) demonstrated a 12% increase in particle dimensions, while M1 exhibited a substantial 24.9% reduction. Similarly, formulations M2 and M3 showed particle size decreases of 8.99% and 24.69%, respectively.

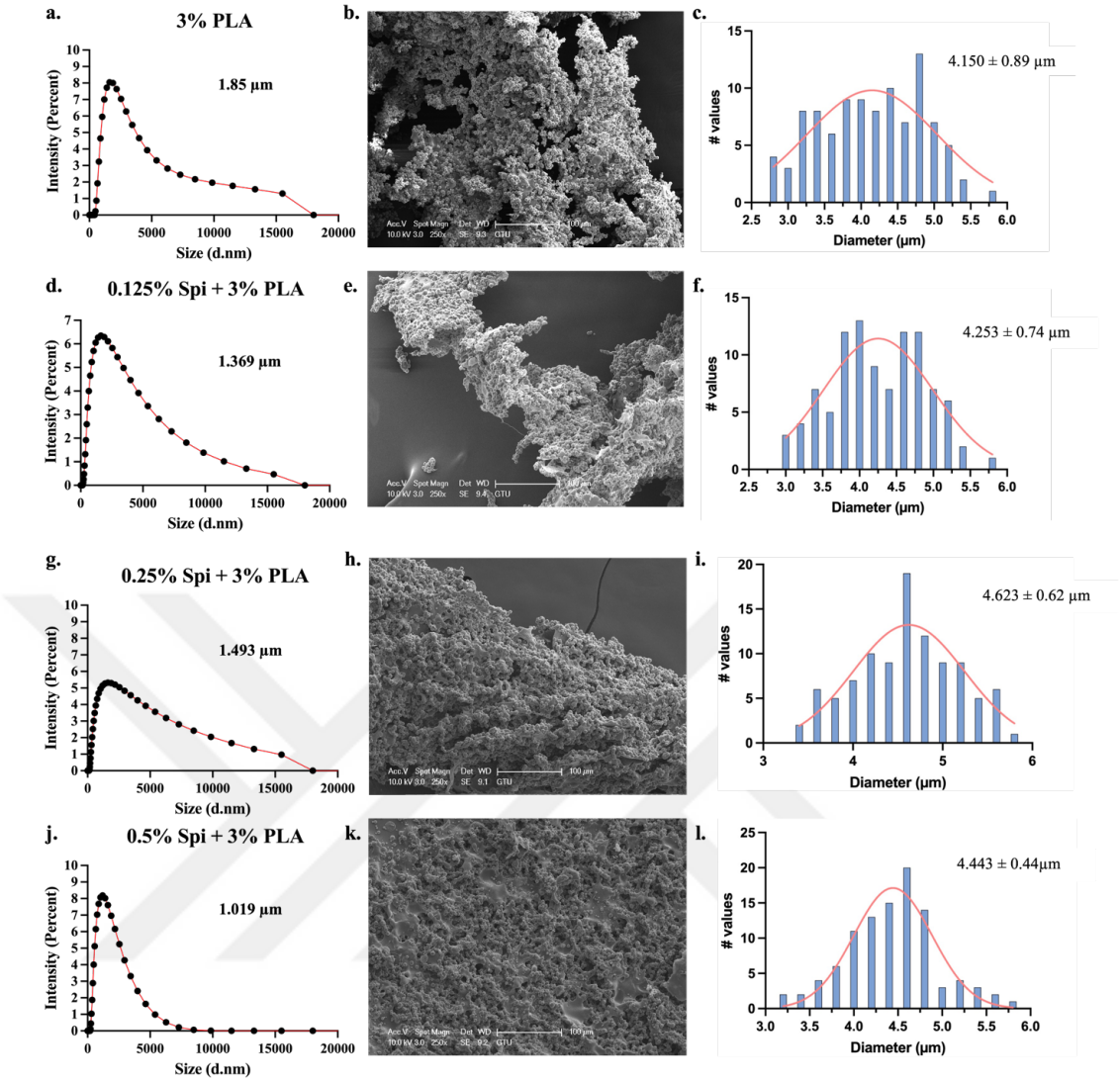


Figure 4.11: a. 3% PLA (2-M0), d. 0.125% Spi + 3% PLA (2-M1), g. 0.25% Spi + 3% PLA (2-M2), and j. 0.5% Spi + 3% PLA (2-M3) size distributions were measured using DLS, with calculations performed using GraphPad 9.2.0. The particle sizes represent the average of three readings. b. 2-M0, e. 2-M1, h. 2-M2, and k. 2-M3 SEM images, with scale bars set at 100 µm. c. 2-M0, f. 2-M1, i. 2-M2 and j. 2-M3 size distributions were calculated from SEM images using Image J and GraphPad 9.2.0 software. At least 100 particles were measured, and the particles'diameters were recorded as averages along with their standard deviations.

4.2.4. FT-IR and Release Profile Analysis

The observed particle size variations induced by changes in nozzle diameter did not affect the chemical integrity of the microparticles, as evidenced by FT-IR spectroscopic analysis (**Figure 4.12**). All formulations maintained characteristic PLA

bond signatures, consistent with the polymer's predominance in the composite microparticles. Notably, the 0.5% Spirulina + 3% PLA formulation exhibited distinct spectral modifications compared to the pure PLA control, including shifts in the C=O stretching vibration (1749 cm^{-1}) and C-O bond (1080 cm^{-1}), confirming successful Spirulina incorporation (Batista et al., 2013). The presence of typical PLA-associated peaks at 1453 cm^{-1} (-CH_3 asymmetric bending) and 2946 cm^{-1} (-CH_3 symmetric stretching) (Tasci et al., 2021) further demonstrated the preservation of the polymer's chemical structure across all formulations. These results collectively indicate that while nozzle diameter significantly influenced particle size distribution, it did not alter the fundamental chemical composition of the microparticles.

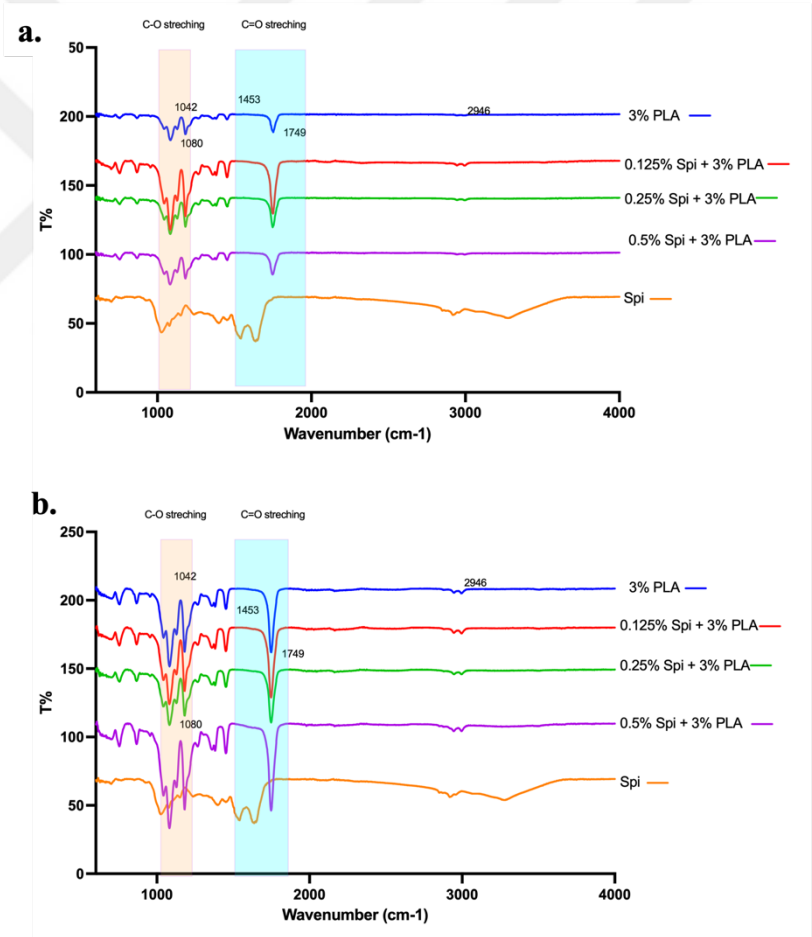


Figure 4.11: FT-IR analysis of M0 (red), pure Spirulina extract (dark green), M1 (blue), M2 (green), and M3 (purple) a. particles from larger nozzle diameter and b. particles from a smaller inner needle diameter. The y-axis represents T%, which denotes the transmittance percentage of the samples.

Besides the chemical bond analysis, the existence of Spirulina in microparticles was identified using the autofluorescence property of Spirulina (Prabakaran et al., 2020). Release microparticle profiles were examined at 37 °C in pH 7.4 PBS for 48 h (**Figure 4.13**). The release of the particles was measured via a fluorescence plate reader at 355/535 nm (**Figure 4.13a**). The samples were taken at the mentioned time, and the fluorescence unit was read. The release profile was converted from fluorescence units to concentration using the standard curve of 70% ethanol extract of Spirulina (**Figure 4.13b**).

The release profile of particles indicated that almost all Spirulina was obtained within the first 6 hours (**Figure 4.13c**), and the loading capacity was calculated based on the release profile (**Figure 4.14**). The actual loading capacity was defined as the expected loading depending on the sprayed liquid and the collected particle amount. The theoretical and actual loading capacities of the particles increased with increased Spirulina content, as expected.

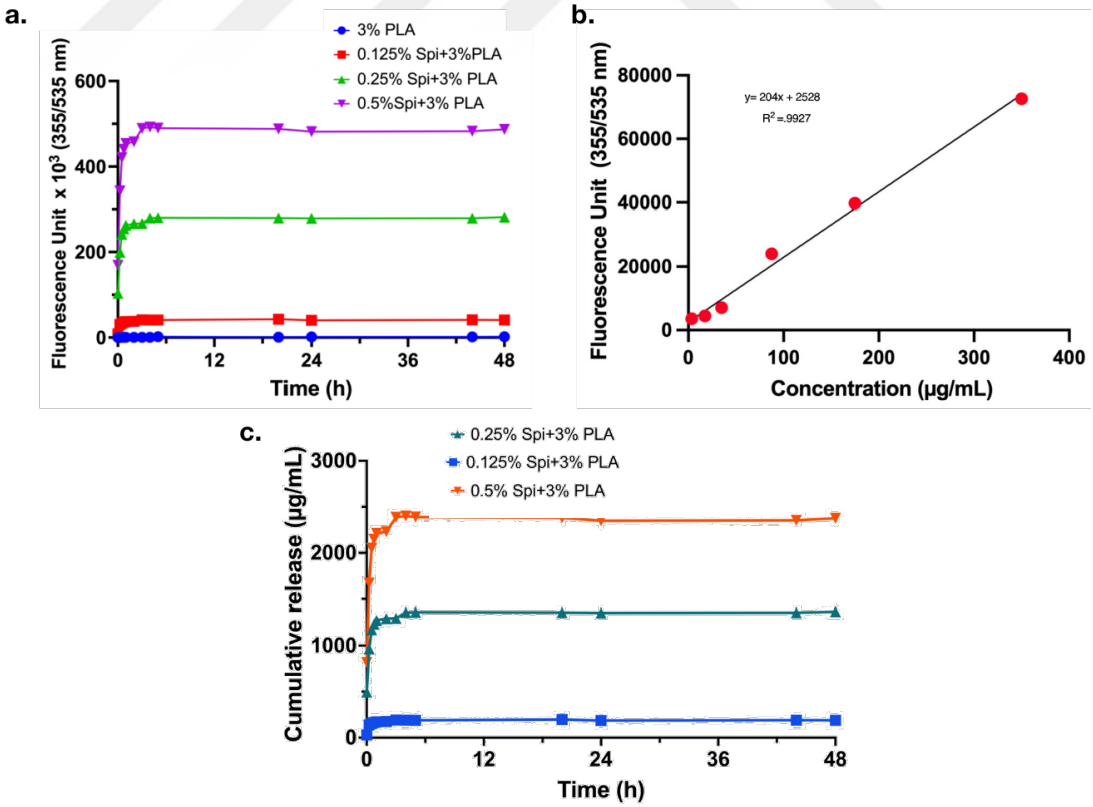


Figure 4.12: Release profile of produced microparticles using PBS at pH 7.4. a. fluorescence unit at 355/535 nm, b. Standard curve for Spirulina extract, and cumulative release profile calculated using the standard curve.

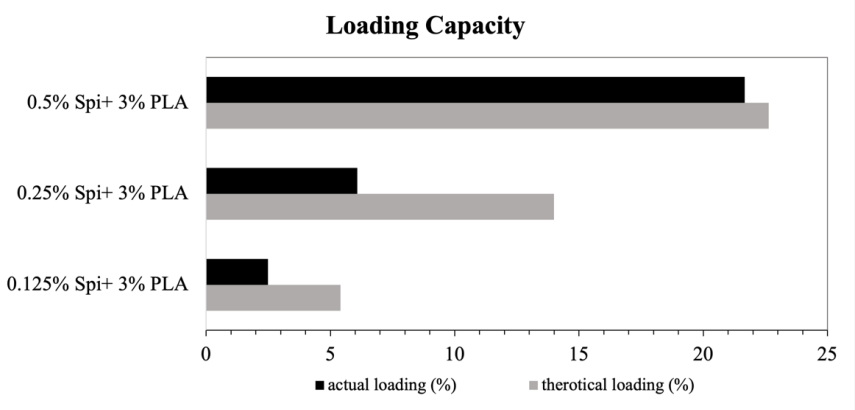


Figure 4.13: Loading capacity of produced microparticles; the loading capacity was calculated as theoretical, gray, and measured loading, black. The loading capacity was calculated based on the released profile.

4.2.5. Cell Fate of Produced Microparticles

Microparticles produced by two electrospraying setup methods were examined to determine the effects of size distribution on cell fate in HUVEC and HaCaT cell lines using MTT, colony formation, and cell survival assays with fluorescence imaging.

For the initial setup of microparticles, the MTT results of HUVEC cell lines showed no cytotoxic effects compared to the non-treated groups after 24 h of treatment at all applied dosages (0.5, 1, 5, 10, and 25 µg/mL) for all microparticles. The statistical analysis was repeated with the comparison between 1-M0 and Spi-included microparticles for each applied dosage. 1-M1 significantly increased cell viability at the concentrations of 5 ($p < 0.01$), 10 ($p < 0.01$), and 25 ($0.01 < p \leq 0.001$) µg/mL (**Figure 4.15a**). For colony formations, 5 and 10 µg/mL of all microparticles enhanced the colonization capability after 24 h of application (**Figure 4.15b**). Based on the MTT and colony formation assays, concentrations of 5 and 10 µg/mL were selected as optimized for further experiments.

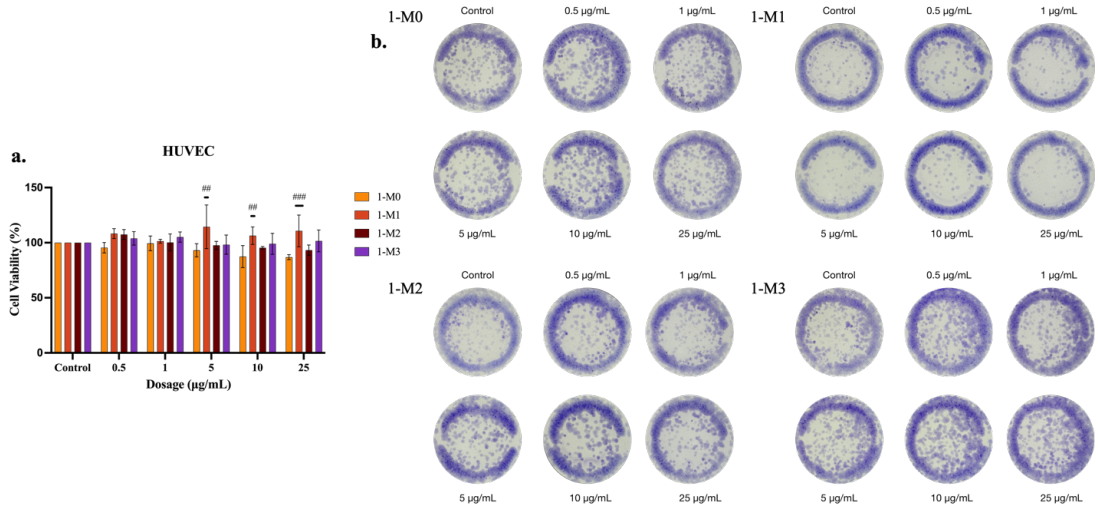


Figure 4.14: a. MTT assay and b. colony formation of HUVEC cell lines after the application of 1-M0, 1-M1, 1-M2, and 1-M3 microparticle application for 24 h for the MTT and colony formation using five different concentrations (0.5, 1, 5, 10, 25 µg/mL). The MTT results represented the average of three biological replicates of quartiles, with standard deviation, and two biological replicates for colony formation. The analysis was conducted using GraphPad Prism 9.2.0 software with a two-way ANOVA followed by Dunnett's comparison test against the initial control. ns $p > 0.05$, **** $p < 0.0001$, *** $0.0001 \leq p < 0.001$, ** $0.001 \leq p < 0.01$, * $0.01 \leq p < 0.05$. # $0.01 \leq p < 0.05$, ## $0.001 \leq p < 0.01$, ### $p < 0.001$ comparison between 1-M0 and Spi-included microparticles for each dosage.

A cell survival assay on HUVECs using 1-microparticles was conducted for 24, 48, and 72 hours of application. For the 1-M0 non-treated control groups, proliferation was significantly ($p < 0.01$) increased after 72 h of application compared to time 0 h. Moreover, at 72 h, the 10 µg/mL application dosage showed proliferation compared to the 0 h time point ($p < 0.05$), whereas the 5 µg/mL treated group did not exhibit statistically significant proliferation ($p > 0.05$) compared to the 0 h group. No statistical differences were calculated between the control and treated groups for each time point (**Figure 4.16a**). 1-M1 applied HUVECs were counted for 72 h after 5 and 10 µg/mL were applied, and at 48 h, the control group showed an increase in cell number ($p < 0.01$) with 10 µg/mL ($p < 0.05$), while no statistical differences were observed 5 µg/mL group ($p > 0.05$). Furthermore, at 72 hours after application, cell proliferation was enhanced in both the control and treated groups (for the control and 10 µg/mL, $p < 0.01$; for 5 µg/mL, $p < 0.05$, compared to the control at 0 hours) (**Figure 4.14b**). For 1-M2, the cell number was significantly increased in non-treated group ($p < 0.05$,

compared to time 0 h) for 48 h and 72 h ($p < 0.05$), while treated groups showed a similar increase at 72 h ($p < 0.01$ for 5 µg/mL, $p < 0.05$ for 10 µg/mL, compared to time 0 h) (**Figure 4.16c**). For the 1-M3 application, the 5 µg/mL applied group increased proliferation for 72 h compared to time 0 h ($p < 0.05$) (**Figure 4.16d**).

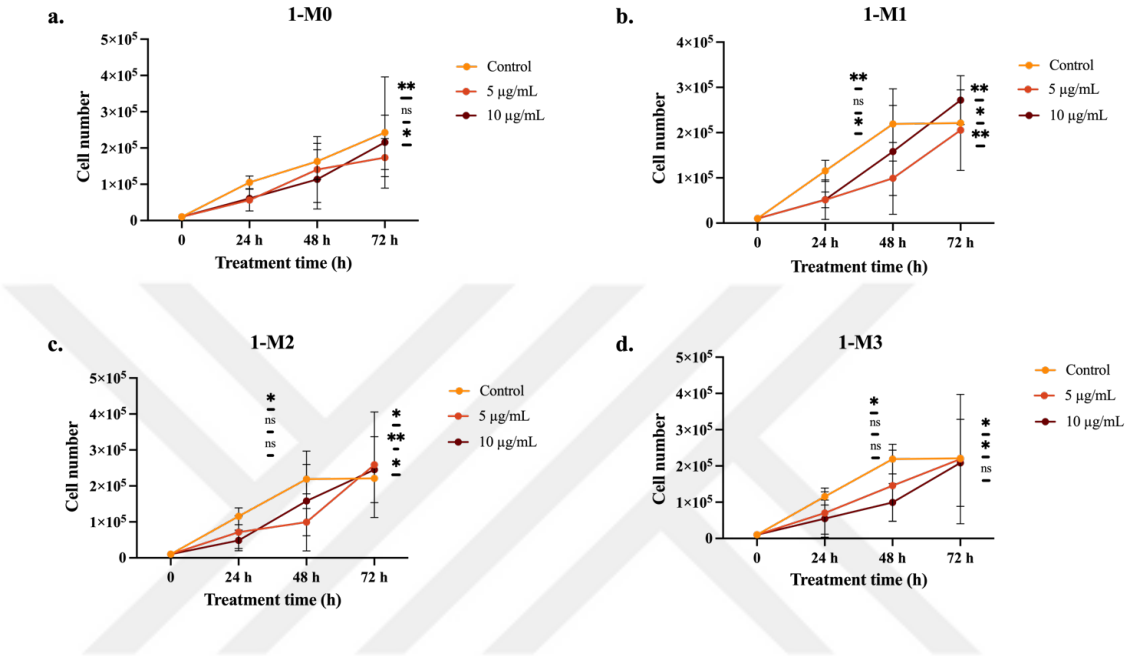


Figure 4.15: a. 1-M0, b. 1-M1, c. 1-M2, and d. 1-M3 microparticle applied to HUVEC cell lines' cell survival results after two concentrations (5 and 10 µg/mL) applied for 24, 48, and 72 h. The results represent the average of two biological replicates, each with two technical replicates, along with the standard deviation. The analysis was conducted using GraphPad Prism 9.2.0 software with a two-way ANOVA followed by Dunnett's comparison test against the initial control. ns $p > 0.05$, **** $p < 0.0001$, *** $0.0001 \leq p < 0.001$, ** $0.001 \leq p < 0.01$, * $0.01 \leq p < 0.05$.

Fluorescence images of HUVECs at a 5 µg/mL applied concentration indicated that reactive oxygen species were decreased, as indicated by the intensity of the images in 1-M0 and 1-M1 compared to the control groups. The $DiOC_6$ and PI images showed no toxic effects (**Figure 4.17**).

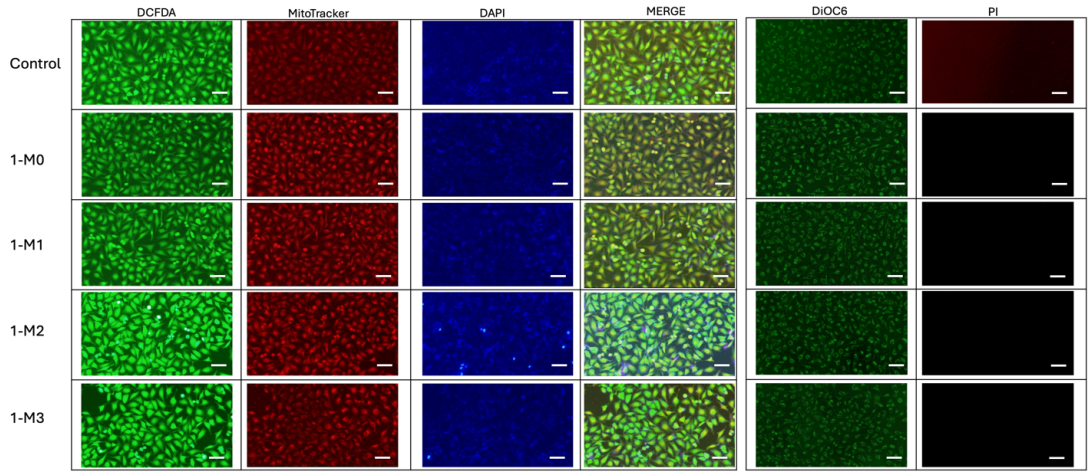


Figure 4.16: Fluorescence images of HUVEC after 5 µg/mL microparticles produced using a nozzle with a larger inner diameter (1-). Control: no treatment applied, 1-M0: 3% PLA, 1-M1: 0.125% Spi + 3% PLA; 1-M2: 0.25% Spi + 3% PLA; 1-M3: 0.5% Spi + 3% PLA. The scale bar in the images was 150 µm.

Increasing the microparticle application dosage did not cause any qualitative variations compared to the non-treated control groups after 24 hours of application for HUVEC cell lines. The cell viability, as determined by $DiOC_6$/PI staining, showed that none of the microparticles caused cytotoxic effects, as indicated by PI staining (red, stained dead cells) (**Figure 4.18**).

Microparticles produced by the first setup of the equipment were examined for use in cellular experiments on HUVEC cell lines; the MTT assay indicated cytotoxic effects at all applied dosages (0.5-25 µg/mL). However, 1-M2 caused a significant reduction in cell viability compared to 1-M0 at a concentration of 0.5 µg/mL (**Figure 4.19a**). In colony formation assay results, no reduction in colony numbers and colonizations was observed in all 1-microparticles. Furthermore, colonization was increased with 1-M1, 1-M2, and 1-M3 applications after dosages of 0.5 and 10 µg/mL were applied qualitatively (**Figure 4.19b**).

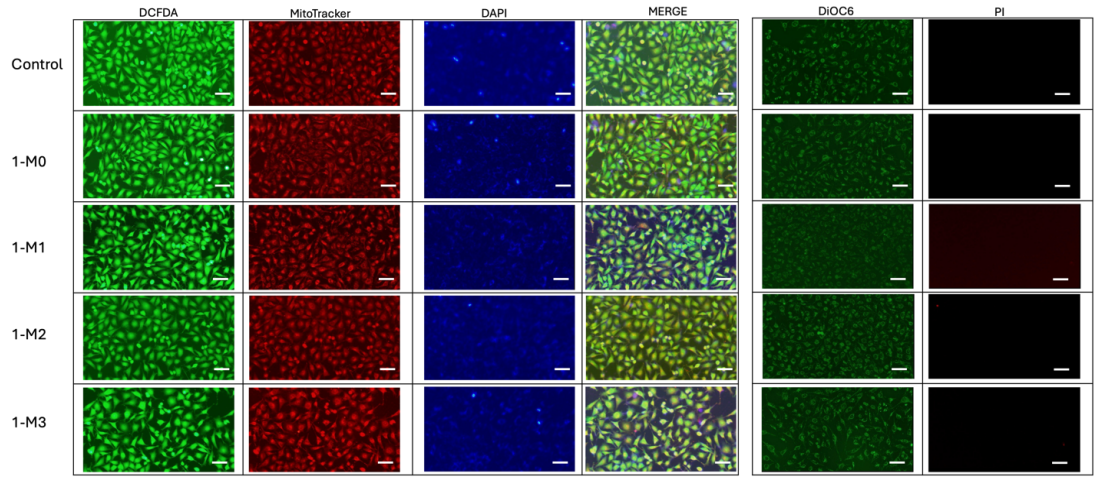


Figure 4.17: Fluorescence images of HUVEC after 10 µg/mL microparticles produced using a nozzle with a larger inner diameter (1-). Control: no treatment applied, 1-M0: 3% PLA, 1-M1: 0.125% Spi + 3% PLA; 1-M2: 0.25% Spi + 3% PLA; 1-M3: 0.5% Spi + 3% PLA. The scale bar in the images was 150 µm.

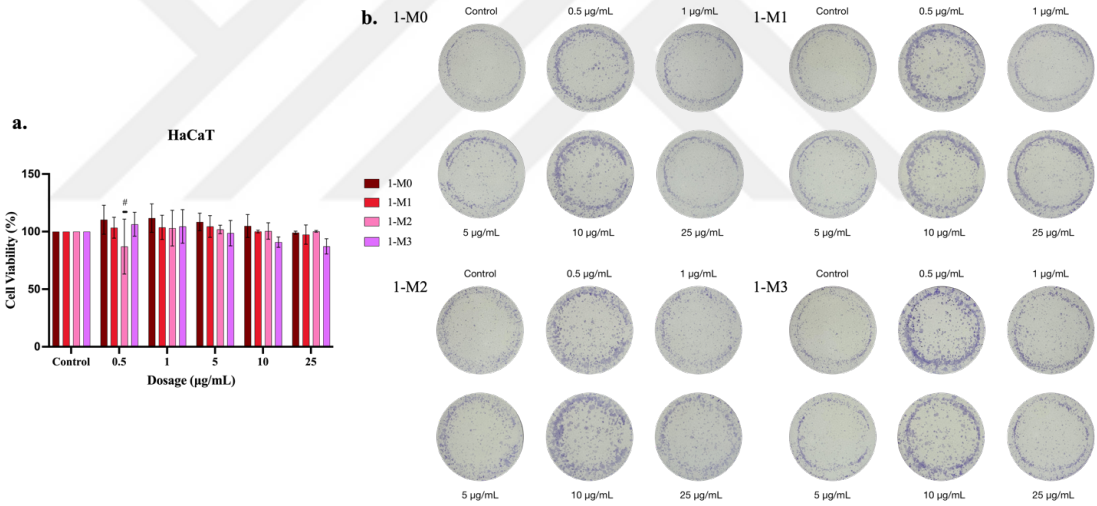


Figure 4.18: a. MTT assay and b. Colony formation of HaCaT cell lines after the application of 1-M0, 1-M1, 1-M2, and 1-M3 microparticle application for 24 h for the MTT and colony formation using five different concentrations (0.5, 1, 5, 10, 25 µg/mL). The MTT results represented the average of three biological replicates of quartiles, with standard deviation; two biological replicates for colony formation; and two biological replicates of two technical replicates for cell survival. The analysis was conducted using GraphPad Prism 9.2.0 software with a two-way ANOVA followed by Dunnett's comparison test against the initial control. ns $p > 0.05$, **** $p < 0.0001$, *** $0.0001 \leq p < 0.001$, ** $0.001 \leq p < 0.01$, * $0.01 \leq p < 0.05$.

For the cell survival assay on the HaCaT cell line, after 1-microparticles were applied for 24, 48, and 72 h, 1-M0 caused a significant increase after 72 h compared to time 0 h at a concentration of 5 µg/mL ($p < 0.05$). However, the control group and the 10 µg/mL applied groups did not show a statistically significant increase over 72 h (**Figure 4.20a**). For the 1-M1 application, cell proliferation was significantly affected after 48 h at a concentration of 5 µg/mL ($p < 0.05$). At the same time, no statistical increase was observed in the non-treated and 10 µg/mL treated groups ($p > 0.05$) (**Figure 4.20b**). Over a 72-h application of 1-M2, significant proliferation was observed at 5 µg/mL ($p < 0.05$) and 10 µg/mL ($p < 0.01$), while the non-treated group showed no statistical increase in cell number ($p > 0.05$) (**Figure 4.20c**). 1-M3 application caused an increase in cell number over 48 h, but this proliferation was not significant based on statistical analysis compared to the control at 0 h ($p > 0.05$) (**Figure 4.20d**).

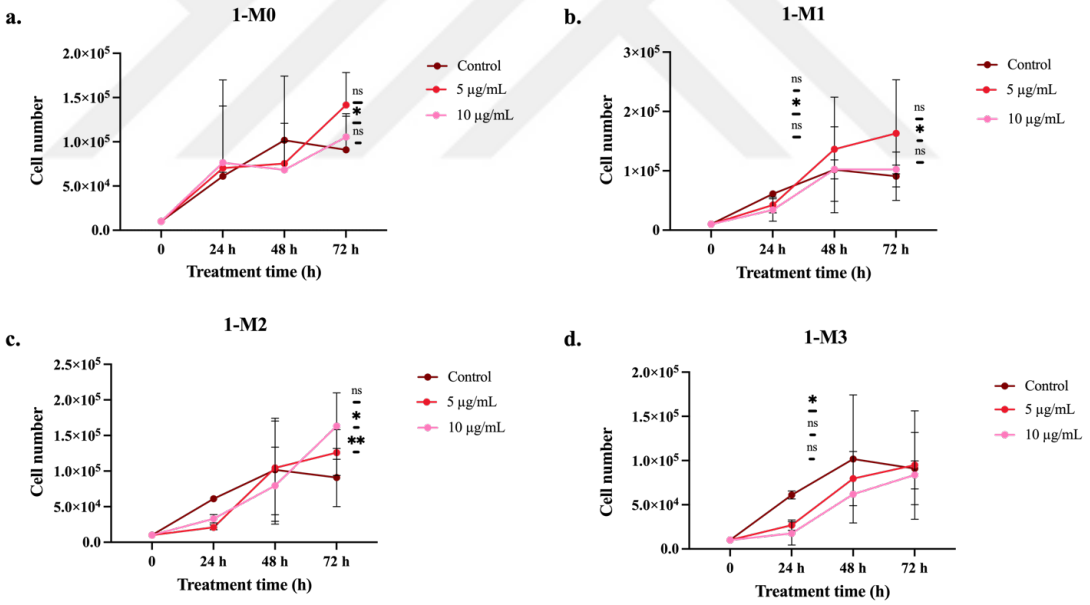


Figure 4.19: a. 1-M0, b. 1-M1, c. 1-M2, and d. 1-M3 microparticle applied to HaCaT cell lines' cell survival results after two concentrations (5 and 10 µg/mL) applied for 24, 48, and 72 h. The results represent the average of two biological replicates, each with two technical replicates, along with the standard deviation. The analysis was conducted using GraphPad Prism 9.2.0 software with a two-way ANOVA followed by Dunnett's comparison test against the initial control. ns $p > 0.05$, **** $p < 0.0001$, *** $0.0001 \leq p < 0.001$, ** $0.001 \leq p < 0.01$, * $0.01 \leq p < 0.05$.

Fluorescence images of HaCaT cell lines after 24 h application of 1-microparticles were investigated with H_2-DCFDA (ROS detection), MitoTracker (mitochondrial activity), DAPI (DNA stain), $DiOC_6$ (mitochondrial identification), and PI (dead cell detection). A 5 µg/mL application of 1-M1 and 1-M2 microparticles caused a slight reduction in ROS fluorescence intensity, accompanied by an increase in mitochondrial activity, without inducing cell death (**Figure 4.21**).

For 10 µg/mL application of all microparticles caused a slight reduction in ROS levels with increasing mitochondrial activity without inducing cell death (**Figure 4.22**). Overall, the cellular experiments on HUVEC and HaCaT cell lines suggest that 1-M1 could be promising microparticles due to their enhanced biological properties compared to the blank form (1-M0).

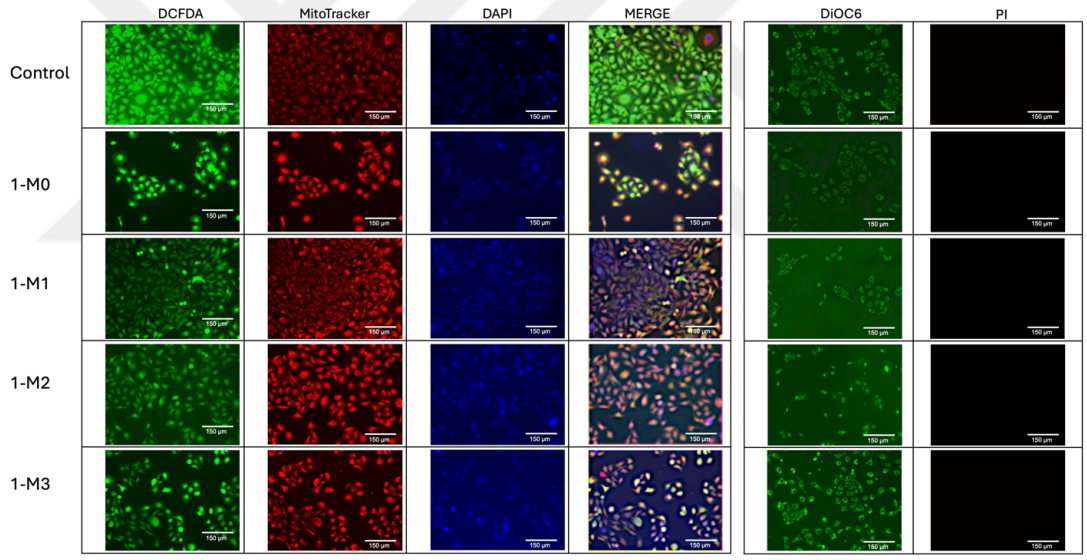


Figure 4.20: Fluorescence images of HaCaT cells after 5 µg/mL microparticle, produced using a nozzle with a larger inner diameter, application. Control: no treatment applied, 1-M0: 3% PLA, 1-M1: 0.125% Spi + 3% PLA; 1-M2: 0.25% Spi + 3% PLA; 1-M3: 0.5% Spi + 3% PLA. Scale bar 150 µm.

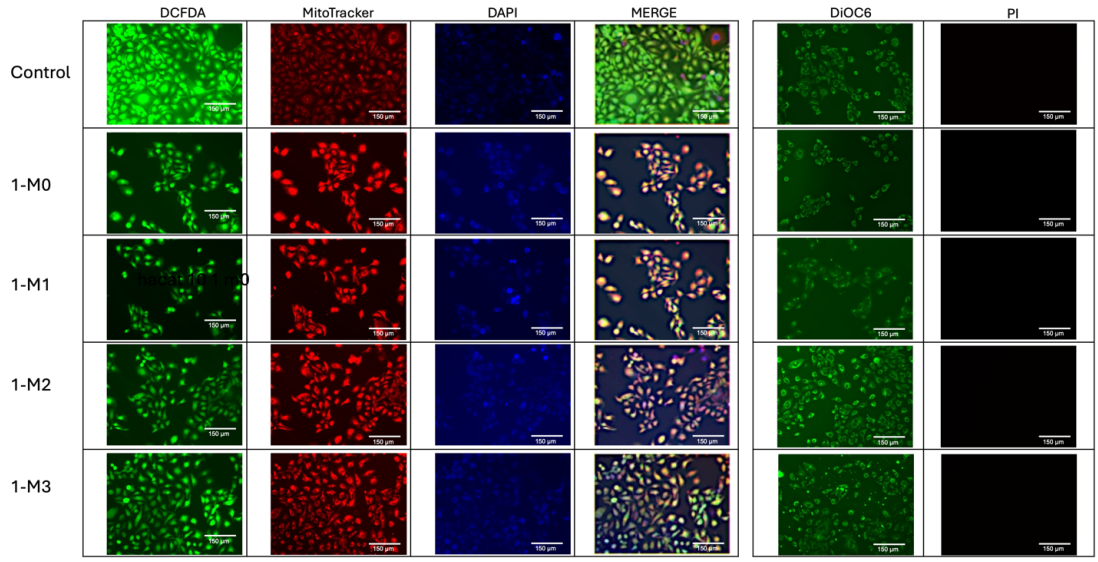


Figure 4.21: Fluorescence images of HaCaT cells after 10 µg/mL microparticle, produced using a nozzle with a larger inner diameter, application. Control: no treatment applied, 1-M0: 3% PLA, 1-M1: 0.125% Spi + 3% PLA; 1-M2: 0.25% Spi + 3% PLA; 1-M3: 0.5% Spi + 3% PLA. The scale bar was 150 µm.

Following the first setup of experiments, microparticles were examined under the same assays as those with 1-microparticles for the second setup. The differences in sizes of microparticles were investigated under the same conditions as 1-microparticles in terms of cell fate. In the HUVEC cell line, statistically significant cytotoxic effects were not detected using the MTT assay compared to the non-treated control groups. Nevertheless, at 25 and 50 µg/mL applications, 2-M2 showed an increase in cell viability compared to 2-M0 (**Figure 4.23a**). Colony formation assay results showed no adverse effects on colonization capability after 2-microparticle application for all applied dosages (**Figure 4.23b**). Moreover, combining the MTT and colony formation results, concentrations of 5 and 10 µg/mL were accepted as optimized dosages for further experiments.

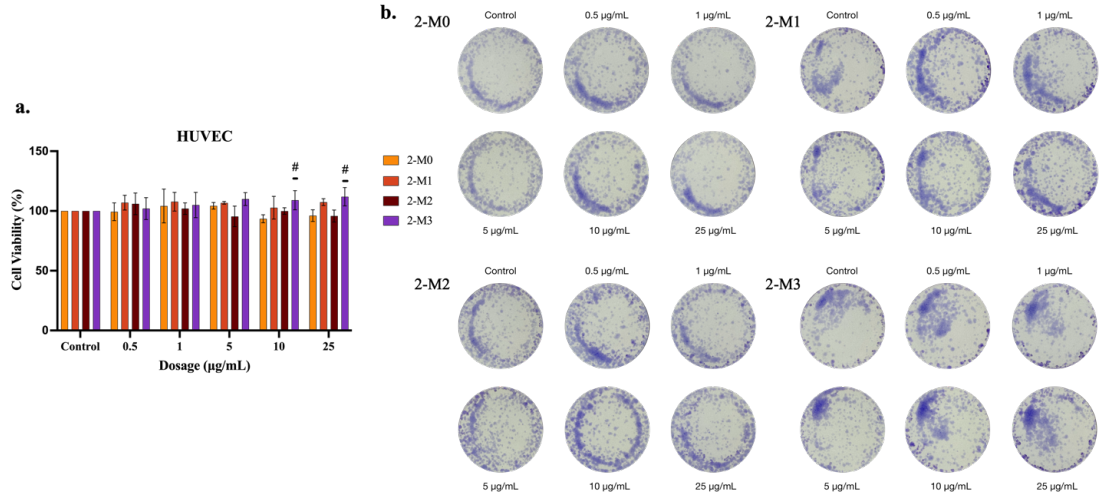


Figure 4.22: a. MTT assay and b. colony formation of HUVEC cell lines after the application of 1-M0, 1-M1, 1-M2, and 1-M3 microparticle application for 24 h for the MTT and colony formation using five different concentrations (0.5, 1, 5, 10, 25 µg/mL). The MTT results represented the average of three biological replicates of quartiles, with standard deviation; two biological replicates for colony formation; and two biological replicates of two technical replicates for cell survival. The analysis was conducted using GraphPad Prism 9.2.0 software with a two-way ANOVA followed by Dunnett's comparison test against the initial control. ns $p > 0.05$, **** $p < 0.0001$, *** $0.0001 \leq p < 0.001$, ** $0.001 \leq p < 0.01$, * $0.01 \leq p < 0.05$. # $0.01 \leq p < 0.05$, ## $0.001 \leq p < 0.01$, ### $p < 0.001$ comparison between 1-M0 and Spi-included microparticles for each dosage.

The cell survival assay for 2-microparticles indicated that the control group proliferated more than the treated HUVECs. Although the 1-M0 application at a five µg/mL concentration resulted in statistically increased proliferation, the control groups proliferated more than the treated groups ($p < 0.001$) compared to the control at 0 hours. Additionally, statistical analysis was performed to compare the control and treated groups at each time point. At 72 hours, the proliferation rate was significantly reduced in 10 µg/mL compared to the control (**Figure 4.24a**). For 2-M1, HUVEC proliferation rate was higher than the microparticle applied groups, statistically at 72 h ($p < 0.05$ between 5 µg/mL and control, $p < 0.01$ between 10 µg/mL and non-treated group) (**Figure 4.24b**). After 2-M2 application on the HUVECs, although the cell number increase was improved compared to the other 2-microparticles, the proliferation was not significantly different from the control at 0 hours (**Figure 4.24c**). For the 2-M3 application at 5 and 10 µg/mL for 72 h, cell proliferation was reduced compared to the control groups, while the 5 µg/mL application caused a significant

increase ($p < 0.05$). Additionally, the cell number comparison between the control and 2-M3 applied groups revealed less proliferation ($p < 0.05$) (**Figure 4.24d**).

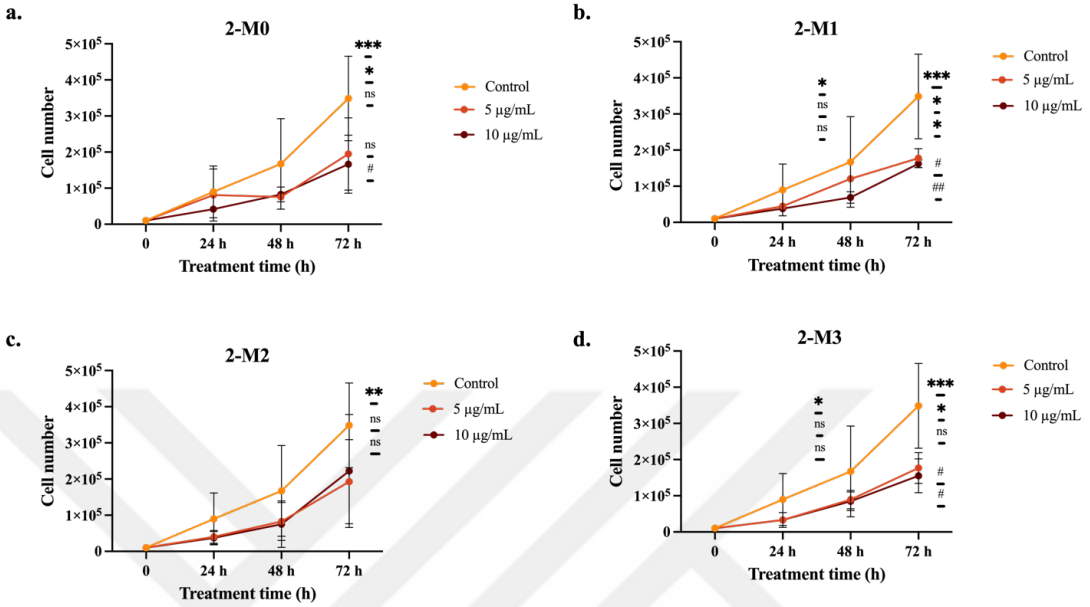


Figure 4.23: a. 1-M0, b. 1-M1, c. 1-M2, and d. 1-M3 microparticle applied to HUVEC cell lines' cell survival results after two concentrations (5 and 10 µg/mL) applied for 24, 48, and 72 h. The results represent the average of two biological replicates, each with two technical replicates, along with the standard deviation. The analysis was conducted using GraphPad Prism 9.2.0 software with a two-way ANOVA followed by Dunnett's comparison test against the initial control. ns $p > 0.05$, **** $p < 0.0001$, *** $0.0001 \leq p < 0.001$, ** $0.001 \leq p < 0.01$, * $0.01 \leq p < 0.05$.

The fluorescence analysis conducted over a 24-hour period following the application of 2-microparticles revealed no significant qualitative differences between the control and treated groups (5 µg/mL, **Figure 4.25**, and 10 µg/mL, **Figure 4.26**). A comprehensive examination of the fluorescence images confirmed that both groups exhibited comparable cellular responses, suggesting that the treatment did not induce any detectable adverse effects under the tested conditions.

Furthermore, propidium iodide (PI) staining was meticulously evaluated across all samples to assess cell viability. The results indicated the absence of dead cells in both the control and treated groups, reinforcing the conclusion that the 2-microparticles did not cause cytotoxicity at the administered concentration. In addition to viability

assessment, mitochondrial activity was monitored as a key indicator of cellular health. The data showed that mitochondrial function in the treated cells followed a trend nearly identical to that of the control group, further supporting the notion that the 2-microparticles had no detrimental impact on metabolic activity. These findings suggest that the tested concentration is non-toxic and well-tolerated by the cells, at least within the 24-hour observation period.

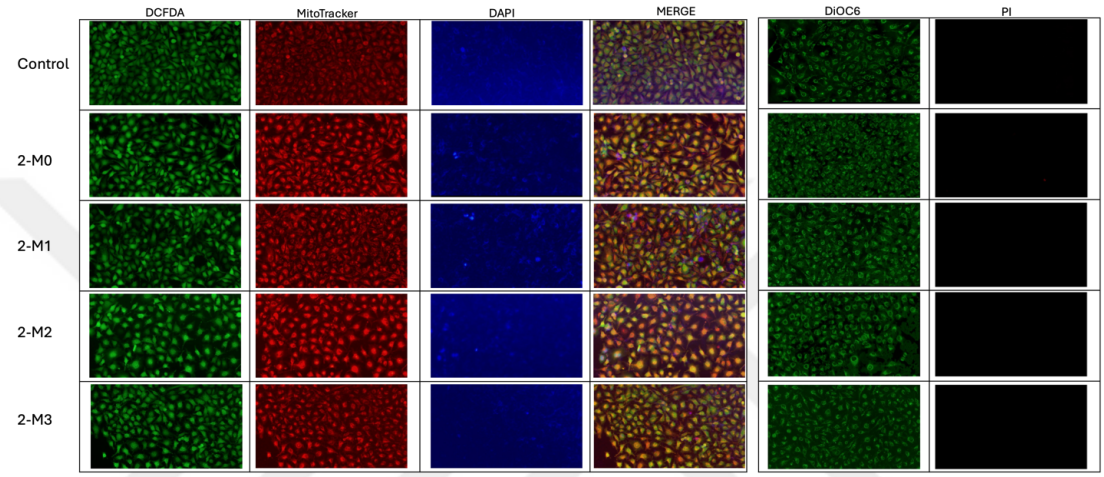


Figure 4.24: Fluorescence images of HUVEC cells after 5 µg/mL 2-microparticle, Control: no treatment applied, 2-M0: 3% PLA, 2-M1: 0.125% Spi + 3% PLA, 2-M2: 0.25% Spi + 3% PLA, 2-M3: 0.5% Spi + 3% PLA.

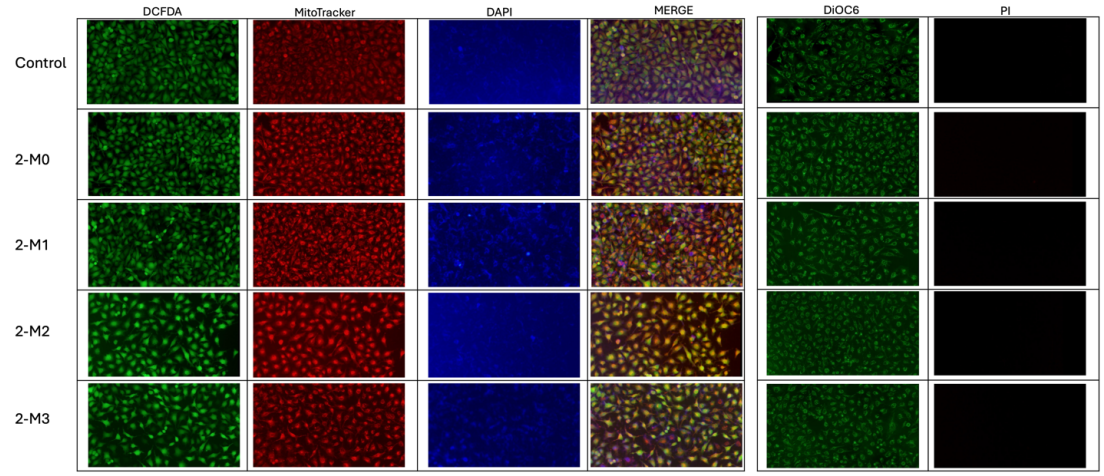


Figure 4.25: Fluorescence images of HUVEC cells after 10 µg/mL 2-microparticle, Control: no treatment applied, 2-M0: 3% PLA, 2-M1: 0.125% Spi + 3% PLA, 2-M2: 0.25% Spi + 3% PLA, 2-M3: 0.5% Spi + 3% PLA.

The impact of 2-microparticles on HaCaT cell viability was evaluated using an MTT assay following a 24-hour treatment period. The results demonstrated no statistically significant differences in metabolic activity between untreated control cells and those exposed to any of the 2-microparticle variants, including comparisons between 2-M0 and other microparticle types (**Figure 4.27a**). This consistency across treatment groups indicates that none of the tested microparticles induced cytotoxicity at the administered concentrations (1-25 µg/mL) within this timeframe.

In contrast to the viability results, the colony formation assay revealed proliferative responses depending on both microparticle composition and dosage. Treatment with 2-M0 consistently enhanced colony formation across all tested concentrations, suggesting a general stimulatory effect on HaCaT cell proliferation. The 2-M1 variant similarly increased colony numbers, though this effect was restricted to concentrations of 5, 10, and 25 µg/mL, implying a dose-dependent proliferative response. 2-M2 and 2-M3 exhibited nearly identical effects on colony formation at every concentration tested. (**Figure 4.27b**).

The combination of these assays led to the selection of 5 and 10 µg/mL concentrations for subsequent experiments. These intermediate dosages were selected based on their demonstrated biological activity in the colony formation assay, while maintaining the absence of cytotoxic effects, as confirmed by the MTT assay. The 5 µg/mL concentration was particularly noteworthy as it represented the lowest dose at which proliferative effects were observed for multiple microparticles.

Comprehensive cell survival assays in HaCaT cell lines revealed time-dependent proliferation patterns following the application of 2-microparticles. While 48-hour treatments showed comparable proliferation trends between treated groups and non-treated controls (**Figure 4.28**), extended 72-hour treatments resulted in significantly reduced cellular proliferation across all 2-microparticle variants relative to control conditions.

The 2-M0 variant exhibited particularly noteworthy dynamics, with significant proliferation increases observed at both 48 hours ($p < 0.05$) and 72 hours ($p < 0.0001$ for control, $p < 0.05$ for 5 µg/mL, and $p < 0.01$ for 10 µg/mL) when compared to control measurements at time 0 h. However, the 72-hour timepoint revealed a dose-

dependent suppression of proliferation, where both 5 and 10 µg/mL applications showed markedly reduced growth rates ($p < 0.0001$) compared to untreated controls (**Figure 4.28a**).

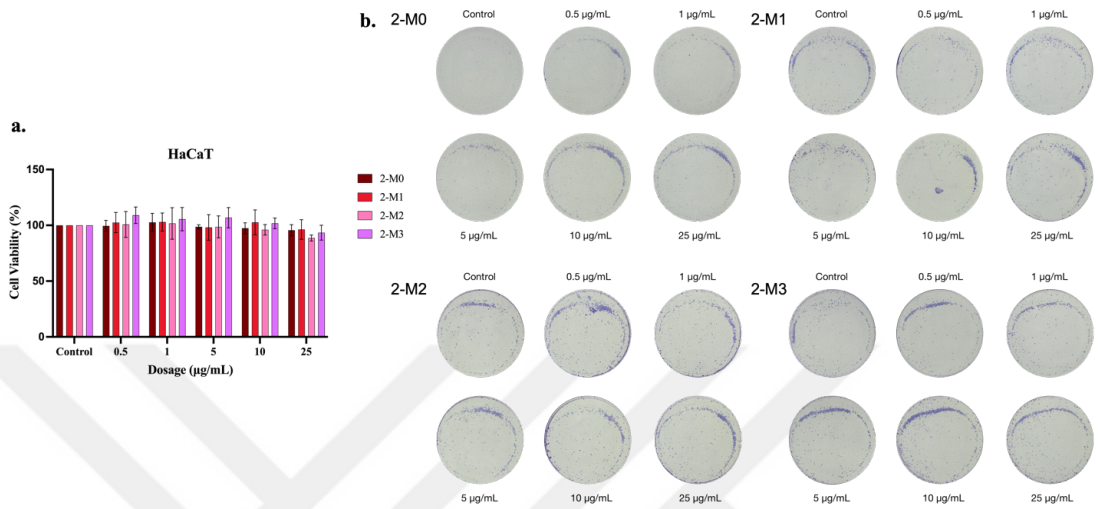


Figure 4.26: a. MTT assay and b. Colony formation of HaCaT cell lines after the application of 1-M0, 1-M1, 1-M2, and 1-M3 microparticle application for 24 h for the MTT and colony formation using five different concentrations (0.5, 1, 5, 10, 25 µg/mL). The MTT results represented the average of three biological replicates of quartiles, with standard deviation; two biological replicates for colony formation; and two biological replicates of two technical replicates for cell survival. The analysis was conducted using GraphPad Prism 9.2.0 software with a two-way ANOVA followed by Dunnett's comparison test against the initial control. ns $p > 0.05$, **** $p < 0.0001$, *** $0.0001 \leq p < 0.001$, ** $0.001 \leq p < 0.01$, * $0.01 \leq p < 0.05$. # $0.01 \leq p < 0.05$, ## $0.001 \leq p < 0.01$, ### $p < 0.001$ comparison between 1-M0 and Spi-included microparticles for each dosage.

Similar patterns emerged with 2-M1 treatment, where cellular proliferation remained significantly elevated relative to control at both concentrations ($p < 0.0001$ at 72 h), yet still demonstrated reduced growth compared to parallel control conditions (**Figure 4.28b**). The 2-M2 variant likewise increased absolute cell numbers after both 48 and 72 hours of exposure, though untreated controls displayed significantly greater proliferation acceleration ($p < 0.0001$) by the 72-hour treatment (**Figure 4.28c**). An identical response profile was observed for 2-M3, where control groups exhibited superior proliferative capacity compared to treated samples ($p < 0.01$) after 72 hours of culture (**Figure 4.28d**).

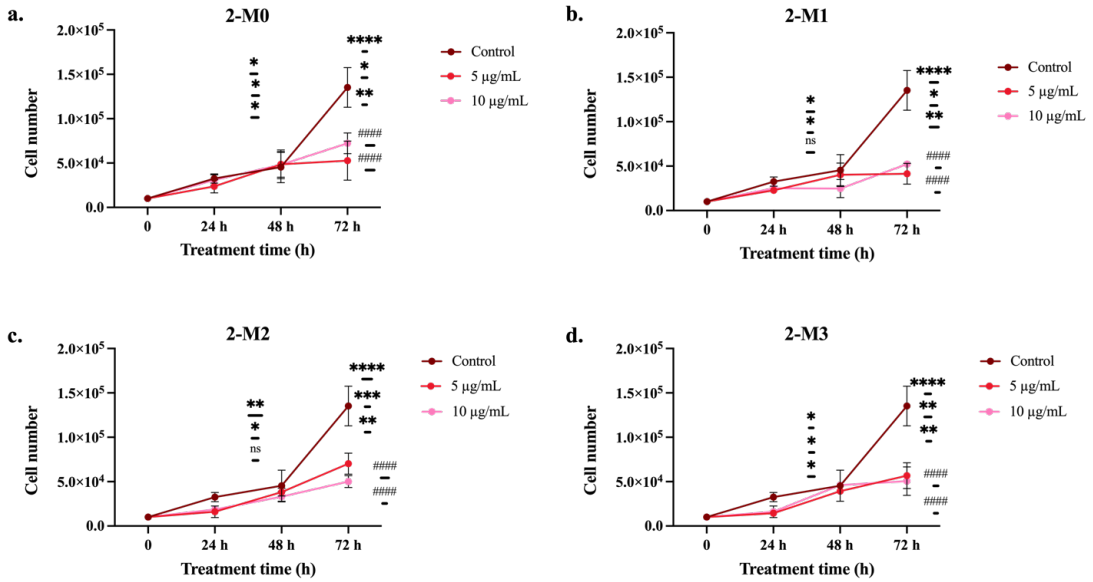


Figure 4.27: a. 1-M0, b. 1-M1, c. 1-M2, and d. 1-M3 microparticle applied to HaCaT cell lines' cell survival results after two concentrations (5 and 10 µg/mL) applied for 24, 48, and 72 h. The results represent the average of two biological replicates, each with two technical replicates, along with the standard deviation. The analysis was conducted using GraphPad Prism 9.2.0 software with a two-way ANOVA followed by Dunnett's comparison test against the initial control. ns $p > 0.05$, **** $p < 0.0001$, *** $0.0001 \leq p < 0.001$, ** $0.001 \leq p < 0.01$, * $0.01 \leq p < 0.05$. # $0.01 \leq p < 0.05$, ## $0.001 \leq p < 0.01$, ### $p < 0.001$ comparison between each time point's control group.

Fluorescence-based analysis of HaCaT cell lines following 24-hour exposure to 2-microparticles (5 µg/mL) revealed distinct cellular responses across different evaluation parameters. Reactive oxygen species (ROS) assessment demonstrated a significant reduction in oxidative stress levels, specifically with 2-M0 treatment, while all other microparticle variants (2-M1, 2-M2, and 2-M3) showed contrasting effects with measurable ROS enhancement. Mitochondrial activity, as evaluated by MitoTracker fluorescence, exhibited consistent enhancement across all tested microparticle formulations, indicating a generalized stimulatory effect on mitochondrial function. Notably, propidium iodide staining confirmed the absence of cytotoxic effects at this concentration and exposure duration, with no observable dead cells in any treatment group (**Figure 4.29**).

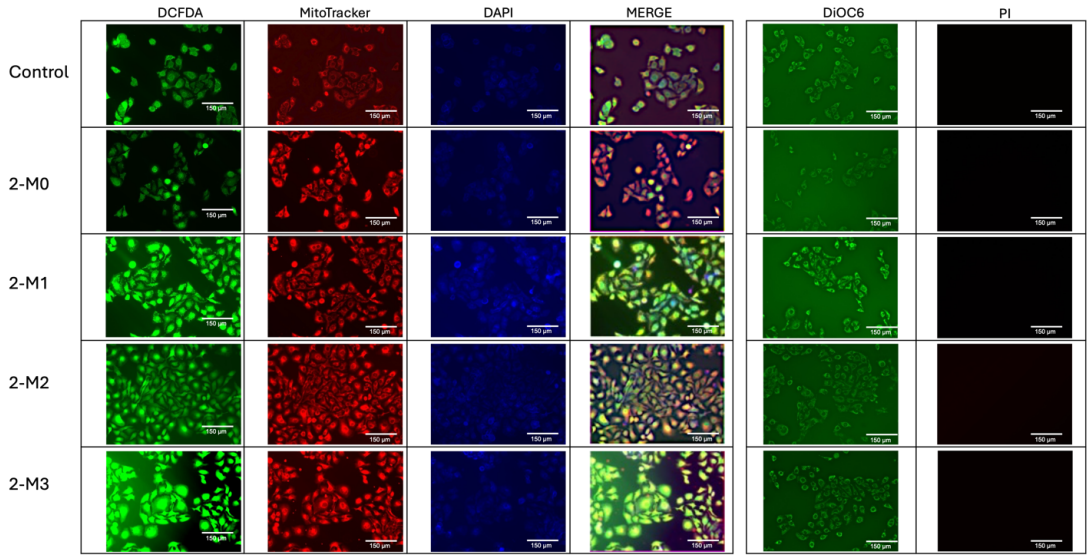


Figure 4.28: Fluorescence images of HaCaT cells after 5 µg/mL 2-microparticle, Control: no treatment applied, 2-M0: 3% PLA, 2-M1: 0.125% Spi + 3% PLA, 2-M2: 0.25% Spi + 3% PLA, 2-M3: 0.5% Spi + 3% PLA. The scale bar was 150 µm.

Increasing the microparticle concentration to 10 µg/mL revealed distinct biological responses among the different variants. Qualitative analysis demonstrated enhanced mitochondrial activity following treatment with 2-M0, 2-M1, and 2-M2 particles, suggesting these formulations may stimulate cellular bioenergetics at higher concentrations. In contrast, 2-M3 application at this concentration produced markedly different effects, characterized by a qualitative elevation in reactive oxygen species (ROS) levels accompanied by reduced mitochondrial function. This divergent response profile suggests unique structure-activity relationships among the microparticle variants, with 2-M3 potentially inducing mild oxidative stress that impacts mitochondrial performance. Notably, propidium iodide (PI) staining confirmed the absence of cytotoxic effects across all microparticle treatments at this elevated concentration following 24-hour exposure (**Figure 4.30**).

The study comprehensively evaluated the biological effects of electrosprayed microparticles (1-M and 2-M) on HUVEC and HaCaT cell lines through multiple assays. Initial screening of 1-microparticles demonstrated excellent biocompatibility, with no cytotoxic effects observed in either cell line across a broad concentration range (0.5-25 µg/mL). Among these, 1-M1 emerged as particularly promising, showing significant enhancement of HUVEC viability at intermediate to high concentrations

(5-25 µg/mL, $p < 0.01$) and consistent promotion of colony formation. In HaCaT cells, 1-M1 exhibited beneficial effects, including reduced ROS levels and enhanced mitochondrial activity without compromising cell viability, suggesting potential antioxidant properties. These favorable characteristics were maintained at higher concentrations (10 µg/mL), as confirmed by fluorescence imaging, which demonstrated preserved membrane integrity and metabolic function.

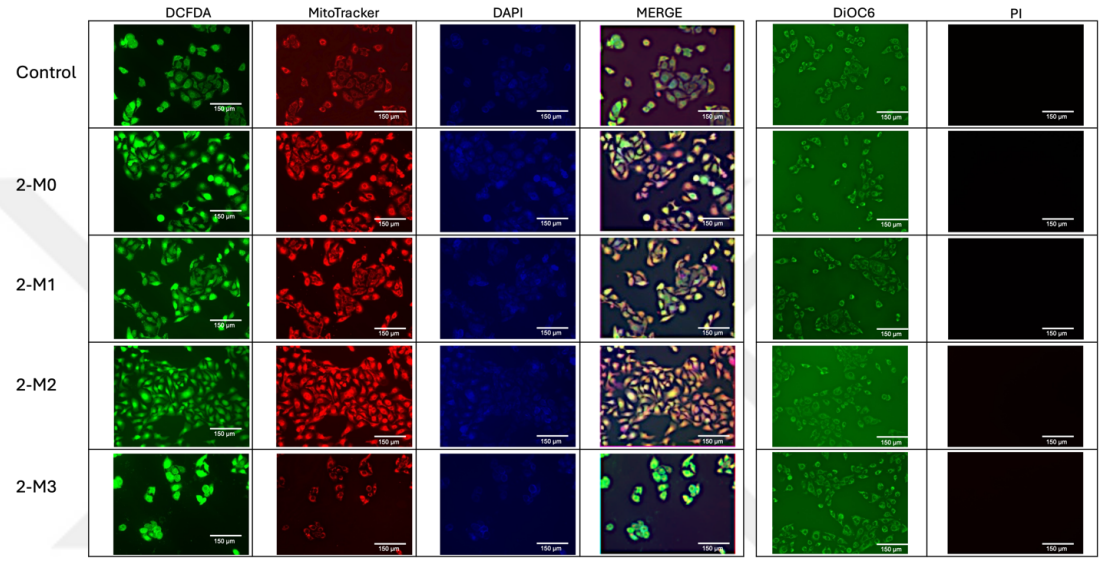


Figure 4.29: Fluorescence images of HaCaT cells after 5 µg/mL 2-microparticle, Control: no treatment applied, 2-M0: 3% PLA, 2-M1: 0.125% Spi + 3% PLA, 2-M2: 0.25% Spi + 3% PLA, 2-M3: 0.5% Spi + 3% PLA. The scale bar was 150 µm.

The 2-microparticle series showed more variable biological effects. While maintaining general biocompatibility, these particles displayed time-dependent modulation of proliferation patterns in both cell lines. Notably, 2-M0 and 2-M1 demonstrated initial proliferative effects at 48 hours that diminished by 72 hours, particularly at higher concentrations. Comparative analysis revealed that 1-M1 consistently outperformed its 2-series counterpart in terms of sustained proliferative effects and metabolic enhancement. The differential responses between particle series likely reflect variations in physicochemical properties arising from distinct electrospraying setups, with 1-M1's superior performance potentially attributable to its optimized size distribution or surface characteristics.

The selection of 1-M1 for further investigation is supported by its multifaceted beneficial effects across all evaluated parameters. Its ability to enhance cell viability and proliferation while reducing oxidative stress suggests potential applications in wound healing or tissue engineering. The concentration-dependent effects, particularly the optimal activity at 5-10 µg/mL, provide clear guidance for dosage selection in subsequent studies. Furthermore, 1-M1's consistent performance across two distinct cell types indicates broad applicability, while its contrast with the more variable 2-series particles underscores the importance of production methodology in determining biological activity. These findings position 1-M1 as a promising candidate for further development and mechanistic studies.

4.2.6. Antimicrobial Effects of Microparticles

The antimicrobial potential of all 1-and 2-microparticles and 70% ethanol-derived Spirulina extract was assessed against four clinically relevant bacterial strains—*Escherichia coli*, *Staphylococcus aureus*, *Pseudomonas aeruginosa*, and *Staphylococcus epidermidis*—using the standard disc diffusion assay. Results demonstrated no detectable antimicrobial activity for any of the tested microparticles or the Spirulina extract, as evidenced by the absence of inhibition zones around the discs (**Figure 4.31**). In contrast, the positive control (2 mg/mL ciprofloxacin) exhibited clear zones of growth inhibition, confirming the validity of the experimental conditions.

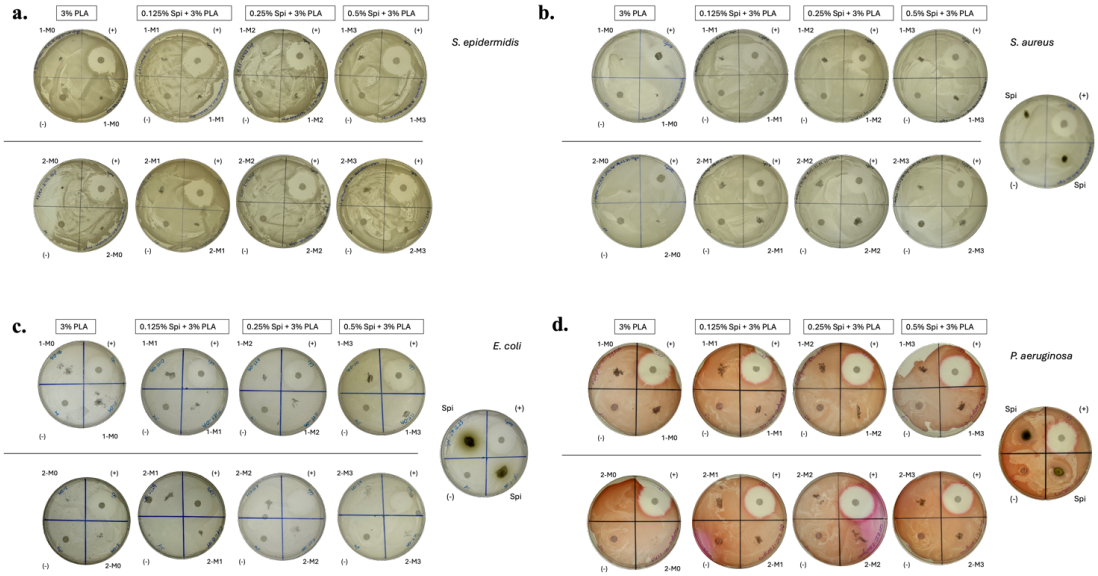


Figure 4.30: Disc diffuson assay results for all microparticles and Spirulina ethanol extract in a. *S.epidermidis*, b. *S.aureus*, c. *E.coli*, and d. *P.aeruginosa*. Negative control was dH2O, and positive control was 2 mg/mL ciprofloxacin.

Quantitative measurements of inhibition zone diameters (**Table 4.3**) further supported these observations, with no significant bacterial suppression observed for the test compounds. The lack of activity across both Gram-negative (*E. coli, P. aeruginosa*) and Gram-positive (*S. aureus, S. epidermidis*) strains suggests that neither the microparticles nor the Spirulina extract possesses broad-spectrum antibacterial properties under the tested conditions. These findings indicate that alternative formulations, higher concentrations, or additive combinations may be necessary to achieve antimicrobial effects, if applicable.

Table 4.3: Inhibition zone diameters (cm) of *S. epidermidis*, *S. aureus*, *E. coli*, and *P. aeruginosa* from **Figure 4.31**.

	S. epidermidis				***S. aureus***			
(cm)	Sample1	Sample2	Cipro (2 mg/mL)	dh_20	Sample1	Sample2	Cipro (2 mg/mL)	dh_20
1-M0	0	0	2.514	0	0	0	2.133	0
1-M1	0	0	2.838	0	0	0	2.362	0
1-M2	0	0	2.705	0	0	0	2.143	0
1-M3	0	0	2.421	0	0	0	2.21	0
2-M0	0	0	2.579	0	0	0	2.222	0
2-M1	0	0	2.515	0	0	0	2.39	0
2-M2	0	0	2.593	0	0	0	2.4	0
2-M3	0	0	2.733	0	0	0	2.45	0
Spi	0	0		0	0	0	2.314	0
	E. coli				***P. aeruginosa***			
(cm)	Sample1	Sample2	Cipro (2 mg/mL)	dh_20	Sample1	Sample2	Cipro (2 mg/mL)	dh_20
1-M0	0	0	5.857	0	0	0	2.844	0
1-M1	0	0	5.086	0	0	0	3.126	0
1-M2	0	0	5.429	0	0	0	2.979	0
1-M3	0	0	5.234	0	0	0	3.124	0
2-M0	0	0	5.343	0	0	0	2.998	0
2-M1	0	0	5.315	0	0	0	2.998	0
2-M2	0	0	5.386	0	0	0	3.195	0
2-M3	0	0	5.317	0	0	0	2.8	0
Spi	0	0		0	0	0	2.608	0

4.2.7. Antioxidant Capacity of Produced Microparticles

The Folin-Ciocalteu test was applied to determine the total phenolic compounds. The 1-microparticles were prepared at a concentration of 3 mg/mL, and the 70% ethanol extract of Spirulina was prepared at a concentration of 6.8 mg/mL in PBS. These compounds were incubated overnight at room temperature and 300 rpm to facilitate the release of Spirulina-containing microparticles. The standard curve for total phenolic compounds was established using gallic acid (0.005-1 mg/mL) to identify the concentration from absorbance values at 765 nm (**Figure 4.32**), and the results were expressed as milligrams of gallic acid (GA) per gram of extract.

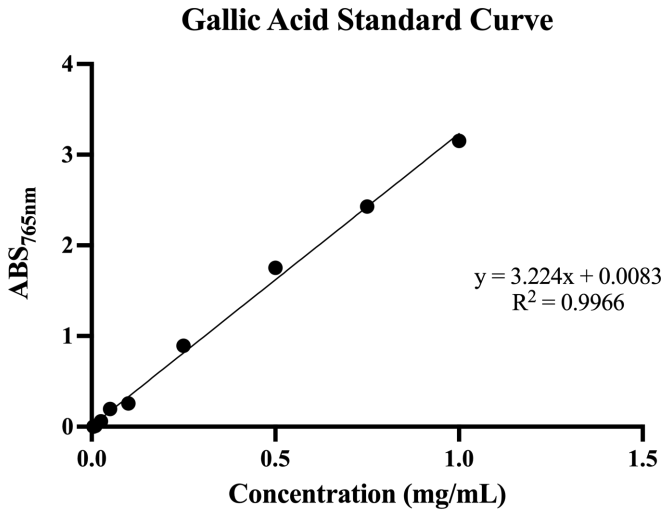


Figure 4.31: Standard curve of gallic acid at different concentrations (0.005-1 mg/mL) obtained by the Folin-Ciocalteu test and read at 765 nm.

In the 70% ethanol Spirulina extract, the total phenolic content was determined to be 24.07 ± 0.97 mg GAE/g of Spirulina. However, no detectable phenolic content was found for the microparticles within the concentration range of the gallic acid standard curve (0.005–1 mg/mL).

In the experiment to determine the antioxidant capacity using the DPPH method, the EC_{50} value of Spirulina was determined to be 2.84 mg/mL (**Figure 4.33**), and the TEAC equivalent was calculated to be 2.40 µM (**Figure 4.34**). This value was also calculated for the microparticles; however, due to the trace amount of Spirulina in the microparticles and the lack of antioxidant properties in PLA, the DPPH antioxidant test results showed that the % inhibition values were, on average, below 10% for microparticles at a concentration of 3 mg/mL.

The TEAC equivalent was calculated in 2.4 µM by taking the ratio of the slope of the graph obtained from the DPPH test of Spirulina (**Figure 4.33**) to the slope of the Trolox graph (**Figure 4.34**).

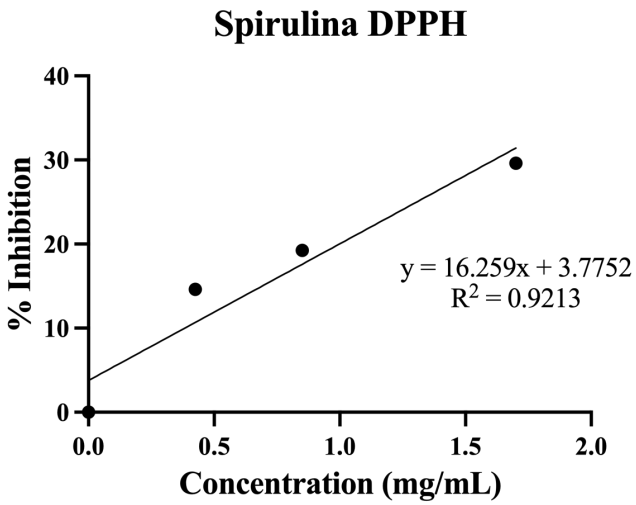


Figure 4.32: Concentration-dependent DPPH reactive inhibition graph obtained from the DPPH antioxidant test of Spirulina. Values are the average of at least three repeated measurements.

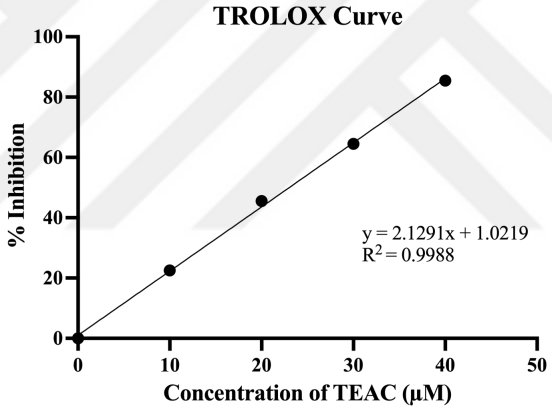


Figure 4.33: Trolox curve obtained with TEAC at different concentrations (0-40 µM) and read at 715 nm. Values are the average of at least three replicates.

4.3. Biocompound-Loaded Microparticle Production and Cell Fate

Niacinamide, palmotyl-tripeptide-1, and a combination of these microparticles were encapsulated into the 1-M1 microparticles to determine the biological properties and encapsulation yields, comparing the free forms in cellular experiments after optimizing the formulations in electrospraying techniques. Before biocompound encapsulation in the 1-M1 microparticles, the cellular uptake ability of the released material was tested with encapsulated 0.1% Nile Red-loaded microparticles in the 1-M0.

4.3.1. Nile-Loaded Microparticle Production and Cellular Uptake

The 0.1% Nile Red production parameters were the same as those for 1-M0 (18 µL/min, 20 kV, 15 cm distance between nozzle and collector).

The Nile red-loaded microparticles were characterized by their size distribution in the SEM image; the particle size was measured using ImageJ and analyzed by GraphPad 9.2.0 software (**Figure 4.35**). The average particle size of 0.1% Nile Red loaded particles was 3.77 ± 0.546 µm with monodisperse particle formation.

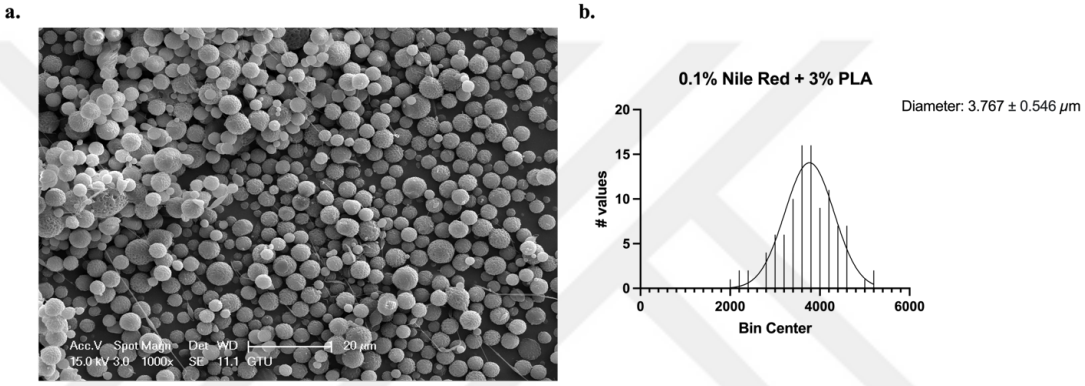


Figure 4.34: 0.1% Nile Red + 3% PLA microparticle a. SEM image and b. size distribution by selecting 100 microparticles from SEM images using ImageJ software, and the distribution graph was achieved by GraphPad 9.2.0; the scale bar of the SEM image is 20 µm.

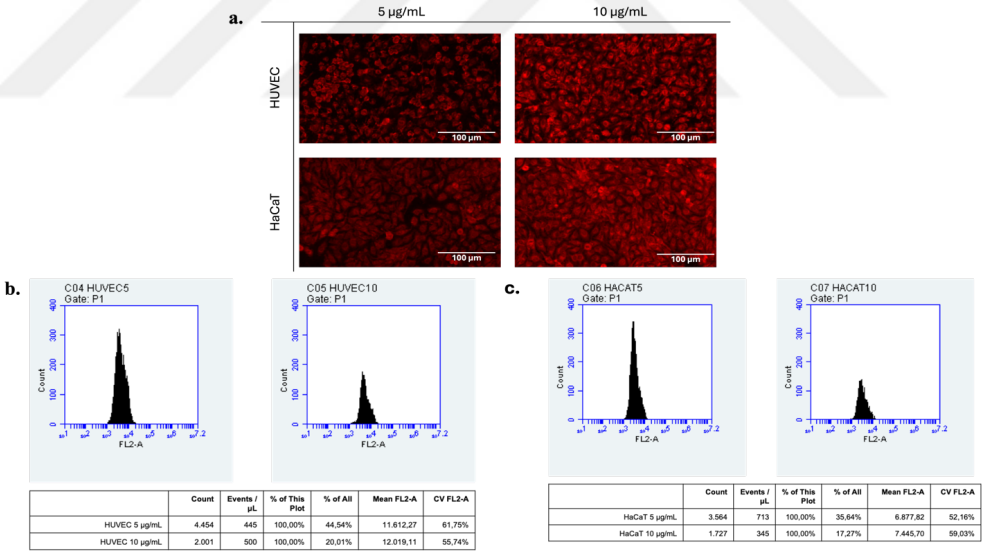
The cellular uptake of microparticles was determined by encapsulating 0.1% Nile Red in 3% PLA and applying it to the HUVEC and HaCaT cell lines at optimized dosages of 5 and 10 µg/mL for 24 h. Fluorescence microscopy was used to determine the presence of Nile Red in the cells after the application time had elapsed. The fluorescence images are shown in **Figure 4.36a**, indicating that the released microparticle ingredient was taken up by cells at both concentrations. Due to the increased concentration of microparticles in the cells, the Nile Red concentration in the cells also increased; however, at both concentrations, Nile Red was successfully released from the microparticles.

The BD Accuri B6 Flow Cytometry Device was also used to detect Nile Red within the cells. For this purpose, the cells were fixed in cold 70% ethanol, and the readings

were performed with 20,000 events. Flow cytometry analyses were conducted by gating to include only live cells. According to the flow cytometry results, limited to 20,000 events, the proportion of Nile Red-containing microparticles within HUVEC cells was determined to be 44.54% of the total cells at a concentration of 5 µg/mL and 20.01% at 10 µg/mL (**Figure 4.36b**). For HaCaT cells, these values were 35.64% and 17.27% of the total cells at concentrations of 5 µg/mL and 10 µg/mL, respectively (**Figure 4.36c**).

Based on fluorescence microscopy and FACS results, substances loaded into the microparticles were released into the medium and subsequently internalized by the cells within 24 hours. The 5 µg/mL concentration resulted in a greater intracellular presence than the higher concentration.

This finding suggests that the obtained microparticles hold promise as microcarrier systems and demonstrate high efficiency even at low concentrations.



	Count	Events / µL	% of This Plot	% of All	Mean FL2-A	CV FL2-A
HUVEC 5 µg/mL	4.454	445	100,00%	44,54%	11.612,27	61,75%
HUVEC 10 µg/mL	2.001	500	100,00%	20,01%	12.019,11	55,74%

	Count	Events / µL	% of This Plot	% of All	Mean FL2-A	CV FL2-A
HaCaT 5 µg/mL	3.564	713	100,00%	35,64%	6.877,82	52,16%
HaCaT 10 µg/mL	1.727	345	100,00%	17,27%	7.445,70	59,03%

Figure 4.35: Cellular uptake of Nile Red-loaded PLA microparticles in HUVEC and HaCaT cells after 24 h incubation. a. Fluorescence microscopy images show intracellular localization of Nile Red released from e-Nile microparticles at concentrations of 5 and 10 µg/ml. Scale bar: 100 µm. b. Flow cytometry results, graphs, and analyses for HUVEC cells exposed to Nile Red-loaded microparticles at concentrations of 5 µg/mL (HUVEC5) and 10 µg/mL (HUVEC10) for 24 hours are presented. The counted cells were limited to live cells. c. Flow cytometry, the result graphs, and analyses for HaCaT cells exposed to Nile Red, including microparticles at concentrations of 5 µg/mL (HaCaT5) and 10 µg/mL (HaCaT10) for 24 h. The counted cells were limited to live cells.

4.3.2. Biocompound-Loaded Microparticle Production and Optimization

To enhance the biological functionality of the electrosprayed microparticles, niacinamide (Nia)—a well-characterized dermatological active compound known for its cellular repair, anti-inflammatory, and antioxidant properties—was incorporated into the formulation. This modification aimed to leverage niacinamide's therapeutic mechanisms to improve the microparticles' potential for dermal applications.

The niacinamide-loaded microparticles were prepared using the same electrospraying parameters as the 1-M1 (e-Spi) formulation: a flow rate of 20 µL/min, an applied voltage of 16.8 kV, and a 15 cm nozzle-to-collector distance. The biocompounds (niacinamide and Spirulina) were dissolved in ethanol and added dropwise to the PLA-containing chlorophase (chloroform: ethanol, 19:1). Particle morphology and size distribution were analyzed via SEM imaging, with measurements performed using ImageJ and GraphPad software.

SEM analysis revealed that microparticles containing 0.1% niacinamide + 0.125% Spirulina + 3% PLA had an average diameter of 3.95 ± 0.505 µm with a homogeneous morphology (**Figure 4.37**). Increasing the niacinamide concentration to 0.25% resulted in a slightly larger average size (4.29 ± 0.91 µm) while maintaining structural homogeneity (**Figure 4.38**). Further loading to 0.5% niacinamide yielded particles with a comparable size (4.23 ± 0.65 µm) and uniform distribution (**Figure 4.39**). However, at higher concentrations (1%, 5%, and 10% niacinamide), the microparticles lost their spherical, monodisperse structure, exhibiting irregular fiber formation (**Figure 4.40**). Therefore, the 0.5% Nia + 0.125% Spi + 3% PLA (e-Nia) was selected for further microparticle production and cellular experiments.

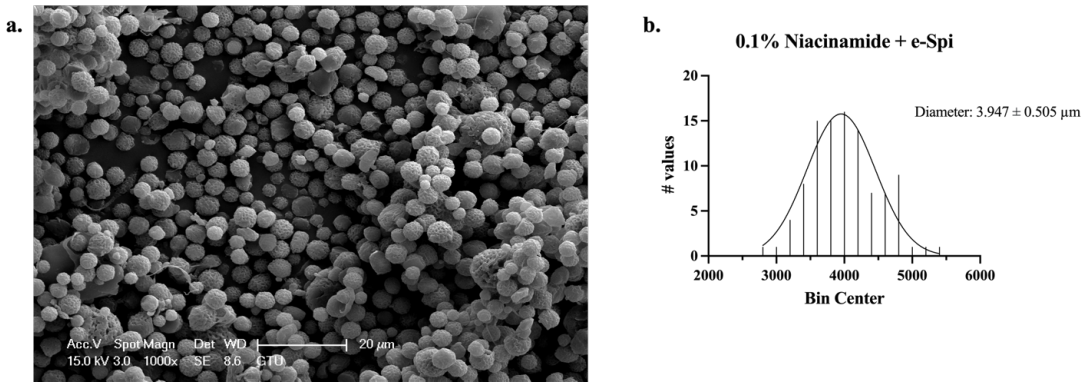


Figure 4.36: 0.1% Nia + 0.125% Spi + 3% PLA microparticle. a. SEM image and b. size distribution by selecting 100 microparticles from SEM images using ImageJ software, and the distribution graph was achieved using GraphPad 9.2.0. The scale bar of the SEM image is 20 µm.

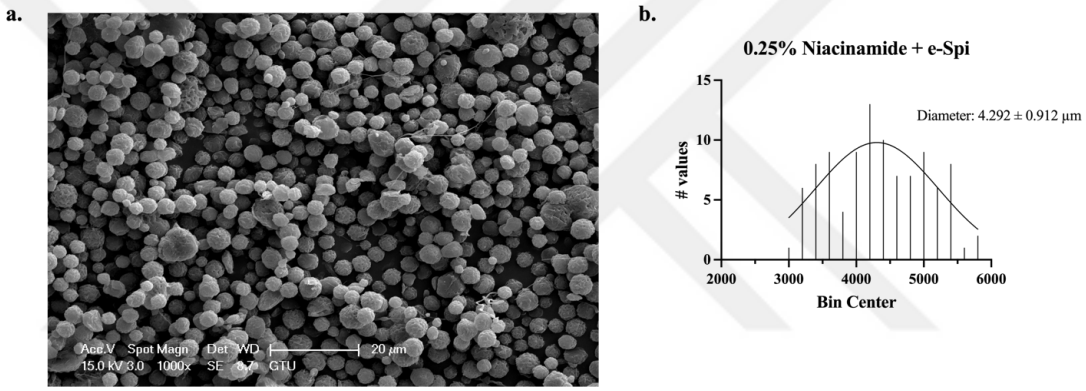


Figure 4.37: The 0.25% Nia + 0.125% Spi + 3% PLA microparticles' a. SEM image and b. Size distribution by selecting 100 microparticles from SEM images using ImageJ software, and the distribution graph was achieved using GraphPad 9.2.0. The scale bar of the SEM image is 20 µm.

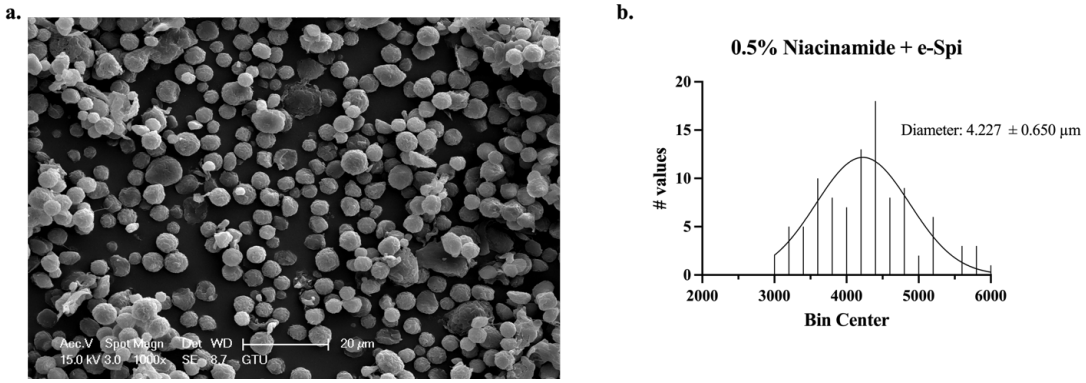


Figure 4.38: The 0.5% Nia + 0.125% Spi + 3% PLA microparticles' a. SEM image and b. Size distribution by selecting 100 microparticles from SEM images using ImageJ software, and the distribution graph was achieved using GraphPad 9.2.0. The scale bar of the SEM image is 20 µm.

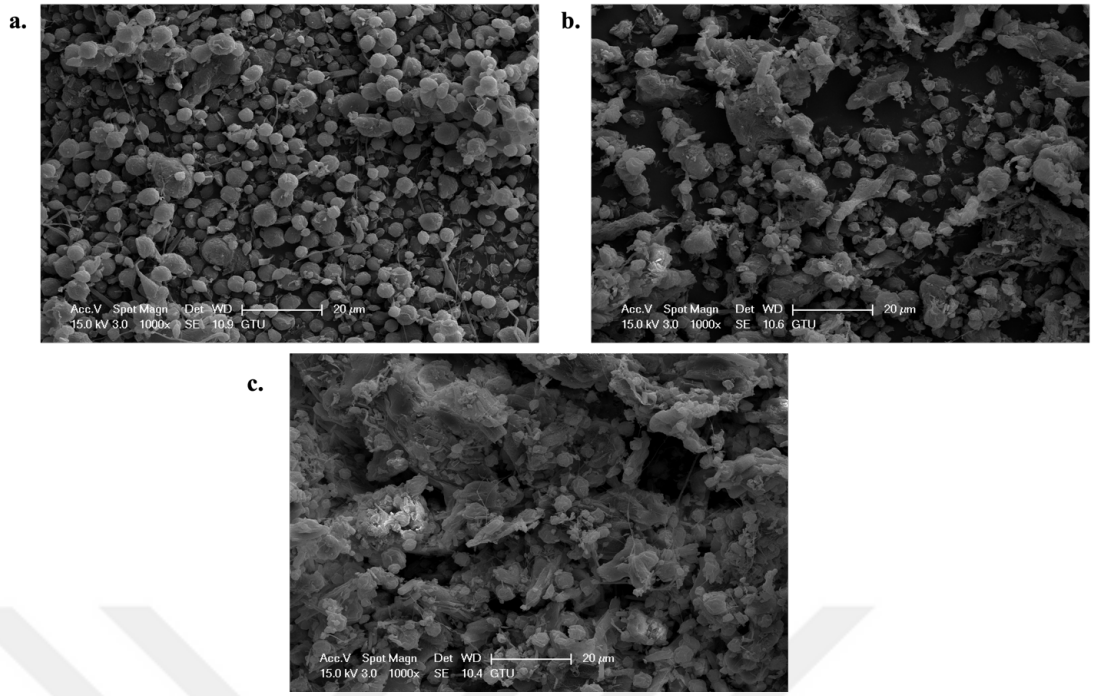


Figure 4.39: SEM images of a. 1% Nia-loaded, b. 5% Nia-loaded and c. 10% Nia-loaded microparticles. The scale of the SEM images was 20 µm.

To enhance the reparative and regenerative capacity of the electrosprayed microparticles, palmitoyl tripeptide-1 (Tri) - a bioactive peptide conjugate combining the tripeptide GHK (Gly-His-Lys) with palmitic acid for enhanced skin permeability - was incorporated into the formulation. This modification leveraged Pal-GHK's well-documented roles in extracellular matrix remodeling and tissue regeneration to create microparticles with optimized wound-healing and anti-aging potential. The peptide's ability to upregulate collagen synthesis, modulate matrix metalloproteinase (MMP) activity, and promote angiogenesis makes it particularly suitable for dermal repair applications.

SEM analysis of 0.1% Tri + 0.125% Spi + 3% PLA microparticles revealed a homogeneous spherical morphology with an average diameter of 4.19 ± 0.58 µm (**Figure 4.41**). However, increasing the peptide content resulted in a progressive loss of structural homogeneity, as evident in irregular fiber formation (**Figures 4.42 and 4.43**). Notably, while 0.25% Tri-loaded microparticles exhibited extensive fiber networks, the 0.5% Tri formulation showed reduced fiber prevalence with a smaller average particle diameter (3.30 ± 0.36 µm, **Figure 4.43**), suggesting a concentration-dependent threshold for morphology transition. Considering the homogeneity of the

microparticles and fiber formations caused by Tri, 0.1% Tri + 0.125% Spi + 3% PLA (e-Tri) was selected as tripeptide-loaded formulations.

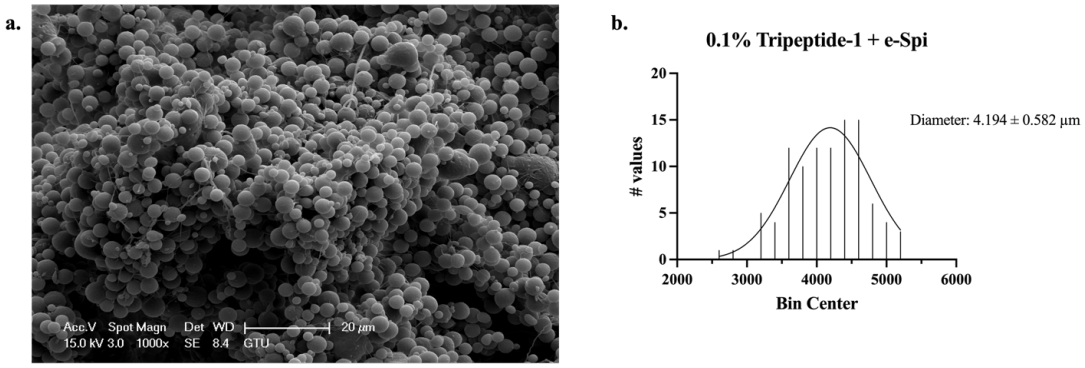


Figure 4.40: The 0.1% Tri + 0.125% Spi + 3% PLA microparticles' a. SEM image and b. Size distribution by selecting 100 microparticles from SEM images using ImageJ software, and the distribution graph was achieved using GraphPad 9.2.0. The scale bar of the SEM image is 20 µm.

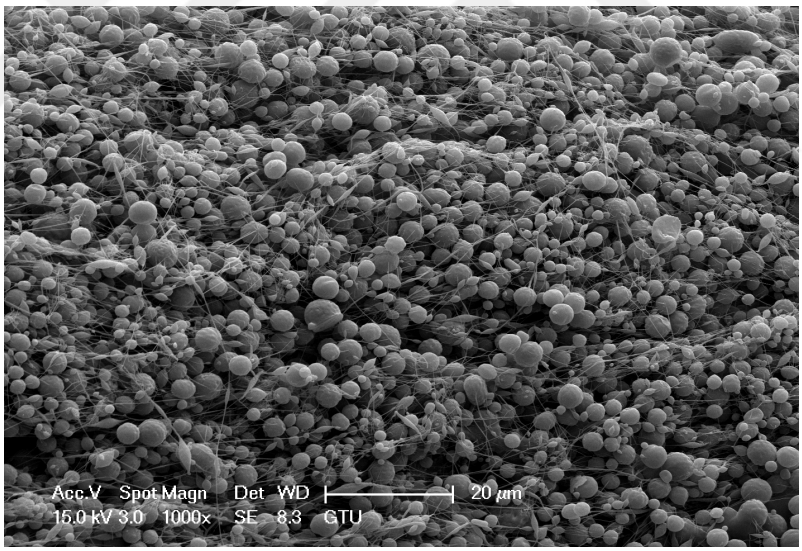


Figure 4.41: The 0.25% Tri + 0.125% Spi + 3% PLA microparticles' SEM image. The scale bar of the SEM image is 20 µm.

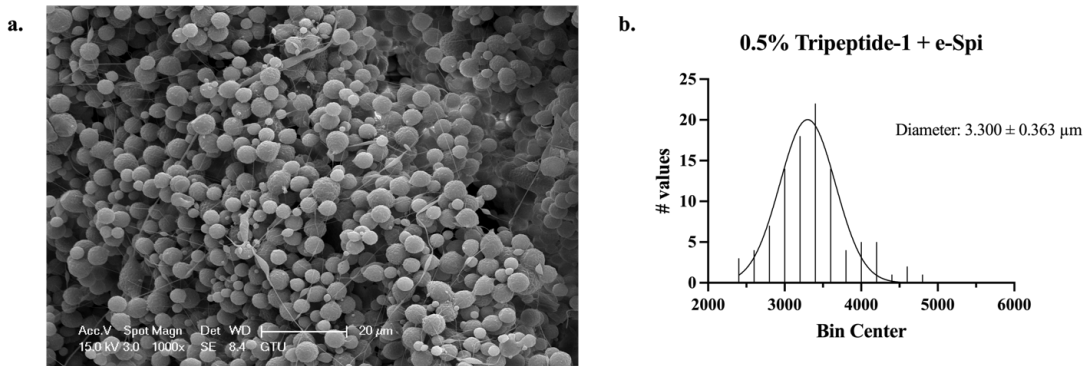


Figure 4.42: The 0.5% Tri + 0.125% Spi + 3% PLA microparticles' a. SEM image and b. Size distribution by selecting 100 microparticles from SEM images using ImageJ software, and the distribution graph was achieved using GraphPad 9.2.0. The scale bar of the SEM image is 20 µm.

The composite system containing 0.5% Nia + 0.1% Tri + 0.125% Spi + 3% PLA (e-NiaTri) demonstrated superior microparticle morphology, exhibiting optimal monodispersity and minimal fiber defects (**Figure 4.44**). Comparative analysis revealed that increasing tripeptide content to 0.25% or 0.5% (while maintaining 0.5% niacinamide) significantly compromised structural integrity, yielding non-uniform particles with extensive fiber formation (**Figure 4.45**). This concentration-dependent morphological degradation guided the selection of the 0.1% Tri formulation for its balanced bioactivity and particulate stability.

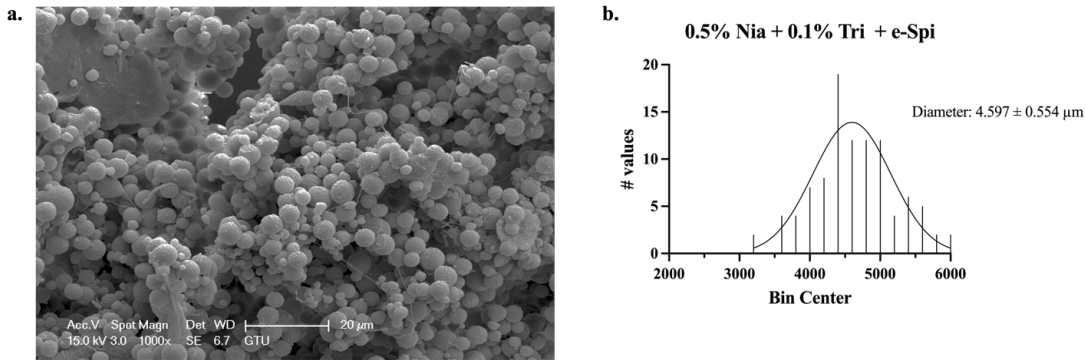


Figure 4.43: The 0.5% Nia + 0.1% Tri + 0.125% Spi + 3% PLA microparticles a. SEM image and b. Size distribution by selecting 100 microparticles from SEM images using ImageJ software, and the distribution graph was achieved using GraphPad 9.2.0. The scale bar of the SEM image is 20 µm.

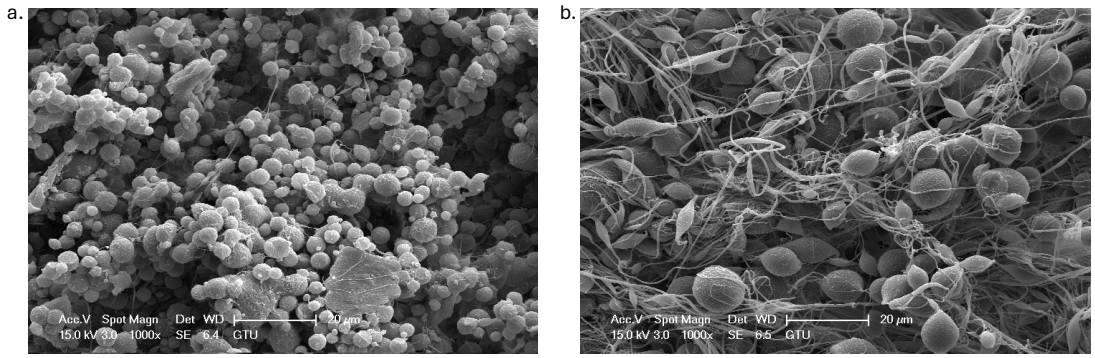


Figure 4.44: SEM images of a. 0.5% Nia + 0.25% Tri-loaded and b. 0.5% Nia + 0.5% Tri-loaded; the scale of images was 20 µm.

Depending on SEM images, 0.5% Nia + 0.125% Spi + 3% PLA (e-Nia) microparticles were selected for cellular experiments, considering their size and in-particle concentrations. For palmitoyl-tripeptide-1, 0.1% Tri + 0.125% Spi + 3% PLA (e-Tri) microparticle was chosen due to particle formation and size distribution analysis for cellular experiments. For two bioactive molecule-loaded microparticles, 0.5% Nia + 0.1% Tri + 0.125% Spi + 3% PLA (e-NiaTri) was selected for further experiments.

4.3.3. Cellular Experiments of Biocompound-Loaded Microparticles

Before biocompound-loaded microparticles, the cytotoxicity of pure (non-encapsulated) niacinamide (Nia) and pal-tripeptide-1 (Tri) was assessed under the same experimental conditions as the microparticle formulations, utilizing a range of concentrations (1–75 µM for Nia and 1–50 µM for Tri) to compare the free form and encapsulating form in a concentration-dependent manner.

4.3.3.1. Cellular Experiments of the Free Form of Nia and Tri

The results of the MTT assay demonstrated that Nia exhibited no significant cytotoxic effects on either the HUVEC or HaCaT cell lines at any of the tested concentrations (**Figure 4.46a**), confirming its high biocompatibility.

In contrast, Tri treatment led to a dose-dependent reduction in cell viability, although sensitivity varied among cell lines. In HUVECs, a statistically significant decrease in viability was noted starting at 10 µM ($p < 0.05$). Meanwhile, in HaCaT cells, a more pronounced reduction occurred at higher concentrations, with significant cytotoxicity

detected at 25 µM and 50 µM ($p < 0.0001$ for both) (**Figure 4.46b**). These findings suggest that while Tri remains relatively safe at lower doses, its potential cytotoxic effects should be carefully evaluated, particularly in HUVECs, which appear more sensitive to the peptide than HaCaT cells.

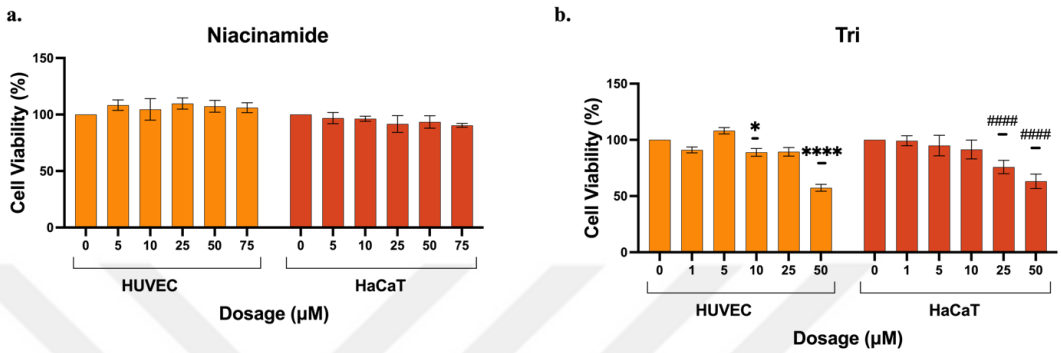


Figure 4.45: MTT results of 24 h a. Nia and b. Tri application for HUVEC (orange) and HaCaT (red) cell lines. Standard errors were from 3 biological replicates, and bars were an average of 3 biological replicates with four technical replicates. Statistical analysis were conducted two-way ANOVA combined with Dunnett's comparasion tests for each cell line, ns $p > 0.05$, **** $p < 0.0001$, *** $0.0001 \leq p < 0.001$, ** $0.001 \leq p < 0.01$, * $0.01 \leq p < 0.05$ for HUVECs, # $0.01 \leq p < 0.05$, ## $0.001 \leq p < 0.01$, ### $p < 0.001$ for HaCaT cell line compared to the control.

Cell viability assays were conducted on both HUVEC and HaCaT cell lines after a 72-hour treatment with free-form niacinamide (Nia) and pal-tripeptide-1 (Tri). For HUVECs, the 10 µM Nia treatment group showed a proliferation pattern similar to that of the controls at 48 hours, with this trend continuing through 72 hours ($p < 0.05$) (**Figure 4.47a**). HaCaT cells exhibited more pronounced responses to Nia, as both 10 µM and 25 µM concentrations significantly enhanced proliferation compared to both initial cell counts ($p < 0.001$ for 10 µM; $p < 0.01$ for 25 µM) and 72-hour controls ($p < 0.01$ for 10 µM; $p < 0.05$ for 25 µM) (**Figure 4.47c**).

Tri treatment produced distinct concentration-dependent effects across cell types. In HUVECs, 5 µM Tri kept proliferation rates similar to those of the controls at both 48 hours ($p < 0.05$) and 72 hours ($p < 0.01$) (**Figure 4.47b**). HaCaT cells exhibited increased proliferation with both Tri concentrations at 48 hours ($p < 0.05$), while control groups remained stable ($p > 0.05$) (Figure **4.47d**). These varying responses

highlight cell-type-specific sensitivity to the test compounds, with HaCaT keratinocytes generally showing greater proliferative responses than vascular endothelial cells under the tested conditions.

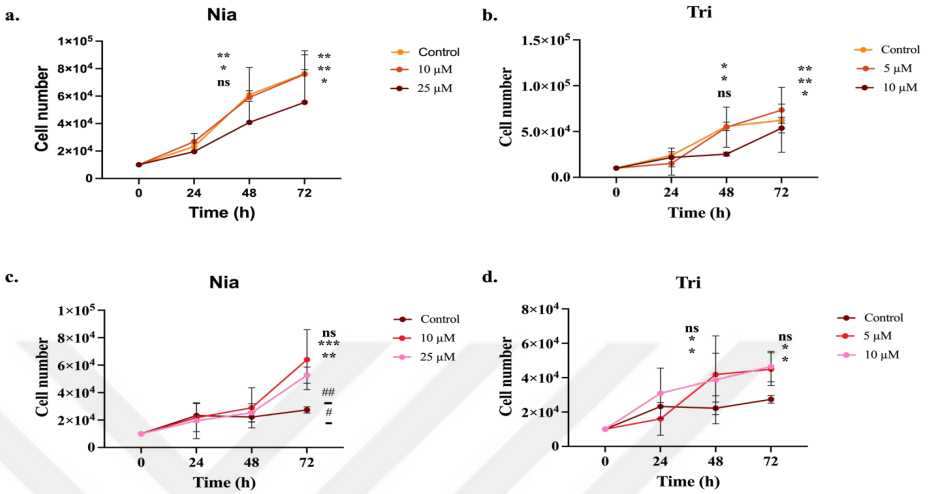


Figure 4.46: a. Nia, b. Tri in HUVEC cells, c. Nia and d. Tri in HaCaT cell lines' cell survival results after two concentrations (10 and 25 µM for Nia, 5 and 10 µM for Tri) applied for 24, 48, and 72 h. The results represent the average of two biological replicates, each with two technical replicates, along with the standard deviation. The analysis was conducted using GraphPad Prism 9.2.0 software with a two-way ANOVA followed by Dunnett's comparison test against the initial control. ns $p > 0.05$, **** $p < 0.0001$, *** $0.0001 \leq p < 0.001$, ** $0.001 \leq p < 0.01$, * $0.01 \leq p < 0.05$. # $0.01 \leq p < 0.05$, ## $0.001 \leq p < 0.01$, ### $p < 0.001$ comparison between each time point's control group.

4.3.3.2. Cellular Experiments of Biocompound-Loaded Microparticles

Microparticles were applied to the HUVEC and HaCaT cell lines to identify the cytotoxicity effects with proliferative capacity in comparison with non-biocompound loaded e-Spi (blank microparticle). Also, ROS levels were identified after microparticle applications, as detected via fluorescence images and ImageJ software.

The cytotoxicity effects of microparticles containing niacinamide and pal-tripeptide-1 were investigated using an MTT assay on HUVEC and HaCaT cell lines after a 24-hour application period.

For e-Nia, no significant toxic effects were observed in either the HUVEC or HaCaT cell lines at any of the tested concentrations, except at the highest dose of 50 μg/mL, where a slight reduction in cell viability was detected compared to the control group ($p < 0.05$ for both cell lines) (**Figure 4.48a**). This suggests that e-Nia exhibits a favorable safety profile within the tested dosage range of 0-50 μg/mL. In the case of pal-tripeptide-1, a comprehensive safety assessment was conducted by evaluating its cytotoxic effects on both HUVEC and HaCaT cells across increasing concentrations. The results, illustrated in **Figure 4.48b**, confirmed that the peptide did not induce significant cytotoxicity at the tested doses, supporting its potential for further experimental use.

Regarding e-Tri microparticles, the MTT assay revealed that concentrations of 5 and 10 μg/mL were optimal for subsequent experiments, as these dosages maintained cell viability above 75% in both cell lines. Although a statistically significant decrease in viability was noted compared to untreated control cells ($p < 0.05$ for 5 μg/mL in HUVEC, $p < 0.05$ for 5 μg/mL, $p < 0.01$ for 10 μg/mL, $p = 0.001$ for 25 μg/mL, and $p < 0.001$ for 50 μg/mL in HaCaT cell line), the reduction was not substantial enough to indicate toxicity, making these concentrations suitable for further investigation.

Similarly, for niacinamide and tripeptide co-encapsulated microparticles (e-NiaTri), the MTT assay results demonstrated no cytotoxic effects on either HUVEC or HaCaT cells at concentrations of 5 and 10 μg/mL (**Figure 4.48c**). Based on these findings, the selected dosages were deemed optimal for follow-up studies. Finally, in the case of e-Spi, no cytotoxicity was detected at any of the tested concentrations (**Figure 4.48d**), further confirming its biocompatibility and safety for cellular applications.

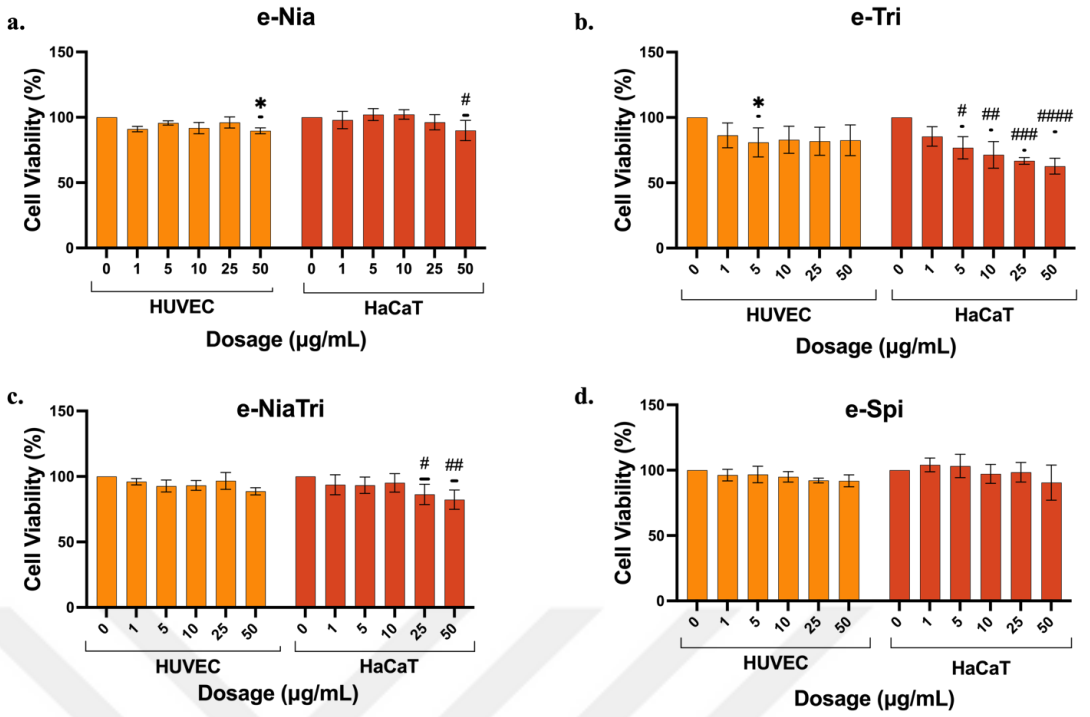


Figure 4.47: MTT results of microparticles a. e-Nia, b. e-Tri, and c. e-Niatri, and d. e-Spi. Orange represents HUVEC, and ed indicates HaCaT cell lines. Standard errors were from 3 biological replicates, and bars were an average of 3 biological replicates with four technical replicates. Statistical analysis were conducted two-way ANOVA combined with Dunnett's comparasion tests for each cell line, ns $p > 0.05$, **** $p < 0.0001$, *** $0.0001 \leq p < 0.001$, ** $0.001 \leq p < 0.01$, * $0.01 \leq p < 0.05$ for HUVECs, # $0.01 \leq p < 0.05$, ## $0.001 \leq p < 0.01$, ### $p < 0.001$ for HaCaT cell line compared to the control.

A 72-hour cell proliferation assay was performed on HUVEC cells to evaluate the effects of biocompound-loaded microparticles, including e-Spi formulations, at concentrations of 5 and 10 µg/mL (**Figure 4.49**).

For e-Nia, a significant enhancement in cell proliferation was observed at 5 µg/mL after 72 hours compared to the control group ($p < 0.01$). This increase was also significantly higher than both the non-treated control ($p < 0.05$) and the 10 µg/mL treatment group ($p < 0.05$) (**Figure 4.49a**). In contrast, e-Tri only exhibited a statistically significant proliferative effect at 5 µg/mL after 72 hours relative to the initial cell count ($p < 0.05$) (**Figure 4.49b**).

For the co-encapsulated microparticles (e-NiaTri), both concentrations (5 and 10 µg/mL) stimulated a marked increase in cell proliferation after 48 hours ($p < 0.0001$).

The non-treated group also showed a significant rise in cell number by 72 hours compared to baseline ($p < 0.01$). However, cells treated with e-NiaTri at both dosages demonstrated further proliferation by 72 hours, surpassing the initial control levels (**Figure 4.49c**).

As for e-Spi (the blank microparticles), both concentrations induced a moderate increase in cell proliferation after 72 hours, though this effect remained lower than that of the non-treated control (**Figure 4.49d**).

These findings suggest that the loaded microparticles not only enhanced cellular proliferation but also effectively released their bioactive cargo, demonstrating their potential for improving biological activity in the HUVEC cell line.

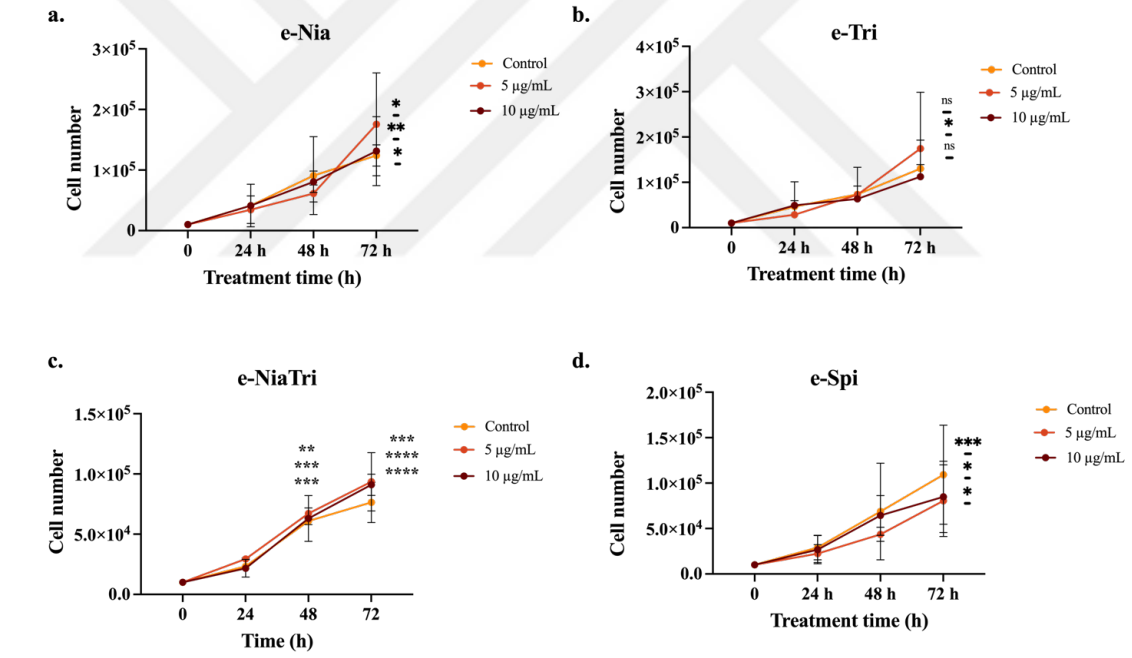


Figure 4.48: a. e-Nia, b. e-Tri, c. e-NiaTri, and d. e-Spi microparticle applied to HUVEC cell lines' cell survival results after two concentrations (5 and 10 µg/mL) applied for 24, 48, and 72 h. The results represent the average of two biological replicates, each with two technical replicates, along with the standard deviation. The analysis was conducted using GraphPad Prism 9.2.0 software with a two-way ANOVA followed by Dunnett's comparison test against the initial control. ns $p > 0.05$, **** $p < 0.0001$, *** $0.0001 \leq p < 0.001$, ** $0.001 \leq p < 0.01$, * $0.01 \leq p < 0.05$. # $0.01 \leq p < 0.05$, ## $0.001 \leq p < 0.01$, ### $p < 0.001$ comparison between each time point's control group.

Fluorescence imaging was performed 24 hours post-treatment to evaluate reactive oxygen species (ROS) production and mitochondrial activity in HUVEC and HaCaT cell lines following exposure to biocompound-loaded microparticles. The experimental setup employed three distinct fluorescent markers: H_2-DCFDA for ROS detection (green fluorescence), MitoSPY for mitochondrial membrane potential assessment (red fluorescence), and DAPI for nuclear counterstaining (blue fluorescence).

Analysis of the fluorescence images for HUVECs (**Figures 4.50-4.52**) revealed no significant qualitative alterations in either ROS levels or mitochondrial activity patterns compared to untreated controls. The H_2-DCFDA signal intensity remained consistent across all treatment groups, suggesting stable oxidative stress conditions. Similarly, MitoSPY staining patterns showed no observable changes in mitochondrial morphology or distribution, indicating preserved mitochondrial function. Nuclear morphology, as visualized by DAPI staining, appeared normal in all samples, confirming maintenance of cellular integrity following treatment.

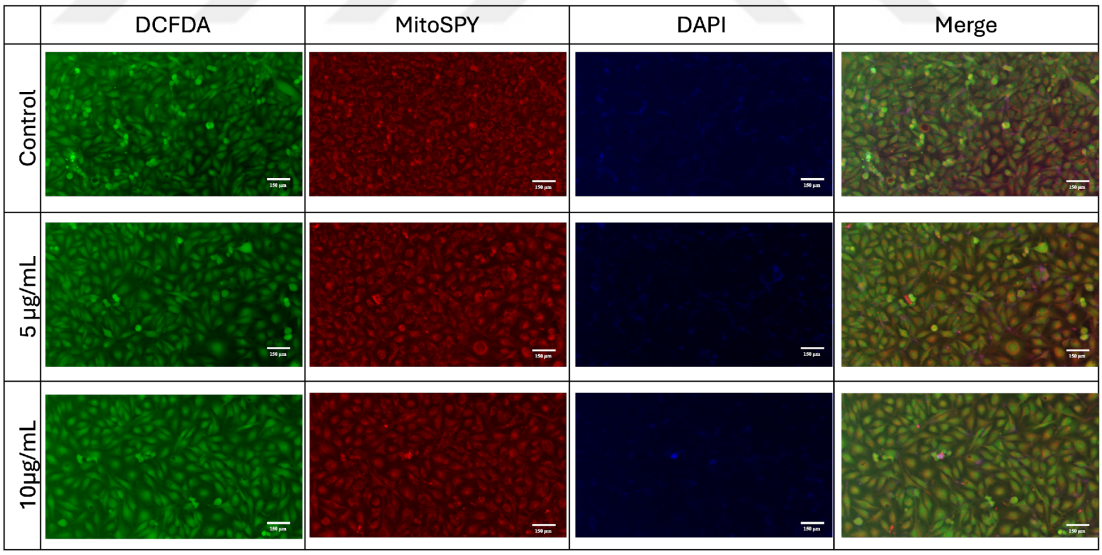


Figure 4.49: Fluorescence images of HUVEC after 5 and 10 µg/mL e-Nia application for 24 h. Control: non-treatment. The scale bar of the images was 150 µm.

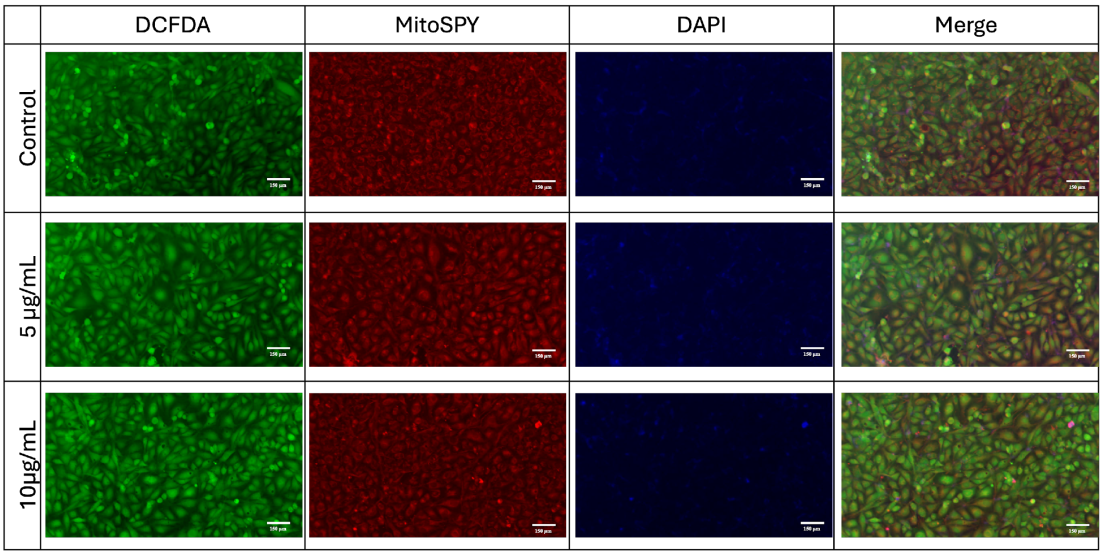


Figure 4.50: Fluorescence images of HUVEC after 5 and 10 µg/mL e-Tri application for 24 h. Control: non-treatment. The scale bar of the images was 150 µm.

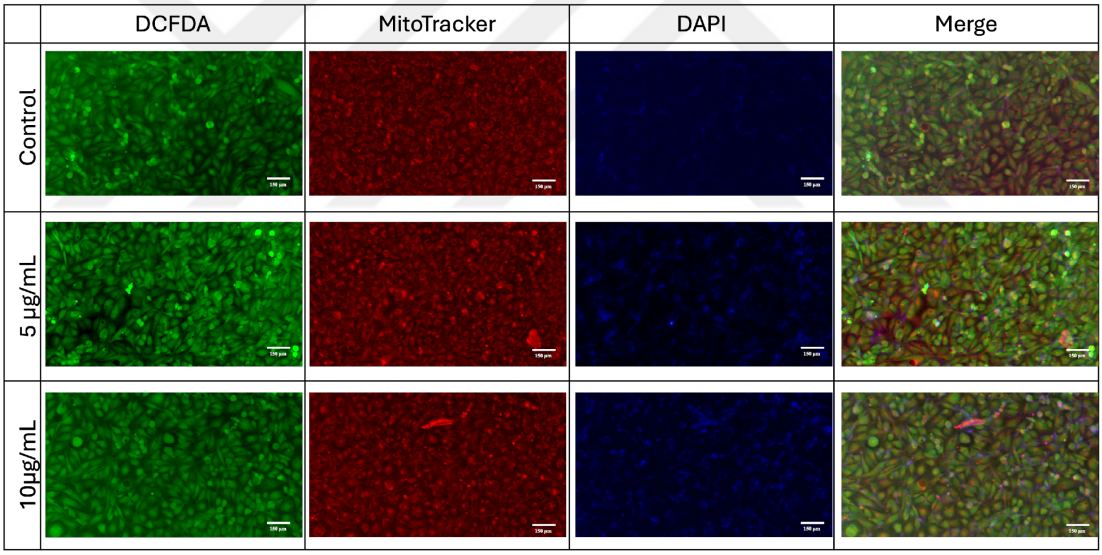


Figure 4.51: Fluorescence images of HUVEC after 5 and 10 µg/mL e-NiaTri application for 24 h. Control: non-treatment. The scale bar of the images was 150 µm.

Quantitative analysis of ROS levels of HUVEC cell lines after microparticles application for 24 h, the corrected total cell fluorescence (CTCF) analysis was analyzed with the following equation;

$$CTCF = ID - (Area\ of\ SC\ x\ Mean\ FB) \quad (4.1)$$

where ID is integrated density, SC is selected cells, and FB is fluorescence of background.

For each biological replicate, a minimum of 50 cells was analyzed using ImageJ software, with statistical significance determined by two-way ANOVA followed by Dunnett's multiple comparison test in GraphPad. The results demonstrated significant ROS reduction in several treatment groups, with e-Nia (5 µg/mL), e-Tri (10 µg/mL), and e-NiaTri (10 µg/mL) showing powerful effects ($p < 0.0001$), while e-NiaTri (5 µg/mL) also exhibited significant but less pronounced ROS reduction ($p < 0.01$) compared to untreated controls (**Figure 4.53**). These findings indicate that the microparticle formulations exhibit concentration-dependent antioxidant effects in vascular endothelial cells.

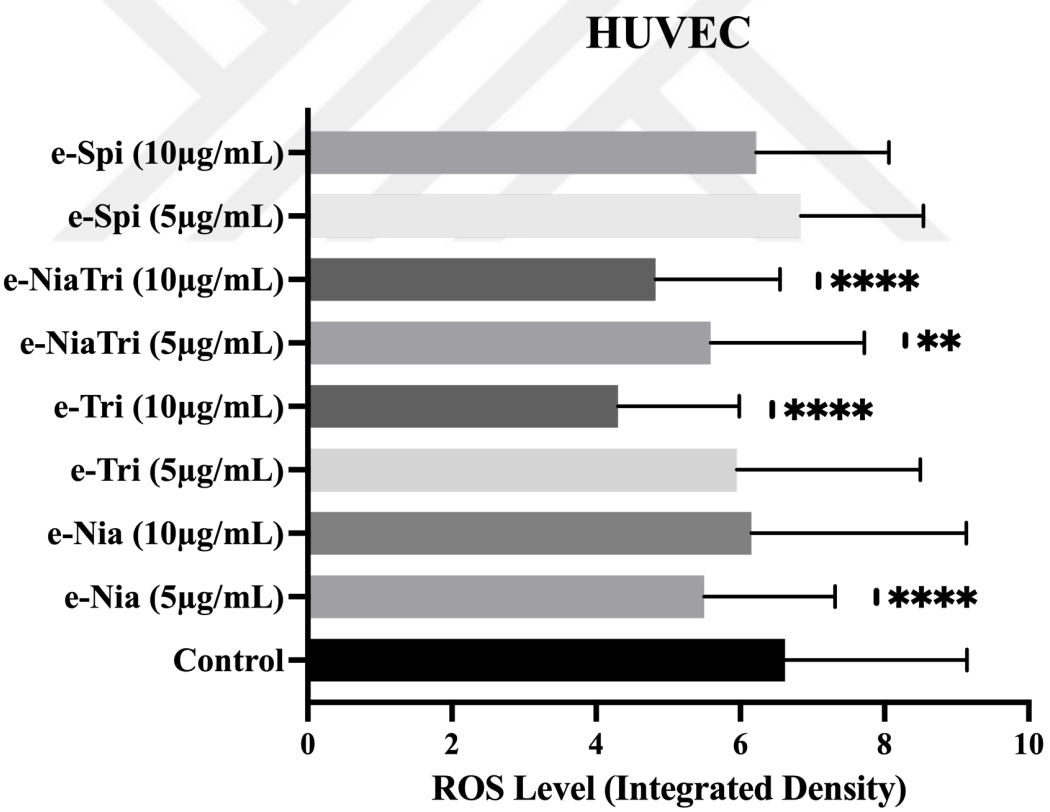


Figure 4.52: ROS intensity level of HUVEC cells, analyzed from 3 biological replicates of HUVEC cells after fluorescence imaging using ImageJ software. The statistical analysis was calculated using two-way ANOVA with Dunnett's comparison test. At least 50 cells were selected for ROS for each biological replicate. ns $p > 0.05$, **** $p < 0.0001$, *** $0.0001 \leq p < 0.001$, ** $0.001 \leq p < 0.01$, * $0.01 \leq p < 0.05$, comparison between treated groups and control group.

The cell survival test conducted on HaCaT cell lines demonstrated distinct proliferation patterns in response to different microparticle treatments (**Figure 4.54**). For e-Nia, cellular proliferation rates were generally similar between non-treated and treated cells; however, the 10 µg/mL dose induced a significant increase compared to the initial cell count ($p < 0.01$). Both the 5 µg/mL-treated group and the control showed significant proliferation after 72 hours relative to time 0 h ($p < 0.05$) (**Figure 4.54a**). A comparable trend emerged with e-Tri treatment, where 10 µg/mL caused a significant increase in proliferation compared to the control at 0 h ($p < 0.001$). Meanwhile, the control and 5 µg/mL groups also exhibited significant growth relative to their starting cell numbers ($p < 0.01$) (**Figure 4.54b**).

The co-encapsulated e-NiaTri formulation produced similar proliferation rates between the control and treated groups after 72 hours, although all conditions demonstrated significant increases compared to the initial cell counts ($p < 0.01$) (**Figure 4.54c**). Notably, the blank e-Spi microparticles themselves stimulated early proliferation at 10 µg/mL ($p < 0.05$ versus initial count), with this enhanced growth rate being maintained at significantly higher levels than both the control and 5 µg/mL treatment by 72 hours ($p < 0.001$) (**Figure 4.54d**).

These results collectively indicate that while higher concentrations (10 µg/mL) of e-Nia and e-Tri promoted greater cellular proliferation than lower doses, the combined e-NiaTri formulation maintained more consistent growth patterns. The significant proliferative effects observed with blank e-Spi microparticles suggest that the carrier system itself has inherent bioactivity. The concentration-dependent responses observed across treatments may have important implications for optimizing therapeutic applications of these microparticle systems.

Fluorescence imaging analysis of HaCaT keratinocytes following 24-hour treatment with biocompound-loaded microparticles (5 and 10 µg/mL) revealed consistent patterns of oxidative stress response and mitochondrial function. Qualitative evaluation demonstrated a noticeable reduction in intracellular ROS levels across all three microparticle formulations, as indicated by a decrease in H_2-DCFDA fluorescence intensity compared to untreated controls (**Figures 4.55-4.57**). This ROS attenuation occurred without any observable impairment of mitochondrial function, as evidenced by the maintenance of MitoSPY staining intensity and the characteristic

mitochondrial network morphology. The consistent preservation of mitochondrial integrity across both tested concentrations suggests that the observed antioxidant effects were achieved without compromising cellular bioenergetics. These findings indicate that the loaded microparticles may possess intrinsic ROS-scavenging properties while maintaining mitochondrial homeostasis in epidermal keratinocytes under the experimental conditions.

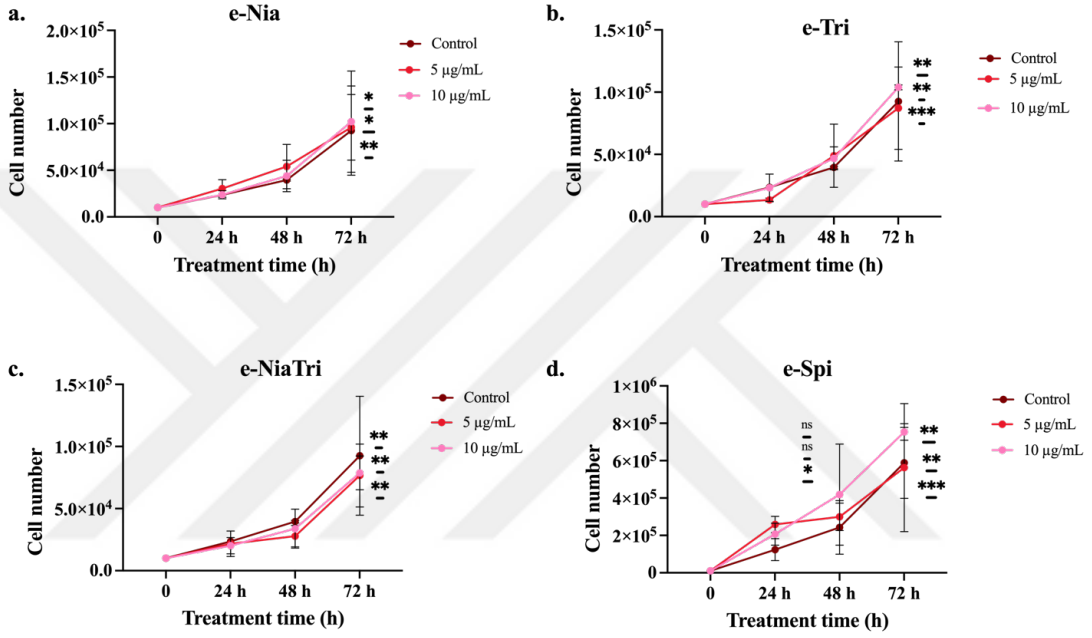


Figure 4.53: a. e-Nia, b. e-Tri, c. e-NiaTri, and d. e-Spi microparticle applied to HaCaT cell lines' cell survival results after two concentrations (5 and 10 µg/mL) applied for 24, 48, and 72 h. The results represent the average of two biological replicates, each with two technical replicates, along with the standard deviation. The analysis was conducted using GraphPad Prism 9.2.0 software with a two-way ANOVA followed by Dunnett's comparison test against the initial control. ns $p > 0.05$, **** $p < 0.0001$, *** $0.0001 \leq p < 0.001$, ** $0.001 \leq p < 0.01$, * $0.01 \leq p < 0.05$. # $0.01 \leq p < 0.05$, ## 0.001.

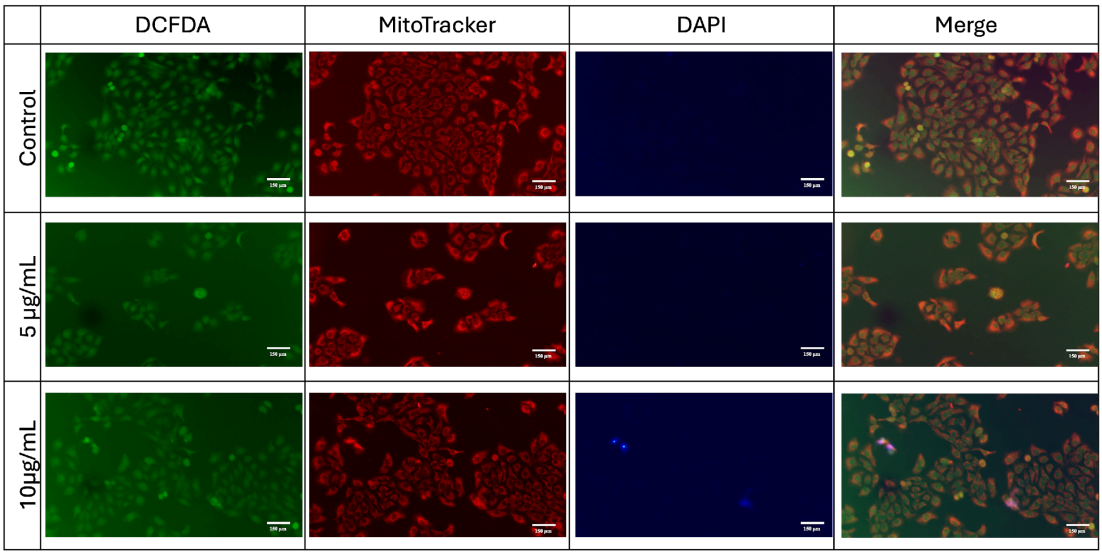


Figure 4.54: Fluorescence images of HaCaT after 5 and 10 µg/mL e-Nia application for 24 h. Control: non-treatment. The scale bar of the images was 150 µm.

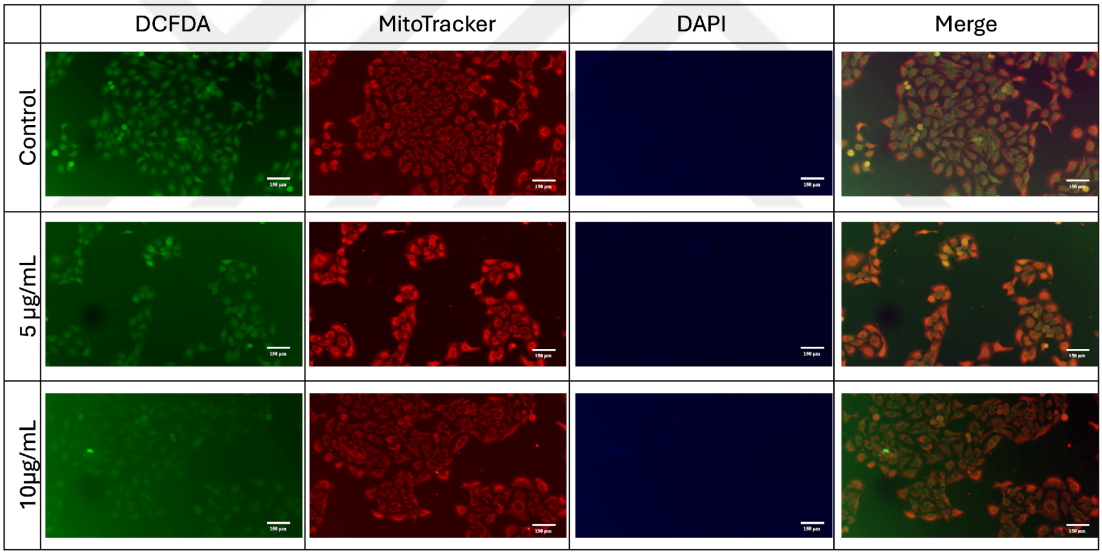


Figure 4.55: Fluorescence images of HaCaT after 5 and 10 µg/mL e-Tri application for 24 h. Control: non-treatment. The scale bar of the images was 150 µm.

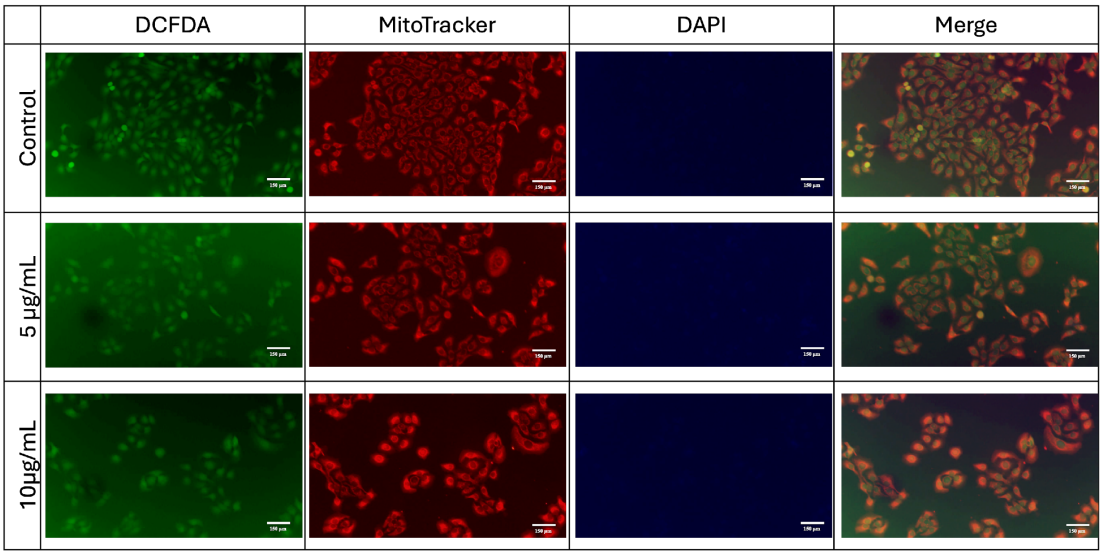


Figure 4.56: Fluorescence images of HaCaT after 5 and 10 µg/mL e-NiaTri application for 24 h. Control: non-treatment. The scale bar of the images was 150 µm.

Quantitative analysis of ROS levels in HaCaT cells was performed using the same methodology as for HUVECs. The results demonstrated a significant reduction in ROS levels following 24-hour treatment with e-Nia (5 and 10 µg/mL), e-Tri (5 and 10 µg/mL), and e-NiaTri (5 and 10 µg/mL) ($p < 0.0001$ for all concentrations). In contrast, e-Spi (blank microparticles) showed no significant effect on ROS levels ($p > 0.05$) (**Figure 4.58**). These findings confirm that the loaded biocompounds (niacinamide, tripeptide, and their combination) effectively attenuated oxidative stress in HaCaT cells. In contrast, the unloaded microparticle formulation (e-Spi) had no impact, suggesting that the ROS-scavenging activity was specifically attributable to the encapsulated bioactive compounds rather than the carrier system itself.

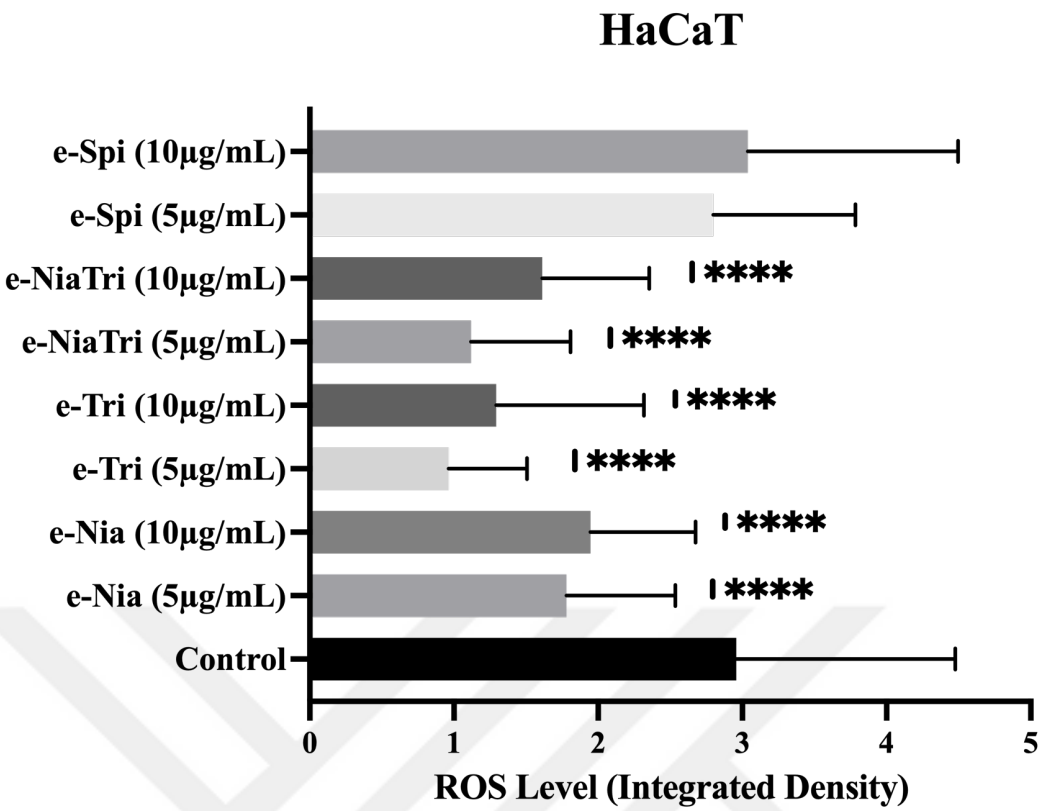


Figure 4.57: ROS level of HaCaT cells, analyzed from 3 biological replicates of HaCaT cells after fluorescence imaging using ImageJ software. The statistical analysis was calculated using two-way ANOVA with Dunnett's comparison test. For ROS expression, at least 50 cells were selected for a biological replication. ns $p > 0.05$, **** $p < 0.0001$, *** $0.0001 \leq p < 0.001$, ** $0.001 \leq p < 0.01$, * $0.01 \leq p < 0.05$, comparison between treated groups and control group.

4.3.3.3. Wound Healing Potential of Biocompound-loaded Microparticles

Niacinamide, pal-tripeptide-1, and both loaded microparticles' wound healing capacity were tested with HUVEC and HaCaT cell lines after scratching the surface of a 24-well plate with a 10 µL pipette tip in the shape of "+." After the wound model was established, the cell medium was replaced with 1x PBS to wash away cell debris, and the medium containing microparticles was then applied. The wound images were taken at various time points (0, 1, 2, 4, 6, 12, and 24 hours after application) in the same region using inverted light microscopy. The wound area was analyzed with ImageJ software's WoundHealing tool, following the procedure developed by Suarez-Arnedo et al. **(Suarez-Arnedo et al., 2020)**.

Due to the capability of migration and proliferation of HUVEC and HaCaT cell lines, the wound area was almost closed after 12 h for HUVEC cells and 24 h for HaCaT cells.

The wound healing potential of niacinamide (Nia) and pal-tripeptide-1 (Tri)-loaded microparticles was evaluated using an *in vitro* scratch assay. Both HUVEC and HaCaT cell lines demonstrated complete wound closure within 12 and 24 hours, respectively, highlighting their inherent capacity for migration and proliferation. In HUVEC cultures, treatment with 10 µg/mL e-Nia significantly accelerated wound closure compared to the initial wound area after 12 hours ($p < 0.05$), while control groups showed no significant reduction in wound size (**Figure 4.59a**). Similarly, both concentrations of e-Tri (5 and 10 µg/mL) promoted statistically significant wound closure compared to untreated controls at the 12-hour time point ($p < 0.05$) (**Figure 4.59b**). However, neither the dual-loaded e-NiaTri formulation nor blank e-Spi microparticles enhanced wound healing beyond control levels in HUVEC cells ($p > 0.05$) (**Figures 4.59c and d**).

For HaCaT keratinocytes, single-component formulations demonstrated notable effects on wound closure. Both concentrations of e-Nia significantly reduced the wound area after 24 hours of treatment ($p < 0.001$), showing slightly enhanced migration compared to control cells ($p < 0.01$), which exhibited natural wound closure (**Figure 4.60a**). The e-Tri formulation produced similar wound closure patterns to those of e-Nia in the HaCaT cell line. The wound closure after 24 hours was significantly reduced at both applied dosages ($p < 0.01$) (**Figure 4.60b**). Interestingly, while the combination e-NiaTri formulation showed no improvement over control conditions (**Figure 4.60c**), blank e-Spi microparticles unexpectedly promoted greater wound closure than untreated controls in HaCaT cells ($p < 0.01$ for 5 µg/mL, $p < 0.001$ for 10 µg/mL) (**Figure 4.60d**).

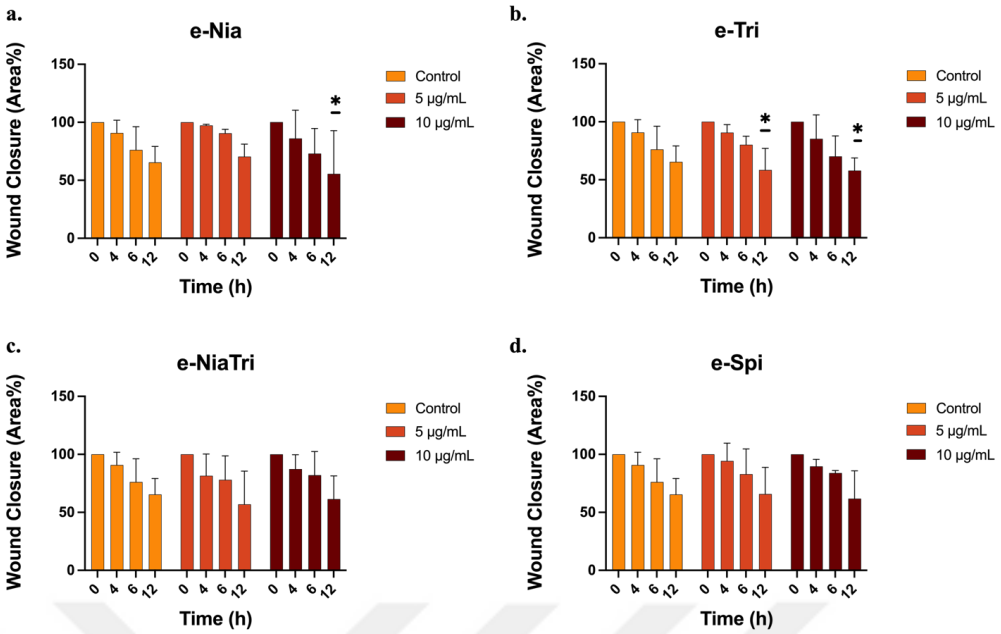


Figure 4.58: Wound healing analysis of HUVEC cells after applying 5 and 10 µg/mL of a. e-Nia, b. e-Tri, c. e-NiaTri, and d. e-Spi. The bars represent the average of two biological replicates, each containing two technical replicates, and the error bars indicate the the standard deviation of the replicates. A two-way ANOVA with Dunnett's multiple comparisons was used to analyze the differences between time zero and each time point for each treatment, ns $p > 0.05$, **** $p < 0.0001$, *** $0.0001 \leq p < 0.001$, ** $0.001 \leq p < 0.01$, * $0.01 \leq p < 0.05$.

These findings suggest that single-component microparticle formulations containing either Nia or Tri effectively promote wound healing in both endothelial and keratinocyte cell lines. The absence of an additive effect from the dual-loaded formulation indicates that combination therapy may require further optimization of component ratios or release kinetics. The observed activity of blank e-Spi microparticles in HaCaT cells merits additional investigation, as it implies that the carrier system itself may have intrinsic bioactive properties that affect keratinocyte migration. Collectively, these results provide valuable insights for developing optimized topical formulations for wound healing applications.

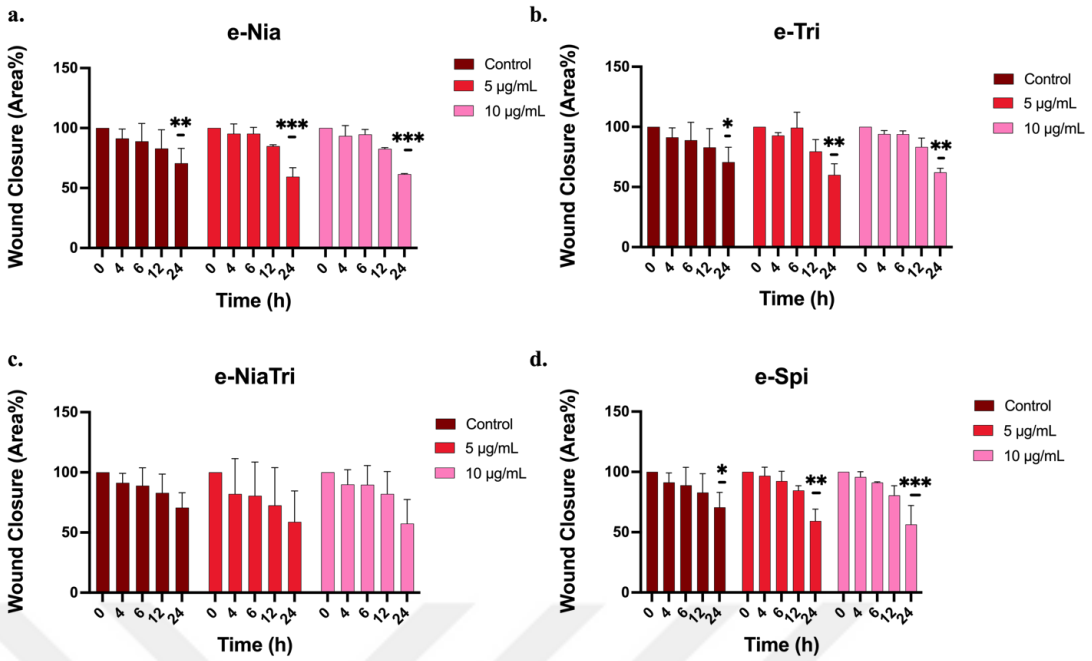


Figure 4.59: Wound healing analysis of HaCaT cells after applying 5 and 10 µg/mL of a. e-Nia, b. e-Tri, c. e-NiaTri, and d. e-Spi. The bars represent the average of two biological replicates, each containing two technical replicates, and the error bars indicate the standard deviation of the replicates. A two-way ANOVA with Dunnett's multiple comparisons was used to analyze the differences between time zero and each time point for each treatment, ns $p > 0.05$, **** $p < 0.0001$, *** $0.0001 \leq p < 0.001$, ** $0.001 \leq p < 0.01$, * $0.01 \leq p < 0.05$.

The wound healing effects of non-encapsulated niacinamide (Nia) and pal-tripeptide-1 (Tri) were evaluated in both endothelial and keratinocyte cell models. In HUVEC cells, free Nia at concentrations of 10 µM and 25 µM significantly facilitated wound closure compared to the initial wound dimensions ($p < 0.001$) (**Figure 4.61a**). However, the degree of closure was statistically similar to that achieved by untreated controls, suggesting that while Nia preserved normal endothelial migration capacity, it did not offer additional stimulation beyond the cells' inherent healing potential. Notably, neither concentration showed any adverse effects on cellular migration processes.

HaCaT keratinocytes exhibited a more pronounced response to Nia treatment. Exposure to 10 and 25 µM Nia significantly accelerated wound closure within 24 hours ($p < 0.01$) compared to untreated cultures ($p < 0.05$) (**Figure 4.61c**). Control groups eventually reached similar closure levels by 48 hours due to their natural migratory

activity, indicating that Nia primarily enhanced the kinetics rather than the final extent of keratinocyte migration.

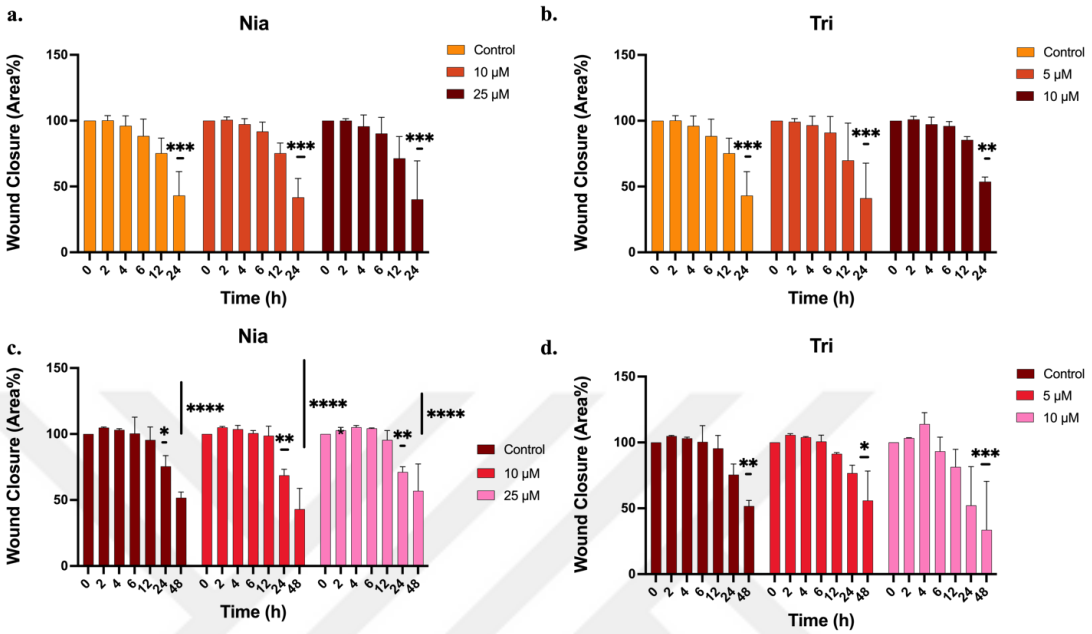


Figure 4.60: Wound healing analysis of a. Nia for HUVEC, b. Tri for HUVEC, c. Nia for HaCaT, and d. Tri for HaCaT. The bars represent the average of two biological replicates, each containing two technical replicates, and the error bars indicate the standard deviation of the replicates. A two-way ANOVA with Dunnett's multiple comparisons was used to analyze the differences between time zero and each time point for each treatment, ns $p > 0.05$, **** $p < 0.0001$, *** $0.0001 \leq p < 0.001$, ** $0.001 \leq p < 0.01$, * $0.01 \leq p < 0.05$.

The peptide Tri exhibited cell-type-specific activity patterns. In HUVECs, both 5 µM and 10 µM Tri treatments produced migration kinetics that closely paralleled those of the control groups, showing no additional pro-migratory benefit (**Figure 4.61b**). In contrast, HaCaT cells demonstrated concentration-dependent responses to Tri. The 10 µM treatment group significantly outperformed ($p < 0.001$) both the control group ($p < 0.01$) and those receiving 5 µM Tri ($p < 0.05$), establishing superior wound closure by the 48-hour endpoint (**Figure 4.61d**). These differential responses underscore the importance of considering cell-type specificity when evaluating potential wound-healing compounds.

4.3.3.4. Immunoblot Assay of Biocompound-Loaded Microparticles

After 24 hours of treatment, HUVEC cells displayed distinct alterations in AKT and Smad2/3 protein expression across the different conditions (**Figure 4.62**). Compared to the control, AKT levels were reduced in all extract-treated groups except for Tri, with the most pronounced decrease observed in the e-NiaTri group (0.35-fold), followed by e-Spi (0.51-fold), e-Tri (0.57-fold), and e-Nia and Nia (both at 0.67-fold). Notably, Tri treatment alone did not affect AKT expression, maintaining levels similar to the control. In contrast, Smad2/3 expression was upregulated in all treatment groups, with the highest increase in the Nia group (4.08-fold), followed by Tri (2.61-fold), e-Spi (2.19-fold), e-NiaTri (2.16-fold), e-Tri (2.14-fold), and e-Nia (1.67-fold). β-Actin expression remained consistent across all samples, confirming equal protein loading and validating the observed changes in AKT and Smad2/3 levels.

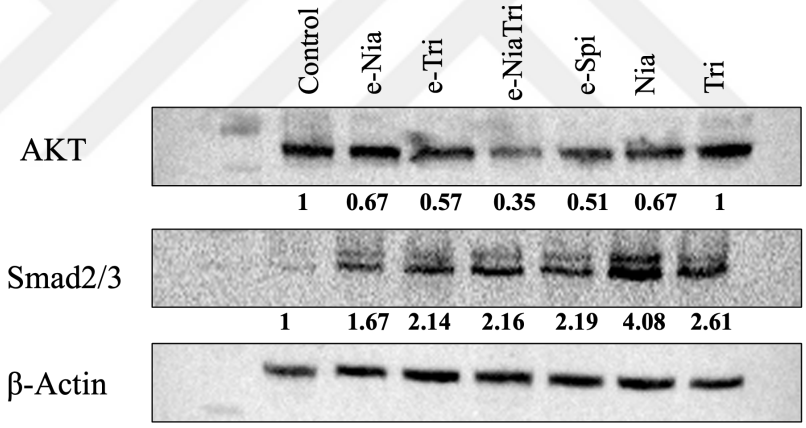


Figure 4.61: Representative Western blot analysis of AKT, Smad2/3, and β-Actin protein expression in HUVEC cells after 24-hour treatment with control, e-Nia (5 µg/mL), e-Tri (5 µg/mL), e-NiaTri (5 µg/mL), e-Spi (5 µg/mL), Nia (25 µM), and Tri (5 µM). Densitometric quantification of each protein band is shown below the blots, normalized to control (set as 1) used by Image J software. β-Actin was used as a loading control to confirm equal protein loading across samples.

HaCaT keratinocyte cells were treated for 24 hours with various compounds and extracts to evaluate their effects on AKT and Smad2/3 protein expression (**Figure 4.63**). The experimental conditions included control (untreated), e-Nia (5 µg/mL), e-Tri (5 µg/mL), e-NiaTri (5 µg/mL), e-Spi (5 µg/mL), Nia (25 µM), and Tri (5 µM).

AKT protein levels showed variable responses across treatment groups compared to control. Free niacinamide (Nia) demonstrated the highest upregulation at 1.56-fold, followed by encapsulated niacinamide (e-Nia) at 1.49-fold. The combination treatment e-NiaTri increased AKT expression to 1.23-fold, while e-Spi showed a modest increase to 1.10-fold. In contrast, both Tri treatments resulted in AKT downregulation, with e-Tri reducing levels to 0.88-fold and free Tri to 0.83-fold of control values. All treatment conditions resulted in upregulation of Smad2/3 protein expression. The encapsulated Spirulina extract (e-Spi) produced the most pronounced increase at 3.41-fold of control levels. e-Nia and the combination treatment (e-NiaTri) showed substantial increases at 2.44-fold and 2.18-fold, respectively. e-Tri elevated Smad2/3 levels to 1.93-fold, while the free compounds Tri and Nia showed more moderate increases at 1.43-fold and 1.33-fold, respectively.

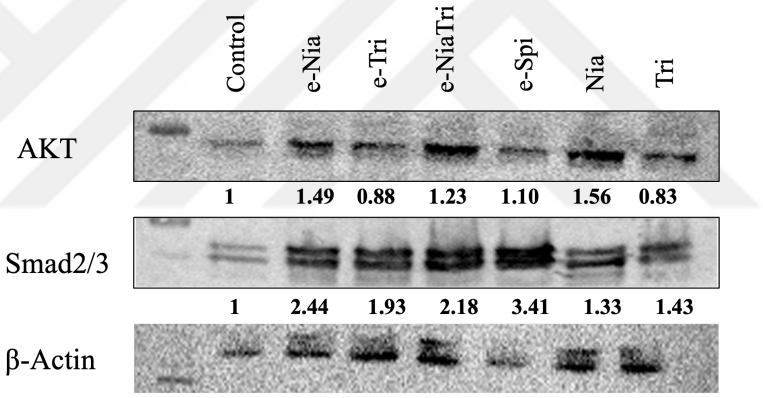


Figure 4.62: Representative Western blot analysis of AKT, Smad2/3, and β-Actin protein expression in HaCaT cells after 24-hour treatment with control, e-Nia (5 µg/mL), e-Tri (5 µg/mL), e-NiaTri (5 µg/mL), e-Spi (5 µg/mL), Nia (25 µM), and Tri (5 µM). Densitometric quantification of each protein band is shown below the blots, normalized to control (set as 1) used by Image J software. β-Actin was used as a loading control to confirm equal protein loading across samples.

The results demonstrate distinct cellular responses in HaCaT keratinocytes compared to endothelial cells, with Nia-containing treatments generally promoting AKT upregulation while Tri treatments reduced AKT expression. The Smad2/3 pathway showed consistent activation across all treatments, with encapsulated formulations generally producing more pronounced effects than their free counterparts, particularly evident with e-Spi treatment.

4.3.3.5. Cellular Experiments of Biocompound-Loaded Microparticles on UV-Induced Cell Lines

Nia and Tri are known for their preventive properties against the causes of photoaging; therefore, niacinamide and pal-tripeptide-1 were initially applied to HUVEC and cells to understand the cytotoxicity effects of these biomolecules on cell viability via MTT assay (**Figure 4.64**). For niacinamide, after UV application (1200 J), no statistical increase or decrease was observed compared to the control group in either cell line (**Figure 4.64a**). However, Tri application causes a reduction in both cell lines compared to the control group at 50 µM application ($p < 0.0001$) (**Figure 4.64b**).

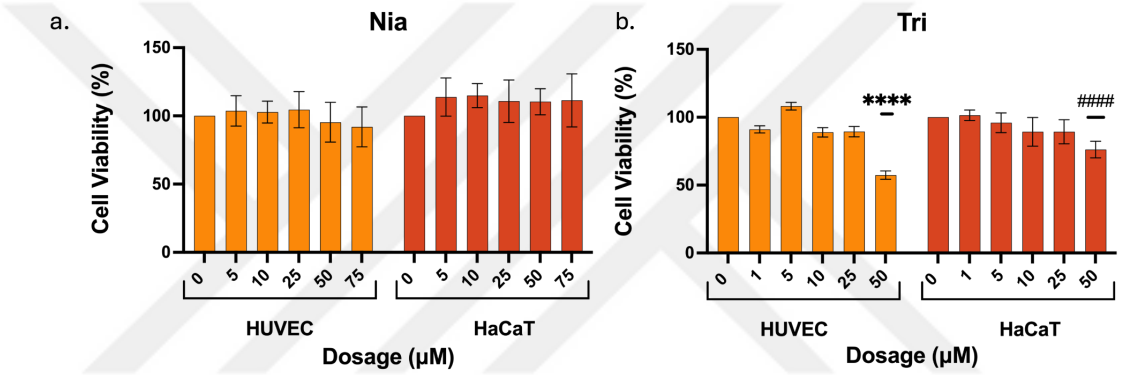


Figure 4.63: MTT assay results for 1200 J UV applied HUVEC and HaCaT cells before a. Nia (Nia, 5-75 µM) and b. Tri (Tri, 1-50 µM) affects the viability of HUVEC and HaCaT cells after 1200 J UV exposure and 24 h treatment. Data represent mean ± SD of ≥3 biological replicates (4 technical replicates each). Statistical analysis by two-way ANOVA with Dunnett's post-hoc test: ****$p < 0.0001$ (HUVEC), #### $p < 0.0001$ (HaCaT) vs untreated control; ns ($p > 0.05$).

Free Nia (10 and 25 µM) and Tri (5 and 10 µM) were applied to both cell lines for 72 h after 1200 J UV exposure (**Figure 4.65**). Nia treatment (25 µM) significantly increased cell number after 3 days of application in HUVECs ($p < 0.05$) (**Figure 4.65a**), while no change was detected in HaCaT cells (**Figure 4.65c**). The Tri application on HUVECs resulted in a significant increase at 5 µM at 72 h compared to the control ($p < 0.05$) (**Figure 4.65b**). However, Tri caused a toxic effect on HaCaT cell lines after 72 h of application at 10 µM (**Figure 4.65d**), while no effect was observed at 5 µM.

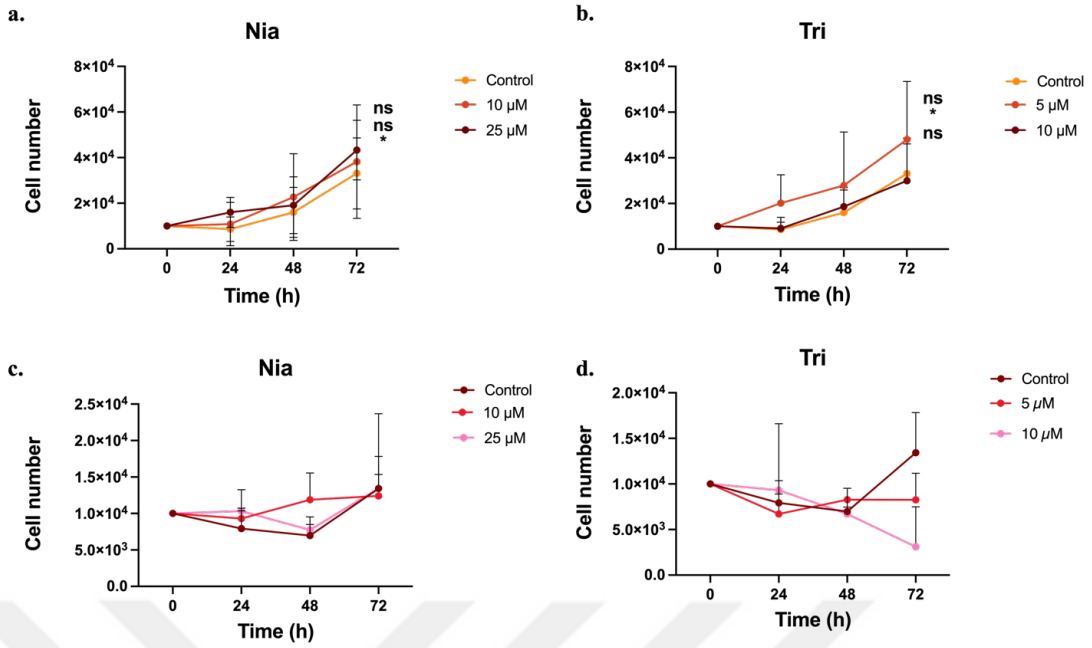


Figure 4.64: Cell survival assay results for HUVEC, a. Nia, and b. Tri and HaCaT cells c. Nia and d. Tri application for 24 h after 1200 J UV induction. Data represent mean ± SD of three independent biological replicates (two technical replicates each). Statistical analysis was performed using two-way ANOVA with Dunnett's post-hoc test: ns $p > 0.05$, **** $p < 0.0001$, *** $0.0001 \leq p < 0.001$, ** $0.001 \leq p < 0.01$, * $0.01 \leq p < 0.05$. # $0.01 \leq p < 0.05$, ## $0.001 \leq p < 0.01$, ### $p < 0.001$ comparison between each time point's control group.

After exposure to 1200 J of UV radiation, HUVEC and HaCaT cells were treated with biocompound-loaded microparticles for 24 hours. Treatment with e-Nia (0.5–25 µg/mL) resulted in a slight yet consistent increase in viability in HUVECs at all tested concentrations ($p > 0.05$). In contrast, the viability of HaCaT cells remained unchanged compared to untreated controls (**Figure 4.66a**). e-Tri had a more significant effect on HUVECs, with 1 µg/mL significantly increasing viability ($p < 0.05$ vs. control), although higher concentrations did not further enhance this effect. Similar to e-Nia, e-Tri did not affect the viability of HaCaT cells (**Figure 4.66b**). The dual-loaded e-NiaTri formulation displayed additive activity, moderately enhancing viability in both cell lines at concentrations of 5–10 µg/mL (**Figure 4.66c**). Blank e-Spi particles provided comparable cytoprotection to drug-loaded formulations, underscoring their inherent bioactivity and biocompatibility (**Figure 4.66d**).

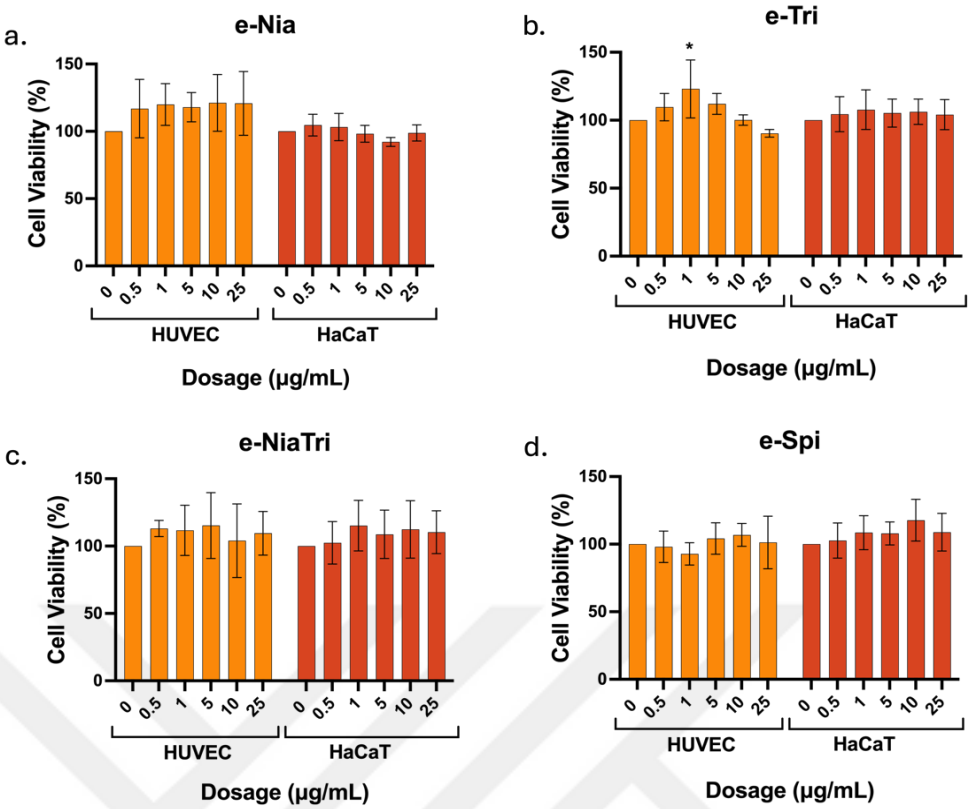


Figure 4.65: MTT assay results showing cell viability of a. e-Nia (0.5-25 µg/mL), b. e-Tri (0.5-25 µg/mL), c. e-NiaTri (0.5-25 µg/mL), and d. e-Spi (0.5-25 µg/mL) treated HUVEC and HaCaT cells following 1200 J UV irradiation and 24 h incubation. Data represent mean ± SD of three independent biological replicates (four technical replicates each). Statistical analysis was performed using two-way ANOVA with Dunnett's post-hoc test (*$p < 0.05$ *vs* untreated control; ns = not significant $p > 0.05$).

Following the MTT assay, the optimized dosages were also confirmed as 5 and 10 µg/mL for all microparticles in 72 h cell survival experiments, due to the moderate effect observed at these dosages (**Figures 4.67 and 4.68**). After UV exposure, e-Nia was applied to both cell lines at these two concentrations. Like other microparticles, the results indicated that cell proliferation was enhanced after 72 h of application at both 5 and 10 µg/mL, significantly compared with the control at day 0 for HUVECs ($p < 0.0001$ for 5 and 10 µg/mL e-Nia, $p < 0.01$ for control) (**Figure 4.67a**). For HaCaT cells, the significance of cell number was observed at 72 h for only 10 µg/mL ($p < 0.05$) (**Figure 4.68a**). For e-Tri, 48 h results showed that cell proliferation was enhanced with a 10 µg/mL application on HUVECs ($p < 0.05$), while at 72 h, the 5 µg/mL e-Tri increased cell number more ($p < 0.0001$) than both the control and 10

µg/mL ($p < 0.001$) (**Figure 4.67b**). In HaCaT cells, no statistically significant enhancement in cell numbers was observed in either the e-Tri-treated or control groups for all applied periods ($p > 0.05$) (**Figure 4.67b**). The dual-loaded e-NiaTri application on 5 µg/mL slightly enhanced the cell proliferation rate compared to the control at 72 h ($p < 0.001$). However, there were significant increases compared to day 0 for both the 10 µg/mL applied and control groups of HUVECs ($p < 0.01$) (**Figure 4.67c**). Moreover, e-Spi significantly increased the cell number at the applied dosages after 3 days, following the same trend as the control ($p < 0.01$) (**Figure 4.67d**). For HaCaT cell lines, no effectiveness was observed after e-NiaTri application ($p > 0.05$) (**Figure 4.68c**), similar to e-Spi ($p > 0.05$) (**Figure 4.68d**).

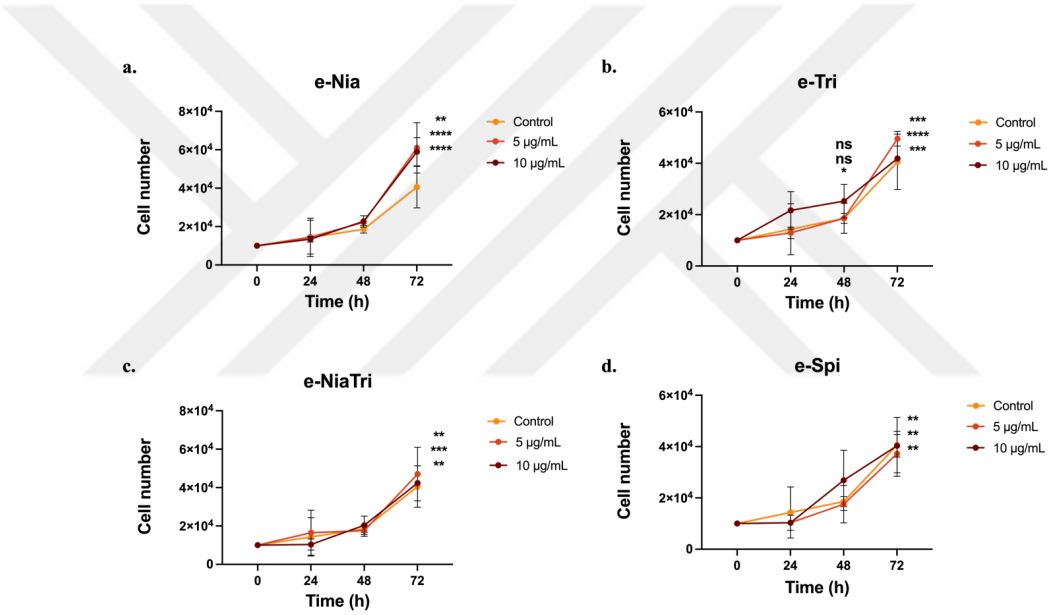


Figure 4.66: Cell survival assay results for a. e-Nia (5 and 10 µg/ml), b. e-Tri 5 and 10 µg/mL), c. e-NiaTri (5 and 10 µg/ml), and d. e-Spi (5 and 10 µg/ml) treated HUVECs following 1200 J UV irradiation and 24 h incubation. Data represent mean ± SD of three independent two biological replicates (two technical replicates each). Statistical analysis was performed using two-way ANOVA with Dunnett's post-hoc test (ns $p > 0.05$, **** $p < 0.0001$, *** $0.0001 \leq p < 0.001$, ** $0.001 \leq p < 0.01$, * $0.01 \leq p < 0.05$. # $0.01 \leq p < 0.05$, ## $0.001 \leq p < 0.01$, ### $p < 0.001$ comparison between each time point's control group).

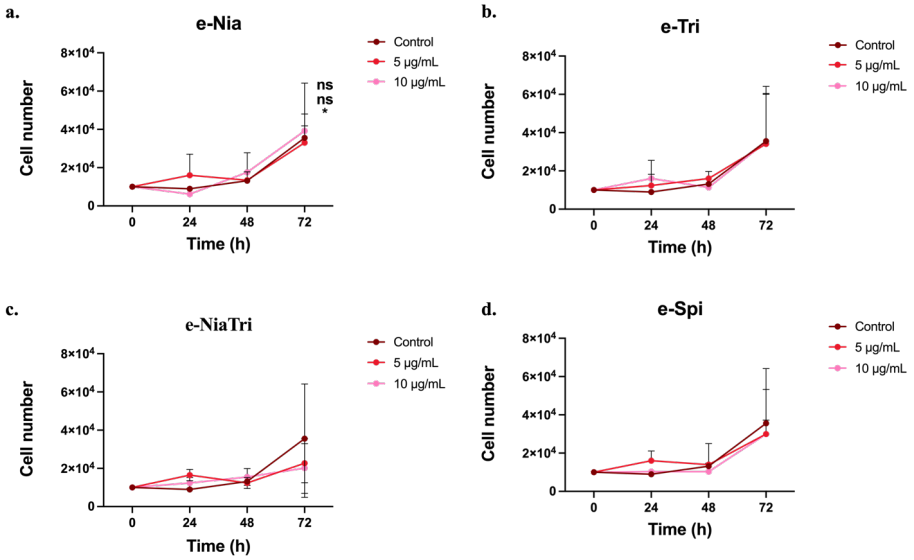


Figure 4.67: Cell survival assay results for a. e-Nia (5 and 10 µg/ml), b. e-Tri 5 and 10 µg/mL), c. e-NiaTri (5 and 10 µg/ml), and d. e-Spi (5 and 10 µg/ml) treated HaCaT following 1200 J UV irradiation and 24 h incubation. Data represent mean ± SD of three independent two biological replicates (two technical replicates each). Statistical analysis was performed using two-way ANOVA with Dunnett's post-hoc test (ns $p > 0.05$, **** $p < 0.0001$, *** $0.0001 \leq p < 0.001$, ** $0.001 \leq p < 0.01$, * $0.01 \leq p < 0.05$. # $0.01 \leq p < 0.05$, ## $0.001 \leq p < 0.01$, ### $p < 0.001$ comparison between each time point's control group).

5. DISCUSSION

This study presents a novel microcarrier system based on PLA/Spirulina composite microparticles, demonstrating unprecedented versatility in encapsulating both hydrophilic (niacinamide) and amphiphilic (palmitoyl tripeptide-1) bioactive compounds without compromising their structural integrity or biological activity. The developed platform overcomes a critical challenge in dermal delivery by simultaneously accommodating compounds with divergent solubility profiles while significantly enhancing their therapeutic efficacy at remarkably reduced dosages. Through advanced electrospraying techniques and optimized formulation parameters, we achieved a breakthrough in co-delivery efficiency, where the encapsulated actives not only maintain their native bioactivity but also exhibit additive effects at concentrations orders of magnitude lower than those required for free compounds. The system's unique capacity to preserve and amplify the pharmacological properties of diverse molecular structures, from water-soluble vitamins to lipid-modified peptides, represents a significant advancement in multifunctional carrier design. This dual-loading capability, combined with Spirulina's intrinsic antioxidant properties, creates a comprehensive anti-photoaging strategy that targets oxidative stress and extracellular matrix remodeling through a single, precisely controlled delivery vehicle. The microcarrier's ability to achieve enhanced biological effects at ultralow doses addresses both efficacy and safety concerns in chronic dermatological applications, establishing a new paradigm for sustainable, high-performance cosmeceutical formulations.

This innovation is further enhanced by the strategic use of Spirulina, whose intrinsic properties have been optimized through controlled cultivation conditions to maximize its nutritional and functional benefits. The mineral composition of Spirulina is known to be highly dependent on cultivation conditions, and the results presented in **Table 4.1** demonstrate that optimizing the Zarrouk’s medium leads to significant improvements in both the nutritional and safety profiles of the biomass. This observation is consistent with previous studies, which have shown that nutrient-rich and carefully balanced media can promote higher growth rates and yields in Spirulina

cultures, thereby enhancing their commercial viability **(Kumar et al., 2011)**. The elevated levels of essential minerals such as calcium, sodium, magnesium, boron, and potassium observed in the optimized Spirulina are in agreement with literature reports, which highlight Spirulina as a rich source of these elements. For instance, Becker (2007) reported that Spirulina typically contains potassium (1400–1600 mg/100 g), calcium (700–1500 mg/100 g), sodium (250–900 mg/100 g), and magnesium (370–400 mg/100 g), concentrations that are considerably higher than those found in many staple foods **(E. W. Becker, 2007)**. The nutritional significance of these minerals is well established, as they play a crucial role in maintaining bone health, supporting cardiovascular function, and regulating overall physiological processes **(Capelli & Cysewski, 2010)**.

In addition to the enrichment of beneficial minerals, the reduction in potentially harmful elements such as aluminum, zinc, and copper, as seen in **Table 4.1**, is a noteworthy safety advantage. Since Spirulina can accumulate trace elements from its environment, the composition of the growth medium and cultivation practices play a critical role in determining the final content of both beneficial and undesirable minerals. Studies have shown that Spirulina grown under controlled or organic conditions generally contains low levels of heavy metals, and that careful monitoring of production can further minimize the presence of these elements **(Khan et al., 2005)**. A low level of undesirable minerals, combined with high levels of beneficial minerals, supports the safety of the optimized biomass for nutritional and therapeutic use.

The nutritional significance of minerals found in Spirulina is well established, as they play a crucial role in maintaining bone health, supporting cardiovascular function, and regulating overall physiological processes. For example, calcium and magnesium are essential for bone mineralization and structural integrity, while potassium and sodium are vital electrolytes that help regulate fluid balance, nerve transmission, and muscle contraction. Besides these benefits, Spirulina's exceptional nutritional profile translates into a wide range of benefits for skin health, making it a valuable ingredient in both dietary and topical skincare applications. Rich in proteins, all essential amino acids, vitamins (notably A, B-complex, C, and E), and minerals such as iron and zinc, Spirulina provides the building blocks necessary for cellular regeneration and tissue repair, which are fundamental processes for maintaining healthy, resilient skin **(Ikeda et al., 2022; Ragusa et al., 2021)**. Its high content of antioxidants—including

phycocyanin, beta-carotene, vitamin E, and superoxide dismutase—plays a critical role in neutralizing free radicals, thereby protecting skin cells from oxidative stress and environmental damage that accelerate aging **(Ikeda et al., 2022)**.

Scientific studies have demonstrated that Spirulina and its bioactive compounds can stimulate the proliferation of dermal fibroblasts and keratinocytes, enhance extracellular matrix and collagen production, and exert decisive anti-inflammatory and photoprotective actions **(Ikeda et al., 2022; P. Liu et al., 2020)**. These properties contribute to improved skin elasticity, reduced appearance of fine lines and wrinkles, and better wound healing outcomes. The anti-inflammatory effects, primarily attributed to phycocyanin and essential fatty acids like gamma-linolenic acid, help soothe redness and irritation, making Spirulina especially beneficial for individuals with sensitive, dry, or problematic skin, including those affected by acne, eczema, or psoriasis **(P. Liu et al., 2019, 2020; Syarina et al., 2015)**.

Collectively, the scientific and clinical evidence underscores Spirulina's multi-faceted role in skin care, from anti-aging and photoprotection to hydration, soothing, and detoxification. Its rich nutritional value not only supports systemic health when consumed as a supplement but also delivers targeted benefits when incorporated into skincare formulations, highlighting its promise as a natural, multifunctional ingredient for maintaining and enhancing skin health **(Ikeda et al., 2022; Ragusa et al., 2021)**.

Building on this broad spectrum of skin-related benefits, the present cellular studies further reinforce Spirulina's versatility by demonstrating its favorable effects on cell viability and proliferation in both endothelial and keratinocyte models. These findings not only confirm the safety and compatibility of various Spirulina extracts with skin-relevant cell types but also suggest that the bioactive compounds present, particularly those enriched in the ethanol extract, can actively support cellular health, regeneration, and resilience. Thus, the observed results provide additional mechanistic insight and experimental validation for Spirulina's growing reputation as a multifunctional ingredient in advanced skin care and biomedical applications.

The effects of Spirulina extracts (water, 70% ethanol, and biomass) on HUVEC and HaCaT cell lines, as detailed in the results, align with and expand upon broader literature findings that underscore Spirulina's multifaceted bioactivity across diverse cell types and applications. While the biomass and aqueous extracts exhibited no

cytotoxicity and enhanced proliferation in endothelial and keratinocyte cells—consistent with Spirulina's GRAS designation—the 70% ethanol extract demonstrated unique dose- and time-dependent effects, including improved viability at moderate concentrations (25–50 μg/mL) (**Figures 4.5a, 4.5c**) and reduced colony formation at higher doses (75 μg/mL) in HUVECs (**Figures 4.1b, 4.5b**). These observations align with studies on other cell lines, where Spirulina extracts exhibit selective bioactivity that depends on solvent polarity, extraction efficiency, and the target cell's physiology.

For instance, Spirulina ethanol extracts have demonstrated enhanced anti-inflammatory effects in LPS-induced microglia (BV-2 cells), significantly suppressing TNF-α, IL-6, and IL-1β production. Notably, ultrasonically processed ethanol extracts exhibit double the anti-inflammatory potency of conventional ethanol extracts, likely due to higher chlorophyll retention **(Choi et al., 2019)**. Similarly, in cancer cell lines, ethanol extracts of *Spirulina platensis* exhibit selective cytotoxicity, reducing viability by more than 50% in gastric (AGS) and chronic myelogenous leukemia (K562) cells, while sparing healthy cells **(Flores Hernandez et al., 2017)**. This aligns with the observed proliferative effects in HUVEC/HaCaT cells at lower ethanol extract doses (10–25 μg/mL) (**Figures 4.5c, 4.6c**) and contrasts with the cytotoxic effects at higher concentrations, suggesting a therapeutic window where Spirulina supports healthy cell function while targeting malignant cells.

Spirulina's immunomodulatory properties further extend to stem cell regulation. In bone marrow and CD34+ stem cells, Spirulina extracts increase mitochondrial respiration and proliferation, synergizing with formulations like NT-020 (blueberry/green tea extracts) to enhance repair mechanisms **(Bachstetter et al., 2010)**. This parallels the improved colony formation in HaCaT cells treated with 25 μg/mL ethanol extract (**Figure 4.6b**), indicating Spirulina's potential to support regenerative processes in both epithelial and mesenchymal lineages. Additionally, Spirulina protein hydrolysates modulate immune responses by enhancing phagocytic activity and cytokine production, as seen in murine models where oral Spirulina administration counteracts LPS-induced declines in neural stem cell proliferation **(Akao et al., 2009)**.

The ethanol extract's efficacy in the current study may stem from its enriched lipid-soluble bioactive compounds, such as flavonoids, which are poorly extracted in

aqueous preparations. Ultrasonic-assisted ethanol extraction, for example, yields Spirulina extracts with 2.8× higher chlorophyll content than conventional methods, correlating with more potent anti-inflammatory and antioxidant effects **(Choi et al., 2019)**. These compounds inhibit NF-κB and COX-2 pathways, reducing pro-inflammatory mediators in microglia and protecting keratinocytes from UVB-induced oxidative stress **(Jang & Kim, 2021)**. In HaCaT cells, Spirulina-derived C-phycocyanin (C-PC) mitigates UVB damage by scavenging ROS, preserving skin barrier proteins (filaggrin, involucrin), and suppressing MMP-1/MMP-9 expression, which prevents collagen degradation **(Jang & Kim, 2021)**.

Notably, Spirulina's dual role—promoting healthy cell proliferation while exerting anticancer effects—is evident across models. In human dermal fibroblasts (HDFs), aqueous extracts (50 μg/mL) enhance migration and wound closure, comparable to allantoin, without cytotoxicity **(Syarina et al., 2015)** (**Figure 4.2c**). Conversely, in melanoma (B16D8) and leukemia (K562) cells, ethanol extracts induce apoptosis via ROS-mediated pathways **(Flores Hernandez et al., 2017)**. This dichotomy highlights the context-dependent bioactivity of Spirulina, where composition and concentration determine the outcomes.

In summary, the proliferative and non-cytotoxic effects of Spirulina extract on HUVEC/HaCaT cells (**Figures 4.1–4.6**) are part of a broader therapeutic profile validated in diverse models, including anti-inflammatory (microglia), regenerative (stem cells), anticancer (leukemia/gastric), and dermatoprotective (keratinocytes) systems. The 70% ethanol extract's superior performance, attributed to its lipid-soluble actives (flavonoids), highlights its potential for further studies during the thesis. These findings collectively position Spirulina as a versatile, multi-modal agent in biomedicine, capable of addressing inflammation, oxidative stress, and tissue repair across cell types.

To enhance the delivery and therapeutic efficacy of Spirulina's bioactive compounds, polylactic acid (PLA)—a biodegradable, biocompatible polymer widely used in drug delivery—serves as an ideal encapsulation matrix. PLA-based microparticles improve the stability, controlled release, and bioavailability of Spirulina's flavonoids while protecting them from degradation. This is particularly critical for hydrophobic antioxidants, as demonstrated by Stoyanova et al., where PLA-based nanofibers

significantly enhanced the sustained release and anti-inflammatory effects of quercetin, a flavonoid with similar solubility limitations to Spirulina's lipophilic components **(Stoyanova et al., 2025)**.

The transition to PLA/Spirulina microparticle production represents a strategic approach to improve targeted delivery and therapeutic efficiency. The encapsulation of the 70% ethanol Spirulina extract, rich in antioxidants and anti-inflammatory agents, is supported by multiple studies on polymer-based delivery systems. For example, Varga et al. showed that core-shell PLA/PLGA nanoparticles significantly improved the stability and prolonged release of vitamin E, a lipid-soluble antioxidant structurally similar to Spirulina's tocopherols **(Varga et al., 2019)**. This confirms that PLA encapsulation can effectively protect and deliver hydrophobic bioactive compounds. Further evidence comes from Guo et al., who demonstrated that modified PEG-PLA nanoparticles enhanced resveratrol's bioavailability and anti-inflammatory effects in both *in vitro* and *in vivo* models **(W. Guo et al., 2013)**. Collectively, these studies in the literature validate PLA as a versatile platform for optimizing Spirulina's regenerative, anti-inflammatory, and dermatoprotective applications.

Building on these established principles, the solution optimization of PLA/Spirulina-based (**Table 4.2**) indicate that all PLA/Spirulina formulations (3% PLA [M0], 0.125% Spi + M0 [M1], 0.25% Spi + M0 [M2], and 0.5% Spi + M0 [M3]) maintained consistent density and exhibited increasing viscosity and surface tension with higher Spirulina content, parameters that are critical for reproducible electrospraying and uniform particle formation. These findings are consistent with previous research on electrospraying of both PLA-based and other polymer or bioactive systems, which emphasizes the critical role of solution viscosity in the process. Viscosity directly influences the formation and stability of the Taylor cone—a conical meniscus that develops at the tip of the needle under an applied electric field and is essential for generating uniform droplets or particles during electrospraying **(Fernández de la Mora, 2007; Kim et al., 2021; Rosell-Llompart et al., 2018)**.

Literature shows that if the viscosity is too low, the solution lacks sufficient polymer chain entanglement, leading to dripping or the formation of irregular, non-uniform particles, rather than a stable jet and reproducible microparticles **(Jiamian Wang et al., 2019)**. Conversely, excessively high viscosity can hinder jet formation, sometimes

resulting in fiber formation (as in electrospinning) or even clogging the needle, which disrupts the Taylor cone and the entire electrospraying process **(Bock et al., 2012)**. Studies by Kim et al. have demonstrated that, in the cone-jet mode, droplet size increases linearly with viscosity and flow rate, and the stability window for the Taylor cone broadens with higher viscosity, allowing for more controlled and monodisperse particle production **(Kim et al., 2021)**.

The ability to maintain a stable Taylor cone is not only fundamental for achieving uniform particle size and morphology but also for ensuring high encapsulation efficiency and reproducibility, which are especially important for biomedical applications where batch-to-batch consistency is required **(Jiamian Wang et al., 2019)**. The solution parameters observed in **Table 4.2**—where viscosity increases with higher Spirulina content—are in line with these principles, ensuring that the system remains within the optimal window for stable Taylor cone formation and efficient electrospraying. The optimization of PLA/Spirulina solutions for electrospraying (**Table 4.2**) not only ensures the stability and bioactivity of encapsulated Spirulina extracts but also leverages the process advantages of electrospraying to maximize therapeutic efficacy. By integrating the superior performance of the 70% ethanol extract with the protective and customizable properties of PLA microparticles, this approach advances the development of multifunctional delivery systems capable of addressing a wide range of biomedical challenges, including oxidative stress, inflammation, and tissue repair.

These formulation principles were directly validated in the production and characterization of PLA/Spirulina microparticles via electrospraying revealed the critical interplay between solution properties, process parameters, and bioactive delivery efficacy. The first set of optimization experiments (**Figures 4.7–4.10**) revealed that increasing Spirulina content (1-M0 to 1-M3) resulted in larger microparticle diameters. This phenomenon aligns with established electrospray encapsulation principles, as demonstrated by Xu and Hanna for BSA-loaded PLA systems, where increasing the protein-to-polymer ratio similarly led to larger particle diameters (0.84-3.95 μm) due to elevated solution viscosity **(Y. Xu & Hanna, 2008)**. These findings are further supported by the comprehensive study of Xu and Hanna (2006), which systematically established higher bioactive payloads increase solution viscosity and droplet size during electrospraying, optimal polymer concentrations are

crucial for maintaining particle sphericity and monodispersity, and encapsulation efficiency shows a non-linear relationship with initial loading concentrations **(Y. Xu & Hanna, 2006)**. Together, these studies confirm that our observed size trends with Spirulina loading reflect fundamental electrohydrodynamic principles governing the encapsulation of bioactive compounds in polymeric matrices.

Extending beyond formulation parameters, the impact of hardware configuration was equally evident in this thesis, where reducing the nozzle diameter from 0.65 mm to 0.4 mm led to a substantial decrease in particle diameter for Spirulina-loaded formulations (**Figures 4.11b, e, h, k**). This observation is corroborated by Wang et al.'s comprehensive review of electrospray technology, which emphasizes that smaller nozzle diameters - when combined with optimized flow rates - consistently yield smaller, more uniform particles through enhanced jet stability and finer droplet formation **(Jiamian Wang et al., 2019)**. Also, FT-IR analysis confirmed the chemical integrity of PLA in all formulations, with characteristic peaks for C=O and C-O bonds, and spectral shifts indicating successful incorporation of Spirulina, a result that mirrors the interaction observed in curcumin-loaded PLA nanoparticles, where peak shifts in FT-IR spectra confirmed drug-polymer interactions and successful encapsulation **(Rachmawati et al., 2016)**.

The release profile and encapsulation characteristics of the Spirulina-loaded PLA system further demonstrate its alignment with established polymeric delivery systems. The release studies showed a burst release pattern (within 6 hours, **Figure 4.13c**) and loading capacities reaching approximately 50% of theoretical values (**Figure 4.14**). These findings fit within the spectrum of behaviors reported for similar PLA-based encapsulation systems. Xu and Hanna, 2006 in their study of water-soluble protein encapsulation with PLA observed that burst release intensity directly correlated with initial loading concentrations, while encapsulation efficiency showed an inverse relationship - mirroring the observed trade-off between loading and release kinetics **(Y. Xu & Hanna, 2006)**. Cardoso et al. demonstrated in cardanol-loaded PLA microparticles that natural hydrophobic compounds exhibit pronounced burst effects (80% release within 15 minutes) followed by sustained release, with encapsulation efficiency improving at higher additive concentrations - a pattern remarkably similar to the Spirulina system **(Cardoso et al., 2018)**. Rachmawati et al.'s curcumin-loaded PLA nanoparticles showed a comparable biphasic release profile (40% initial burst

followed by sustained release) **(Rachmawati et al., 2016)**. Notably, our DLS versus SEM comparisons confirmed previous reports about the limitations of DLS for hydrophobic PLA systems, reinforcing SEM as the gold standard for accurate particle sizing in such delivery systems.

Collectively, microparticle production and characterization findings indicate that the electrospraying process used for PLA/Spirulina microparticles produces results that are highly consistent with the broader literature on PLA-based microcarriers and encapsulated bioactives. The system's tunability, high encapsulation efficiency, and rapid release kinetics make it a promising platform for biomedical applications, such as targeted drug delivery, antioxidant therapy, and tissue engineering. These technological advantages gain further significance when combined with the demonstrated as microcarrier system based on biocompatibility and bioactivity of the PLA/Spirulina microparticles in HUVEC and HaCaT cell lines.

The comprehensive evaluation of PLA/Spirulina microparticles reveals both consistent therapeutic benefits and cell-type-specific responses across HUVEC and HaCaT cell lines. In HUVECs, all formulations demonstrated excellent biocompatibility (no cytotoxicity up to 25 μg/mL, **Figure 4.15a**), with the 1-M1 formulation showing particular promise through enhanced cell viability at 5-25 μg/mL concentrations. This optimal therapeutic window aligns with established Nrf2-mediated mechanisms, where low-to-moderate Spirulina concentrations stimulate endothelial proliferation while avoiding oxidative stress, as demonstrated by Liu et al. **(Runze Liu et al., 2022)**. The sustained proliferative effects were further confirmed through colony formation assays (**Figure 4.15b**) and longitudinal cell survival studies (**Figures 4.16a-d**), with Spirulina's phycocyanin and antioxidant compounds (β-carotene, tocopherols) modulating key pathways like VEGF and TGF-β1 to promote endothelial health **(Krüger-Genge et al., 2024)**. Transitioning to oxidative stress protection, fluorescence imaging revealed significant ROS reduction in HUVECs treated with both pure PLA (1-M0) and Spirulina-loaded microparticles (**Figures 4.17-4.18**). While PLA itself exhibited mild antioxidant activity - consistent with its established biocompatibility profile **(Baek et al., 2022; X. Shi et al., 2019)**- the enhanced effects in Spirulina-loaded formulations (particularly 1-M1 and 1-M3) underscore the additive potential of this combined system. These findings mirror Sibiya et al.'s observations in hepatic cells **(Sibiya et al., 2022)** and Krüger-Genge et

al.'s work on endothelial protection **(Krüger-Genge et al., 2024)**, collectively demonstrating the platform's dual capacity for cellular protection and proliferation enhancement.

The HaCaT studies revealed more nuanced, dose-dependent responses that highlight the importance of cell-type-specific optimization. While pure PLA microparticles (1-M0) showed excellent epithelial compatibility (**Figure 4.20a**), paralleling Karabay et al.'s findings with dermal fibroblasts **(Karabay et al., 2019)**, the Spirulina-loaded formulations exhibited complex bioactivity patterns. The transient cytotoxicity observed for 1-M2 at 0.5 µg/mL (**Figure 4.19a**) - which did not affect long-term colony formation (**Figure 4.19b**) - suggests an adaptive cellular response mechanism similar to Ahmed et al.'s observations of biphasic effects in wound healing models **(Ahmed Bahei-Eldin et al., 2017)**. The observed proliferative effects in HaCaT cells showed distinct temporal patterns across formulations, with 1-M1 (0.125% Spi) demonstrating early activity at 48 hours (**Figure 4.20b**) and 1-M2 (0.25% Spi) exhibiting sustained proliferation (**Figure 4.20c**). These results align with established dermatological research on Spirulina's epithelial benefits. The early response seen with 1-M1 parallels findings from Gunes et al.'s *in vitro* evaluation of *Spirulina platensis* extract in skin cream formulations, where incorporated Spirulina enhanced keratinocyte viability and migration capacity during early wound healing phases **(Gunes et al., 2017)**. The sustained proliferative effects of 1-M2 correlate strongly with the cytoprotective mechanisms identified by Jang et al. in their study of C-phycocyanin against UVB-induced HaCaT damage, particularly their demonstration that Spirulina-derived C-phycocyanin maintains long-term cell viability **(Jang & Kim, 2021)**. The antioxidant protection in HaCaT cells (**Figures 4.21-4.22**) further validated the system's therapeutic potential, with mechanisms echoing those observed in HUVECs but with distinct dose-response characteristics. Jang et al.'s work on C-phycocyanin's ROS-scavenging capacity (55% reduction in UVB-induced stress) provides particular insight into these epithelial-specific effects **(Jang & Kim, 2021)**. Importantly, the consistent safety profile across both cell types, evidenced by absent PI staining (**Figure 4.18**) and maintained viability at therapeutic doses, underscores the platform's translational potential for both vascular and dermatological applications targeting oxidative stress and tissue regeneration. Together, these studies confirm that our PLA-encapsulated Spirulina preserves the native biological activity of its

components while overcoming formulation challenges noted in topical applications, particularly regarding compound stability and controlled release.

Building on the promising results observed with the first set of PLA/Spirulina microparticles, where both biocompatibility and enhanced cellular proliferation were demonstrated in HUVEC and HaCaT models, the investigation proceeded to evaluate whether adjustments in microparticle size would influence cellular responses. To this end, a second set of microparticles was produced with modified electrospraying parameters to alter particle size distribution (comparing particle sizes of 2-M from 1-M, M0 increased by 12% while M1, M2, and M3 decreased by 24.9%, 8.99%, and 24.69%, respectively). Compared to the first set of PLA/Spirulina microparticles (1-M), which showed clear enhancement of cell proliferation and metabolic activity in HUVECs and HaCaT cells at optimized doses, the second set (2-M) demonstrated a more nuanced cellular response, strongly influenced by particle size and Spirulina loading. In the HUVECs, 2-microparticles maintained the excellent biocompatibility characteristic of PLA-based carriers, with no cytotoxicity observed across the tested concentrations, consistent with established literature on PLA microparticles and their safe cellular interactions **(Vlachopoulos et al., 2022)**. Notably, 2-M2 even promoted cell viability at higher concentrations, a phenomenon that parallels reports where optimized antioxidant or bioactive loading in PLA systems activates cellular protective pathways and supports resilience without toxicity **(Y. Li & Zhang, 2018)**. Colony formation assays for both 1-M and 2-M microparticles confirmed that neither formulation impairs the long-term proliferative capacity of HUVECs, which is in line with findings that PLA microparticles, regardless of their size, support cell colonization and do not induce adverse effects on cell survival **(Anderson & Shive, 2012; Vlachopoulos et al., 2022)**. However, cell survival assays revealed that while 1-M microparticles could enhance proliferation at specific doses, 2-M3 at 10 µg/mL led to reduced proliferation compared to controls, suggesting that more rapid release from smaller particles may transiently overwhelm cellular antioxidant defenses—a size-dependent effect also observed in other biodegradable microparticle systems **(Shamszadeh et al., 2022; Siepmann et al., 2004)**. Fluorescence imaging and mitochondrial activity measurements further supported these findings, as no significant differences in ROS levels, mitochondrial function, or cell death were observed between control and 2-microparticle-treated groups. This reinforces the

overall biocompatibility and safety of the PLA/Spirulina system, even as particle size and loading are modulated **(Krüger-Genge et al., 2024)**. These results highlight the importance of optimizing both size and bioactive content to achieve the desired balance between rapid therapeutic action and cellular tolerance.

The evaluation of 2-M in HaCaT cells revealed a clear absence of cytotoxicity across all tested concentrations (1–25 µg/mL) after 24 hours, as shown by the MTT assay (**Figure 4.27a**), like 1-M. This finding aligns with the well-documented biocompatibility of PLA-based carriers, which are non-cytotoxic in various epithelial and keratinocyte models. Despite the absence of cytotoxicity, the colony formation assay indicated that 2-microparticles could modulate the proliferative capacity of HaCaT cells depending on both composition and dose (**Figure 4.27b**). Pure PLA microparticles (2-M0) consistently enhanced colony formation at all concentrations, suggesting that the PLA itself provides a favorable substrate for keratinocyte proliferation. This is in line with the literature, which shows that PLA scaffolds and particles support epithelial cell attachment and proliferation due to their biocompatibility and suitable surface properties **(Nim et al., 2023)**. Fluorescence imaging revealed distinct ROS and metabolic responses to 2-microparticles in HaCaT cells. At 5 µg/mL, pure PLA microparticles (2-M0) significantly reduced ROS levels, while Spirulina-loaded variants (2-M1, 2-M2, 2-M3) exhibited either no change in ROS, depending on formulation (**Figure 4.29**). All microparticles enhanced mitochondrial activity and showed no cell death (PI-negative staining), confirming biocompatibility. However, at 10 µg/mL, 2-M3 was associated with elevated ROS and reduced mitochondrial function (**Figure 4.30**), suggesting rapid Spirulina release disrupted redox homeostasis. These findings are supported by Piao et al., which demonstrate that exposure to small particles, such as PM2.5, leads to oxidative stress, impairs subcellular organelle function, and triggers apoptosis in skin cells, emphasizing how smaller particle size and higher doses can adversely affect keratinocyte health **(K C et al., 2023; Piao et al., 2018)**.

Both 1-M and 2-M microparticles demonstrated excellent biocompatibility in HUVEC and HaCaT cells, with no cytotoxicity observed at therapeutic doses. However, 1-M particles exhibited more consistent antioxidant effects, reducing ROS and promoting proliferation across formulations. In contrast, 2-M particles, particularly the smaller 2-M3, showed dose-limited efficacy, with rapid Spirulina release at higher

concentrations leading to transient oxidative stress and reduced proliferation. This size-dependent behavior aligns with findings in bioplastic research, where particle geometry has a critical influence on cellular redox responses **(K C et al., 2023)**.

Depending on the cell fate experiments for 1- and 2-M, 1-M1 microparticles demonstrated superior biocompatibility and proliferative support in both HUVEC and HaCaT cell lines, as evidenced by MTT and colony formation assays, without inducing cytotoxicity or oxidative stress at optimized concentrations. These results indicate that 1-M1 is an ideal microcarrier candidate for further dermal applications, offering balanced cellular compatibility and antioxidant protection in both endothelial and epithelial models.

For examining of the all produced microparticle's (1-M and 2-M series) and the 70% ethanol Spirulina extract's (**Figure 4.31, Table 4.3**) antimicrobial tests showed the absence of antimicrobial activity, which contrasts with literature reports of Spirulina's antibacterial properties. This discrepancy can be attributed to several factors rooted in formulation, extraction methods, and experimental design. While Spirulina is widely reported to exhibit antimicrobial activity, its efficacy depends critically on the extraction solvent and the bioactive compounds isolated. Studies demonstrating Spirulina's antibacterial effects often use methanolic or aqueous extracts, which efficiently solubilize polar antimicrobial agents, such as phycocyanin, phenolic acids, and peptides **(Abdel-Moneim et al., 2022; Finamore et al., 2017)**. In contrast, the 70% ethanol extract used here may fail to extract these hydrophilic compounds, instead prioritizing non-polar constituents with limited antimicrobial potency. This aligns with findings that ethanol extracts of Spirulina show reduced activity compared to methanol or water-based preparations **(Bencheikh et al., 2022)**. Literature reports of antimicrobial activity often use Spirulina extracts at ≥10 mg/mL **(Abdel-Moneim et al., 2022)**. Additionally, disc diffusion assays require sufficient compound diffusion to form inhibition zones, a process impeded by low solubility or slow-release kinetics. For antioxidant capacity assays, the literature reports a 40% inhibition value of Spirulina's water extract at a 25 µg/mL concentration in the DPPH antioxidant assay. Additionally, another study found that Spirulina extracted with 70% ethanol had an EC_{50} value of 0.279 mg/mL in the DPPH assay, with a total phenolic content of 42% **(Habibi et al., 2024)**. Within the scope of this thesis, the total phenolic content of the Spirulina extract was determined to be 24.07 mg GAE/g Spirulina, and the EC50 value

was found to be 2.84 mg/mL. These differences arise from the extraction method, as reported in the literature **(Fratelli et al., 2021)**. It is essential to modify the extraction method for further studies to enhance the antioxidant capacity. Since the Spirulina content in the microparticles was at most 0.5%, it was expected that % inhibition values could not be determined in the DPPH test at low concentrations such as 3 mg/mL. However, for future studies, it is anticipated that scaling up the production to obtain a larger quantity of microparticles and performing the experiments at concentrations at least 10 times higher could enable the detection of antioxidant capacity. The Folin-Ciocalteu analysis, which determines total phenolic content, determined that the phenolic content of Spirulina extracted with 70% ethanol was 24.07 mg GAE/g Spi. In contrast, unlike the DPPH assay, no detectable phenolic content could be identified for the 3 mg/mL microparticles. Repeating these experiments with microparticles obtained from larger-scale production could result in measurements of the antioxidant capacities of Spirulina-containing microparticles within the detection range.

To confirm that bioactive compounds encapsulated within the microparticles could be effectively released and internalized by target cells, Nile Red—a well-established fluorescent probe for tracking cellular uptake—was incorporated as a model compound **(Snipstad et al., 2014)**. The use of Nile Red enabled direct visualization and quantification of microparticle-derived material within both HUVEC and HaCaT cells, providing a reliable indicator of successful cellular internalization and release. The successful encapsulation of Nile Red into 1-M0 microparticles (**Figure 4.35**), demonstrates the reproducibility of the electrospraying technique for generating monodisperse microparticles. The low standard deviation relative to the mean size confirms uniform particle formation, a critical factor for consistent drug delivery kinetics and predictable release profiles **(Danaei et al., 2018; Q. Xu et al., 2009)**. Monodispersity is essential for minimizing variability in cellular interactions, as irregular particle sizes can lead to heterogeneous uptake and release rates, as noted in studies on PLGA-based systems **(Vlachopoulos et al., 2022)**. Fluorescence microscopy and flow cytometry analyses revealed efficient cellular uptake of Nile Red-loaded microparticles in both HUVEC and HaCaT cells (**Figure 4.36a–c**). Notably, the 5 µg/mL dose resulted in higher intracellular Nile Red fluorescence (44.54% in HUVECs, 35.64% in HaCaT cells) compared to 10 µg/mL (20.01% and

17.27%, respectively). This inverse relationship between concentration and uptake efficiency may reflect particle aggregation at higher doses, which reduces effective surface area for cellular internalization, or saturation of endocytic pathways, as observed in nanoparticle studies **(Behzadi et al., 2017; Oh & Park, 2014)**. The absence of cytotoxicity at these concentrations (as shown in prior assays) further supports the biocompatibility of the PLA, even under conditions of active microparticle internalization. The differential uptake between HUVECs and HaCaT cells aligns with cell-type-specific endocytic activity. Endothelial cells (HUVECs) often exhibit a higher phagocytic capacity compared to keratinocytes, a phenomenon documented in studies comparing the responses of vascular and epithelial cells to microparticles **(Gopinath et al., 2021; Terrisse et al., 2010)**. The retained fluorescence in both cell types after 24 hours suggests sustained release of Nile Red from the PLA, a desirable trait for prolonged therapeutic delivery.

These findings validate 1-M1 microparticles as a viable platform for encapsulating and delivering bioactive compounds like niacinamide and palmitoyl-tripeptide-1. The efficient uptake at low doses (5 μg/mL) indicates that therapeutic efficacy can be achieved without high payload concentrations, minimizing potential off-target effects. Furthermore, the monodisperse nature of the particles ensures uniform release kinetics, critical for maintaining steady-state drug levels in applications such as anti-aging skincare or wound healing.

Niacinamide (Nia), a well-known dermatological agent with anti-inflammatory and antioxidant properties, was successfully encapsulated into PLA/Spirulina microparticles (1-M1= e-Spi) using electrospraying. The optimal formulation (0.5% niacinamide + 0.125% Spirulina + 3% PLA, e-Nia) yielded monodisperse microparticles, which is consistent with literature indicating that microparticles in the 3–5 μm range are suitable for dermal delivery and controlled release due to their favorable interaction with skin microstructures and hair follicles **(Vlachopoulos et al., 2022)**. Increasing the niacinamide concentration to 1% or higher resulted in fiber formation and loss of spherical morphology, a phenomenon also reported in studies where excessive bioactive loading alters solution viscosity and disrupts the electrospraying process, leading to non-uniform particle formation **(Lagreca et al.,**

2020). This highlights the importance of balancing drug loading with particle integrity for optimal formulation performance.

Palmitoyl tripeptide-1 (Tri), a collagen-stimulating peptide, was incorporated to enhance regenerative potential. At 0.1% loading, spherical microparticles (**Figure 4.41**) were achieved, but higher concentrations (≥0.25%) resulted in fiber formation (**Figures 4.42-4.43**), reflecting the need for low peptide loading to maintain particle homogeneity and bioactivity—a principle supported by literature showing that higher concentrations of peptides can disrupt polymer chain interactions and compromise structural integrity **(Johnson et al., 2018; Resende et al., 2021)**. Regarding safety, palmitoyl tripeptide-1 has been extensively evaluated. Acute and repeated dose toxicity studies in animals have found it to be nontoxic (LD50 > 2,000 mg/kg), and human skin irritation and sensitization studies have consistently reported no significant irritation or sensitization, even at concentrations up to 1,000 ppm **(Johnson et al., 2018)**. Thus, while low concentrations are optimal for formulation stability, tripeptide-1 is considered safe and well-tolerated in dermal applications.

The composite formulation (0.5% Nia + 0.1% Tri + 0.125% Spi + 3% PLA, e-NiaTri) demonstrated optimal monodispersity (**Figure 4.44**), whereas higher Tri concentrations (0.25–0.5%) compromised structural integrity (**Figure 4.45**). The additive effects of combining bioactive molecules with differing physicochemical properties—such as niacinamide's hydrophilicity and a tripeptide's amphiphilicity—can significantly impact phase separation and crystallization during microparticle formulation, independent of the polymer used. As highlighted in a recent review, the particle size distribution and the interplay between drug solubility, hydrophilicity, and formulation parameters are crucial for drug release kinetics, stability, and homogeneity in multi-drug-loaded systems, necessitating empirical optimization to avoid phase separation or crystallization **(Ainurofiq et al., 2025)**. Additionally, the shape and geometry of micro- and nanoparticles, which can be influenced by the presence of multiple bioactives, play a central role in modulating drug release and ensuring uniformity, further emphasizing the importance of careful formulation design and process control **(Moore et al., 2022)**.

The optimized e-Nia, e-Tri, and e-NiaTri microparticles leverage the antioxidant and regenerative properties of niacinamide and palmitoyl tripeptide-1 while maintaining

structural integrity. First, the free form of loaded biocompounds was an asset for comparing the efficacy of loaded microparticles in terms of cell fate. For that purpose, the cytotoxicity of free niacinamide (Nia) and palmitoyl tripeptide-1 (Tri) was systematically evaluated in HUVEC and HaCaT cell lines. Free Nia demonstrated no significant cytotoxicity at concentrations up to 75 µM in either cell type (**Figure 4.46a**), confirming its high biocompatibility and supporting literature showing that niacinamide is well-tolerated in both keratinocytes and endothelial cells **(Marques et al., 2024)**. In contrast, Tri exhibited a dose-dependent reduction in cell viability, with HUVECs displaying significant sensitivity at concentrations as low as 10 µM, and HaCaT cells showing significant cytotoxicity at 25 and 50 µM (**Figure 4.46b**). This aligns with literature indicating that while palmitoyl tripeptide-1 is generally safe in topical formulations, higher concentrations may disrupt cellular homeostasis **(Schagen, 2017)**. Proliferation assays over 72 hours further highlighted the distinct biological activities of these compounds. Free Nia promoted proliferation in HaCaT cells at 10 and 25 µM (**Figure 4.47c**), consistent with its role in DNA repair, anti-inflammatory signaling, and support of keratinocyte differentiation and migration **(Marques et al., 2024; Wessels et al., 2014)**. In HUVECs, Nia maintained proliferation comparable to controls (**Figure 4.47a**), which is in line with literature indicating niacinamide's ability to preserve endothelial cell viability and function **(Marques et al., 2024)**. At lower concentrations, free Tri maintained or slightly increased proliferation, but higher doses reduced viability, especially in HUVECs (**Figure 4.47b, d**), reflecting the narrow therapeutic window often reported for bioactive peptides **(Md Fadilah et al., 2021)**.

Advancing beyond free form, the encapsulation of niacinamide (Nia), palmitoyl tripeptide-1 (Tri), and their combination (e-NiaTri) within PLA/Spirulina microparticles (e-Spi) demonstrated significant improvements in both safety and efficacy profiles, as evidenced by MTT assays showing no cytotoxicity at 5-10 µg/mL and only slight viability reduction at the highest e-Nia dose (**Figures 4.48a-c**). This is consistent with studies reporting that encapsulation can mitigate the cytotoxic effects of free peptides and enhance their therapeutic window **(Md Fadilah et al., 2021)**. The blank carrier (e-Spi) was non-cytotoxic (**Figure 4.48d**), confirming the biocompatibility of the PLA/Spirulina matrix, which is consistent with recent findings that PLA/Spirulina microparticles produced by electrospraying show excellent

biocompatibility in both HUVEC and HaCaT cell lines, as demonstrated by MTT and colony formation assays **(Dalbayrak et al., 2025)**. Proliferation assays in this thesis revealed that both e-Nia and e-Tri significantly enhanced HUVEC proliferation at 5 µg/mL after 72 hours (**Figures 4.49a-b**), while the dual-loaded e-NiaTri formulation produced even greater proliferation at both 5 and 10 µg/mL after 48 hours (**Figure 4.49c**). This observation is in line with literature on polymeric encapsulation, where co-encapsulation of two or more bioactive ingredients in microparticles—such as dual-sized PLGA systems or microparticles containing combinations of growth factors or immunomodulators—often results in additive or additive effects on cell proliferation or immune modulation compared to single-loaded systems **(Lewis et al., 2015)**. For example, dual-sized PLGA microparticles loaded with different immunomodulatory agents have been shown to condition antigen-presenting cells and enhance functional T cell responses, while combination-loaded microparticles can stimulate proliferation to levels comparable to or exceeding those achieved with single agents **(Lewis et al., 2015)**. Thus, the enhanced proliferation observed with the dual-loaded e-NiaTri microparticles is well-supported by the literature on multi-component polymeric delivery systems.

Expanding these findings to HaCaT cells, both e-Nia and e-Tri at 10 µg/mL promoted significant proliferation compared to initial cell counts (**Figure 4.54a, b**). These results align with literature demonstrating that niacinamide enhances keratinocyte proliferation and wound healing through mechanisms such as NAD+ restoration, DNA repair, and inhibition of NADPH oxidase-mediated oxidative stress, as shown in studies on skin damage **(Zhen et al., 2019)**. Similarly, palmitoyl tripeptide-1 promotes collagen synthesis and tissue regeneration by stimulating fibroblast activity and extracellular matrix remodeling, as evidenced in rodent wound models **(Md Fadilah et al., 2021)**. The controlled-release delivery via PLA/Spirulina microparticles amplifies these effects by ensuring sustained bioavailability and minimizing cytotoxicity, a principle supported by research on polymeric systems for dermal applications **(Vlachopoulos et al., 2022)**. This synergy between bioactive compounds and encapsulation technology underscores the therapeutic advantage of optimized formulations for skin repair and regeneration.

Further supporting these observations, fluorescence imaging and quantitative ROS analysis demonstrated that all biocompound-loaded microparticles significantly reduced intracellular ROS in both HUVEC and HaCaT cells, with the most potent effects for e-Nia (5 µg/mL in HUVECs), e-Tri (10 µg/mL in HUVECs), and both concentrations in HaCaT cells (**Figures 4.53, 4.58**). These antioxidant effects are supported by mechanistic studies showing that niacinamide decreases ROS by restoring NAD reserves, increasing superoxide dismutase, and inhibiting NADPH oxidase in keratinocytes **(Marques et al., 2024; Zhen et al., 2019)**. Palmitoyl tripeptide-1 also exhibits significant antioxidant properties, reducing ROS, enhancing antioxidant enzyme activity, and protecting against oxidative damage in skin and other tissues **(Badilli & Inal, 2025; Q. He et al., 2025; X. He et al., 2024)**.

In addition to antioxidant effects, *in vitro* scratch assays showed that e-Nia at 10 µg/mL and e-Tri at both 5 and 10 µg/mL significantly accelerated wound closure in HUVECs after 12 hours ($p < 0.05$; **Figures 4.59a, b**). In HaCaT cells, both e-Nia and e-Tri at 5 and 10 µg/mL significantly reduced wound area after 24 hours ($p < 0.001$ and $p < 0.01$, respectively; **Figures 4.60a, b**). These findings are consistent with literature demonstrating that niacinamide enhances keratinocyte migration and wound healing **(Esfahani et al., 2015; Wessels et al., 2014)**, and that palmitoyl tripeptide-1 promotes collagen synthesis, tissue regeneration, and re-epithelialization **(Md Fadilah et al., 2021; Pintea et al., 2025)**. The dual-loaded e-NiaTri formulation did not show additional benefit, suggesting that further optimization of component ratios or release kinetics may be needed. Notably, the blank e-Spi microparticles also promoted wound closure in HaCaT cells ($p < 0.01$ and $p < 0.001$; **Figure 4.60d**), indicating possible enhanced biological properties of e-Spi due to Spirulina's wound healing ability **(Refai et al., 2023; Syarina et al., 2015)**.

While these wound healing assays demonstrate functional improvements in cell migration and tissue repair, molecular analyses reveal that the treatments simultaneously modulate key signaling pathways involved in these processes. The observed reduction in AKT protein levels in HUVEC cells following treatment with the various extracts and compounds suggests a suppression of the PI3K/AKT signaling pathway, which plays a central role in endothelial cell survival, proliferation, migration, and angiogenesis **(Fujio & Walsh, 1999; M. Y. Lee et al., 2014; Shiojima**

& Walsh, 2002). AKT, also known as protein kinase B, is a critical mediator of cytoprotective signals in endothelial cells, particularly in response to growth factors like VEGF. Reduced AKT expression or activity is associated with decreased cell survival and increased susceptibility to apoptosis, as AKT normally promotes anti-apoptotic and pro-survival responses in endothelial cells **(Fujio & Walsh, 1999; H. Shi & Feng, 2011; Shiojima & Walsh, 2002)**. This downregulation, especially pronounced with the e-NiaTri treatment, may indicate that these compounds inhibit endothelial cell survival pathways, potentially leading to reduced angiogenic activity or increased cell death.

Conversely, the marked increase in Smad2/3 protein levels across all treatments points to an activation of the TGF-β/Smad signaling axis. Smad2/3 are intracellular mediators of TGF-β family cytokines, which, upon activation, translocate to the nucleus and regulate gene expression relevant to endothelial cell function, including proliferation, migration, and extracellular matrix production **(Deng et al., 2021; Saura et al., 2002; Y.-H. Zhang et al., 2016)**. In endothelial cells, activation of Smad2/3 can have context-dependent effects: it may promote cell migration and proliferation under certain conditions, but sustained or excessive activation is often linked to vascular remodeling, endothelial–mesenchymal transition, and even pathological vessel narrowing, as seen in atherosclerosis or fibrosis **(Deng et al., 2021)**. Increased Smad2/3 signaling has also been associated with upregulation of genes like eNOS, contributing to changes in vascular tone and homeostasis **(Saura et al., 2002)**.

Notably, recent studies highlight a complex interplay between the AKT and Smad2/3 pathways. There is evidence of reciprocal regulation, where inhibition of AKT can enhance Smad2/3 activity and vice versa, suggesting that the observed changes may not be independent but rather reflect a coordinated shift in endothelial signaling dynamics **(Shepherd et al., 2011; Shim et al., 2021; Suwanabol et al., 2012)**. In this context, the simultaneous decrease in AKT and increase in Smad2/3 may additively promote a switch from a proliferative, survival-oriented endothelial phenotype to one more prone to remodeling, differentiation, or apoptosis.

In summary, the treatments that reduce AKT and increase Smad2/3 in HUVEC cells likely suppress survival and angiogenic signaling while activating pathways involved in vascular remodeling and potentially pathological changes in the endothelium. This

dual modulation could have significant implications for vascular health, influencing processes such as angiogenesis, vessel stability, and response to injury or inflammation.

The distinction between free and encapsulated (e-) forms of the compounds reveals important differences in their biological activity and cellular uptake mechanisms. The encapsulated forms appear to demonstrate enhanced or modified effects compared to their free counterparts, particularly evident in the case of e-NiaTri. The encapsulated combination e-NiaTri exhibited the most pronounced reduction in AKT expression, which was significantly greater than either free Nia or free Tri alone. This suggests that encapsulation not only preserves the bioactive compounds but may also enhance their cellular uptake and intracellular bioavailability. Encapsulation can protect compounds from degradation, improve their solubility, and facilitate targeted delivery to specific cellular compartments, potentially explaining the enhanced potency observed with the encapsulated forms. The enhanced effects of encapsulated forms, particularly e-NiaTri, suggest improved therapeutic potential through better bioavailability and sustained release characteristics.

The presented Western blot results in HaCaT keratinocytes after 24-hour treatment with various free and encapsulated compounds reveal distinct modulation of AKT and Smad2/3 signaling pathways, which are central to skin cell homeostasis, repair, and inflammation. AKT, a serine/threonine kinase, is crucial for keratinocyte proliferation, survival, and barrier function **(Roy et al., 2023; Teng et al., 2021)**. Here, both free niacinamide (Nia, 1.56-fold) and encapsulated niacinamide (e-Nia, 1.49-fold) substantially upregulated AKT expression compared to control, suggesting enhanced activation of pro-survival and proliferative pathways. This aligns with literature showing that increased AKT activity supports skin regeneration and barrier function, and its dysregulation is implicated in various skin disorders **(Roy et al., 2023; Teng et al., 2021)**. The e-NiaTri combination also upregulated AKT (1.23-fold), though less than e-Nia alone, indicating a possible modulatory effect of the combination. In contrast, both forms of palmitoyl tripeptide-1 (Tri and e-Tri) downregulated AKT (0.83- and 0.88-fold), which may reflect a shift toward differentiation or reduced proliferation, as lower AKT activity can promote keratinocyte maturation and limit hyperproliferation **(Roy et al., 2023; N. Xu et al., 2012)**. Spirulina extract (e-Spi)

showed a modest increase in AKT (1.10-fold), consistent with reports that Spirulina proteins can activate AKT and ERK pathways to promote wound healing and cell survival **(P. Liu et al., 2020)**. Smad2/3 proteins are central mediators of TGF-β signaling, regulating extracellular matrix production, wound healing, and cellular differentiation **(Huang et al., 2020; Uemura et al., 2005)**. All treatments increased Smad2/3 expression, with the most pronounced effect from e-Spi (3.41-fold), followed by e-Nia (2.44-fold), e-NiaTri (2.18-fold), and e-Tri (1.93-fold). Free Nia and Tri induced more moderate increases (1.33- and 1.43-fold). These results are consistent with studies showing that natural compounds, including Spirulina protein and niacin, can activate the TGF-β/Smad pathway, thereby promoting tissue repair, collagen synthesis, and anti-inflammatory effects **(P. Liu et al., 2020; Torres-Moral et al., 2024)**.The robust Smad2/3 upregulation by e-Spi supports findings that Spirulina enhances both TGF-β1 and Smad2 phosphorylation, facilitating wound repair and matrix remodeling **(P. Liu et al., 2020)**.

The observed patterns suggest a nuanced interplay between the AKT and Smad2/3 pathways. Literature indicates these pathways can have opposing or cooperative roles depending on context: AKT generally promotes proliferation and survival, while Smad2/3 activation is closely linked to differentiation, extracellular matrix production, and sometimes growth inhibition **(Suwanabol et al., 2012; Z. Zhang et al., 2014)**. For example, in some systems, AKT can inhibit Smad3-mediated transcription and apoptosis, while Smad3 can also promote AKT phosphorylation, indicating bidirectional crosstalk. The simultaneous upregulation of both AKT and Smad2/3 by niacin and Spirulina may thus foster an environment conducive to both proliferation and repair, potentially accelerating wound healing and tissue regeneration. The downregulation of AKT by Tri, alongside moderate Smad2/3 induction, may favor keratinocyte differentiation and matrix deposition, which are beneficial for skin remodeling and anti-aging effects **(Huang et al., 2020; Uemura et al., 2005)**.

All in all, the encapsulation allows for lower effective concentrations while maintaining or enhancing biological activity, as evidenced by the potent effects observed at the tested concentrations. This approach could potentially reduce side effects while maximizing therapeutic benefits, making encapsulated combinations a promising strategy for modulating endothelial cell function and vascular health.

Collectively, the results for biocompound loaded microparticles demonstrate that microcarrier solution efficiently encapsulates hydrophilic (niacinamide, Nia) and amphiphilic (palmitoyl-tripeptide-1, Tri) compounds while enabling remarkable dose reduction compared to free forms of biocompounds. For niacinamide, the optimal applicational dose to HUVEC and HaCaT cell lines (5 µg/mL e-Nia) demonstrated similar biological effects to 25 µM free Nia, representing a 122.2-fold reduction in applied dose, even assuming 100% encapsulation efficiency. Similarly, palmitoyl-tripeptide-1 showed comparable efficacy at 5 µg/ml e-Tri versus 5 µM free Tri, constituting a 578.8-fold dose reduction under the same 100% encapsulation assumption. This translates to dose reductions of 99.18% for Nia and 99.83% for Tri, highlighting the system's exceptional capacity to enhance therapeutic efficiency while minimizing active ingredient requirements. Overall, these findings reinforce the utility of PLA-based microparticles as versatile, biocompatible carriers for delivering bioactive compounds with antioxidant and regenerative properties. The observed dose-dependent effects, antioxidant activity, and wound healing efficacy are in strong agreement with the literature, which emphasizes the importance of precise formulation and concentration control for maximizing therapeutic benefit while minimizing cytotoxic risk.

The efficacy of this delivery system becomes particularly significant when applied to UV-induced photoaging models, where oxidative stress and cellular damage pose major therapeutic challenges. The UV-induced cellular models using HUVEC and HaCaT cells highlight critical mechanisms of photoaging, including oxidative stress, DNA damage, and senescence. Specifically, UVB irradiation triggers the formation of DNA lesions (e.g., cyclobutane pyrimidine dimers, CPDs) and the overproduction of reactive oxygen species (ROS), leading to mitochondrial dysfunction, a senescence-associated secretory phenotype (SASP), and collagen degradation via matrix metalloproteinases (MMPs) **(Ge et al., 2024; Gromkowska-Kępka et al., 2021; K. Guo et al., 2022)**. The cellular evaluation of niacinamide (Nia) and palmitoyl tripeptide-1 (Tri) in UV-exposed HUVEC and HaCaT cell lines provides valuable insights into their potential as preventive agents against photoaging. The differential responses observed between free and encapsulated forms (**Figures 4.64-4.68**) align with established mechanisms of these compounds in skin protection. The limited cytoprotection of free niacinamide against UV-induced damage (**Figure 4.64a**)

corresponds with niacinamide's therapeutic efficacy in skin health and anti-aging is highly dependent on sustained bioavailability, as evidenced by studies comparing free niacinamide with advanced delivery systems. For instance, *in vivo* human studies using confocal Raman spectroscopy (CRS) demonstrated that conventional niacinamide solutions achieved only 6.5% skin deposition **(Y. Zhang et al., 2021)**, while hybrid nanogel formulations incorporating permeation enhancers like jojoba oil increased deposition to 32.5% **(Marques et al., 2024)**. This 5-fold improvement underscores the critical role of sustained release in maintaining therapeutic niacinamide levels within the skin. Without sustained bioavailability, rapid clearance or degradation of niacinamide limits its ability to suppress oxidative stress, reverse UV-induced DNA damage, or inhibit collagen glycation **(Marques et al., 2024)**. The moderate improvement seen with encapsulated e-Nia **(Figure 4.66a)** supports the concept that controlled release systems can enhance niacinamide's antioxidant capacity, consistent with the pharmacokinetic advantages. The concentration-dependent effects of Tri (**Figures 4.64b, 4.65b, d**) mirror the dual nature of peptide-based therapeutics, where optimal biological activity occurs within a narrow concentration window. This phenomenon has been well-documented in studies of palmitoylated peptides, where lower concentrations stimulate collagen production while higher doses may cause membrane disruption **(Pintea et al., 2025; Tałałaj et al., 2019)**. The significant improvement in cell viability with encapsulated e-Tri (**Figure 4.66b**) reinforces findings by Tałałaj et al. that nanoencapsulation of bioactive peptides can reduce cytotoxicity while maintaining efficacy, particularly for amphiphilic compounds like palmitoyl peptides **(Tałałaj et al., 2019)**. The additive activity observed with the dual-loaded e-NiaTri formulation (**Figures 4.66c, 4.67c**) reflects a growing trend in dermatological research toward multi-target approaches for photoaging. This aligns with the combinatorial strategy demonstrated in clinical studies **(Boo, 2022; Martín-Martínez et al., 2022)**, where synergistic combinations of antioxidants (e.g., ascorbic acid, α-tocopherol) and collagen-stimulating agents (e.g., glycinamide, recombinant prolyl 4-hydroxylase) target complementary pathways to mitigate oxidative stress (via ROS reduction and MMP inhibition) and enhance extracellular matrix integrity (via collagen synthesis and stabilization). These systems mirror the e-NiaTri formulation's ability to balance bioactive release and stability, underscoring the importance of engineered delivery platforms in modern dermatology. By integrating antioxidant and collagen-stimulating mechanisms within a single carrier, such strategies address both

oxidative damage (via NADPH oxidase inhibition and SOD upregulation) and extracellular matrix degradation (via MMP suppression and collagen stabilization).

The inherent bioactivity of blank e-Spi particles (**Figures 4.66d, 4.67d**) aligns with established research on Spirulina's photoprotective properties. For instance, Spirulina extracts have been shown to scavenge UVB-induced reactive oxygen species (ROS) in human keratinocytes, reducing DNA damage and inflammation through antioxidant pathways mediated by phycocyanin and phenolic compounds **(Jang & Kim, 2021)**. These findings explain the cytoprotection observed in our system, where Spirulina's bioactive components likely mitigated oxidative stress in UV-exposed cells. Furthermore, the dual role of Spirulina as both a structural carrier and bioactive agent reflects advancements in multifunctional delivery systems, as highlighted in reviews emphasizing natural biomaterials for dermatology. This synergy underscores the value of Spirulina-based carriers in addressing complex dermatological challenges like photoaging through combined mechanical and biochemical interventions.

The cell-type-specific responses observed in this study (**Figures 4.67, 4.68**) underscore the importance of tissue heterogeneity in photoaging research. The differential effects between HUVECs and HaCaT cells align with established variations in UV response mechanisms between endothelial and epithelial lineages. For instance, endothelial cells (HUVECs) exhibit heightened sensitivity to UV-induced oxidative stress, which disrupts vascular integrity and promotes inflammatory cascades. In contrast, keratinocytes (HaCaT) prioritize DNA damage repair and maintenance of barrier function, as detailed in comparative studies by Pillai et al. on skin photoaging mechanisms **(Pillai et al., 2005)**.

This study successfully establishes a groundbreaking paradigm in cutaneous therapeutics by integrating advanced material science with bioactive optimization to create a next-generation delivery platform. The PLA/Spirulina microcarrier system represents a significant leap forward in dermal technology, demonstrating unparalleled versatility in co-encapsulating hydrophilic and amphiphilic compounds while overcoming traditional formulation challenges. By harmonizing several key innovations—such as cultivation-optimized Spirulina biomass with enhanced mineral profiles and precision-engineered electrosprayed microparticles—it has been developed a multifunctional system that operates on multiple therapeutic fronts. The

platform's unique ability to deliver niacinamide and palmitoyl tripeptide-1 at dramatically reduced doses while amplifying their bioactivity through controlled release and Spirulina's intrinsic properties addresses fundamental limitations in current photoaging interventions. Importantly, the system's design principles - combining the structural advantages of PLA with Spirulina's nutritional and antioxidant assets - create an additive therapeutic effect greater than the sum of its components. This work not only provides a blueprint for developing efficient, sustainable cosmeceutical formulations but also opens new possibilities for treating complex dermatological conditions through precision multi-targeting. The demonstrated success of this integrated approach, combining biomaterial engineering with bioactive optimization, sets a new standard for future developments in cutaneous delivery systems and beyond, offering a template that could be adapted for various therapeutic applications requiring sophisticated carrier solutions.

6. CONCLUSION

This thesis has explored the development, characterization, and biological evaluation of poly(lactic acid) (PLA)-based microparticles loaded with Spirulina extract and bioactive compounds, including niacinamide and palmitoyl tripeptide-1, for potential applications in tissue engineering, wound healing, and skin regeneration. Through a systematic approach involving advanced electrospraying techniques, detailed physicochemical characterization, and a series of *in vitro* cellular assays, the work provides new insights into how formulation parameters, encapsulation strategies, and bioactive selection influence microparticle performance and cellular responses.

The successful fabrication of monodisperse, spherical PLA microparticles encapsulating Spirulina, Nile Red, niacinamide, and palmitoyl tripeptide-1 was achieved via electrospraying, with careful optimization of solution properties and process parameters. The selection of a 70% ethanol extract of Spirulina was guided by its proven efficacy in extracting a broad spectrum of bioactive compounds while maintaining compatibility with PLA and the electrospraying process. SEM analysis confirmed the production of microparticles with controlled size distributions, typically ranging from 3 to 5 μm, and demonstrated that formulation variables such as nozzle diameter, solvent composition, and additive concentration critically influence particle morphology and homogeneity.

The morphological stability of the microparticles was found to be sensitive to the concentration of loaded bioactives. While low to moderate concentrations of niacinamide and palmitoyl tripeptide-1 preserved spherical morphology, higher concentrations led to irregular fiber formation, likely due to altered solvent evaporation dynamics and polymer–additive interactions.

Encapsulation of Spirulina and other bioactives within the PLA was confirmed by FT-IR spectroscopy, which showed the preservation of characteristic PLA peaks and the presence of bioactive-specific vibrational bands. The *in vitro* release profiles revealed a rapid, burst release of encapsulated compounds within the first 6 hours, a pattern typical for PLA-based systems with high surface-area-to-volume ratios. Although the

actual loading efficiency was approximately half of the theoretical value, this finding aligns with previous reports and reflects the challenges associated with solvent evaporation-based encapsulation methods.

Significantly, the encapsulation process did not compromise the chemical integrity of either the polymer or the bioactive compounds, as evidenced by consistent FT-IR spectra and preserved functional activity in downstream cellular assays.

The cellular uptake studies using Nile Red-loaded microparticles demonstrated efficient internalization by both HUVEC and HaCaT cell lines, as confirmed by flow cytometry and fluorescence microscopy, which showed dose-dependent uptake and release of the encapsulated dye.

Biocompatibility assays revealed that both blank and bioactive-loaded PLA/Spirulina microparticles were non-cytotoxic across a wide concentration range, with some formulations even promoting cell proliferation and colony formation. Notably, the e-Nia, e-Tri, and e-NiaTri microparticles enhanced cell viability and proliferation in HUVECs and, to a lesser extent, in HaCaT cells, particularly under oxidative stress conditions induced by UV exposure.

Fluorescence imaging and ROS quantification further demonstrated that bioactive-loaded microparticles significantly reduced intracellular oxidative stress, preserved mitochondrial function, and maintained normal nuclear morphology, supporting their cytoprotective and anti-photoaging potential.

The wound healing assays provided compelling evidence that bioactive-loaded PLA microparticles can accelerate scratch closure in both endothelial and keratinocyte models, with effects comparable to or exceeding those of the free compounds. This is particularly significant given the dual role of niacinamide and palmitoyl tripeptide-1 in promoting extracellular matrix remodeling, collagen synthesis, and angiogenesis—key processes in tissue repair and regeneration. The observed synergy in dual-loaded formulations, though moderate, suggests that further optimization of bioactive ratios and release kinetics could yield even greater therapeutic benefit.

Mechanistically, the data support a model in which PLA encapsulation buffers the direct toxicity of potent bioactives, modulates their release, and enhances their cellular

uptake and efficacy. The observed dose-dependent effects and the prioritization of barrier repair over proliferation in keratinocytes under UV stress are consistent with known cellular adaptive responses.

In summary, this thesis demonstrates that PLA-based microparticles, especially when combined with Spirulina and dermatologically relevant bioactives, represent a promising platform for safe, effective, and multifunctional delivery in regenerative medicine. The integration of antioxidant, anti-inflammatory, and regenerative mechanisms within a biocompatible carrier system opens up new avenues for treating wounds, photoaging, and other skin pathologies. These findings contribute to the growing body of evidence supporting the use of biodegradable polymeric carriers for advanced biomedical applications, laying the groundwork for future translational research in this field.

7. LIMITATIONS AND FUTURE DIRECTIONS

While the findings are robust, several limitations warrant further investigation. The burst release profile of the microparticles may limit sustained therapeutic action, suggesting a need for further tuning of polymer composition or the incorporation of release-modifying excipients. Additionally, expanding cellular experiments to include other skin-related cell lines, such as human dermal fibroblasts (HDFs), 3D skin equivalents, and co-culture models would provide a more comprehensive understanding of the system's effects on skin regeneration and repair. *In vivo* studies are also essential to confirm pharmacokinetics, biodistribution, and long-term safety, as well as to evaluate functional outcomes such as collagen deposition and wound healing in relevant animal models. From a product development perspective, future work should focus on integrating these microparticles into topical formulations, assessing their stability, skin penetration, and efficacy in *ex vivo* and clinical settings. Scaling up production using advanced electrospraying, followed by consumer testing for anti-aging and skin-repair outcomes, will be critical steps toward clinical and commercial translation. Addressing these limitations through targeted experimental and product-based approaches will help bridge the gap between *in vitro* promise and real-world dermatological applications.

REFERENCES

Abdelghany, A. K., Gamal, A., Abdel-Wahab, A., Abdel-Razik, A. R. H., El-Samannoudy, S. I., Ibrahim, M. A., Hassan, W. H., & El-Ela, F. I. A. (2023). Evaluating the neuroprotective effect of Spirulina platensis–loaded niosomes against Alzheimer's disease induced in rats. *Drug Delivery and Translational Research*. https://doi.org/10.1007/s13346-023-01301-2

Abdel-Moneim, A. M. E., El-Saadony, M. T., Shehata, A. M., Saad, A. M., Aldhumri, S. A., Ouda, S. M., & Mesalam, N. M. (2022). Antioxidant and antimicrobial activities of Spirulina platensis extracts and biogenic selenium nanoparticles against selected pathogenic bacteria and fungi. *Saudi Journal of Biological Sciences*, *29*(2), 1197–1209. https://doi.org/10.1016/j.sjbs.2021.09.046

Acharya, S., & Sahoo, S. K. (2011). PLGA nanoparticles containing various anticancer agents and tumour delivery by EPR effect. In *Advanced Drug Delivery Reviews* (Vol. 63, Number 3, pp. 170–183). https://doi.org/10.1016/j.addr.2010.10.008

Adamo, G., Fierli, D., Romancino, D. P., Picciotto, S., Barone, M. E., Aranyos, A., Božič, D., Morsbach, S., Raccosta, S., Stanly, C., Paganini, C., Gai, M., Cusimano, A., Martorana, V., Noto, R., Carrotta, R., Librizzi, F., Randazzo, L., Parkes, R., … Bongiovanni, A. (2021). Nanoalgosomes: Introducing extracellular vesicles produced by microalgae. *Journal of Extracellular Vesicles*, *10*(6). https://doi.org/10.1002/jev2.12081

Agustini, N. W. S., & Wijayanto, Y. (2020). Isolation, identification of fatty acids from Spirulina platensis as antibacterial. *IOP Conference Series: Earth and Environmental Science*, *457*(1). https://doi.org/10.1088/1755-1315/457/1/012033

Ahmad, A., Inthikhab, A., Zafar, S., Farooq, U., Shah, H., Akram, S., Abid, J., Parveen, Z., & Iqbal, S. (2023). Spirulina, an FDA-approved functional food: Worth the hype? *Cellular and Molecular Biology*, *69*(1), 137–144. https://doi.org/http://dx.doi.org/10.14715/cmb/2022.69.1.24 Copyright: © 2023 by the C.M.B. Association. All rights reserved. Introduction

Ahmed Bahei-Eldin, I., Hamed Elgazzar, M., Ibrahim Ahmed, A., & Saeed Attia Mohamed, S. (2017). The Effect of Spirulina Extract on the Healing of Skin Wounds in Adult Albino Rats: A Light and Scanning Electron Microscopic Study The effecT of Spirulina exTracT on The healing of Skin WoundS in. In *Egyptian Journal of Anatomy* (Vol. 40, Number 1).

Ai, X., Yu, P., Li, X., Lai, X., Yang, M., Liu, F., Luan, F., & Meng, X. (2023). Polysaccharides from Spirulina platensis: Extraction methods, structural features and bioactivities diversity. In *International Journal of Biological Macromolecules* (Vol. 231). Elsevier B.V. https://doi.org/10.1016/j.ijbiomac.2023.123211

Ainurofiq, A., Suryanto, A. A., Beltiartono, B. S., Merdekawati, N. A., Ardiyani, N. P., Farohma, Q. Y. C., Budiman, A., Wardhana, Y. W., & Nugraha, Y. P. (2025). Literature review: The role of particle size distribution in drug delivery. In

Multidisciplinary Reviews (Vol. 8, Number 9). Malque Publishing. https://doi.org/10.31893/multirev.2025269

Akao, Y., Ebihara, T., Masuda, H., Saeki, Y., Akazawa, T., Hazeki, K., Hazeki, O., Matsumoto, M., & Seya, T. (2009). Enhancement of antitumor natural killer cell activation by orally administered Spirulina extract in mice. *Cancer Science*, *100*(8), 1494–1501. https://doi.org/10.1111/j.1349-7006.2009.01188.x

Albicance, C. (2015). *EVALUATION OF ANTICANDIDAL ACTIVITIES OF SPIRULINA METABOLITE EVALUATION OF ANTICANDIDAL ACTIVITIES OF SPIRULINA METABOLITE AGAINST INTRODUCTION : A number of cyanobacteria and microalgae produce various intracellular and alga such as Chlorella vulgaris* . *6*(April 2020). https://doi.org/10.13040/IJPSR.0975-8232.6(3).1000-07

Amponsah, O., Nopuo, P. S. A., Manga, F. A., Catli, N. B., & Labus, K. (2025). *Future-Oriented Biomaterials Based on Natural Polymer Resources: Characteristics, Application Innovations and Development Trends*. https://doi.org/10.20944/preprints202505.0979.v1

Anderson, J. M., & Shive, M. S. (2012). Biodegradation and biocompatibility of PLA and PLGA microspheres. In *Advanced Drug Delivery Reviews* (Vol. 64, Number SUPPL., pp. 72–82). https://doi.org/10.1016/j.addr.2012.09.004

Aquino, R. P., Auriemma, G., Conte, G. M., Esposito, T., Sommella, E., Campiglia, P., & Sansone, F. (2020). Development of chitosan/mannitol microparticles as delivery system for the oral administration of a Spirulina bioactive peptide extract. *Molecules*, *25*(9), 1–19. https://doi.org/10.3390/molecules25092086

Bachstetter, A. D., Jernberg, J., Schlunk, A., Vila, J. L., Hudson, C., Cole, M. J., Shytle, R. D., Tan, J., Sanberg, P. R., Sanberg, C. D., Borlongan, C., Kaneko, Y., Tajiri, N., Gemma, C., & Bickford, P. C. (2010). Spirulina promotes stem cell genesis and protects against LPS induced declines in neural stem cell proliferation. *PLoS ONE*, *5*(5). https://doi.org/10.1371/journal.pone.0010496

Badilli, U., & Inal, O. (2025). Current Approaches in Cosmeceuticals: Peptides, Biotics and Marine Biopolymers. In *Polymers* (Vol. 17, Number 6). Multidisciplinary Digital Publishing Institute (MDPI). https://doi.org/10.3390/polym17060798

Baek, S. W., Kim, D. S., Song, D. H., Lee, S., Lee, J. K., Park, S. Y., Kim, J. H., Kim, T. H., Park, C. G., & Han, D. K. (2022). PLLA Composites Combined with Delivery System of Bioactive Agents for Anti-Inflammation and Re-Endothelialization. *Pharmaceutics*, *14*(12). https://doi.org/10.3390/pharmaceutics14122661

Baik, S., Heo, H., Hong, S., Sang Jeong, H., Lee, J., & Lee, H. (2024). Combination of Nicotinamide and Agastache rugosa Extract: A Potent Strategy for Protecting Hs68 Cells from UVB-Induced Photoaging. *Preventive Nutrition and Food Science*, *29*(2), 162–169. https://doi.org/10.3746/pnf.2024.29.2.162

Batista, A. P., Gouveia, L., Bandarra, N. M., Franco, J. M., & Raymundo, A. (2013). Comparison of microalgal biomass profiles as novel functional ingredient for food products. *Algal Research*, *2*(2), 164–173. https://doi.org/10.1016/j.algal.2013.01.004

Baylan, M., Devrim Özcan, B., Işik, O., & Akar, M. (2012). *A Mini Review on Spirulina*. www.nobel.gen.tr

Bazgir, M., Saeinasab, M., Zhang, W., Zhang, X., Min Tsui, K., Maasoumi Sarvestani, A., Nawaz, S., Coates, P., Youseffi, M., Elies, J., & Sefat, F. (2022). Investigation of Cell Adhesion and Cell Viability of the Endothelial and Fibroblast Cells on Electrospun PCL, PLGA and Coaxial Scaffolds for Production of Tissue Engineered Blood Vessel. *Journal of Functional Biomaterials*, *13*(4). https://doi.org/10.3390/jfb13040282

Becker, E. W. (2007). Micro-algae as a source of protein. In *Biotechnology Advances* (Vol. 25, Number 2, pp. 207–210). https://doi.org/10.1016/j.biotechadv.2006.11.002

Becker, M. L., & Burdick, J. A. (2021). Introduction: Polymeric Biomaterials. In *Chemical Reviews* (Vol. 121, Number 18, pp. 10789–10791). American Chemical Society. https://doi.org/10.1021/acs.chemrev.1c00354

Behzadi, S., Serpooshan, V., Tao, W., Hamaly, M. A., Alkawareek, M. Y., Dreaden, E. C., Brown, D., Alkilany, A. M., Farokhzad, O. C., & Mahmoudi, M. (2017). Cellular uptake of nanoparticles: Journey inside the cell. In *Chemical Society Reviews* (Vol. 46, Number 14, pp. 4218–4244). Royal Society of Chemistry. https://doi.org/10.1039/c6cs00636a

Bencheikh, A., Mamache, W., Gharzouli, A., Kouachi, A., Khadidja, H., Daichi, M. B., & Rouag, N. (2022). Evaluation of The Spirulina (Arthrospira platensis Gomont) Antimicrobial Activity. *Turkish Journal of Agriculture - Food Science and Technology*, *10*(10), 2051–2055. https://doi.org/10.24925/turjaf.v10i10.2051-2055.5307

Berrak, Ö., Akkoç, Y., Arisan, E. D., Çoker-Gürkan, A., Obakan-Yerlikaya, P., & Palavan-Ünsal, N. (2016). The inhibition of PI3K and NFκB promoted curcumin-induced cell cycle arrest at G2/M via altering polyamine metabolism in Bcl-2 overexpressing MCF-7 breast cancer cells. *Biomedicine and Pharmacotherapy*, *77*, 150–160. https://doi.org/10.1016/j.biopha.2015.12.007

Bock, N., Dargaville, T. R., & Woodruff, M. A. (2012). Electrospraying of polymers with therapeutic molecules: State of the art. In *Progress in Polymer Science* (Vol. 37, Number 11, pp. 1510–1551). https://doi.org/10.1016/j.progpolymsci.2012.03.002

Boda, S. K., Li, X., & Xie, J. (2018). Electrospraying an enabling technology for pharmaceutical and biomedical applications: A review. In *Journal of Aerosol Science* (Vol. 125, pp. 164–181). Elsevier Ltd. https://doi.org/10.1016/j.jaerosci.2018.04.002

Boo, Y. C. (2022). Ascorbic Acid (Vitamin C) as a Cosmeceutical to Increase Dermal Collagen for Skin Antiaging Purposes: Emerging Combination Therapies. In *Antioxidants* (Vol. 11, Number 9). MDPI. https://doi.org/10.3390/antiox11091663

Bortolini, D. G., Maciel, G. M., Fernandes, I. de A. A., Pedro, A. C., Rubio, F. T. V., Branco, I. G., & Haminiuk, C. W. I. (2022). Functional properties of bioactive compounds from Spirulina spp.: Current status and future trends. *Food Chemistry: Molecular Sciences*, *5*. https://doi.org/10.1016/j.fochms.2022.100134

Brand-Williams, W., Cuvelier, M. E., & Berset, C. (1995). Use of a free radical method to evaluate antioxidant activity. *LWT - Food Science and Technology*, *28*(1), 25–30. https://doi.org/10.1016/S0023-6438(95)80008-5

Branyikova, I., & Lucakova, S. (2021). Technical and physiological aspects of microalgae cultivation and productivity—Spirulina as a promising and feasible choice. *Organic Agriculture*, *11*(2), 269–276. https://doi.org/10.1007/s13165-020-00323-1

Brito, S., Baek, M., & Bin, B. H. (2024). Skin Structure, Physiology, and Pathology in Topical and Transdermal Drug Delivery. In *Pharmaceutics* (Vol. 16, Number 11). Multidisciplinary Digital Publishing Institute (MDPI). https://doi.org/10.3390/pharmaceutics16111403

Calella, P., Cerullo, G., Di Dio, M., Liguori, F., Di Onofrio, V., Gallè, F., & Liguori, G. (2022). Antioxidant, anti-inflammatory and immunomodulatory effects of Spirulina in exercise and sport: A systematic review. In *Frontiers in Nutrition* (Vol. 9). Frontiers Media S.A. https://doi.org/10.3389/fnut.2022.1048258

Capelli, B., & Cysewski, G. R. (2010). Potential health benefits of Spirulina microalgae. A review of the existing literature. *Nutra Food*, *9*(2), 19–26.

Capuana, E., Lopresti, F., Ceraulo, M., & La Carrubba, V. (2022). Poly-L-Lactic Acid (PLLA)-Based Biomaterials for Regenerative Medicine: A Review on Processing and Applications. In *Polymers* (Vol. 14, Number 6). MDPI. https://doi.org/10.3390/polym14061153

Cardoso, J. J. F., Ricci-Júnior, E., Gentili, D., Spinelli, L. S., & Lucas, E. F. (2018). Influence of cardanol encapsulated on the properties of poly(lactic acid) microparticles. *Quimica Nova*, *41*(3), 273–283. https://doi.org/10.21577/0100-4042.20170165

Casalini, T., Rossi, F., Castrovinci, A., & Perale, G. (2019). A Perspective on Polylactic Acid-Based Polymers Use for Nanoparticles Synthesis and Applications. In *Frontiers in Bioengineering and Biotechnology* (Vol. 7). Frontiers Media S.A. https://doi.org/10.3389/fbioe.2019.00259

Cepoi, L., Chiriac, T., Sadovnic, D., Xvi /, T., Rudi, L., Miscu, V., & Cojocari, A. (2009). *Antioxidative activity of ethanol extracts from Spirulina platensis and Nostoc linckia measured by various methods Analele Universitii din Oradea, Fascicula Biologie ANTIOXIDATIVE ACTIVITY OF ETHANOL EXTRACTS FROM Spirulina platensis AND Nostoc linckia ME*. *February 2014*, 43–48. https://www.researchgate.net/publication/40422973

Černochová, P., Blahová, L., Medalová, J., Nečas, D., Michlíček, M., Kaushik, P., Přibyl, J., Bartošíková, J., Manakhov, A., Bačáková, L., & Zajíčková, L. (2020). Cell type specific adhesion to surfaces functionalised by amine plasma polymers. *Scientific Reports*, *10*(1). https://doi.org/10.1038/s41598-020-65889-y

Choi, W. Y., Sim, J. H., Lee, J. Y., Kang, D. H., & Lee, H. Y. (2019). Increased anti-inflammatory effects on LPS-induced microglia cells by Spirulina maxima extract

from ultrasonic process. *Applied Sciences (Switzerland)*, *9*(10). https://doi.org/10.3390/app9102144

Chou, T. H., Lin, C. H., & Chang, J. Y. (2024). The impact of palmitoyl glycyl-histidyl-lysine on phospholipid model membranes. *Journal of the Taiwan Institute of Chemical Engineers*, *160*. https://doi.org/10.1016/j.jtice.2023.105289

Ciarlantini, C., Francolini, I., Silvestro, I., Mariano, A., d'Abusco, A. S., & Piozzi, A. (2024). Design of bioactive and biomimetic scaffolds based on chitosan-alginate polyelectrolyte complexes for tissue engineering. *Carbohydrate Polymers*, *327*. https://doi.org/10.1016/j.carbpol.2023.121684

Coker-Gurkan, A., Bulut, D., Genc, R., Arisan, E. D., Obakan-Yerlikaya, P., & Palavan-Unsal, N. (2019). Curcumin prevented human autocrine growth hormone (GH) signaling mediated NF-κB activation and miR-183-96-182 cluster stimulated epithelial mesenchymal transition in T47D breast cancer cells. *Molecular Biology Reports*, *46*(1), 355–369. https://doi.org/10.1007/s11033-018-4479-y

Cramer, M. C., & Badylak, S. F. (2020). Extracellular Matrix-Based Biomaterials and Their Influence Upon Cell Behavior. *Annals of Biomedical Engineering*, *48*(7), 2132–2153. https://doi.org/10.1007/s10439-019-02408-9

da Silva, R. Y. P., de Menezes, D. L. B., Oliveira, V. da S., Converti, A., & de Lima, Á. A. N. (2023). Microparticles in the Development and Improvement of Pharmaceutical Formulations: An Analysis of In Vitro and In Vivo Studies. In *International Journal of Molecular Sciences* (Vol. 24, Number 6). Multidisciplinary Digital Publishing Institute (MDPI). https://doi.org/10.3390/ijms24065441

Dalbayrak, B., Aksan Kurnaz, I., Cesur, S., Gunduz, O., & Arısan, E. D. (2025). Biocompatible PLA/Spirulina microparticles via electrospraying for targeted drug delivery in HUVEC and HaCaT cell lines. *Journal of Biomaterials Science, Polymer Edition*. https://doi.org/10.1080/09205063.2025.2503928

Danaei, M., Dehghankhold, M., Ataei, S., Hasanzadeh Davarani, F., Javanmard, R., Dokhani, A., Khorasani, S., & Mozafari, M. R. (2018). Impact of particle size and polydispersity index on the clinical applications of lipidic nanocarrier systems. In *Pharmaceutics* (Vol. 10, Number 2). MDPI AG. https://doi.org/10.3390/pharmaceutics10020057

Danhier, F., Ansorena, E., Silva, J. M., Coco, R., Le Breton, A., & Préat, V. (2012). PLGA-based nanoparticles: An overview of biomedical applications. In *Journal of Controlled Release* (Vol. 161, Number 2, pp. 505–522). https://doi.org/10.1016/j.jconrel.2012.01.043

De Freitas Brito, A., Silva, A. S., De Souza, A. A., Ferreira, P. B., De Souza, I. L. L., Da Cunha Araujo, L. C., Da Silva Félix, G., De Souza Sampaio, R., Da Conceicąõ Correia Silva, M., Tavares, R. L., De Andrade Pereira, R., Neto, M. M., & Silva, B. A. (2019). Supplementation with Spirulina platensis Modulates Aortic Vascular Reactivity through Nitric Oxide and Antioxidant Activity. *Oxidative Medicine and Cellular Longevity*, *2019*. https://doi.org/10.1155/2019/7838149

De Jong, W. H., & Borm, P. J. (2008). Drug delivery and nanoparticles: Applications and hazards. In *International Journal of Nanomedicine* (Vol. 3, Number 2).

Deng, H., Min, E., Baeyens, N., Coon, B. G., Hu, R., Zhuang, Z. W., Chen, M., Huang, B., Afolabi, T., Zarkada, G., Acheampong, A., Mcentee, K., Eichmann, A., Liu, F., Su, B., Simons, M., & Schwartz, M. A. (2021). Activation of Smad2/3 signaling by low fluid shear stress mediates artery inward remodeling. *Proc Natl Acad Sci U S A*, 118–137. https://doi.org/10.1073/pnas.2105339118/-/DCSupplemental

Desai, N. (2012). Challenges in development of nanoparticle-based therapeutics. In *AAPS Journal* (Vol. 14, Number 2, pp. 282–295). https://doi.org/10.1208/s12248-012-9339-4

ElFar, O. A., Billa, N., Lim, H. R., Chew, K. W., Cheah, W. Y., Munawaroh, H. S. H., Balakrishnan, D., & Show, P. L. (2022). Advances in delivery methods of Arthrospira platensis (Spirulina) for enhanced therapeutic outcomes. In *Bioengineered* (Vol. 13, Number 6, pp. 14681–14718). Taylor and Francis Ltd. https://doi.org/10.1080/21655979.2022.2100863

El-Naggar, N. E. A., Hussein, M. H., Shaaban-Dessuuki, S. A., & Dalal, S. R. (2020). Production, extraction and characterization of Chlorella vulgaris soluble polysaccharides and their applications in AgNPs biosynthesis and biostimulation of plant growth. *Scientific Reports*, *10*(1). https://doi.org/10.1038/s41598-020-59945-w

Elsawy, M. A., Kim, K. H., Park, J. W., & Deep, A. (2017). Hydrolytic degradation of polylactic acid (PLA) and its composites. In *Renewable and Sustainable Energy Reviews* (Vol. 79, pp. 1346–1352). Elsevier Ltd. https://doi.org/10.1016/j.rser.2017.05.143

Esfahani, S. A., Khoshneviszadeh, M., Namazi, M. R., Noorafshan, A., Geramizadeh, B., Nadimi, E., & Razavipour, S. T. (2015). Topical nicotinamide improves tissue regeneration in excisional full-thickness skin wounds: A stereological and pathological study. *Trauma Monthly*, *20*(4). https://doi.org/10.5812/traumamon.18193

Eze, C. N., Onyejiaka, C. K., Ihim, S. A., Ayoka, T. O., Aduba, C. C., Ndukwe, J. K., Nwaiwu, O., & Onyeaka, H. (2023). Bioactive compounds by microalgae and potentials for the management of some human disease conditions. In *AIMS Microbiology* (Vol. 9, Number 1, pp. 55–74). AIMS Press. https://doi.org/10.3934/microbiol.2023004

Fernández de la Mora, J. (2007). The fluid dynamics of Taylor Cones. In *Annual Review of Fluid Mechanics* (Vol. 39, pp. 217–243). https://doi.org/10.1146/annurev.fluid.39.050905.110159

Finamore, A., Palmery, M., Bensehaila, S., & Peluso, I. (2017). Antioxidant, Immunomodulating, and Microbial-Modulating Activities of the Sustainable and Ecofriendly Spirulina. In *Oxidative Medicine and Cellular Longevity* (Vol. 2017). Hindawi Limited. https://doi.org/10.1155/2017/3247528

Flores Hernandez, F. Y., Khandual, S., & Ramírez López, I. G. (2017). Cytotoxic effect of Spirulina platensis extracts on human acute leukemia Kasumi-1 and chronic

myelogenous leukemia K-562 cell lines. *Asian Pacific Journal of Tropical Biomedicine*, *7*(1), 14–19. https://doi.org/10.1016/j.apjtb.2016.10.011

Fratelli, C., Burck, M., Amarante, M. C. A., & Braga, A. R. C. (2021). Antioxidant potential of nature's "something blue": Something new in the marriage of biological activity and extraction methods applied to C-phycocyanin. In *Trends in Food Science and Technology* (Vol. 107, pp. 309–323). Elsevier Ltd. https://doi.org/10.1016/j.tifs.2020.10.043

Fujio, Y., & Walsh, K. (1999). *Akt Mediates Cytoprotection of Endothelial Cells by Vascular Endothelial Growth Factor in an Anchorage-dependent Manner*.*

Ganceviciene, R., Liakou, A. I., Theodoridis, A., Makrantonaki, E., & Zouboulis, C. C. (2012). Skin anti-aging strategies. In *Dermato-Endocrinology* (Vol. 4, Number 3). https://doi.org/10.4161/derm.22804

Ganju, E., Dubey, R., Shama, S., & Kumar-Gupta, B. (2025). Microspheres as Novel Drug Delivery Advantages and Application: A Review. *Int. J. of Pharm. Sci*, *3*, 1525–1535. https://doi.org/10.5281/zenodo.15202876

Ge, Y., Li, M., Bai, S., Chen, C., Zhang, S., Cheng, J., & Wang, X. (2024). Doxercalciferol alleviates UVB-induced HaCaT cell senescence and skin photoaging. *International Immunopharmacology*, *127*. https://doi.org/10.1016/j.intimp.2023.111357

Ghosh, S., Ganguly, D., Majumder, S., & Chowdhury, A. (2022). Advancement of Targeted Drug Delivery Over Conventional Drug Delivery System Targeting to Colonic Region. *International Journal of Pharmaceutical Sciences Review and Research*, 92–96. https://doi.org/10.47583/ijpsrr.2022.v73i02.018

Giménez Martínez, R. J., Rivas García, F., March Cerdá, J. C., Hernández-Ruíz, Á., González Castro, M. I., Valverde-Merino, M. I., Huertas Camarasa, F. J., Lloris Meseguer, F., & López-Viota Gallardo, M. (2025). Bioactive Substances and Skin Health: An Integrative Review from a Pharmacy and Nutrition Perspective. In *Pharmaceuticals* (Vol. 18, Number 3). Multidisciplinary Digital Publishing Institute (MDPI). https://doi.org/10.3390/ph18030373

Goldberg, M., Langer, R., & Jia, X. (2006). Nanostructured materials for applications in drug delivery and tissue engineering. In *J. Biomater. Sci. Polymer Edn* (Vol. 17, Number 11).

Gopinath, P. M., Twayana, K. S., Ravanan, P., John Thomas, Mukherjee, A., Jenkins, D. F., & Chandrasekaran, N. (2021). Prospects on the nano-plastic particles internalization and induction of cellular response in human keratinocytes. *Particle and Fibre Toxicology*, *18*(1). https://doi.org/10.1186/s12989-021-00428-9

Gorzelanny, C., Mess, C., Schneider, S. W., Huck, V., & Brandner, J. M. (2020). Skin barriers in dermal drug delivery: Which barriers have to be overcome and how can we measure them? In *Pharmaceutics* (Vol. 12, Number 7, pp. 1–31). MDPI AG. https://doi.org/10.3390/pharmaceutics12070684

Gregor, A., Filová, E., Novák, M., Kronek, J., Chlup, H., Buzgo, M., Blahnová, V., Lukášová, V., Bartoš, M., Nečas, A., & Hošek, J. (2017). Designing of PLA scaffolds for bone tissue replacement fabricated by ordinary commercial 3D printer. *Journal of Biological Engineering*, *11*(1). https://doi.org/10.1186/s13036-017-0074-3

Gromkowska-Kępka, K. J., Puścion-Jakubik, A., Markiewicz-Żukowska, R., & Socha, K. (2021). The impact of ultraviolet radiation on skin photoaging — review of in vitro studies. In *Journal of Cosmetic Dermatology* (Vol. 20, Number 11, pp. 3427–3431). John Wiley and Sons Inc. https://doi.org/10.1111/jocd.14033

Grosshagauer, S., Kraemer, K., & Somoza, V. (2020). The True Value of Spirulina. In *Journal of Agricultural and Food Chemistry* (Vol. 68, Number 14, pp. 4109–4115). American Chemical Society. https://doi.org/10.1021/acs.jafc.9b08251

Gul, A., Ahmed, D., Fazil, M. M., Aslam, T., Rashid, M. A., Khan, H., Ali, A., & Ali, S. (2023). Biofabrication of silver nanoparticles using Spirulina platensis: In vitro anti-coagulant, thrombolytic and catalytic dye degradation activity. *Microscopy Research and Technique*, *May*, 1–11. https://doi.org/10.1002/jemt.24344

Gunes, S., Tamburaci, S., Dalay, M. C., & Gurhan, I. D. (2017). In vitro evaluation of Spirulina platensis extract incorporated skin cream with its wound healing and antioxidant activities. *Pharmaceutical Biology*, *55*(1), 1824–1832. https://doi.org/10.1080/13880209.2017.1331249

Guo, K., Liu, R., Jing, R., Wang, L., Li, X., Zhang, K., Fu, M., Ye, J., Hu, Z., Zhao, W., & Xu, N. (2022). Cryptotanshinone protects skin cells from ultraviolet radiation-induced photoaging via its antioxidant effect and by reducing mitochondrial dysfunction and inhibiting apoptosis. *Frontiers in Pharmacology*, *13*. https://doi.org/10.3389/fphar.2022.1036013

Guo, W., Li, A., Jia, Z., Yuan, Y., Dai, H., & Li, H. (2013). Transferrin modified PEG-PLA-resveratrol conjugates: In vitro and in vivo studies for glioma. *European Journal of Pharmacology*, *718*(1–3), 41–47. https://doi.org/10.1016/j.ejphar.2013.09.034

Habibi, R., Tadayoni, M., & Mohammadpour, H. (2024). Evaluation of the functional properties of ethanolic and polysaccharide extracts of Spirulina platensis. *Bioactive Carbohydrates and Dietary Fibre*, *31*. https://doi.org/10.1016/j.bcdf.2024.100401

He, Q., Liao, Y., Wu, Y., Zhang, H., Long, X., & Zhang, Y. (2025). Bioactive oligopeptides and the application in skin regeneration and rejuvenation. In *Journal of Applied Biomaterials and Functional Materials* (Vol. 23). SAGE Publications Ltd. https://doi.org/10.1177/22808000251330974

He, X., Gao, X., Guo, Y., & Xie, W. (2024). Research Progress on Bioactive Factors against Skin Aging. In *International Journal of Molecular Sciences* (Vol. 25, Number 7). Multidisciplinary Digital Publishing Institute (MDPI). https://doi.org/10.3390/ijms25073797

Hu, T., Fang, J., Shen, Y., Li, M., Wang, B., Xu, Z., & Hu, W. (2024). Advances of naturally derived biomedical polymers in tissue engineering. In *Frontiers in*

Chemistry (Vol. 12). Frontiers Media SA. https://doi.org/10.3389/fchem.2024.1469183

Huang, S., Chen, B., Humeres, C., Alex, L., Hanna, A., & Frangogiannis, N. G. (2020). The role of Smad2 and Smad3 in regulating homeostatic functions of fibroblasts in vitro and in adult mice. *Biochimica et Biophysica Acta - Molecular Cell Research*, *1867*(7). https://doi.org/10.1016/j.bbamcr.2020.118703

Ikeda, I. K., Sydney, E. B., & Sydney, A. C. N. (2022). Potential application of Spirulinain dermatology. In *Journal of Cosmetic Dermatology* (Vol. 21, Number 10, pp. 4205–4214). John Wiley and Sons Inc. https://doi.org/10.1111/jocd.14997

Jadach, B., Mielcarek, Z., & Osmałek, T. (2024). Use of Collagen in Cosmetic Products. In *Current Issues in Molecular Biology* (Vol. 46, Number 3, pp. 2043–2070). Multidisciplinary Digital Publishing Institute (MDPI). https://doi.org/10.3390/cimb46030132

Janda-Milczarek, K., Szymczykowska, K., Jakubczyk, K., Kupnicka, P., Skonieczna-Żydecka, K., Pilarczyk, B., Tomza-Marciniak, A., Ligenza, A., Stachowska, E., & Dalewski, B. (2023). Spirulina Supplements as a Source of Mineral Nutrients in the Daily Diet. *Applied Sciences (Switzerland)*, *13*(2). https://doi.org/10.3390/app13021011

Jang, Y. A., & Kim, B. A. (2021). Protective effect of Spirulina-derived c-phycocyanin against ultraviolet b-induced damage in hacat cells. *Medicina (Lithuania)*, *57*(3). https://doi.org/10.3390/medicina57030273

Jesús Villarreal-Gómez, L., Vera-Graziano, R., Raquel Vega-Ríos, M., Luis Pineda-Camacho, J., Almanza-Reyes, H., Mier-Maldonado, P. A., & Cornejo-Bravo, J. M. (2014). Biocompatibility Evaluation of Electrospun Scaffolds of Poly (L-Lactide) with Pure and Grafted Hydroxyapatite Biocompatibility Evaluation of Electrospun Scaffolds of Poly (L-Lactide) with Pure and Grafted Hydroxyapatite Article. In *Chem. Soc* (Vol. 58, Number 4).

Jiang, L., Wang, Y., Liu, G., Liu, H., Zhu, F., Ji, H., & Li, B. (2018). C-Phycocyanin exerts anti-cancer effects via the MAPK signaling pathway in MDA-MB-231 cells. *Cancer Cell International*, *18*(1). https://doi.org/10.1186/s12935-018-0511-5

Johnson, W., Bergfeld, W. F., Belsito, D. V., Hill, R. A., Klaassen, C. D., Liebler, D. C., Marks, J. G., Shank, R. C., Slaga, T. J., Snyder, P. W., Gill, L. J., & Heldreth, B. (2018). Safety Assessment of Tripeptide-1, Hexapeptide-12, Their Metal Salts and Fatty Acyl Derivatives, and Palmitoyl Tetrapeptide-7 as Used in Cosmetics. *International Journal of Toxicology*, *37*(3_suppl), 90S-102S. https://doi.org/10.1177/1091581818807863

Jung, F., Krüger-Genge, A., Waldeck, P., & Küpper, J. H. (2019). Spirulina platensis, a super food? *Journal of Cellular Biotechnology*, *5*(1), 43–54. https://doi.org/10.3233/JCB-189012

K C, P. B., Maharjan, A., Acharya, M., Lee, D. E., Kusma, S., Gautam, R., Kwon, J. T., Kim, C. Y., Kim, K. S., Kim, H. A., & Heo, Y. (2023). Polytetrafluorethylene microplastic particles mediated oxidative stress, inflammation, and intracellular

signaling pathway alteration in human derived cell lines. *Science of the Total Environment*, *897*. https://doi.org/10.1016/j.scitotenv.2023.165295

Karabay, U., Bugra Husemoglu, R., Yuksel Egrilmez, M., & Havitcioglu, H. (2019). 3D Printed Polylactic Acid Scaffold For Dermal Tissue Engineering Application: The Fibroblast Proliferation in Vitro Dermal Doku Mühendisliği Uygulaması için 3B Baskılı Doku İskelesi: In vitro Fibroblast Proliferasyonu. In *JOMIT Research Article Journal Med. Inv. Tech* (Vol. 1, Number 2).

Karimi, N. (2023). Approaches in line with human physiology to prevent skin aging. In *Frontiers in Physiology* (Vol. 14). Frontiers Media SA. https://doi.org/10.3389/fphys.2023.1279371

Karizi, S. rajabzadeh, Armanmehr, F., Azadi, H. G., Zahroodi, H. S., Ghalibaf, A. A. M., Bazzaz, B. S. F., Abbaspour, M., Boskabadi, J., Eslami, S., & Taherzadeh, Z. (2023). A randomized, double-blind placebo-controlled add-on trial to assess the efficacy, safety, and anti-atherogenic effect of Spirulina platensis in patients with inadequately controlled type 2 diabetes mellitus. *Phytotherapy Research*, *October 2022*, 1435–1448. https://doi.org/10.1002/ptr.7674

Kaval, B., Şen, F. D., Batmaz, K. K., Ekinci, M., & Öztürk, A. A. (2023). Latest research about active pharmaceutical ingredient loaded Poly Lactic Acid-co-Glycolic Acid (PLGA) based drug delivery system in Türkiye. *European Journal of Life Sciences*, *1*(3), 127–139. https://doi.org/10.55971/ejls.1197082

Khan, Z., Bhadouria, P., & Bisen, P. S. (2005). Nutritional and Therapeutic Potential of Spirulina. In *Current Pharmaceutical Biotechnology* (Vol. 6).

Khouri, N. G., Bahú, J. O., Blanco-Llamero, C., Severino, P., Concha, V. O. C., & Souto, E. B. (2024). Polylactic acid (PLA): Properties, synthesis, and biomedical applications – A review of the literature. In *Journal of Molecular Structure* (Vol. 1309). Elsevier B.V. https://doi.org/10.1016/j.molstruc.2024.138243

Kim, J. Y., Lee, S. J., Baik, G. Y., & Hong, J. G. (2021). Viscosity Effect on the Electrospray Characteristics of Droplet Size and Distribution. *ACS Omega*, *6*(44), 29724–29734. https://doi.org/10.1021/acsomega.1c04119

Kohane, D. S., & Langer, R. (2008). *Polymeric Biomaterials in Tissue Engineering*.

Kozlowska, J., Prus, W., & Stachowiak, N. (2019). Microparticles based on natural and synthetic polymers for cosmetic applications. *International Journal of Biological Macromolecules*, *129*, 952–956. https://doi.org/10.1016/j.ijbiomac.2019.02.091

Krüger-Genge, A., Harb, K., Braune, S., Jung, C. H. G., Westphal, S., Bär, S., Mauger, O., Küpper, J.-H., & Jung, F. (2024). *Effects of Arthrospira platensis on Human Umbilical Vein Endothelial Cells*. https://doi.org/10.3390/life

Kumar, M., Kulshreshtha, J., & Singh, G. P. (2011). GROWTH AND BIOPIGMENT ACCUMULATION OF CYANOBACTERIUM SPIRULINA PLATENSIS AT DIFFERENT LIGHT INTENSITIES AND TEMPERATURE. *Brazilian Journal of Microbiology*, *42*, 1128–1135.

Lagreca, E., Onesto, V., Di Natale, C., La Manna, S., Netti, P. A., & Vecchione, R. (2020). Recent advances in the formulation of PLGA microparticles for controlled drug delivery. In *Progress in Biomaterials* (Vol. 9, Number 4, pp. 153–174). Springer Science and Business Media Deutschland GmbH. https://doi.org/10.1007/s40204-020-00139-y

Lee, H., An, S., Kim, S., Jeon, B., Kim, M., & Kim, I. S. (2018). Readily Functionalizable and Stabilizable Polymeric Particles with Controlled Size and Morphology by Electrospray. *Scientific Reports*, *8*(1). https://doi.org/10.1038/s41598-018-34124-0

Lee, J. J., Kim, K. B., Heo, J., Cho, D. H., Kim, H. S., Han, S. H., Ahn, K. J., An, I. S., An, S., & Bae, S. (2017). Protective effect of Arthrospira platensis extracts against ultraviolet B-induced cellular senescence through inhibition of DNA damage and matrix metalloproteinase-1 expression in human dermal fibroblasts. *Journal of Photochemistry and Photobiology B: Biology*, *173*, 196–203. https://doi.org/10.1016/j.jphotobiol.2017.05.042

Lee, M. Y., Luciano, A. K., Ackah, E., Rodriguez-Vitad, J., Bancroft, T. A., Eichmann, A., Simons, M., Kyriakides, T. R., Morales-Ruiz, M., & Sessa, W. C. (2014). Endothelial Akt1 mediates angiogenesis by phosphorylating multiple angiogenic substrates. *Proceedings of the National Academy of Sciences of the United States of America*, *111*(35), 12865–12870. https://doi.org/10.1073/pnas.1408472111

Leonel, C., Sena, I. F. G., Silva, W. N., Prazeres, P. H. D. M., Fernandes, G. R., Mancha Agresti, P., Martins Drumond, M., Mintz, A., Azevedo, V. A. C., & Birbrair, A. (2019). Staphylococcus epidermidis role in the skin microenvironment. *Journal of Cellular and Molecular Medicine*, *23*(9), 5949–5955. https://doi.org/10.1111/jcmm.14415

Lewis, J. S., Dolgova, N. V., Zhang, Y., Xia, C. Q., Wasserfall, C. H., Atkinson, M. A., Clare-Salzler, M. J., & Keselowsky, B. G. (2015). A combination dual-sized microparticle system modulates dendritic cells and prevents type 1 diabetes in prediabetic NOD mice. *Clinical Immunology*, *160*(1), 90–102. https://doi.org/10.1016/j.clim.2015.03.023

Li, F., Chen, H., Chen, D., Zhang, B., Shi, Q., He, X., Zhao, H., & Wang, F. (2023). Clinical evidence of the efficacy and safety of a new multi-peptide anti-aging topical eye serum. *Journal of Cosmetic Dermatology*, *22*(12), 3340–3346. https://doi.org/10.1111/jocd.15849

Li, W., Zhang, L., Ge, X., Xu, B., Zhang, W., Qu, L., Choi, C. H., Xu, J., Zhang, A., Lee, H., & Weitz, D. A. (2018). Microfluidic fabrication of microparticles for biomedical applications. In *Chemical Society Reviews* (Vol. 47, Number 15, pp. 5646–5683). Royal Society of Chemistry. https://doi.org/10.1039/c7cs00263g

Li, Y., & Zhang, Z. Z. (2018). Sustained curcumin release from PLGA microspheres improves bone formation under diabetic conditions by inhibiting the reactive oxygen species production. *Drug Design, Development and Therapy*, *12*, 1453–1466. https://doi.org/10.2147/DDDT.S154334

Liestianty, D., Rodianawati, I., Arfah, R. A., Assa, A., Patimah, Sundari, & Muliadi. (2019). Nutritional analysis of Spirulina sp to promote as superfood candidate. *IOP Conference Series: Materials Science and Engineering*, *509*(1). https://doi.org/10.1088/1757-899X/509/1/012031

Liu, P., Choi, J. W., Lee, M. K., Choi, Y. H., & Nam, T. J. (2020). Spirulina protein promotes skin wound repair in a mouse model of full-thickness dermal excisional wound. *International Journal of Molecular Medicine*, *46*(1), 351–359. https://doi.org/10.3892/ijmm.2020.4571

Liu, P., Lee, M. K., Choi, J. W., Choi, Y. H., & Nam, T. J. (2019). Crude protein from Spirulina increases the viability of CCD-986sk cells via the EGFR/MAPK signaling pathway. *International Journal of Molecular Medicine*, *43*(2), 771–778. https://doi.org/10.3892/ijmm.2018.4025

Liu, Q., Huang, Y., Zhang, R., Cai, T., & Cai, Y. (2016). Medical Application of Spirulina platensis Derived C-Phycocyanin. In *Evidence-based Complementary and Alternative Medicine* (Vol. 2016). Hindawi Limited. https://doi.org/10.1155/2016/7803846

Liu, Ronggang, Li, Y., Zhou, C., & Tan, M. (2023). Pickering emulsions stabilized with a Spirulina protein-chitosan complex for astaxanthin delivery. *Food and Function*, 4254–4266. https://doi.org/10.1039/d3fo00092c

Liu, Runze, Qin, S., & Li, W. (2022). Phycocyanin: Anti-inflammatory effect and mechanism. In *Biomedicine and Pharmacotherapy* (Vol. 153). Elsevier Masson s.r.l. https://doi.org/10.1016/j.biopha.2022.113362

Lopes, M. S., Jardini, A. L., & Filho, R. M. (2014). Synthesis and characterizations of poly (lactic acid) by ring-opening polymerization for biomedical applications. *Chemical Engineering Transactions*, *38*, 331–336. https://doi.org/10.3303/CET1438056

Machu, L., Misurcova, L., Ambrozova, J. V., Orsavova, J., Mlcek, J., Sochor, J., & Jurikova, T. (2015). Phenolic content and antioxidant capacity in algal food products. *Molecules*, *20*(1), 1118–1133. https://doi.org/10.3390/molecules20011118

Makadia, H. K., & Siegel, S. J. (2011). Poly Lactic-co-Glycolic Acid (PLGA) as biodegradable controlled drug delivery carrier. *Polymers*, *3*(3), 1377–1397. https://doi.org/10.3390/polym3031377

Marques, C., Hadjab, F., Porcello, A., Lourenço, K., Scaletta, C., Abdel-Sayed, P., Hirt-Burri, N., Applegate, L. A., & Laurent, A. (2024). Mechanistic Insights into the Multiple Functions of Niacinamide: Therapeutic Implications and Cosmeceutical Applications in Functional Skincare Products. In *Antioxidants* (Vol. 13, Number 4). Multidisciplinary Digital Publishing Institute (MDPI). https://doi.org/10.3390/antiox13040425

Martín-Martínez, A., Sánchez-Marzo, N., Martínez-Casanova, D., Abarquero-Cerezo, M., Herranz-López, M., Barrajón-Catalán, E., & Matabuena-Yzaguirre, M. (2022). High global antioxidant protection and stimulation of the collagen synthesis of new

anti-aging product containing an optimized active mix. *Journal of Cosmetic Dermatology*, *21*(9), 3993–4000. https://doi.org/10.1111/jocd.14703

Masojídek, J., Ranglová, K., Lakatos, G. E., Benavides, A. M. S., & Torzillo, G. (2021). Variables governing photosynthesis and growth in microalgae mass cultures. In *Processes* (Vol. 9, Number 5). MDPI AG. https://doi.org/10.3390/pr9050820

Md Fadilah, N. I., Rahman, M. B. A., Yusof, L. M., Mustapha, N. M., & Ahmad, H. (2021). The therapeutic effect and in vivo assessment of palmitoyl-gdph on the wound healing process. *Pharmaceutics*, *13*(2), 1–26. https://doi.org/10.3390/pharmaceutics13020193

Meyers, J. (2023). The Importance of Drug Delivery: An Innovative Approach for Revolutionizing Helathcare. *Drug Des*, *12*, 1000254–1000255. https://doi.org/10.35248/2169-0138.12.254

Middleton, J. C., & Tipton, A. J. (2000). Synthetic biodegradable polymers as orthopedic devices. *Biomaterials*, *21*, 2335–2346.

Mishra, S., Johnson, L., Sangha, K., Gupta, V., Agarwal, S., & Rajput, S. (2021). An In Vitro Study to Determine the Physicochemical , Mechanical , and Antibacterial Properties of a Novel Spirulina Containing Controlled Release Intrapocket Drug Delivery System An In Vitro Study to Determine the Physicochemical , Mechanical , and Antiba. *Journal of Pharmacy and Bioallied Sciences*, *13*(2), 178–187. https://doi.org/10.4103/jpbs.JPBS_446_20 This

Moore, T. L., Cook, A. B., Bellotti, E., Palomba, R., Manghnani, P., Spanò, R., Brahmachari, S., Di Francesco, M., Palange, A. L., Di Mascolo, D., & Decuzzi, P. (2022). Shape-specific microfabricated particles for biomedical applications: a review. *Drug Delivery and Translational Research*, *12*(8), 2019–2037. https://doi.org/10.1007/s13346-022-01143-4

Morais, A. Í. S., Vieira, E. G., Afewerki, S., Sousa, R. B., Honorio, L. M. C., Cambrussi, A. N. C. O., Santos, J. A., Bezerra, R. D. S., Furtini, J. A. O., Silva-Filho, E. C., Webster, T. J., & Lobo, A. O. (2020). Fabrication of polymeric microparticles by electrospray: The impact of experimental parameters. In *Journal of Functional Biomaterials* (Vol. 11, Number 1). MDPI AG. https://doi.org/10.3390/jfb11010004

Moya-Lopez, C., González-Fuentes, J., Bravo, I., Chapron, D., Bourson, P., Alonso-Moreno, C., & Hermida-Merino, D. (2022). Polylactide Perspectives in Biomedicine: From Novel Synthesis to the Application Performance. In *Pharmaceutics* (Vol. 14, Number 8). MDPI. https://doi.org/10.3390/pharmaceutics14081673

Mukherjee, P. K., Maity, N., Nema, N. K., & Sarkar, B. K. (2011). Bioactive compounds from natural resources against skin aging. *Phytomedicine*, *19*(1), 64–73. https://doi.org/10.1016/j.phymed.2011.10.003

Nair, L. S., & Laurencin, C. T. (2007). Biodegradable polymers as biomaterials. In *Progress in Polymer Science (Oxford)* (Vol. 32, Numbers 8–9, pp. 762–798). https://doi.org/10.1016/j.progpolymsci.2007.05.017

Nguyen, H. X., Kipping, T., & Banga, A. K. (2025). Enhancement of Transdermal Drug Delivery: Integrating Microneedles with Biodegradable Microparticles. *Molecular Pharmaceutics*. https://doi.org/10.1021/acs.molpharmaceut.4c01202

Nim, B., Rahayu, S. S., Thananukul, K., Eang, C., Opaprakasit, M., Petchsuk, A., Kaewsaneha, C., Polpanich, D., & Opaprakasit, P. (2023). Sizing down and functionalizing polylactide (PLA) resin for synthesis of PLA-based polyurethanes for use in biomedical applications. *Scientific Reports*, *13*(1). https://doi.org/10.1038/s41598-023-29496-x

Novoveská, L., Nielsen, S. L., Eroldoğan, O. T., Haznedaroglu, B. Z., Rinkevich, B., Fazi, S., Robbens, J., Vasquez, M., & Einarsson, H. (2023). Overview and Challenges of Large-Scale Cultivation of Photosynthetic Microalgae and Cyanobacteria. In *Marine Drugs* (Vol. 21, Number 8). Multidisciplinary Digital Publishing Institute (MDPI). https://doi.org/10.3390/md21080445

Oh, N., & Park, J. H. (2014). Endocytosis and exocytosis of nanoparticles in mammalian cells. In *International Journal of Nanomedicine* (Vol. 9, Number SUPPL.1, pp. 51–63). Dove Medical Press Ltd. https://doi.org/10.2147/IJN.S26592

Oleksy, M., Dynarowicz, K., & Aebisher, D. (2023). Advances in Biodegradable Polymers and Biomaterials for Medical Applications—A Review. In *Molecules* (Vol. 28, Number 17). Multidisciplinary Digital Publishing Institute (MDPI). https://doi.org/10.3390/molecules28176213

Ong, R. R., & Goh, C. F. (2024). Niacinamide: a review on dermal delivery strategies and clinical evidence. *Drug Delivery and Translational Research*. https://doi.org/10.1007/s13346-024-01593-y

Otleş, S., & Pire, R. (2001). Fatty Acid Composition of Chlorella and Spirulina Microalgae Species. *DRUGS, COSMETICS, FORENSIC SCIENCES*, *84*(6). https://academic.oup.com/jaoac/article-abstract/84/6/1708/5656907

Pandel, R., Poljšak, B., Godic, A., & Dahmane, R. (2013). Skin Photoaging and the Role of Antioxidants in Its Prevention. *ISRN Dermatology*, *2013*, 1–11. https://doi.org/10.1155/2013/930164

Park, W. S., Kim, H. J., Li, M., Lim, D. H., Kim, J., Kwak, S. S., Kang, C. M., Ferruzzi, M. G., & Ahn, M. J. (2018). Two classes of pigments, carotenoids and c-phycocyanin, in Spirulina powder and their antioxidant activities. *Molecules*, *23*(8). https://doi.org/10.3390/molecules23082065

Pez Jaeschke, D., Rocha Teixeira, I., Damasceno Ferreira Marczak, L., & Domeneghini Mercali, G. (2021). Phycocyanin from Spirulina: A review of extraction methods and stability. In *Food Research International* (Vol. 143). Elsevier Ltd. https://doi.org/10.1016/j.foodres.2021.110314

Piao, M. J., Ahn, M. J., Kang, K. A., Ryu, Y. S., Hyun, Y. J., Shilnikova, K., Zhen, A. X., Jeong, J. W., Choi, Y. H., Kang, H. K., Koh, Y. S., & Hyun, J. W. (2018). Particulate matter 2.5 damages skin cells by inducing oxidative stress, subcellular organelle dysfunction, and apoptosis. *Archives of Toxicology*, *92*(6), 2077–2091. https://doi.org/10.1007/s00204-018-2197-9

Pillai, S., Oresajo, C., & Hayward, J. (2005). Ultraviolet radiation and skin aging: Roles of reactive oxygen species, inflammation and protease activation, and strategies for prevention of inflammation-induced matrix degradation - A review. In *International Journal of Cosmetic Science* (Vol. 27, Number 1, pp. 17–34). https://doi.org/10.1111/j.1467-2494.2004.00241.x

Pintea, A., Manea, A., Pintea, C., Vlad, R. A., Bîrsan, M., Antonoaea, P., Rédai, E. M., & Ciurba, A. (2025). Peptides: Emerging Candidates for the Prevention and Treatment of Skin Senescence: A Review. In *Biomolecules* (Vol. 15, Number 1). Multidisciplinary Digital Publishing Institute (MDPI). https://doi.org/10.3390/biom15010088

Place, E. S., George, J. H., Williams, C. K., & Stevens, M. M. (2009). Synthetic polymer scaffolds for tissue engineering. *Chemical Society Reviews*, *38*(4), 1139–1151. https://doi.org/10.1039/b811392k

Prabahar, K., Alanazi, Z., & Qushawy, M. (2021). Targeted drug delivery system: Advantages, carriers and strategies. In *Indian Journal of Pharmaceutical Education and Research* (Vol. 55, Number 2, pp. 346–353). Association of Pharmaceutical Teachers of India. https://doi.org/10.5530/ijper.55.2.72

Prabakaran, G., Sampathkumar, P., Kavisri, M., & Moovendhan, M. (2020). Extraction and characterization of phycocyanin from Spirulina platensis and evaluation of its anticancer, antidiabetic and antiinflammatory effect. *International Journal of Biological Macromolecules*, *153*, 256–263. https://doi.org/10.1016/j.ijbiomac.2020.03.009

Rachmawati, H., Yanda, Y. L., Rahma, A., & Mase, N. (2016). Curcumin-loaded PLA nanoparticles: Formulation and physical evaluation. *Scientia Pharmaceutica*, *84*(1), 191–202. https://doi.org/10.3797/scipharm.ISP.2015.10

Rafiee, M. H., & Rasool, B. K. A. (2022). An Overview of Microparticulate Drug Delivery System and its Extensive Therapeutic Applications in Diabetes. In *Advanced Pharmaceutical Bulletin* (Vol. 12, Number 4, pp. 730–746). Tabriz University of Medical Sciences. https://doi.org/10.34172/apb.2022.075

Ragusa, I., Nardone, G. N., Zanatta, S., Bertin, W., & Amadio, E. (2021). Spirulina for skin care: A bright blue future. *Cosmetics*, *8*(1), 1–19. https://doi.org/10.3390/cosmetics8010007

Ranakoti, L., Gangil, B., Bhandari, P., Singh, T., Sharma, S., Singh, J., & Singh, S. (2023). Promising Role of Polylactic Acid as an Ingenious Biomaterial in Scaffolds, Drug Delivery, Tissue Engineering, and Medical Implants: Research Developments, and Prospective Applications. In *Molecules* (Vol. 28, Number 2). MDPI. https://doi.org/10.3390/molecules28020485

Rancan, F., Papakostas, D., Hadam, S., Hackbarth, S., Delair, T., Primard, C., Verrier, B., Sterry, W., Blume-Peytavi, U., & Vogt, A. (2009). Investigation of polylactic acid (PLA) nanoparticles as drug delivery systems for local dermatotherapy. *Pharmaceutical Research*, *26*(8), 2027–2036. https://doi.org/10.1007/s11095-009-9919-x

Rangel, R., Swanson, W. B., & Wu, D. T. (2023). The future of cell-instructive biomaterials for tissue regeneration–a perspective from early career clinician-scientists. *Frontiers in Materials*, *10*. https://doi.org/10.3389/fmats.2023.1328904

Refai, H., El-Gazar, A. A., Ragab, G. M., Hassan, D. H., Ahmed, O. S., Hussein, R. A., Shabana, S., Waffo-Téguo, P., Valls, J., Al-Mokaddem, A. K., Selim, H. M. R. M., Yousef, E. M., Ali, S. K., Salman, A., Abo-Zalam, H. B., & Albash, R. (2023). Enhanced Wound Healing Potential of Spirulina platensis Nanophytosomes: Metabolomic Profiling, Molecular Networking, and Modulation of HMGB-1 in an Excisional Wound Rat Model. *Marine Drugs*, *21*(3). https://doi.org/10.3390/md21030149

Resende, D. I. S. P., Ferreira, M. S., Sousa-Lobo, J. M., Sousa, E., & Almeida, I. F. (2021). Usage of synthetic peptides in cosmetics for sensitive skin. *Pharmaceuticals*, *14*(8). https://doi.org/10.3390/ph14080702

Revete, A., Aparicio, A., Cisterna, B. A., Revete, J., Luis, L., Ibarra, E., Segura González, E. A., Molino, J., & Reginensi, D. (2022). Advancements in the Use of Hydrogels for Regenerative Medicine: Properties and Biomedical Applications. In *International Journal of Biomaterials* (Vol. 2022). Hindawi Limited. https://doi.org/10.1155/2022/3606765

Rodrigues, N., Benning, M., Ferreira, A. M., Dixon, L., & Dalgarno, K. (2016). Manufacture and Characterisation of Porous PLA Scaffolds. *Procedia CIRP*, *49*, 33–38. https://doi.org/10.1016/j.procir.2015.07.025

Rosario, J. C. J., & Josephine, R. M. (2015). Mineral profile of edible algae Spirulina platensis. *Int.J.Curr.Microbiol.App.Sci*, *4*, 478–483.

Rosell-Llompart, J., Grifoll, J., & Loscertales, I. G. (2018). Electrosprays in the cone-jet mode: From Taylor cone formation to spray development. In *Journal of Aerosol Science* (Vol. 125, pp. 2–31). Elsevier Ltd. https://doi.org/10.1016/j.jaerosci.2018.04.008

Roy, T., Boateng, S. T., Uddin, M. B., Banang-Mbeumi, S., Yadav, R. K., Bock, C. R., Folahan, J. T., Siwe-Noundou, X., Walker, A. L., King, J. A., Buerger, C., Huang, S., & Chamcheu, J. C. (2023). The PI3K-Akt-mTOR and Associated Signaling Pathways as Molecular Drivers of Immune-Mediated Inflammatory Skin Diseases: Update on Therapeutic Strategy Using Natural and Synthetic Compounds. In *Cells* (Vol. 12, Number 12). MDPI. https://doi.org/10.3390/cells12121671

Rutar, J. M., Cillero-Pastor, B., Mohren, R., Ulrih, N. P., Ogrinc, N., & Jamnik, P. (2021). Insight into the antioxidant effect of fermented and non-fermented Spirulina water and ethanol extracts at the proteome level using a yeast cell model. *Antioxidants*, *10*(9). https://doi.org/10.3390/antiox10091366

Saberian, M., & Shahidi Delshad, E. (2023). The role of Spirulina platensis on the proliferation of rat bone marrow-derived mesenchymal stem cells. *Iranian Journal of Microbiology*, *15*(1), 111–120. https://doi.org/10.18502/ijm.v15i1.11925

Sahil, S., Bodh, S., & Verma, P. (2024). Spirulina platensis: A comprehensive review of its nutritional value, antioxidant activity and functional food potential. *Journal of Cellular Biotechnology*, 1–14. https://doi.org/10.3233/jcb-240151

Samiksha B. Rotake, Pooja R. Hatwar, Ravindra L. Bakal, & Nitin B. Kohale. (2024). Transdermal drug delivery system recent advancements: A comprehensive review. *GSC Biological and Pharmaceutical Sciences*, *28*(2), 059–072. https://doi.org/10.30574/gscbps.2024.28.2.0269

Saura, M., Zaragoza, C., Cao, W., Bao, C., Rodríguez-Puyol, M., Rodríguez-Puyol, D., & Lowenstein, C. J. (2002). Smad2 mediates transforming growth factor-β induction of endothelial nitric oxide synthase expression. *Circulation Research*, *91*(9), 806–813. https://doi.org/10.1161/01.RES.0000040397.23817.E5

Schagen, S. K. (2017). Topical peptide treatments with effective anti-aging results. In *Cosmetics* (Vol. 4, Number 2). MDPI AG. https://doi.org/10.3390/cosmetics4020016

Shamszadeh, S., Akrami, M., & Asgary, S. (2022). Size-dependent bioactivity of electrosprayed core–shell chitosan-alginate particles for protein delivery. *Scientific Reports*, *12*(1). https://doi.org/10.1038/s41598-022-24389-x

Sharafeldein, K., Ayesh, H., Salama, S., & Marei, A. M. (2023). The collagen enhancement by Spirulina extract in intrinsic and extrinsic skin aging in albino rat. *The Journal of Basic and Applied Zoology*, *84*(1). https://doi.org/10.1186/s41936-023-00347-5

Shepherd, R. D., Kos, S. M., & Rinker, K. D. (2011). Flow-dependent Smad2 phosphorylation and TGIF nuclear localization in human aortic endothelial cells. *American Journal of Physiology - Heart and Circulatory Physiology*, *301*(1). https://doi.org/10.1152/ajpheart.00668.2010

Shete, Y., & Birade, P. (2024). A Comprehensive Examination of Potential of Peptides and their Role in Cosmeceuticals. *JOURNAL OF PHARMA INSIGHTS AND RESEARCH*. https://doi.org/10.5281/zenodo.10938661

Shi, H., & Feng, J. M. (2011). Aristolochic acid induces apoptosis of human umbilical vein endothelial cells in vitro by suppressing PI3K/Akt signaling pathway. *Acta Pharmacologica Sinica*, *32*(8), 1025–1030. https://doi.org/10.1038/aps.2011.74

Shi, X., Cui, L., Sun, H., Jiang, N., Heng, L., Zhuang, X., Gan, Z., & Chen, X. (2019). Promoting cell growth on porous PLA microspheres through simple degradation methods. *Polymer Degradation and Stability*, *161*, 319–325. https://doi.org/10.1016/j.polymdegradstab.2019.01.003

Shim, M. S., Nettesheim, A., Dixon, A., Liton, P. B., & Peters, D. (2021). Primary cilia and the reciprocal activation of AKT and SMAD2/3 regulate stretch-induced autophagy in trabecular meshwork cells. *Proc Natl Acad Sci U S A*. https://doi.org/10.1073/pnas.2021942118/-/DCSupplemental

Shin, S. H., Lee, Y. H., Rho, N. K., & Park, K. Y. (2023). Skin aging from mechanisms to interventions: focusing on dermal aging. In *Frontiers in Physiology* (Vol. 14). Frontiers Media S.A. https://doi.org/10.3389/fphys.2023.1195272

Shiojima, I., & Walsh, K. (2002). Role of Akt signaling in vascular homeostasis and angiogenesis. In *Circulation Research* (Vol. 90, Number 12, pp. 1243–1250). https://doi.org/10.1161/01.RES.0000022200.71892.9F

Sibiya, T., Ghazi, T., Mohan, J., Nagiah, S., & Chuturgoon, A. A. (2022). Spirulina platensis Ameliorates Oxidative Stress Associated with Antiretroviral Drugs in HepG2 Cells. *Plants*, *11*(22). https://doi.org/10.3390/plants11223143

Siepmann, J., Faisant, N., Akiki, J., Richard, J., & Benoit, J. P. (2004). Effect of the size of biodegradable microparticles on drug release: Experiment and theory. *Journal of Controlled Release*, *96*(1), 123–134. https://doi.org/10.1016/j.jconrel.2004.01.011

Sinetova, M. A., Kupriyanova, E. V., & Los, D. A. (2024). Spirulina/Arthrospira/Limnospira—Three Names of the Single Organism. In *Foods* (Vol. 13, Number 17). Multidisciplinary Digital Publishing Institute (MDPI). https://doi.org/10.3390/foods13172762

Snipstad, S., Westrøm, S., Mørch, Y., Afadzi, M., Åslund, A. K. O., & de Lange Davies, C. (2014). Contact-mediated intracellular delivery of hydrophobic drugs from polymeric nanoparticles. *Cancer Nanotechnology*, *5*(1), 1–18. https://doi.org/10.1186/s12645-014-0008-4

Soni, A. K., & Patil, S. G. (2023). A Review on Microparticles Drug Delivery System. *International Journal of Pharmaceutical Research and Applications*, *8*, 1355. https://doi.org/10.35629/7781-080413551362

Soni, R. A., Sudhakar, K., & Rana, R. S. (2017). Spirulina – From growth to nutritional product: A review. In *Trends in Food Science and Technology* (Vol. 69, pp. 157–171). Elsevier Ltd. https://doi.org/10.1016/j.tifs.2017.09.010

Sow, S., & Ranjan, S. (2021). Cultivation of Spirulina: An innovative approach to boost up agricultural productivity. *The Pharma Innovation*, *10*(3), 799–813. https://doi.org/10.22271/tpi.2021.v10.i3k.5889

Spínola, M. P., Mendes, A. R., & Prates, J. A. M. (2024). Chemical Composition, Bioactivities, and Applications of Spirulina (Limnospira platensis) in Food, Feed, and Medicine. In *Foods* (Vol. 13, Number 22). Multidisciplinary Digital Publishing Institute (MDPI). https://doi.org/10.3390/foods13223656

Stoyanova, N., Nachev, N., Georgieva, A., Toshkova, R., & Spasova, M. (2025). Electrospun Quercetin-Loaded PLA and PLA/Polyethylene Glycol Fibers: Preparation, Characterization, and In Vitro Evaluation. *Pharmaceutics*, *17*(5). https://doi.org/10.3390/pharmaceutics17050577

Suarez-Arnedo, A., Figueroa, F. T., Clavijo, C., Arbeláez, P., Cruz, J. C., & Muñoz-Camargo, C. (2020). An image J plugin for the high throughput image analysis of in vitro scratch wound healing assays. *PLoS ONE*, *15*(7 July). https://doi.org/10.1371/journal.pone.0232565

Sultana, A., Zare, M., Thomas, V., Kumar, T. S. S., & Ramakrishna, S. (2022). Nano-based drug delivery systems: Conventional drug delivery routes, recent developments

and future prospects. In *Medicine in Drug Discovery* (Vol. 15). Elsevier B.V. https://doi.org/10.1016/j.medidd.2022.100134

Suwanabol, P. A., Seedial, S. M., Zhang, F., Shi, X., Si, Y., Liu, B., & Craig Kent, K. (2012). TGF-and Smad3 modulate PI3K/Akt signaling pathway in vascular smooth muscle cells. *Am J Physiol Heart Circ Physiol*, *302*, 2211–2219. https://doi.org/10.1152/ajpheart.00966.2011.-Transforming

Syarina, P. N. A., Karthivashan, G., Abas, F., Arulselvan, P., & Fakurazi, S. (2015). Wound healing potential of Spirulina platensis extracts on human dermal fibroblast cells. *EXCLI Journal*, *14*, 385–393. https://doi.org/10.17179/excli2014-697

Tałałaj, U., Uscinowicz, P., Bruzgo, I., Surazynski, A., Zareba, I., & Markowska, A. (2019). The effects of a novel series of KTTKS analogues on cytotoxicity and proteolytic activity. *Molecules*, *24*(20). https://doi.org/10.3390/molecules24203698

Tamtaji, O. R., Heidari-soureshjani, R., Asemi, Z., & Kouchaki, E. (2023). The effects of Spirulina intake on clinical and metabolic parameters in Alzheimer's disease: A randomized, double-blind, controlled trial. *Phytotherapy Research*, *July 2022*, 1–8. https://doi.org/10.1002/ptr.7791

Tanhaei, A., Mohammadi, M., Hamishehkar, H., & Hamblin, M. R. (2021). Electrospraying as a novel method of particle engineering for drug delivery vehicles. In *Journal of Controlled Release* (Vol. 330, pp. 851–865). Elsevier B.V. https://doi.org/10.1016/j.jconrel.2020.10.059

Tapfumaneyi, P., Imran, M., Mohammed, Y., & Roberts, M. S. (2022). Recent advances and future prospective of topical and transdermal delivery systems. *Frontiers in Drug Delivery*, *2*. https://doi.org/10.3389/fddev.2022.957732

Tasci, M. E., Dede, B., Tabak, E., Gur, A., Sulutas, R. B., Cesur, S., Ilhan, E., Lin, C. C., Paik, P., Ficai, D., Ficai, A., & Gunduz, O. (2021). Production, optimization and characterization of polylactic acid microparticles using electrospray with porous structure. *Applied Sciences (Switzerland)*, *11*(11), 1–13. https://doi.org/10.3390/app11115090

Teekamp, N., Duque, L. F., Frijlink, H. W., Hinrichs, W. L., & Olinga, P. (2015). Production methods and stabilization strategies for polymer-based nanoparticles and microparticles for parenteral delivery of peptides and proteins. In *Expert Opinion on Drug Delivery* (Vol. 12, Number 8, pp. 1311–1331). Taylor and Francis Ltd. https://doi.org/10.1517/17425247.2015.1003807

Teng, Y., Fan, Y., Ma, J., Lu, W., Liu, N., Chen, Y., Pan, W., & Tao, X. (2021). The pi3k/akt pathway: Emerging roles in skin homeostasis and a group of non-malignant skin disorders. In *Cells* (Vol. 10, Number 5). MDPI. https://doi.org/10.3390/cells10051219

Terrisse, A. D., Puech, N., Allart, S., Gourdy, P., Xuereb, J. M., Payrastre, B., & Sié, P. (2010). Internalization of microparticles by endothelial cells promotes platelet/endothelial cell interaction under flow. *Journal of Thrombosis and Haemostasis*, *8*(12), 2810–2819. https://doi.org/10.1111/j.1538-7836.2010.04088.x

Thangsiri, S., Inthachat, W., Temviriyanukul, P., Sahasakul, Y., Trisonthi, P., Pan-Utai, W., Siriwan, D., & Suttisansanee, U. (2024). Bioactive compounds and in vitro biological properties of Arthrospira platensis and Athrospira maxima: a comparative study. *Scientific Reports*, *14*(1), 23786. https://doi.org/10.1038/s41598-024-74492-4

Thauvin, C., Widmer, J., Mottas, I., Hocevar, S., Allémann, E., Bourquin, C., & Delie, F. (2019). Development of resiquimod-loaded modified PLA-based nanoparticles for cancer immunotherapy: A kinetic study. *European Journal of Pharmaceutics and Biopharmaceutics*, *139*, 253–261. https://doi.org/10.1016/j.ejpb.2019.04.007

Torres-Moral, T., Tell-Martí, G., Bague, J., Rosés-Gibert, P., Calbet-Llopart, N., Mateu, J., Pérez-Anker, J., Potrony, M., Alejo, B., Iglesias, P., Espinosa, N., Orte Cano, C., Cinotti, E., Del Marmol, V., Fontaine, M., Miyamoto, M., Monnier, J., Perrot, J. L., Rubegni, P., … Puig, S. (2024). Evaluation of the Biological Effect of a Nicotinamide-Containing Broad-Spectrum Sunscreen on Photodamaged Skin. *Dermatology and Therapy*. https://doi.org/10.1007/s13555-024-01298-7

Trucillo, P. (2024). Biomaterials for Drug Delivery and Human Applications. In *Materials* (Vol. 17, Number 2). Multidisciplinary Digital Publishing Institute (MDPI). https://doi.org/10.3390/ma17020456

Uemura, M., Swenson, E. S., Gaça, M. D. A., Giordano, F. J., Reiss, M., & Wells, R. G. (2005). Smad2 and Smad3 play different roles in rat hepatic stellate cell function and α-smooth muscle actin organization. *Molecular Biology of the Cell*, *16*(9), 4214–4224. https://doi.org/10.1091/mbc.E05-02-0149

Varga, N., Turcsányi, Á., Hornok, V., & Csapó, E. (2019). Vitamin e-loaded pla- and plga-based core-shell nanoparticles: synthesis, structure optimization and controlled drug release. *Pharmaceutics*, *11*(7). https://doi.org/10.3390/pharmaceutics11070357

Vasudevan, S. K., Seetharam, S., Dohnalek, M. H., & Cartwright, E. J. (2021). Spirulina: A daily support to our immune system. *International Journal of Noncommunicable Diseases*, *6*(Suppl 1), S47–S54. https://doi.org/10.4103/2468-8827.330650

Veiga, E., Ferreira, L., Correia, M., Pires, P. C., Hameed, H., Araújo, A. R. T. S., Cefali, L. C., Mazzola, P. G., Hamishehkar, H., Veiga, F., & Paiva-Santos, A. C. (2023). Anti-aging peptides for advanced skincare: Focus on nanodelivery systems. In *Journal of Drug Delivery Science and Technology* (Vol. 89). Editions de Sante. https://doi.org/10.1016/j.jddst.2023.105087

Vinayak A. Katekar, Prafful P. Kothari, Aarti A. Nahar, Pooja A. Salve, Harsha H. Shendurkar, & Shruti A. Adhau. (2023). A review on recent advantages and evaluation of microparticles and their applications. *GSC Biological and Pharmaceutical Sciences*, *24*(2), 297–307. https://doi.org/10.30574/gscbps.2023.24.2.0320

Vlachopoulos, A., Karlioti, G., Balla, E., Daniilidis, V., Kalamas, T., Stefanidou, M., Bikiaris, N. D., Christodoulou, E., Koumentakou, I., Karavas, E., & Bikiaris, D. N. (2022). Poly(Lactic Acid)-Based Microparticles for Drug Delivery Applications: An

Overview of Recent Advances. In *Pharmaceutics* (Vol. 14, Number 2). MDPI. https://doi.org/10.3390/pharmaceutics14020359

Wang, J.-H. H., Ee, I.-T. L., Eng, K.-C. J., Ang, M.-F. W., Chien-Wei OU, R. H., U, S.-M. W., & Han, Y.-C. C. (2011). Spirulina Prevents Memory Dysfunction, Reduces Oxidative Stress Damage and Augments Antioxidant Activity in Senescence-Accelerated Mice. In *J Nutr Sci Vitaminol* (Vol. 57).

Wang, Jiamian, Jansen, J. A., & Yang, F. (2019). Electrospraying: Possibilities and challenges of engineering carriers for biomedical applications - a mini review. In *Frontiers in Chemistry* (Vol. 7, Number APR). Frontiers Media S.A. https://doi.org/10.3389/fchem.2019.00258

Wang, Jianqiang, Wu, Y., Chen, Z., Chen, Y., Lin, Q., & Liang, Y. (2022). Exogenous Bioactive Peptides Have a Potential Therapeutic Role in Delaying Aging in Rodent Models. In *International Journal of Molecular Sciences* (Vol. 23, Number 3). MDPI. https://doi.org/10.3390/ijms23031421

Wessels, Q., Pretorius, E., Smith, C. M., & Nel, H. (2014). The potential of a niacinamide dominated cosmeceutical formulation on fibroblast activity and wound healing in vitro. *International Wound Journal*, *11*(2), 152–158. https://doi.org/10.1111/j.1742-481X.2012.01052.x

Woodruff, M. A., & Hutmacher, D. W. (2010). The return of a forgotten polymer - Polycaprolactone in the 21st century. In *Progress in Polymer Science (Oxford)* (Vol. 35, Number 10, pp. 1217–1256). Elsevier Ltd. https://doi.org/10.1016/j.progpolymsci.2010.04.002

Wu, Q., Liu, L., Miron, A., Klímová, B., Wan, D., & Kuča, K. (2016). The antioxidant, immunomodulatory, and anti-inflammatory activities of Spirulina: an overview. In *Archives of Toxicology* (Vol. 90, Number 8, pp. 1817–1840). Springer Verlag. https://doi.org/10.1007/s00204-016-1744-5

Xu, J., & Hsu, S. H. (2023). Enhancement of Cell Behavior by the Polysaccharide Extract of Arthrospira and Potential Biomedical Applications. *Molecules*, *28*(2), 1–13. https://doi.org/10.3390/molecules28020732

Xu, N., Lao, Y., Zhang, Y., & Gillespie, D. A. (2012). Akt: A double-edged sword in cell proliferation and genome stability. In *Journal of Oncology*. https://doi.org/10.1155/2012/951724

Xu, Q., Hashimoto, M., Dang, T. T., Hoare, T., Kohane, D. S., Whitesides, G. M., Langer, R., Anderson, D. G., & David, H. (2009). Preparation of monodisperse biodegradable polymer microparticles using a microfluidic flow-focusing device for controlled drug delivery. *Small*, *5*(13), 1575–1581. https://doi.org/10.1002/smll.200801855

Xu, Y., & Hanna, M. A. (2006). Electrospray encapsulation of water-soluble protein with polylactide. Effects of formulations on morphology, encapsulation efficiency and release profile of particles. *International Journal of Pharmaceutics*, *320*(1–2), 30–36. https://doi.org/10.1016/j.ijpharm.2006.03.046

Xu, Y., & Hanna, M. A. (2008). Morphological and structural properties of two-phase coaxial jet electrosprayed BSA-PLA capsules. *Journal of Microencapsulation*, *25*(7), 469–477. https://doi.org/10.1080/02652040802049513

Yağmur, N., Şahin, S., & Korkmaz, E. (2021). Microencapsulation of ellagic acid extracted from pomegranate peel onto Spirulina: Characterization, loading, and storage stability properties. *Journal of Food Processing and Preservation*, *45*(1), 1–11. https://doi.org/10.1111/jfpp.15086

Yang, F., Zhang, X., Wang, H., Guo, M., Zhang, J., Feng, X., Yu, J., Yang, J., Zhu, J., & Wang, Y. (2024). Comprehensive evaluation of the efficacy and safety of a new multi-component anti-aging topical eye cream. *Skin Research and Technology*, *30*(7). https://doi.org/10.1111/srt.13790

Yang, L., Wang, Y., Zhou, Q., Chen, P., Wang, Y., Wang, Y., Liu, T., & Xie, L. (2009). Inhibitory effects of polysaccharide extract from Spirulina platensis on corneal neovascularization. In *Molecular Vision* (Vol. 15).

Yang, Zhenqi, Yin, G., Sun, S., & Xu, P. (2024). Medical applications and prospects of polylactic acid materials. In *iScience* (Vol. 27, Number 12). Elsevier Inc. https://doi.org/10.1016/j.isci.2024.111512

Yang, Zizhen, Wang, H., Liu, N., Zhao, K., Sheng, Y., Pang, H., Shao, K., Zhang, M., Li, S., & He, N. (2022). Algal polysaccharides and derivatives as potential therapeutics for obesity and related metabolic diseases. *Food and Function*, *115*, 11387–11409. https://doi.org/10.1039/d2fo02185d

Yu, Y. Q., Yang, X., Wu, X. F., & Fan, Y. Bin. (2021). Enhancing Permeation of Drug Molecules Across the Skin via Delivery in Nanocarriers: Novel Strategies for Effective Transdermal Applications. In *Frontiers in Bioengineering and Biotechnology* (Vol. 9). Frontiers Media S.A. https://doi.org/10.3389/fbioe.2021.646554

Zewail, M., Gaafar, P. M. E., Youssef, N. A. H. A., Ali, M. E., Ragab, M. F., Kamal, M. F., Noureldin, M. H., & Abbas, H. (2023). Novel Siprulina platensis Bilosomes for Combating UVB Induced Skin Damage. *Pharmaceuticals*, *16*(1). https://doi.org/10.3390/ph16010036

Zhang, K., Wang, S., Zhou, C., Cheng, L., Gao, X., Xie, X., Sun, J., Wang, H., Weir, M. D., Reynolds, M. A., Zhang, N., Bai, Y., & Xu, H. H. K. (2018). Advanced smart biomaterials and constructs for hard tissue engineering and regeneration. In *Bone Research* (Vol. 6, Number 1). Sichuan University. https://doi.org/10.1038/s41413-018-0032-9

Zhang, Leilei, Huang, J., Si, T., & Xu, R. X. (2012). Coaxial electrospray of microparticles and nanoparticles for biomedical applications. In *Expert Review of Medical Devices* (Vol. 9, Number 6, pp. 595–612). https://doi.org/10.1586/erd.12.58

Zhang, Lijuan, & Falla, T. J. (2009). Cosmeceuticals and peptides. *Clinics in Dermatology*, *27*(5), 485–494. https://doi.org/10.1016/j.clindermatol.2009.05.013

Zhang, Y., Kung, C. P., Iliopoulos, F., Sil, B. C., Hadgraft, J., & Lane, M. E. (2021). Dermal delivery of niacinamide—in vivo studies. *Pharmaceutics*, *13*(5). https://doi.org/10.3390/pharmaceutics13050726

Zhang, Y.-H., Cheng, F., Du, X.-T., Gao, J.-L., Xiao, X.-L., Li, N., Li, S.-L., & Dong, D.-L. (2016). GDF11/BMP11 activates both smad1/5/8 and smad2/3 signals but shows no significant effect on proliferation and migration of human umbilical vein endothelial cells. In *Oncotarget* (Vol. 7, Number 11). www.impactjournals.com/oncotarget/

Zhang, Z., Wu, L., Wang, J., Li, G., Feng, D., Zhang, B., Li, L., Yang, J., Ma, L., & Qin, H. (2014). Opposing effects of PI3K/Akt and smad-dependent signaling pathways in NAG-1-induced glioblastoma cell apoptosis. *PLoS ONE*, *9*(4). https://doi.org/10.1371/journal.pone.0096283

Zhen, A. X., Piao, M. J., Kang, K. A., Fernando, P. D. S. M., Kang, H. K., Koh, Y. S., Yi, J. M., & Hyun, J. W. (2019). Niacinamide protects skin cells from oxidative stress induced by particulate matter. *Biomolecules and Therapeutics*, *27*(6), 562–569. https://doi.org/10.4062/biomolther.2019.061

Zheng, Y., Hunt, R. L., Villaruz, A. E., Cheung, G. Y. C., Li, M., Zheng, Y., Hunt, R. L., Villaruz, A. E., Fisher, E. L., Liu, R., Liu, Q., Cheung, G. Y. C., & Li, M. (2022). Article Commensal Staphylococcus epidermidis contributes to skin barrier homeostasis by generating protective ceramides ll Article Commensal Staphylococcus epidermidis contributes to skin barrier homeostasis by generating protective ceramides. *Cell Host and Microbe*, *30*(3), 301-313.e9. https://doi.org/10.1016/j.chom.2022.01.004

Zhong, D., Zhang, D., Xie, T., & Zhou, M. (2020). Biodegradable Microalgae-Based Carriers for Targeted Delivery and Imaging-Guided Therapy toward Lung Metastasis of Breast Cancer. *Small*, *16*(20), 1–10. https://doi.org/10.1002/smll.202000819

BIOGRAPHY

Basak Dalbayrak completed her Bachelor of Science (B.Sc.) in Bioengineering at Istanbul Technical University and Montana State University in 2017. She received her Master of Science (M.Sc.) degree in Biomedical Engineering from Bogazici University in 2021. She continued her PhD journey at Gebze Technical University in the Institute of Biotechnology. Throughout her academic journey, Basak has been actively involved in multidisciplinary research projects, particularly focusing on biomaterials, tissue engineering, and regenerative medicine. She has participated in national and international projects funded by TUSEB, TUBITAK, and university research programs, contributing as a principal investigator, scholar, and researcher. Her work has resulted in several peer-reviewed publications and conference presentations in areas such as microcarrier systems, drug delivery, and advanced hydrogel technologies. Basak has gained professional experience through internships and research positions at institutions including Nobel Pharma, Okan University Hospital, Gisbir Hospital, and TOBB ETU Biomechanics Laboratory. She has also received scholarships and participated in international mobility programs such as ERASMUS+, and has been recognized for her academic achievements with various certificates and awards. In addition to her research, Basak is actively engaged in scientific communities, having served as Vice Chairman of the ITU Bioengineering Club and participated in numerous conferences and workshops. Her diverse skill set includes expertise in laboratory techniques, data analysis, and scientific communication.

PUBLICATIONS AND PRESENTATIONS FROM THE THESIS

Dalbayrak, B., Aksan Kurnaz, I., Cesur, S., Gunduz, O., & Arısan, E. D. (2025). Biocompatible PLA/Spirulina microparticles via electrospraying for targeted drug delivery in HUVEC and HaCaT cell lines. Journal of Biomaterials Science, Polymer Edition, 1-24.

Poster Presentation- Dalbayrak, B., Aksan Kurnaz, I., Cesur, S., Gunduz, O., & Arısan, E. D. (2024). Optimization and Characterization of Spirulina-Based Microcarrier Systems Produced by Electrospraying Technique. EFSUN Workshop entitled: Frontiers in Materials Surfaces and Interfaces.

Oral Presentation - Dalbayrak, B., Aksan Kurnaz, I., Cesur, S., Gunduz, O., & Arısan, E. D. (2024). Characterization and Investigation of Biological Effects of the Microalgae-Based Microcarrier Systems Produced by Electrospraying Technique. 1st International Congress on Biotech Solutions for Sustainability.